In vitro and in silico investigation of factors affecting damage related to hip impingement.

Taiyibah Memoona Afzal

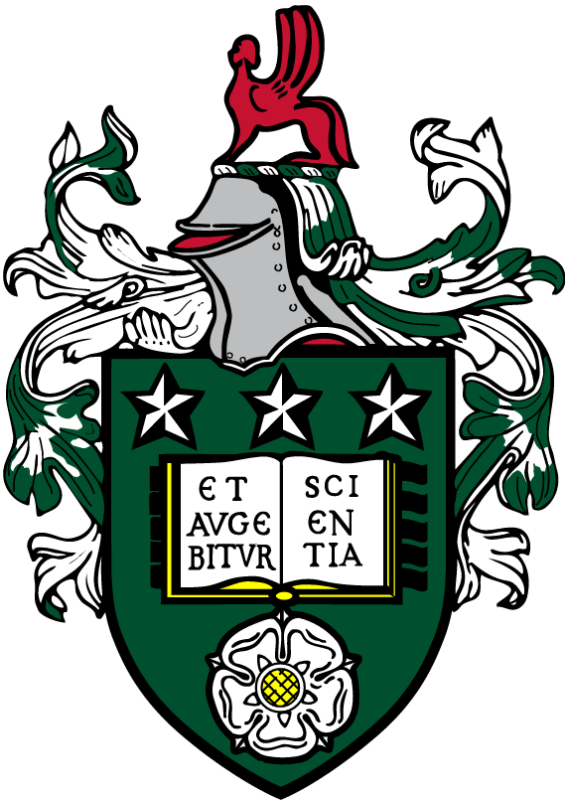

Submitted in accordance with the requirements for the degree of Doctor of Philosophy.

The University of Leeds
School of Mechanical Engineering

December 2025

I confirm that the work submitted is my own and that appropriate credit has been given where reference has been made to the work of others.

Acknowledgements

I would like to express my gratitude to the School of Mechanical Engineering for funding my PhD, and to my supervisors, Professor Sophie Williams and Dr Alison Jones, for their guidance, support and encouragement throughout this project. I am especially grateful to Dr David Jimenez Cruz for his invaluable help in the lab, his advice, and for always being there when things went wrong.

To my amazing parents, who have supported me unconditionally — thank you so much. You have been my biggest supporters through all the highs and lows of this PhD, and I am truly grateful that you were always there whenever I needed you.

To my best friends since secondary school, Emma and Emma – thank you for listening to every rant, for reassuring me, and for always being present and willing to hear my grievances.

During my PhD I have had the privilege of working alongside wonderful people who made the journey feel far more bearable and helped create a real sense of community. Thank you to Beth and Ahranee for the phone call conversations, and in particular to Sophie H for the walking breaks that kept me going. Nick – you're a star! Saudah and Tanya, thank you for always being supportive and for lifting morale when times were difficult. To my desk and snack buddies, Ollie and Meg, thank you for the everyday company that made long days easier.

This is by no means a complete list. There are so many more people I would love to thank, and one page simply is not long enough. I am sorry I cannot name everyone individually – you are all amazing, and it has been a privilege to work alongside you. I wish you all the very best in your own PhD journeys – you've got this.

Finally, I would like to thank the research and technical staff within the Institute of Medical and Biological Engineering for their expertise, guidance and support. In particular, my thanks go to Amisha, Phil Wood, Roberto and Rae, whose technical assistance and advice has been invaluable throughout this work.

Abstract

Femoroacetabular impingement (FAI) can cause hip pain; this can be debilitating, and surgery can be used to alleviate some symptoms. Prevalence of surgical interventions with the aim of alleviating pain and reducing tissue degeneration have increased in recent years. Data from the most recent Non-arthroplasty Hip Registry indicates that 95.6% of non-Arthroplasty hip femoral procedures performed were for the removal of cams (NAHR, 2024). Cam-type FAI is caused by an excess of bone on the femoral neck that in flexion abuts the acetabular rim. This can cause cartilage and labral damage due to increased contact pressure as the cam moves into the acetabulum. Damage mechanisms and the influence of individual mechanical factors are poorly understood. Understanding the biomechanics of FAI has the potential to modify existing and design new interventions to improve surgeries.

This thesis developed a method for parametrically assessing mechanical factors that may be associated with damage in hip impingement, using both experimental and computational methods. An adapted natural tissue in vitro simulation method was used to conduct parametric tests using porcine tissue. Three key parameters were investigated: sliding distance, load and direction. Damage to the natural tissue observations was recorded using photogrammetry and compared between parameter sets. A computational cam impingement hip shape model was used to quantify parameter ranges for a range of activities. Computationally and experimentally quantified real-world parameters were combined and assessed to determine their clinical relevance across findings.

To the author's knowledge, this thesis is the first to have assessed the impact of individual parameters on damage to the hip joint. The most severe types of damage observed experimentally were “blushing” and “bubbling” of the cartilage. The latter was thought to be a precursor to delamination, the type of damage often associated with in vivo cam FAI damage. Computational investigation resulted in identifying a set of quantified parameters that were likely to cause damage to the joint. However, it was not possible to highlight a single activity that would be considered the most likely to result in damage. Findings from both experimental and computational studies showed that an increased load (2500N), shorter sliding distance (±5°) and movements parallel to the cartilage labral junction resulted in the most severe/detrimental types of damage.

Table of Contents

Acknowledgements iii

Abstract iv

Table of Contents v

Table of Figures x

Table of Tables xxii

1 Literature review 25

1.1 General introduction 25

1.2 The Human hip 26

1.2.1 Anatomy 26

1.2.2 Labrum 29

1.2.3 Articular cartilage 32

1.2.4 Osteoarthritis 36

1.2.5 Movement 37

1.3 Femoroacetabular impingement 38

1.4 Quantification of cam-type hip shape 41

1.4.1 Measuring cam-type morphology 41

1.4.2 Size and location of cam lesions 43

1.4.3 Who is affected? 44

1.5 Damage in cam-type hip impingement 45

1.5.1 Mechanisms of cam FAI damage 46

1.5.2 Structural vulnerability and mechanisms of tissue failure 46

1.5.3 Clinical appearance of damage in cam-type FAI 47

1.5.4 Damage characterisation methods 48

1.6 Management of cam-type femoroacetabular impingement 52

1.6.1 Non-operative management 52

1.6.2 Surgical interventions 53
1.6.3 Why surgical practice has remained relatively stable? 54
1.7 Selection and suitability of animal models for in vitro hip impingement studies 55
1.8 Previous in vitro studies of mechanical damage in the hip joint 58
1.8.1 Experimental methods 58
1.8.2 In vitro simulation (Whole joint) 59
1.8.3 Replicating cam geometries 61
1.9 Hip Impingement and Activity 62
1.9.1 Mechanical Loading of the Hip Joint 62
1.9.2 Activities that Increase Prevalence of FAI 63
1.9.3 Effect of Hip Impingement on Hip Motion 64
1.10 Computational models of Cam-Type Femoroacetabular Impingement 65
1.10.1 Geometric Representation of the Hip 65
1.10.2 Types of Computational Models 66
1.10.3 Motion and Loading in Computational Models 67
1.10.4 Contact Pressure and the Role of FEA 67
1.10.5 Benefits and Drawbacks of FEA Compared with Simplified Models 67
1.10.6 Applications of FEA to Impingement Damage and Motion Limits 68
1.10.7 Gaps in Current Models and Contribution of This Work 69
2 Introduction 70
2.1 Rationale 70
2.2 Aim and Objectives 72
3 Development of experimental natural hip simulation using a parameterised approach. 74
3.1 Introduction 74
3.2 Preparation for in vitro simulator testing 75
3.2.1 Porcine hip dissection 76
3.2.2 Geometric measurements 81

3.2.3 Setup and alignment of porcine samples for in vitro hip simulation 83
3.2.4 Refinement of acetabulum alignment method 89
3.2.5 In vitro hip simulator test setup 93
3.3 Development of damage characterisation methods 98
3.3.1 Development of Photogrammetry method 99
3.3.2 Damage characterisation methodology 101
3.4 Development of natural (porcine) hip in vitro simulation methods. 109
3.4.1 Testing Parameters 111
3.4.2 Part 1: Preliminary testing 112
3.4.3 Part 2: Determining Refined Control parameters 124
3.5 Discussion 137
4 Sliding distance, dominant motion, and load during cam impingement 142
4.1 Introduction 142
4.2 Overview 143
4.3 Background methodology and case selection 146
4.3.1 Motion and force database 146
4.3.2 Hip joint shape and impingement model 147
4.3.3 Hip geometry: Shape selection and definitions 147
4.3.4 Hip motion data selection 151
4.3.5 Data filtering method 153
4.4 Quantifying sliding distance during cam-type hip impingement over a set of activities. 154
4.4.1 Method for quantifying sliding distance 155
4.4.2 Results from sliding distance study 163
4.4.3 Discussion of sliding distance study 166
4.5 Peak load during impingement 168
4.5.1 Methods for determining peak load during impingement 169
4.5.2 Results from peak loading study 172

4.5.3 Discussion of Peak load during impingement 177
4.6 Determine the dominant hip rotation during impingement. 179
4.6.1 Methods for determining dominant hip rotation 180
4.6.2 Results from dominant hip rotation study 188
4.6.3 Discussion of Dominant hip rotation 189
4.7 Discussion 191
5 Parameterised experimental natural hip testing: the effects of sliding distance and load 194
5.1 Introduction 194
5.2 Development of a “photography fixture” 195
5.3 Rationale for simulator input settings and parameter justifications 199
5.3.1 Direction of sliding 200
5.3.2 Load scaling and selection 201
5.3.3 Sliding distance feasibility and planned ranges 203
5.4 Initial Results from defined parameters 203
5.4.1 Feasibility of testing within simulator constraints 203
5.4.2 Moment analysis and selection of final sliding distance 206
5.4.3 Findings from Initial Parametric Tests 209
5.5 Application of the Final Parametric Testing Matrix 210
5.5.1 Effect of load 210
5.5.2 Effect of sliding distance 211
5.5.3 Incidences and type of zonal damage 212
5.5.4 Findings and implications 213
5.6 Discussion 215
6 Discussion 218
6.1 Introduction 218
6.2 Discussion of findings 219
6.3 Limitations 222

6.4 Future work 224

6.5 Conclusion 226

7 References 228

8 Appendices 243

8.1 Appendix A: Equipment list 243

8.2 Appendix B: Damage characterisation information sheet 244

8.3 Appendix C: Parametric testing photogrammetry results 246

8.4 Appendix D: Photography fixture drawings 253

8.6 Appendix E: Image permissions 257

Table of Figures

Figure 1: Schematic drawing of the hip joint. 27

Figure 2: Schematic drawing of the acetabulum. 28

Figure 3: Cross sectional diagram of the acetabular rim and labrum illustrating key anatomical features. Highlights the acetabulum, articular cartilage, tidemark, transitional fibrocartilaginous zone, labrum, and the hip capsule. The triangular profile of the labrum, its continuity with the articular cartilage through the transitional zone, and the relationship between the capsular side and articular side are shown. This structure provides the geometric basis for the labrum's sealing and load distributing functions (Adapted from Seldes et al. (2001)). 30

Figure 4: Diagram to illustrate the layered organisation of the labrum. A) The innermost layer located adjacent to the articulating surface, composed of randomly oriented fibrocartilage. B) The intermediate layer, consisting of collagen fibrils arranged in lamellar bundles that intersect at varying angles. C) The outermost layer located near the capsular attachment, composed of dense connective tissue with collagen fibrils aligned in a predominantly circumferential pattern (Adapted from Petersen et al. (2003)). 31

Figure 5: Schematic showing planes used to describe motion in the hip..... 37

Figure 6: Schematic drawing of the different types of impingement pincer (left) and cam (right). 39

Figure 7: Cam-type femoroacetabular impingement demonstrated using radiography and MRI. (A) Anteroposterior pelvic radiograph showing loss of femoral head–neck concavity. (B) Frog leg view highlighting the cam prominence and associated alpha angle. (C) Radial MRI illustrating reduced head–neck offset and associated contour abnormality. (D) Sagittal slice MRI demonstrating soft-tissue involvement at the chondrolabral junction. Reproduced with the permission of Albers et al. (2016). Copyright of Oxford University Press. (See 8.5 Appendix E) 40

Figure 8: Pincer-type femoroacetabular impingement shown using radiography & CT. (A) Anteroposterior pelvic radiograph demonstrating acetabular overcoverage characteristic of pincer morphology. (B) 3D CT image providing detailed visualisation of acetabular rim prominence & depth of overcoverage. Reproduced with the permission of Albers et al. (2016). Copyright of Oxford University Press. (See 8.5 Appendix E) 41

Figure 9: Oblique axial view parallel to femoral neck. (A & C) Alpha angle is measured by drawing a best fit circle over the femoral head, then measuring the angle between the midline of the femur and the point at which the neck no longer sits within the circle. (A) Represents “normal” joint and (C) cam type hip. (B & D) Head-neck offset ratio is calculated by measuring the distance between the two parallel lines for a & b, then calculating the ratio between them. (B) Represents “normal” joint and (D) cam type hip. Reproduced with the permission of Morris et al. (2018). Copyright of Oxford University Press. (See 8.5 Appendix E) 42

Figure 10: Overview of preparing a porcine tissue sample for in vitro simulation testing. .. 76

Figure 11: Right porcine hind leg. a) (Top) Lateral view of porcine hip and (Bottom) medial view of porcine hip with pelvic bone. b) Location of the hip joint capsule. c) Joint disarticulation and ligamentum teres severed. d) The femur's distal end was cut to the required length for potting. e) (Left) Dashed line represents cut line for removing the greater trochanter to prevent impingement. (Right) Acetabulum before potting. 79

Figure 12: Annotations of the right harvested porcine acetabulum and femur show the main structures of interest. 81

Figure 13: (Left) Circular templates used to measure femoral head size. (Right) Femoral head size was measured using the circular guide; the proximal end of the femur was placed into one of the holes, and once the epiphyseal line was parallel to the guide, this was considered the correct head size..... 82

Figure 14: Measuring the diameter of the acetabulum, with the TAL positioned inferiorly. (Left) Perpendicular measurement of the acetabulum starting in the centre of the TAL. (Right) Parallel measurement of the acetabulum. 83

Figure 15: Cementing rig used for aligning the acetabulum (left) and femur (right) correctly. 84

Figure 16: Potting fixtures used for in vitro simulations, (left) acetabular pot and (right) femur pot. 84

Figure 17: Overview of alignment & cementing process of the acetabulum. a) Femoral head size was measured using a template; the proximal end of the femur was placed into the template. When the guide reached the epiphyseal line, this was considered the correct head size. b) Height rig used to set the correct height of the acetabulum in the pot. c) Sample was positioned centrally, and the centre of the TAL was positioned 30° from the sagittal plane of the acetabular pot. Inclination angle was measured to desired angle. d) Using screws, the sample was held in place, and cement was poured in. 86

Figure 18: Overview of femur alignment and cementing process. a) The acetabular pot was mounted onto the femoral alignment rig. b) Proximal end of the femur was attached to the support ring. c) This was lowered into the acetabulum, and the inferior apex was aligned with the centre of TAL. d) Height guide placed across the top of the femoral potting rig; the distal end of the femur was in contact with the underside of the alignment plate. e) Femur removed from the supporting ring and inverted 180°. Supporting ring replaced. The acetabular pot was replaced with the femoral pot on the rig. f) (Left) The distal end of the femur was placed into the mounted femoral pot, and the height of the femur was checked using the height guide. (Right) The correctly aligned femur was then fixed into position with supporting screws, and cement was poured into the femoral pot and left to cure. 88

Figure 19: Revised acetabular pot design, four holes added equidistant around the outside of the pot. Screws were used to help maintain sample positioning and alignment during the cementation process..... 90

Figure 20: Porcine acetabulum positioned in the centre of the pot to ensure that the centre of rotation was coincident with the simulator. The centre of the TAL was rotated 30° clockwise from the AB plane; this was done to maintain the sample's neutral position. 91

Figure 21: The cement mantle was the same height as the labral edge of the porcine acetabulum. The restricted movement of the labrum during testing could lead to unwanted damage caused by the labrum abutting the cement mantle. A successful simulation required an unconstrained labrum edge. 92

Figure 22: Single station hip simulator. 94

Figure 23: Schematic of simulator fixtures, (from top down) acetabular adapter (pink), acetabular pot (blue), femoral pot (green) and femoral adapter (orange). 94

Figure 24: Virtual representations of the simulator component and direction of motions produced. a) Front view: adduction and abduction motions. b) Side view: flexion and extension motions. c) Top view: internal and external rotation. 96

Figure 25: a) Components set up within the simulator. b) Acetabulum lowered onto the femoral head until concentric. c) Gaiter covers the simulator set-up and is filled with Ringer's solution to keep the sample lubricated during testing. 97

Figure 26: Reflection of the PhotoBox light strip seen in images of the acetabulum. 100

Figure 27: Comparison of porcine hip images captured by two different users using the same photography methodology. Top row: wide-angle images; bottom row: macro images. Consistent image quality and perspective were achieved across users when identical camera settings were applied. 101

Figure 28: To assist in describing the location of damage, the hip was split into zones using the Ilizaliturri et al. (2008) zonal method. The acetabulum was divided into six zones using the acetabular notch as an anatomical landmark. This was then mirrored onto the femoral head. 105

Figure 29: Flow chart showing development of testing methodologies for in vitro porcine testing, and assessment of damage causing parameters. 110

Figure 30: Illustration of angular input and resulting arc lengths for a porcine femoral head (average diameter 35.6 mm). Graphs show angular motion across the gait cycle for ±5°, ±10°, and ±20°. Diagrams on the right depict the estimated arc length travelled by the contact point at peak angular displacement: ~1.6 mm for 5°, ~3.1 mm for 10°, and ~6.2 mm for 20°. 116

Figure 31: Front and side view diagrams of the initial experimental setup within the simulator. Both medial-lateral and anterior-posterior displacements were not restricted and left to move freely. Flexion-extension movements were applied to the femur; the acetabulum remained in a fixed position. 118

Figure 32: Parameterised simulator inputs. Axial force is applied for 60% of the gait cycle and increases gradually until it reaches its peak load at 30% of the gait cycle. It is then reduced, and the remaining cycle consists of a constant dwell period. 119

Figure 33: Photogrammetric results of in vitro simulations using Initial Control parameters (n=3). 120

Figure 34: Photogrammetric results from sliding distance comparison at 900N. 121

Figure 35: Photogrammetric results from sliding distance comparison at 1130N. 121

Figure 36: Photogrammetric results from two different loads (900N and 1130N) at a shorter sliding distance..... 122

Figure 37: Photogrammetric results from changing inclination angle at load of 1130N and sliding distance of ±10°. 122

Figure 38: Model of simulator components, lateral displacement was applied to the acetabular pot, constraining the femoral head and preventing dislocation of the sample during testing. 125

Figure 39: Typical simulator input, green dashed line represents the applied 1mm lateral displacement. 126

Figure 40: Model of simulator components. Movements parallel to the cartilage labral junction were completed using movements in the flexion-extension direction. Perpendicular movements were performed using abduction-adduction movements. 127

Figure 41: Contact area measurements: (a) Ink was smeared on the femoral head, the two parts were pushed together till concentric, and the simulator input profile was initiated. Ink was transferred from the head (b) to the acetabulum and was removed from areas where contact occurred (c). 128

Figure 42: Photogrammetric results for inclination angle tests with a 1mm lateral head constraint to improve stability of the simulation. At 35°, both bubbling and blushing were observed, whereas at 45° only blushing occurred. 129

Figure 43: Photogrammetric results showing the effects of the new head constraint on increased loading in the acetabulum. 130

Figure 44: Photogrammetric results showing the impact of directional changes on damage in the hip joint. 130

Figure 45: Photogrammetric results of contact space measurements for sample #228, repeated three times to determine repeatability of the contact area. 131

Figure 46: Photogrammetric results of contact space measurements for sample #174, repeated three times to determine repeatability of the contact area. 132

Figure 47: Photogrammetric results of contact space measurements for sample #122, repeated three times to determine repeatability of the contact area. 132

Figure 48: Photogrammetric results of contact area measurements for sample #174 under parallel and perpendicular motion profiles. One of three repeats for each case is illustrated. 133

Figure 49: Distribution of acetabular damage in Part 1 testing, reported using the Ilizaliturri et al. (2008) zonal method. Each occurrence of damage was assigned one point per affected

zone for each identified damage type. Where multiple damage types co-occurred within a zone, each was counted separately. Incidences per zone: Zone 1 = 1, Zone 2 = 8, Zone 3 = 9, Zone 4 = 6, Zones 5 and 6 = 0..... 134

Figure 50: Distribution of acetabular damage in Part 2 testing, reported using the Ilizaliturri et al. (2008) zonal method. Each occurrence of damage was assigned one point per affected zone for each identified damage type. Where multiple damage types co-occurred within a zone, each was counted separately. Incidences per zone: Zone 1 = 0, Zone 2 = 9, Zone 3 = 14, Zone 4 = 7, Zones 5 and 6 = 0..... 135

Figure 51: Flow chart showing the development of a computational model for the quantification of parameters associated with cam impingement..... 145

Figure 52: Findings from the Hip Impingement model by Jones et al. (2021). Two hip shape models were assessed: large superior (green) and small anterior (blue). Hip shapes were taken from literature, and each hip was aligned in a neutral position, defined by a set of bony alignment measures. Impingement incidences were higher in the anterior cam shape and were more likely to occur in non-walking type activities (replicated with permission)..... 148

Figure 53: Illustration of the anterior cam edge points used in the computational model. a) The alpha angle for each cam edge point is defined as the angle between a line along the femoral neck and a line from the femoral head centre to the cam edge (red curve), equivalent to the clinical alpha angle. b) Clockface representation showing the 24 discrete cam-neck edge points used to define the cam geometry in the model. These points provide the basis for the 3D impingement detection in this study. (Adpated from (Jones et al., 2023).) 149

Figure 54: Representation of the acetabular rim points used in the computational model. (A) Example of the angle defining a rim point, measured between the outward-facing normal of the acetabular plane and a line from the socket centre to the rim point. (B) Clockface layout showing all 21 discrete rim points distributed around the acetabular edge, forming the geometric basis for 3D impingement detection. (Adapted from (Jones et al., 2023).)..... 150

Figure 55: Example of the MATLAB cam impingement model during a squat activity. Black points represent the femoral cam edge, light blue points represent the acetabular rim, and

red points indicate cam points that have penetrated the acetabular rim, signifying impingement. Both femoral and acetabular points are referenced to a common joint centre, giving the appearance of a spherical femoral head. This visualisation exemplifies how impingement is detected by comparing 3D positions of the cam and rim throughout motion. 151

Figure 56: Participant demographics for hip angle and force data used (Layton et al., 2022b). Table of available hip angle data that resulted in an impingement event and the total number of trials for each activity. Table of available hip force data. 153

Figure 57: Flow chart outlining the algorithm developed to calculate sliding distance. Inputs from the impingement model (cam angles and cam positions) were used to identify impingement events and calculate sliding distances using three methods: full path, approximate, and scaled. Maximum values were extracted for each case and averaged at the subject and activity level. 156

Figure 58: Illustration of the sliding distance calculation for the cam impingement model. (A) 3D representation of all cam points (green) and acetabular rim points (purple). Cam points that have penetrated the rim are shown in orange, representing impingement. (B-C) Visualisation of a single cam point at successive cycle points during motion. (B) Approximate sliding distance, measured as the angle between the start and end points of the impingement event. (C) Full Path sliding distance, calculated by summing the angles between consecutive cam points throughout the entire impingement event. The black circle indicates the joint centre used as a reference for angle measurements. 158

Figure 59: Left) Output from the impingement event detection function. Column 1: cam point; Column 2: start of event; Column 3: end of event. Right) Cross-referencing with raw data confirmed that these values corresponded to negative cam angles, verifying that the detection function operated correctly. 161

Figure 60: Sliding distance array output from the code for a single motion case, showing the scaled (mm), approximate (°), and full path (°) sliding distances associated with detected impingement events. 161

Figure 61: Output from the code showing the maximum results array. The first three columns (activity, subject, and trial) are included to track individual cases. Only the longest full path sliding distance (in this example, cam point 12) was identified and carried forward for further analysis. 162

Figure 62: Verification of the sliding distance calculation: (a) formula for calculating the angle between two vectors, (b) screenshot of the computational code, and (c) replication of the calculation in Excel. 163

Figure 63: Verification of sliding distance values by comparison between manual Excel calculations (left) and computational code output (right). The two methods aligned, confirming the correct implementation of the methodology. 163

Figure 64: Subject Full Path sliding distances for each activity during impingement. The outer box is the interquartile range, the median is represented by the line going through the box, the cross is the mean, and the two whiskers on either side are the minimum and maximum values. 164

Figure 65: Comparison of methods used to calculate subject maximum sliding distance. Full Path sliding distance (blue) resulted in higher recorded sliding distances than the Approximate method (green). 165

Figure 66: Flowchart showing how force and angular data from the impingement model were processed to generate outcome measures, including peak load, impingement depth, and their locations. Functions developed in this work are shown in blue, with their inputs and outputs in white and green. 170

Figure 67: (a) Formula within the computational model used to calculate the resultant hip force from the three orthogonal force components. (b) Equivalent hand-written Excel formula used to verify the computational calculation. 171

Figure 68: (a) Resultant force values calculated by the computational model for a sample activity. (b) Verification of the same results using hand-written Excel calculations. Both

methods show identical resultant force values, confirming the accuracy of the computational approach. 172

Figure 69: Variability of the start and end point of impingement events at the subject level for the Golf Swing activity. Average activity impingement window (light grey), average activity resultant force (blue), the start (red) and end (green). 173

Figure 70: Location of impingement window for each activity. Start (blue circle) and end (green circle) of the impingement window, and the peak load (red triangle) throughout the entire cycle. 174

Figure 71: Average activity (red), maximum (blue) and minimum (green) subject resultant force for the whole activity cycle. Average activity impingement depth (purple), the minimum impingement depth (blue dot). Impingement window (dark grey) based on previous impingement event data, non-zero depth (dark grey) based on average activity impingement depth. 176

Figure 72: Flowchart showing algorithm for determining dominant hip rotation from motion data and impingement analysis outputs. Process identifies rotation amplitudes, selects the dominant rotation, and quantifies its relative dominance within the impingement window and across the whole event. 181

Figure 73: Raw hip angle data for a single trial from two activities. Amplitude for each hip rotation is calculated. Dominance was defined by the following equation $\boldsymbol{a} > \boldsymbol{b} + \boldsymbol{c}$. Magnitude of dominance was calculated as the ratio of the largest amplitude to the sum of the other two. Red represents the flexion-extension, blue abduction-adduction and green internal-external rotation. 182

Figure 74: Raw hip angle data for an activity with impingement windows shaded in grey. Amplitude for each hip rotation is calculated. Dominance was defined by the following equation $\boldsymbol{a} > \boldsymbol{b} + \boldsymbol{c}$. Magnitude of dominance was calculated as the ratio of the largest amplitude to the sum of the other two. Red represents the flexion-extension, blue abduction-adduction and green internal-external rotation. 183

Figure 75: (a) Maximum and minimum hip rotations and corresponding amplitudes during the impingement window calculated in the computational model. (b) Verification of the same results using hand-written Excel formulas. Both methods show consistent maximum, minimum, and amplitude values for each motion (flexion-extension, abduction-adduction, and internal-external rotation). 185

Figure 76: (a) Maximum and minimum hip rotations and corresponding amplitudes across the entire activity obtained from the computational model. (b) Verification of the same results using hand-written Excel formulas. Both methods show consistent maximum, minimum, and amplitude values for each motion (flexion-extension, abduction-adduction, and internal-external rotation). 186

Figure 77: (a) Formula used to determine the dominant hip rotation based on amplitude comparison (a > b + c). (b) MATLAB code used to implement the dominance calculation in the computational model. (c) Equivalent hand-written Excel formula for verifying the MATLAB outputs. 187

Figure 78: Comparison of results from the computational model and Excel verification for dominant hip rotation. Dominance is represented as a logical output, where 1 indicates a true (dominant) result and 0 indicates a false (non-dominant) result. Both methods produced identical outcomes, confirming the reliability of the computational approach. 188

Figure 79: a) Samples were cemented at an inclined angle, and as such, parts of the articulating surfaces were obstructed in resultant images. b) The initial solution was to raise the inferior edge of the cup holder so that the labral edge was parallel with the camera lens. c) Inferior edge of the cup holder was lifted, and the overall view of the sample was more complete. 196

Figure 80: 3D render of photography fixture. 198

Figure 81: Photograph of the photography fixture. 198

Figure 82: Pre- and post-test findings at ±35° sliding distance and 2500N load. Pre-test images show the intact femoral head (a) and acetabulum (b). Post-test, the femoral head displayed

an indent and surface ridge from cement mantle contact (c,d). At the same time, the acetabulum showed cracking at the inferior edge and exposure of the cement mantle superiorly (e,f), leading to head–cement contact and sample dislocation. 205

Figure 83: Diagram of femoral head setup in simulator, used to illustrate inputs for moment calculations. 207

Figure 84: Photogrammetric results, increasing load comparison from 1500N to 2500N, change in observed blushing and bubbling. 211

Figure 85: Photogrammetric results: Comparison of observed damage between extremes of sliding distance at 2500N. Shorter sliding distances showed more blistering, whereas longer sliding distances resulted in a larger spread of blushing. 211

Figure 86: Close-up photogrammetric result of extreme sliding distance findings. a) (sample K1) Short sliding distance ±5°, with very prominent blistering. b) (sample L2) Long sliding distance ±15° greater area of blushing. 212

Figure 87: Distribution of acetabular damage in Part 1 testing, reported using the Ilizaliturri et al. (2008) zonal method. Each occurrence of damage was assigned one point per affected zone for each identified damage type. Where multiple damage types co-occurred within a zone, each was counted separately. Incidences per zone: Zone 1 = 0, Zone 2 = 11, Zone 3 = 22, Zone 4 = 6, Zones 5 and 6 = 0..... 213

Table of Tables

Table 1: Widely accepted normal range of motion values in the hip (adapted from Nordin et al. (2022) 38

Table 2: Summary of arthroscopic damage characterisation methods (Beck et al., 2004; Ilizaliturri et al., 2008; Konan et al., 2011; Barros et al., 2019). 49

Table 3: Summary of the refinements made to the acetabular alignment process, including the justification for each adaptation and the added value to the accuracy and stability of the simulation. 92

Table 4: Single station hip simulator programmable ranges, accuracy of each motion, location motion is applied through..... 95

Table 5: Camera settings used during photogrammetry of tissue samples. 99

Table 6: Descriptors used in classifciation of damage created during in vitro simulations. 102

Table 7: Intra-observer reproducibility in damage classification across three time points. Shows the classifications made by one observer using the physical sample immediately after testing, then from images, and repeated two weeks later. (No change (green), Scratching (blue), Blushing (yellow), Delamination (red)). 107

Table 8: Inter-observer reproducibility in damage classification for eight samples by three observers at one time point..... 107

Table 9: Pairwise inter-observer agreement. Summarises the agreement between each pair of observers across the eight samples. Tick indicates agreement, cross indicates disagreement. Totals at the bottom indicate the overall frequency of agreement for each pair. 108

Table 10: Matrix of testing parameters used in in vitro simulations; letters denote testing code..... 111

Table 11: Summary of all parametrised testing and subsequent findings. 136

Table 12: Mean femoral head diameters for four different studies were found within the literature, and an average femoral head size was calculated. 159

Table 13: Mean and standard deviation of the Full Path sliding distance calculated across all subjects for each activity. Mean sliding distance across all activities was calculated. 164

Table 14: Mean Scaled sliding distance for all activities and standard deviation. 166

Table 15: Activity mean peak hip load (xBW) across the whole cycle and during impingement. 174

Table 16: Average peak load during impingement for each activity and the point in the cycle when the impingement occurred. The maximum and minimum subject peak load for each activity across the whole cycle. 175

Table 17: Average activity amplitude angle and dominant direction during impingement and throughout whole event. Colour coding in the last three columns shows wether the activity is dominant in accordance with the dominant direction formula. Green indicates a dominant direction and red not dominant. 189

Table 18: Design requirements, measurable specifications, and design solutions for a photography fixture. 197

Table 19: Original proposed matrix of testing parameters as informed by experimental and computational findings. Each set of test parameters (white) would have been compared to the Refined Control conditions (green). 200

Table 20: List of heights and weights for FAI participant groups from literature..... 201

Table 21: Converted human and porcine loads for the average activity during impingement and maximum load for a subject for a set of activities. 201

Table 22: Findings of moment arm calculations, used to determine appropriate sliding distances for use in experimental testing. Green represents previous successful tests completed, Red represents tests that failed and Grey represents the sliding distance length to test. 208

Table 23: Calculated moments at a reduced load of 2000N across different motion ranges. 208

Table 24: Final matrix of testing parameters used in in vitro simulations; letters denote test code. Each set of test parameters (white) was compared to the Refined Control condition (green). 210

Chapter 1

1 Literature review

1.1 General introduction

Hip pain in young and active adults is increasingly recognised as a major contributor to reduced quality of life and loss of mobility. Femoroacetabular impingement (FAI) is now one of the most common structural causes of this problem, with cam-type FAI particularly associated with activity-related groin pain, reduced range of motion and limitations in sport and daily function (Byrd, 2014; Griffin et al., 2016). For many patients these symptoms arise during the years in which they are most physically active, affecting work, exercise and long-term joint health.

Cam morphology is clinically important not only because it causes pain, but because it is strongly linked to the early onset of hip osteoarthritis. When the aspherical femoral head–neck junction comes into contact with the acetabular rim, it generates concentrated shear forces that damage the labrum and the superficial cartilage (Beck et al., 2005; Albers et al., 2016). Once this structural integrity is disrupted, the joint becomes less able to maintain fluid pressurisation and lubrication, leading to further mechanical overload and initiating biological changes associated with degeneration (Schmidt et al., 2007; Katta et al., 2008; Zimmerman et al., 2021). This combination of mechanical and biological processes explains why cam morphology is one of the clearest predictors of osteoarthritis in young adults.

Given the significant personal and societal impact of early hip degeneration, understanding how cam morphology develops, how it alters joint mechanics, and why certain movement patterns lead to characteristic damage is essential. The purpose of this literature review is

therefore to establish the anatomical, mechanical and clinical foundations necessary to interpret the experimental and computational work in this thesis. It outlines the relevant hip anatomy, mechanisms of impingement, methods for identifying and quantifying cam-type shape, the populations most affected, and the current clinical approaches to treatment. It also critically evaluates existing in vitro and computational models to explain the rationale for the methods adopted in the research that follows.

1.2 The Human hip

1.2.1 Anatomy

The hip is a load bearing synovial ball and socket joint in which the femoral head of the femur articulates with the acetabulum of the pelvis. It links the lower limb to the axial skeleton and must combine stability for weightbearing with sufficient freedom for locomotion and complex daily activities (Keogh and Batt, 2008). Articular cartilage covers the contacting surfaces to provide a low friction interface and to transmit load to the underlying bone.

The proximal femur has several key landmarks: the femoral head, neck, shaft, and the greater and lesser trochanters (Figure 1). The femoral head is not perfectly spherical; roughly two thirds of its surface is smooth and covered by hyaline cartilage, leaving the fovea capitis as a small non articulating depression (Tronzo, 1984; Palastanga, 2002). The femoral neck connects head to shaft and forms an angle with the shaft typically in the range 125° to 135°, with variation by age and sex (Tronzo, 1984; Palastanga, 2002). The trochanters are roughened projections for muscle attachment and influence the moment arms of the surrounding hip muscles.

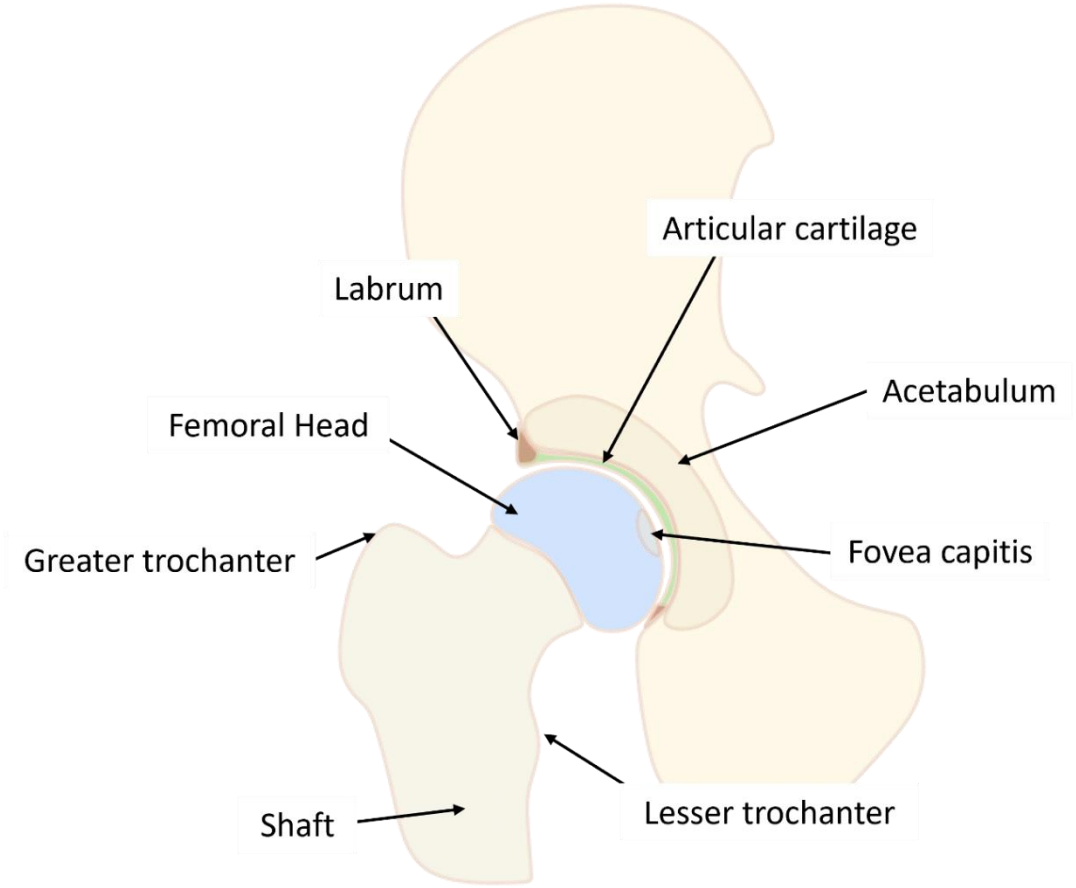

Figure 1: Schematic drawing of the hip joint.

The acetabulum is formed by the fusion of the ilium, ischium and pubis and presents a deep, crescent or half moon shaped articulating surface, the lunate surface, which is covered by hyaline cartilage (Figure 2) (Palastanga, 2002; Calais-Germain, 2007). The acetabular fossa occupies the central non articulating region. The acetabular rim is completed inferiorly by the transverse acetabular ligament that bridges the acetabular notch and permits neurovascular entry into the fossa. Around the rim sits the fibrocartilaginous labrum, which increases concavity and contributes to joint sealing (Palastanga, 2002; Büchler and Keel, 2019).

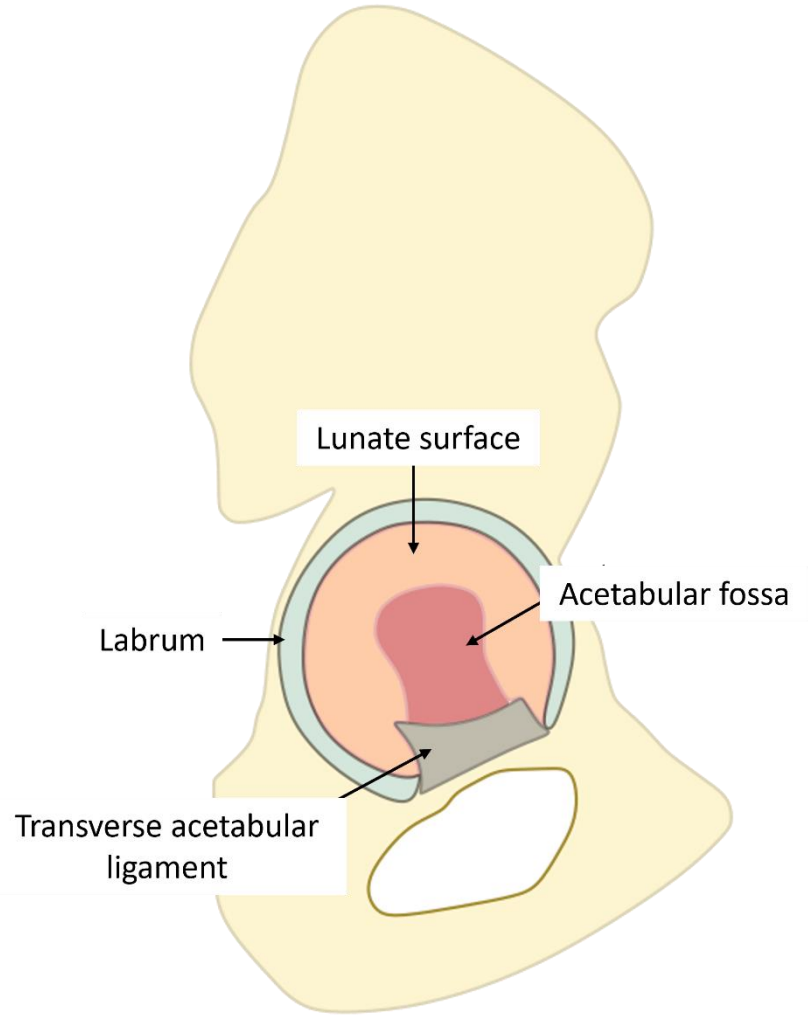

Figure 2: Schematic drawing of the acetabulum.

Movement is produced and constrained by a combination of muscles (21 muscles acting across the hip grouped functionally into flexors, extensors, abductors, adductors, internal and external rotators), the capsuloligamentous complex and the joint geometry (Ranawat and Kelly, 2005; Lunn et al., 2016). The fibrous capsule acts as a closely fitted cuff attaching to the acetabular rim and the base of the femoral neck; it is reinforced by the iliofemoral, pubofemoral and ischiofemoral ligaments which limit excessive translation and rotation (Tronzo, 1984; Calais-Germain, 2007; Lunn et al., 2016). The ligamentum teres connects the acetabular notch and transverse acetabular ligament to the fovea capitis; while not a primary stabiliser in the adult, it is anatomically present and may have roles in joint protection and vascular supply during development (Palastanga, 2002).

1.2.2 Labrum

The acetabular labrum plays an essential role in maintaining hip stability, preserving synovial fluid mechanics and protecting the articular surfaces during daily and high demand activities. Its structure and material composition are closely linked to these functions, and understanding this relationship is important for interpreting patterns of injury, particularly in the context of femoroacetabular impingement.

1.2.2.1 Structure and composition

The acetabular labrum is a triangular wedge shaped ring of fibrocartilage that attaches circumferentially to the acetabular rim and slightly overhangs the femoral head (Figure 3) (Seldes et al., 2001; Palastanga, 2002). In cross section it has a broad base at the acetabular margin and a tapering free edge that blends with the adjacent articular cartilage through a transitional fibrocartilaginous zone and a distinct tidemark (Seldes et al., 2001; Petersen et al., 2003).

Its matrix is composed predominantly of type I collagen arranged circumferentially around the rim, supported by smaller oblique and radial bundles that help stabilise the tissue under complex loading (Seldes et al., 2001; Petersen et al., 2003). Proteoglycan content is lower than in hyaline cartilage, consistent with its primary tensile function.

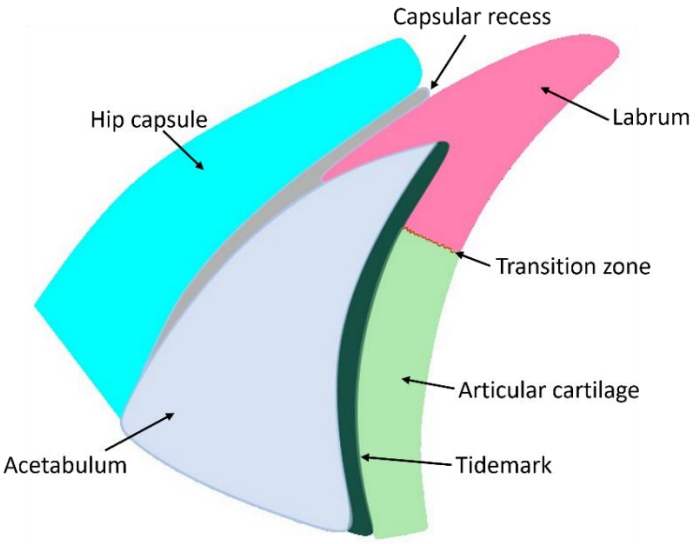

Figure 3: Cross sectional diagram of the acetabular rim and labrum illustrating key anatomical features. Highlights the acetabulum, articular cartilage, tidemark, transitional fibrocartilaginous zone, labrum, and the hip capsule. The triangular profile of the labrum, its continuity with the articular cartilage through the transitional zone, and the relationship between the capsular side and articular side are shown. This structure provides the geometric basis for the labrum's sealing and load distributing functions (Adapted from Seldes et al. (2001)).

Structurally, the labrum is organised into three layers (Figure 4) (Petersen et al., 2003; Safran and Hariri, 2010; Bsat et al., 2016; Büchler and Keel, 2019). The thin innermost layer, located at the chondrolabral junction, consists of delicate, randomly oriented fibrocartilage. The middle layer contains lamellar bundles of collagen that intersect at varying angles, providing resistance to multidirectional loading. The outermost layer, closest to the hip capsule, is the thickest and is composed of dense connective tissue with collagen fibrils arranged predominantly in a circumferential direction.

Figure 4: Diagram to illustrate the layered organisation of the labrum. A) The innermost layer located adjacent to the articulating surface, composed of randomly oriented fibrocartilage. B) The intermediate layer, consisting of collagen fibrils arranged in lamellar bundles that intersect at varying angles. C) The outermost layer located near the capsular attachment, composed of dense connective tissue with collagen fibrils aligned in a predominantly circumferential pattern (Adapted from Petersen et al. (2003)).

Vascularity is mainly restricted to the outer (peripheral) region, near the capsular attachment, while the inner articular portion remains avascular and reliant on synovial diffusion (Seldes et al., 2001). Sensory fibres accompany the peripheral vessels and are concentrated near the base and articular margin, supporting proprioception and sensitivity to mechanical loading (Büchler and Keel, 2019). Geometry also varies regionally, with the anterosuperior labrum typically thicker and broader, reflecting the higher mechanical demands encountered during flexion and internal rotation (Palastanga, 2002).

1.2.2.2 Mechanical function

The labrum deepens the acetabulum and contributes approximately 33 percent of the combined acetabular volume (Palastanga, 2002; Büchler and Keel, 2019). More than half of the femoral head is securely contained within this structure, supported by a tight pressurised seal between the labrum and femoral head (Keogh and Batt, 2008; Bsat et al., 2016; Büchler and Keel, 2019). Any attempt to distract the joint generates a negative pressure gradient, enhancing stability and reducing strain on the underlying cartilage.

The fluid seal also creates a pressurised environment that retains synovial fluid within the joint space. This supports a nutrient rich milieu and enables the formation of a uniform fluid film across the articulating surfaces, improving lubrication and reducing friction during movement (Keogh and Batt, 2008; Bsat et al., 2016).

The circumferential collagen fibres allow the labrum to resist hoop stress, a tensile force that develops around the curved rim when the femoral head pushes outward during loading. This property helps redistribute loads away from the cartilage and stabilises the joint during activities involving rotation or weight bearing.

1.2.2.3 Labral damage

Although the circumferential collagen architecture enables the labrum to resist tensile forces, repetitive rim loading or excessive mechanical demand can produce longitudinal splits or partial separation at the attachment site or along the chondrolabral junction (Seldes et al., 2001; Narvani et al., 2003). The transitional region between fibrocartilage and hyaline cartilage, marked by the tidemark, represents a mechanically vulnerable interface, particularly where tissue integration is less uniform.

This vulnerability is heightened in the anterosuperior quadrant, where combined flexion and internal rotation generate higher shear forces. These structural and loading characteristics are consistent with the predominance of anterosuperior labral tears reported clinically and in cadaveric studies (Seldes et al., 2001; McCarthy et al., 2003).

1.2.3 Articular cartilage

Articular cartilage provides the hip with a smooth, low friction surface and protects the underlying bone by distributing load during weightbearing activities. Its structure varies with depth, and its mechanical behaviour reflects interactions between the solid extracellular matrix and the interstitial fluid contained within it. Together, these features enable the tissue to support substantial forces while maintaining joint mobility and resisting wear. They also shape how cartilage responds to abnormal loading environments such as those present in femoroacetabular impingement (FAI).

1.2.3.1 Structure and composition

Articular cartilage is a specialised hyaline tissue composed of water, type II collagen, proteoglycans and chondrocytes arranged in depth dependent zones (Bhosale and Richardson, 2008; Little et al., 2011; Eschweiler et al., 2021). Water is the most abundant

component, accounting for 70–85% of the total weight, with the highest concentration in the superficial zone. Water is critical for both lubrication and load support. The high water content allows the tissue to deform under load, store elastic energy, and redistribute pressure, while also supporting fluid film lubrication at the joint surface. This reliance on water balance is clinically important because changes in tissue hydration and osmotic pressure are early features of osteoarthritis.

Collagen contributes 60–70% of the dry weight, forming the fibrillar scaffold responsible for tensile strength and shape retention. Proteoglycans make up roughly 30% of the dry weight and play a key role in resisting compression through their ability to attract and retain water. Chondrocytes comprise around 2% of the tissue volume and are responsible for synthesising and maintaining the extracellular matrix.

Cartilage thickness is not uniform across the acetabulum. It is typically thickest anterosuperiorly, where contact stresses are greatest, and thinnest adjacent to the acetabular fossa (Büchler and Keel, 2019).

The tissue is commonly described in four zones:

- The superficial zone contains flattened chondrocytes and collagen fibrils aligned parallel to the surface, providing shear resistance and maintaining smooth articulation.
- The middle (transitional) zone has a more random fibril orientation and dissipates strain between superficial and deep layers.
- The deep zone contains vertically aligned fibrils and the highest proteoglycan concentration, providing compressive stiffness.
- Finally, the calcified zone anchors the tissue to subchondral bone through the tidemark (Little et al., 2011; Eschweiler et al., 2021).

This gradual change in composition and organisation allows the tissue to resist combined compressive and shear forces effectively.

1.2.3.2 Biphasic behaviour and load support

Articular cartilage behaves as a biphasic material, meaning it is composed of two interacting phases: a solid matrix of collagen and proteoglycans, and a fluid phase formed by the interstitial water occupying the matrix pores. When the tissue is loaded, the interstitial fluid becomes pressurised and initially carries much of the load, limiting deformation of the solid matrix (Mow et al., 1980; Little et al., 2011). With sustained loading, fluid gradually exudes from the tissue and the solid matrix takes up a greater proportion of the load. This shifting balance between fluid support and matrix deformation gives rise to the tissue's viscoelastic behaviour, in which the mechanical response depends on both the magnitude and the duration of loading.

As a result, cartilage does not behave like a simple elastic material. Instead, it displays creep, where deformation increases gradually under a constant load, and stress relaxation, where stress declines over time under a constant deformation. These time dependent responses allow cartilage to absorb impact, redistribute forces across the joint and minimise stress concentrations at the bone–cartilage interface.

1.2.3.3 Synovial fluid

Synovial fluid plays an essential role in maintaining the normal function of the hip joint. It is an ultrafiltrate of plasma enriched with molecules produced by the synovial membrane, including hyaluronan, lubricin and phospholipids (Schmidt et al., 2007; Katta et al., 2008). These molecules give synovial fluid its distinct viscoelastic behaviour, allowing it to resist rapid deformation and support load during movement. Its viscosity changes with shear rate, becoming less viscous during fast motion and more viscous at slower rates, which helps stabilise the lubrication environment during different activities.

A further function of synovial fluid is maintaining the osmotic and ionic environment required for cartilage health. The high glycosaminoglycan content of the cartilage matrix draws water into the tissue, while synovial fluid provides the external environment that helps regulate this balance. Zimmerman et al. (2021) showed that changes in osmotic pressure influence how cartilage retains or releases interstitial fluid, underscoring the importance of synovial composition for sustaining normal hydration and mechanical function. Synovial fluid also

supplies nutrients to the avascular cartilage surface and removes metabolic waste. Together, these properties allow synovial fluid to support load transfer, protect the cartilage surface and maintain the fluid environment required for normal joint function.

1.2.3.4 Lubrication mechanisms in the hip

Lubrication in the hip is maintained through several complementary mechanisms that work together to control friction and protect the articular surfaces:

- Fluid film lubrication arises from interstitial fluid pressurisation within the cartilage. During rapid or cyclic loading, this pressurised fluid supports most of the applied load and separates the surfaces, maintaining very low friction (Katta et al., 2008).
- Boundary lubrication is provided by molecules within synovial fluid, including hyaluronan, lubricin and surface active phospholipids. These molecules adsorb to the cartilage surface and create a protective molecular layer that resists shear when the joint surfaces come into close contact (Schmidt et al., 2007; Katta et al., 2008).
- Mixed lubrication operates during much of normal motion, where fluid pressurisation persists but boundary lubricants also contribute. This regime reflects the balance between load support from interstitial fluid and the surface protection provided by synovial molecules.

The ability of cartilage to sustain these lubrication regimes depends on its high water content and the fixed negative charges of proteoglycans, which draw in and retain interstitial fluid. This helps maintain internal pressure and slows the rate of fluid exudation under load. Synovial fluid also plays a key role in maintaining the osmotic environment around the tissue. Zimmerman et al. (2021) demonstrated that changes in osmotic pressure can influence how cartilage retains or releases water, affecting its ability to support fluid film lubrication. Disturbances in hydration, alterations in synovial fluid composition, or damage to the cartilage surface can therefore reduce lubrication efficiency and accelerate wear.

1.2.3.5 Cartilage damage

The pattern of cartilage damage reflects its depth dependent structure and biphasic behaviour. The earliest changes typically occur in the superficial zone, where the collagen

fibrils are aligned parallel to the surface. Shear forces disrupt this network, producing surface fibrillation, loss of smoothness and weakening of the lamina splendens. As loading continues, reduced fluid pressurisation increases strain within the middle and deep zones. Proteoglycan loss, matrix softening and internal fissures develop, reflecting the tissue's reduced ability to retain water and resist compression.

As damage progresses, these internal defects may extend towards the subchondral bone, resulting in full thickness cartilage loss. At this stage, the bone becomes exposed and friction increases, accelerating wear and greatly increasing mechanical stress. The tidemark, which forms the interface between the deep zone and calcified cartilage, is also a mechanically vulnerable plane. Because the calcified layer is much stiffer than the uncalcified cartilage above it, repeated loading can cause delamination, where the layers begin to separate.

These damage pathways are consistent with the patterns observed in early osteoarthritis and in mechanical environments where load is abnormally concentrated, such as in femoroacetabular impingement.

1.2.4 Osteoarthritis

Osteoarthritis is a progressive joint disorder characterised by deterioration of the articular cartilage and accompanying changes in the subchondral bone and synovial tissues. The earliest structural changes typically occur within the superficial cartilage layer, where disruption of the collagen network and loss of proteoglycans reduce the tissue's ability to maintain fluid pressurisation and resist shear. As degeneration progresses, the cartilage becomes softer, more permeable and less capable of sustaining compressive loads, leading to fibrillation, fissuring and eventual full thickness cartilage loss (Little et al., 2011; Bhosale and Richardson, 2008). These structural changes account for the clinical features of OA, including pain, stiffness and reduced range of motion. Although multiple factors contribute to its development, including ageing, mechanical overload and joint morphology, the central pathological feature is the gradual failure of the articular cartilage to maintain its normal mechanical and biological function.

1.2.5 Movement

The hip joint permits movement in three planes and has a large overall range of motion. Hip motion is typically described in terms of flexion and extension in the sagittal plane, abduction and adduction in the frontal plane, and internal and external rotation in the transverse plane (Figure 5). These movements occur around three orthogonal axes that intersect at the centre of the femoral head. In a healthy hip, rotational movements are largely unconstrained, while excessive anterior to posterior or medial to lateral translation is restricted by the joint capsule, ligaments and surrounding musculature.

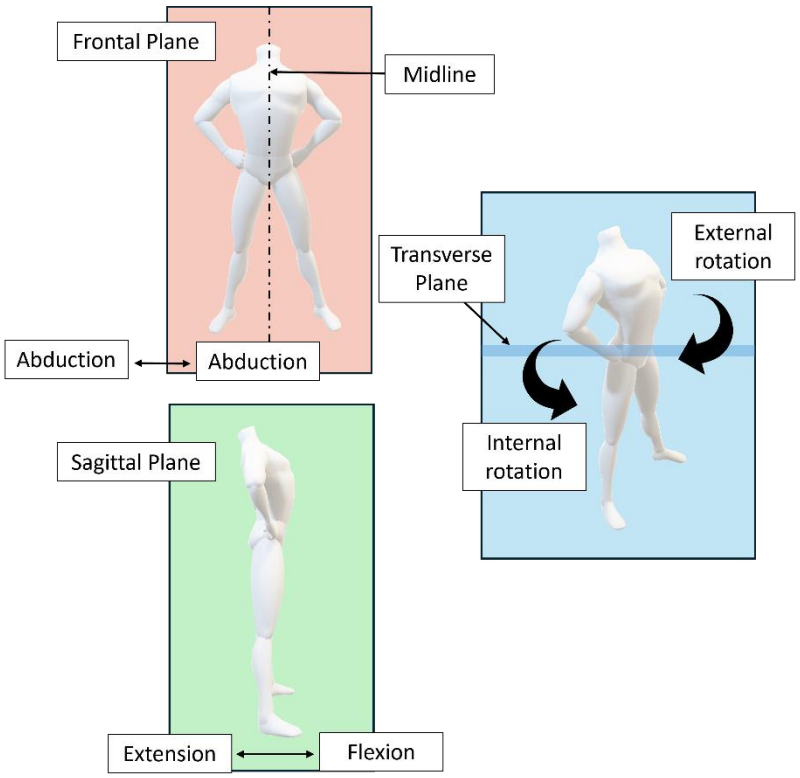

Figure 5: Schematic showing planes used to describe motion in the hip.

Although range of motion varies between individuals, Table 1 summarises widely accepted reference values for a normal hip joint. Flexion and extension in the sagittal plane provide the greatest range of movement. Overall, the physiological range of motion of the hip exceeds that required for most activities of daily living.

Table 1: Widely accepted normal range of motion values in the hip (adapted from Nordin et al. (2022) .

Plane	Movement	Normal Range of Motion
Sagittal	Flexion	0° - 140°
	Extension	15° - 0°
Frontal	Abduction	0° - 30°
	Adduction	25° - 0°
Transverse	External Rotation	0° - 90°
	Internal Rotation	70° - 0°

1.3 Femoroacetabular impingement

Descriptions of femoroacetabular impingement (FAI) within the literature are often inconsistent, particularly where symptomatic and asymptomatic findings are reported together (Griffin et al., 2016). To address this, the Warwick Agreement provides a clinically accepted definition, stating that a diagnosis of FAI should be based on the combined presence of symptoms, clinical signs and imaging findings. Morphology alone is not sufficient for diagnosis, and many individuals with cam or pincer features remain asymptomatic.

FAI arises from abnormal bone morphology at the acetabulum, femoral head neck junction or both. During movements such as flexion, rotation or combined motion, these regions come into earlier or more forceful contact than in a normally shaped joint, creating pain, reduced range of motion and, over time, damage to the labrum and cartilage (Byrd, 2014; Griffin et al., 2016). The most common symptom is groin pain, although discomfort can radiate to the lateral hip, thigh or buttock and may occur during high demand activities, routine movements or even sedentary postures.

A range of clinical tests are used to support the diagnosis of FAI, and these rely on provoking the patient's symptoms by placing the hip into positions where abnormal bony contact is most likely to occur. The flexion, adduction and internal rotation (FADIR) test, also referred to as the anterior impingement test, is the most commonly used manoeuvre (Byrd, 2014). Although these assessments can be sensitive, their specificity is limited because hip pain can arise from several intra and extra-articular sources. Reproducing the high-load conditions that trigger symptoms during daily or sporting activities is also challenging during a manual

examination. For this reason, it is generally recommended that more than one clinical test is used when evaluating a patient for FAI.

Diagnostic imaging is essential for identifying FAI morphology and associated soft tissue pathology. Two primary types of FAI are recognised: cam, defined by flattening or convexity at the femoral head neck junction, and pincer, characterised by excessive acetabular coverage (Griffin et al., 2016). These morphologies are illustrated in Figure 6.

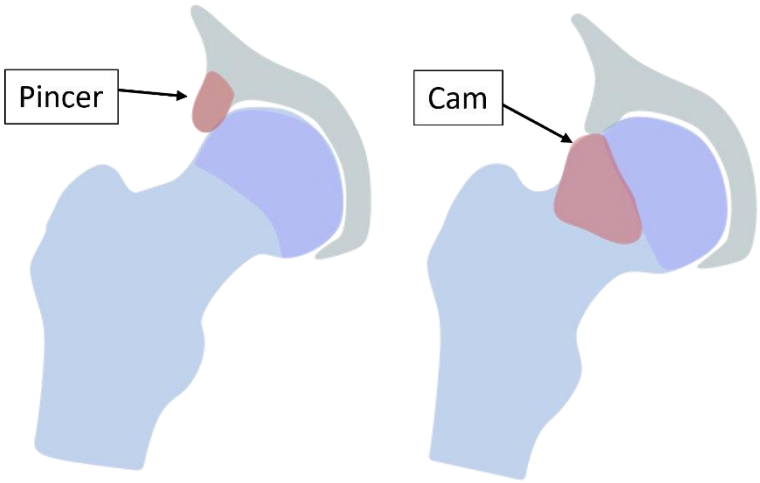

Figure 6: Schematic drawing of the different types of impingement pincer (left) and cam (right).

Radiographs are the first line imaging modality and provide an overview of bone morphology. They allow assessment of acetabular coverage, head neck offset and potential indicators of impingement, such as the crossover sign for pincer morphology and the alpha angle for cam morphology. Radiographs taken in anteroposterior and lateral or Dunn views can reveal the location and size of a cam deformity, the presence of acetabular retroversion, and any excessive lateral or anterior coverage of the femoral head (Tannast et al., 2007b). More advanced imaging, such as MRI and magnetic resonance arthrography, is used to evaluate soft tissue structures including the labrum, cartilage and chondrolabral junction. Computed tomography (CT) provides the most accurate assessment of bony morphology and is often used when 3D reconstruction is required, especially for surgical planning (Tannast et al., 2007b; Leunig et al., 2009).

Figure 7 and Figure 8 from Albers et al. (2016) demonstrate the level of detail that can be obtained from routine clinical imaging. Figure 7 presents examples of cam morphology

visualised with radiography and MRI, illustrating how these modalities complement each other by showing both the bony contour abnormality and the associated soft tissue changes. Figure 8 provides comparable examples for pincer morphology, combining radiographs and CT to highlight acetabular overcoverage and the precise configuration of the acetabular rim. Together, these figures illustrate how multimodal imaging contributes to the diagnosis of FAI.

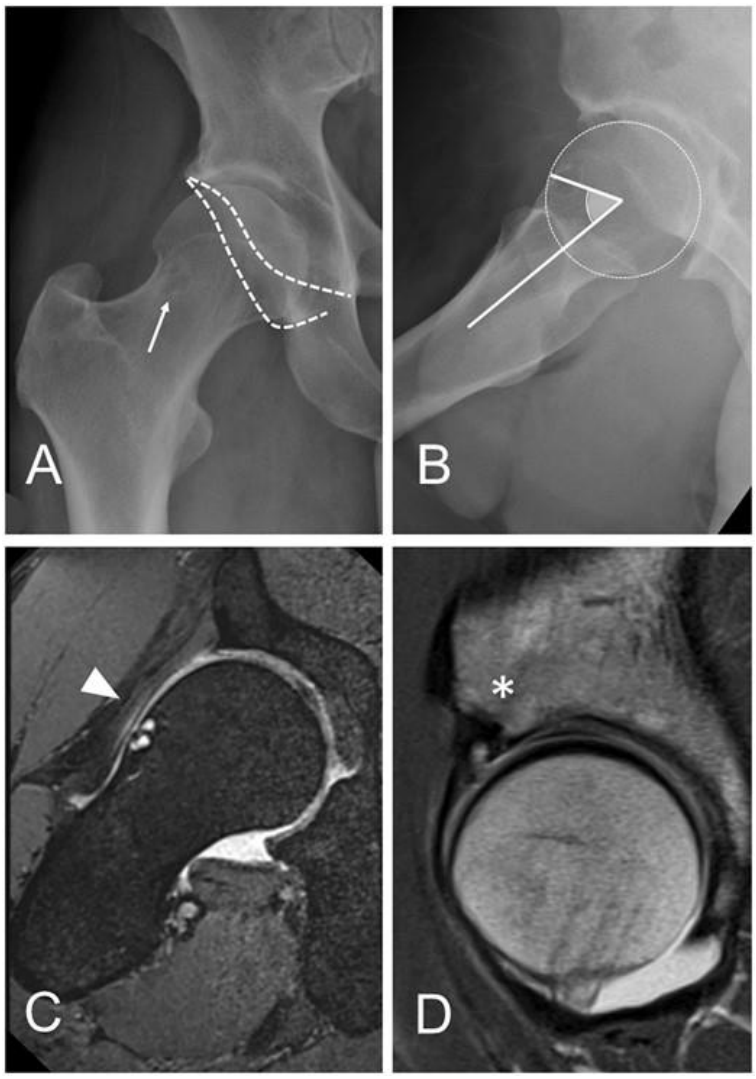

Figure 7: Cam-type femoroacetabular impingement demonstrated using radiography and MRI. (A) Anteroposterior pelvic radiograph showing loss of femoral head–neck concavity. (B) Frog leg view highlighting the cam prominence and associated alpha angle. (C) Radial MRI illustrating reduced head–neck offset and associated contour abnormality. (D) Sagittal slice MRI demonstrating soft-tissue involvement at the chondrolabral junction. Reproduced with the permission of Albers et al. (2016). Copyright of Oxford University Press. (See 8.5 Appendix E)

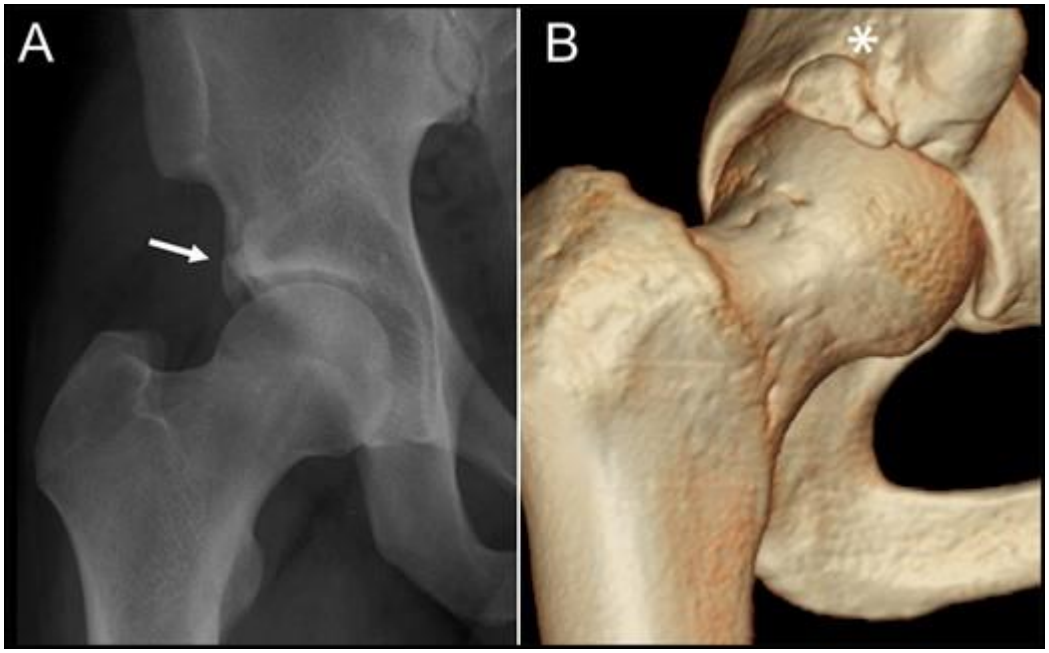

Figure 8: Pincer-type femoroacetabular impingement shown using radiography & CT. (A) Anteroposterior pelvic radiograph demonstrating acetabular overcoverage characteristic of pincer morphology. (B) 3D CT image providing detailed visualisation of acetabular rim prominence & depth of overcoverage. Reproduced with the permission of Albers et al. (2016). Copyright of Oxford University Press. (See 8.5 Appendix E)

1.4 Quantification of cam-type hip shape

1.4.1 Measuring cam-type morphology

Cam morphology is commonly quantified using imaging measurements that describe the degree of asphericity at the femoral head–neck junction. The most widely used of these are the alpha angle and the head–neck offset, both of which can be assessed on MRI or on specific radiographic projections. Figure 9 shows MRI examples from Morris et al. (2018) illustrating how these measurements are obtained.

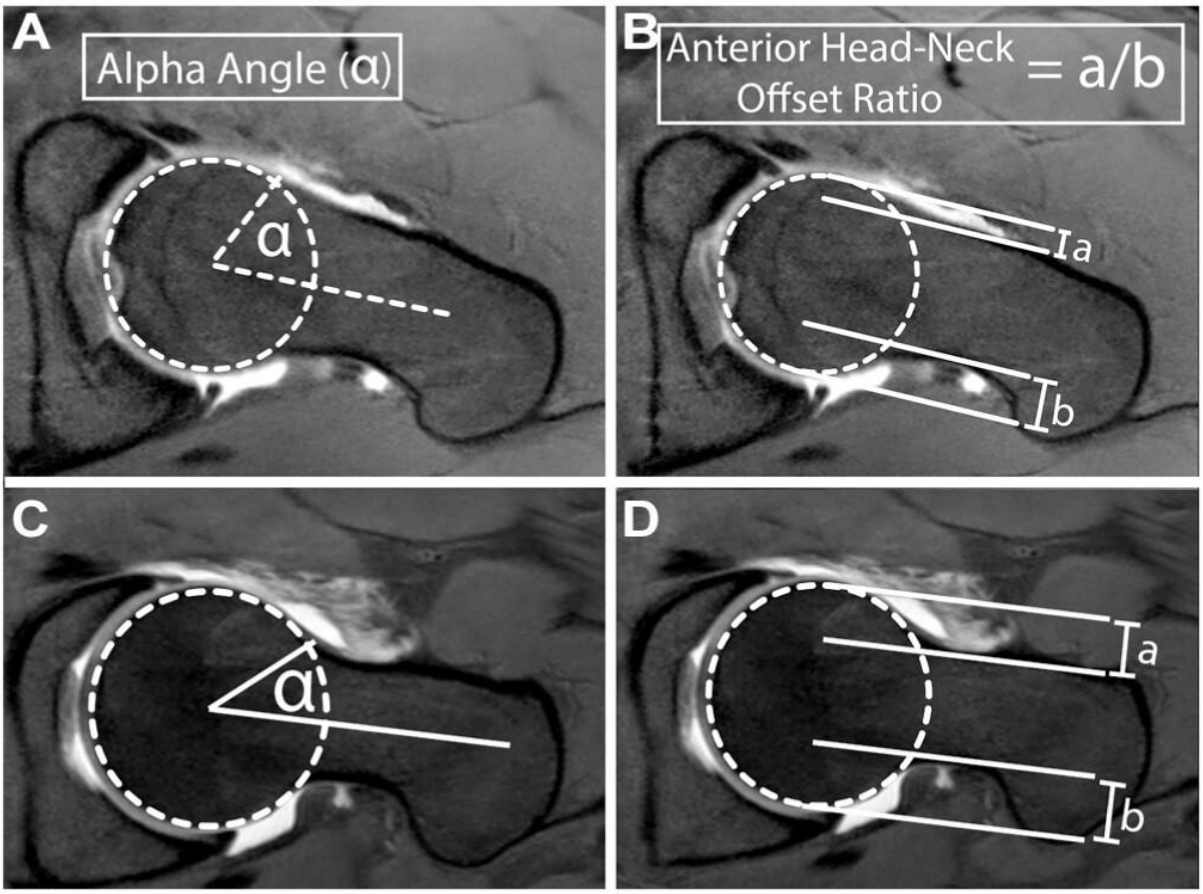

Figure 9: Oblique axial view parallel to femoral neck. (A & C) Alpha angle is measured by drawing a best fit circle over the femoral head, then measuring the angle between the midline of the femur and the point at which the neck no longer sits within the circle. (A) Represents "normal" joint and (C) cam type hip. (B & D) Head-neck offset ratio is calculated by measuring the distance between the two parallel lines for a & b, then calculating the ratio between them. (B) Represents "normal" joint and (D) cam type hip. Reproduced with the permission of Morris et al. (2018). Copyright of Oxford University Press. (See 8.5 Appendix E)

In routine clinical practice, radiographic assessment of cam morphology relies on specific projections that maximise visualisation of the anterior head–neck junction. Recommended views include:

- a standing anteroposterior pelvic radiograph,
- a lateral projection of the proximal femur, most commonly the Dunn 45° view,
- and, where appropriate, a cross-table lateral or frog-leg lateral.

These views are consistently described in the diagnostic literature as the most sensitive for detecting cam lesions (Tannast et al., 2007b; Leunig et al., 2009; Byrd, 2014; Albers et al., 2016). They allow the alpha angle to be measured reliably, while MRI provides higher soft-tissue contrast and a more precise depiction of the anterior contour.

The alpha angle quantifies the point at which the femoral head contour deviates from a perfect sphere. It is defined as the angle between the central axis of the femoral neck and the point on the head–neck junction where the contour diverges from the circle of best fit (Philippon et al., 2007; Morris et al., 2018). In Figure 9 (A & C), the measurement is shown on an axial–oblique MRI slice, the plane most commonly used to assess anterior cam morphology because it aligns with the region where asphericity typically develops (Albers et al., 2016).

The head–neck offset provides a related measure of concavity. It is calculated by drawing one line tangential to the anterior surface of the femoral head and another to the anterior surface of the neck, then measuring the perpendicular distance between them (Morris et al., 2018). Reduced offset reflects diminished concavity and is characteristic of cam morphology. Figure 9 (B & D) demonstrates this measurement on the same MRI plane.

Although the figure used here shows MRI-based examples, the fundamental principles of these measurements apply across imaging modalities. Radiographs are typically used as the first-line assessment, while MRI provides additional detail when evaluating the extent of associated labral or cartilage changes.

1.4.2 Size and location of cam lesions

There is considerable variation in the alpha angle thresholds used to define cam morphology. Reported values across the literature range from 58° to more than 90°, reflecting differences in measurement technique, radiographic view and whether the population studied was symptomatic or asymptomatic (van Klij et al., 2020). A threshold of ≥60° has been recommended in several recent papers as a practical cut off that reduces misclassification, particularly when identifying cam morphology in asymptomatic individuals (Mascarenhas et al., 2018; van Klij et al., 2020). Differing radiographic projections partly explain inconsistencies in the literature, as small changes in the angle of imaging can alter the

location of the point where the contour of the femoral head neck junction deviates from sphericity (Morris et al., 2018).

The prevalence and characteristics of cam morphology also appear to differ between men and women. Several clinical series have reported higher rates in men (Ganz et al., 2008; Byrd, 2014). Mascarenhas et al. (2018) found cam morphology in 44% of males and 26% of females in an asymptomatic cohort, using an alpha angle threshold of 60°. Sex based differences in cam geometry have also been described. Yanke et al. (2015) reported that females tend to have smaller and shallower cam lesions, which may be less visible on certain radiographic projections. Furthermore, cam position may differ by sex: females commonly exhibit a more superior cam, whereas males tend to present with a more anterior prominence (Cooper et al., 2017). These positional differences mean that the apparent severity of the cam can vary between imaging views. A lesion that appears prominent on an anterior posterior view may appear less pronounced, or even absent, on a more lateral view.

Although the anterosuperior region of the acetabulum is the most consistently affected in cam type FAI, it is not the only region where damage may develop. The precise location of damage depends on the size, extent and orientation of the cam deformity. Larger or more proximally extending cams may shift contact closer to the superior rim (Pascual-Garrido et al., 2019), while anterolateral lesions may initiate engagement more anteriorly (Kaya et al., 2016). Posterior acetabular damage is uncommon in isolated cam morphology and, when present, is usually associated with combined cam pincer patterns or with contre coup loading in pincer hips (Ganz et al., 2003). Accordingly, while the classic pattern of cam related injury is anterosuperior, the overall distribution of damage exists along a spectrum influenced by anatomical variation.

1.4.3 Who is affected?

Cam morphology is most commonly acquired during adolescence, when the proximal femoral physis remains open and responsive to mechanical loading. Longitudinal work has shown that adolescents who participate in high-impact or high-volume sports are significantly more likely to develop cam morphology (Agricola et al., 2014; Frank et al., 2015; Morris et al., 2018). These activities load the hip in deep flexion and internal rotation, producing repeated compressive and shear forces across the developing head–neck junction.

Over time, this loading environment is thought to alter physeal growth, causing the capital femoral epiphysis to extend towards the metaphysis and reduce the normal head–neck concavity (Agricola et al., 2014; Morris et al., 2018).

This mechanism is directly relevant to FAI because the movements associated with cam formation (flexion, internal rotation, pivoting) are the same movements that later produce impingement. Once the growth plate closes, the cam shape becomes fixed, and the individual continues to perform the same high-demand motions. Thus, the biomechanics that shape the developing femur continue to shape joint loading in adulthood.

Demographic trends reflect this developmental pattern. Males, who often engage in higher-impact sports during physeal maturation, exhibit a higher prevalence of cam morphology and typically present with larger, more anteriorly located lesions (Ganz et al., 2008; Byrd, 2014; Mascarenhas et al., 2018). Females tend to show smaller, more superior cam shapes (Yanke et al., 2015; Cooper et al., 2017). These positional differences influence the point of first contact during flexion–rotation and help explain sex-specific variations in FAI symptoms and damage patterns.

Not all cam lesions arise through adolescent loading. Secondary cam morphology can result from conditions such as slipped capital femoral epiphysis, Legg–Calve–Perthes disease, trauma or infection, all of which alter the head–neck contour (Byrd, 2014). Regardless of the underlying cause, the defining feature is loss of concavity, which increases the likelihood that flexion and rotation will generate elevated shear forces at the acetabular rim.

In summary, cam morphology most often develops under mechanical conditions that mirror those that later provoke hip impingement. The mechanical environment during growth determines the geometry that governs rim contact in adulthood, explaining why physically active young males represent the most frequently affected group.

1.5 Damage in cam-type hip impingement

Cam-type femoroacetabular impingement produces damage through the abnormal contact of an aspherical femoral head–neck junction with the anterosuperior acetabulum during hip

flexion and internal rotation. Compared with pincer morphology, which typically causes more focal rim compression, cam morphology drives a larger arc of shear across the chondrolabral junction and is widely regarded as the more destructive pattern (Beck et al., 2005; Frank et al., 2015; Morris et al., 2018). The characteristic appearance and progression of damage are best understood by considering the specific organisation of the labrum and the depth-dependent fibre architecture of articular cartilage.

1.5.1 Mechanisms of cam FAI damage

As the cam enters the joint, the lack of a normal head–neck offset produces combined shear and compressive loading at the anterosuperior acetabulum. The superficial fibres of articular cartilage, which normally run parallel to the surface, experience high tangential shear. At the same time, compressive load is transmitted into the deeper zones and the tidemark, where the stiff calcified layer restricts deformation relative to the overlying cartilage. The labrum, with its predominantly circumferential collagen alignment and firm rim attachment, is pulled outward as the cartilage is pushed centrally (Beck et al., 2005; Keogh and Batt, 2008; Bsat et al., 2016). This opposing displacement sets up the classic “outside-in” failure mode described in surgical studies.

Because the anterosuperior acetabulum has thicker cartilage, higher contact forces and a sharper transition between the labrum and cartilage, this region is particularly vulnerable to shear-driven separation and early cartilage debonding (Beck et al., 2005; Kaya et al., 2016).

1.5.2 Structural vulnerability and mechanisms of tissue failure

Cam-type impingement produces damage in predictable regions of the joint because loading occurs in a consistent direction during movements. The location and pattern of injury reflect how the cam engages the acetabular rim and how the local tissue architecture responds. The structural organisation of the chondrolabral junction, cartilage and labrum determines which areas are most vulnerable and how each tissue fails under shear and compression. The following section outlines the regions most commonly affected and explains the key mechanisms that give rise to their characteristic damage patterns.

- Chondrolabral junction: The transitional zone between the fibrocartilaginous labrum and hyaline cartilage is thin, only one to two millimetres, and contains collagen fibres shifting orientation as they blend from circumferential to oblique and vertical arrangements (Petersen et al., 2003). This makes the junction inherently weaker in shear. During impingement the cam pushes the cartilage centrally while the labrum is displaced outward, placing opposing forces across this interface. As a result, early internal separation frequently develops at the junction before obvious surface tearing of either tissue occurs (Beck et al., 2005; Keogh and Batt, 2008).
- Articular cartilage: The superficial zone, with its parallel fibrils oriented to support shear glide, is the first region to experience disruption when shear stresses exceed local strength. Beneath this, the deep zone is stiffer and firmly anchored to the bone at the tidemark. This mismatch in compliance creates a natural shear plane where the more compliant superficial and middle zones can slide over the calcified cartilage. Repeated loading deepens this cleavage, producing the characteristic pattern of anterosuperior delamination in cam hips (Bhosale and Richardson, 2008; Little et al., 2011).
- Labrum: The labrum's circumferential collagen network resists hoop tension but can split longitudinally when stretched around the rim. Although the anterosuperior labrum is structurally thicker, this region experiences the greatest tensile strain during flexion and internal rotation (Safran et al., 2011). With repeated cam loading, this produces localised tearing, partial detachment and fraying patterns that often develop secondary to chondrolabral separation and cartilage delamination (Beck et al., 2005).

These structural mechanisms explain where damage initiates and how failure progresses at the tissue level. The clinical appearance of these lesions, as observed arthroscopically, is described in Section 1.5.3.

1.5.3 Clinical appearance of damage in cam-type FAI

Many of the damage patterns associated with cam morphology have been described in vivo through arthroscopy and open surgery. These clinical descriptions provide a useful reference for interpreting the appearance of damage in vitro. The following section summarises the

main lesion types and explains how their macroscopic appearance relates to the underlying structural mechanisms.

- Carpet phenomenon/wave sign: Shear at the chondrolabral junction lifts the superficial cartilage while deeper layers remain attached, producing a rippled or wave like appearance (Beck et al., 2005; Konan et al., 2011; Barros et al., 2019). This reflects early disruption of the superficial collagen network with partial loss of fixation but without exposure of subchondral bone. It is consistent with the superficial zone being the first layer to fail under shear.
- Delamination: Delamination is the hallmark lesion of cam impingement. It refers to partial separation of the hyaline cartilage shell from the calcified cartilage and underlying bone (Beck et al., 2005; Jannelli et al., 2019). The mechanism arises because the deep zone remains stiff and anchored, while the superficial and middle zones are displaced by repeated shear from the cam. Over time, these differential motions deepen the internal cleavage plane. The labrum usually remains intact at this stage because its rim attachment is stronger than the cartilage–bone interface.
- Chondrolabral separation: Chondrolabral separation develops when loading at the transitional zone exceeds the strength of its fibre arrangement. During impingement the fibrocartilaginous labrum is pulled outward and the hyaline cartilage is pushed centrally, creating opposing forces across the junction. Histology consistently demonstrates failure within this transitional region rather than at the bony attachment (Beck et al., 2005; Kappe et al., 2011), supporting the “outside in” mechanism described for early FAI injury (Keogh and Batt, 2008).
- Labral tearing: Although not the earliest structure to fail, the labrum can tear as impingement loads accumulate. Longitudinal splits follow the circumferential fibre direction, while partial detachments and fraying occur adjacent to regions of cartilage delamination. These patterns mirror the regional strain environment reported by Safran et al. (2011) as well as the mechanical interplay between labral tension and cartilage shear during cam loading.

1.5.4 Damage characterisation methods

Several clinical grading systems are used to describe cartilage and labral injury in the hip, and three of these were considered relevant to this project: the Outerbridge, Beck and Konan

systems. Each was reviewed to assess how well it could describe the patterns of damage seen in the in vitro acetabula (Table 2). Importantly, none of the existing clinical systems include descriptors for subtle or early stage surface changes, such as blushing or the initial stages of bubbling, which are observed in vitro but do not appear in the clinical grading literature. These early features are relevant in simulation based studies because they represent the first indications of matrix deformation before more advanced lesions develop.

Table 2: Summary of arthroscopic damage characterisation methods (Beck et al., 2004; Ilizaliturri et al., 2008; Konan et al., 2011; Barros et al., 2019).

Method	Outerbridge	Beck	Konan (or Haddad)
Grading system	Grade 0: Normal Grade I: Softening and swelling Grade II: Fragmenting or fissuration less than 1 cm Grade III: Fragmenting or fissuration more than 1 cm Grade IV: Exposed subchondral bone.	0 Normal: macroscopically sound cartilage. 1 Malacia: roughening of surface, fibrillation. 2 Debonding: loss of fixation to the subchondral bone, macroscopically sound cartilage, carpet phenomenon. 3 Cleavage: loss of fixation from subchondral bone; frayed edges, thinning of the cartilage. 4 Defect: full thickness defect.	0: Normal articular cartilage. 1: Softening/wave sign; loss of attachment to subchondral bone. 2: Cleavage lesion, separation from chondrolabral junction, no evidence of delamination. 3: Delamination 4: Exposed bone With further classification of letters to describe what proportion of the zone was damaged. A: less than one third of the distance from the acetabular rim to the cotyloid fossa. B: one-third to two-thirds of this distance. C: greater than two thirds.
Location of damage		Location of damage was based on the clockface method. (12 o' clock superior and 6 o'clock inferior.)	Location of the damaged area is described using a zonal method (created by Ilizaliturri et al. (2008). Six zones that are used to dissect the femoral head and acetabular surface.
Advantages	Grading system that considers the size/extent of any possible lesions	Designed for classifying damage in the hip.	Reliable method for describing the location of damage. Designed for classifying damage in the hip.

Disadvantages	Categories used in classification may not be helpful in describing damage in the hip. The parameters for determining the size and grade of a lesion may not translate to a smaller porcine acetabulum.	Often difficult to differentiate between grades. Clockface method of describing location has been linked to perception errors. Not all grade descriptors will be applicable for use in describing in vitro simulation damage.	Not all grade descriptors will be applicable for use in describing in vitro simulation damage

The Outerbridge system provides a simple four stage scale based on surface changes and the size of a lesion. Although widely used in knee surgery, it is less suited to hip pathology. Grades two and three differ only by whether the fissuring is above or below one centimetre, which means the classification focuses on size rather than the mechanical characteristics of the lesion (Amenabar et al., 2015). In addition, common patterns seen in femoroacetabular impingement, such as loss of fixation or cleavage at the chondrolabral junction, are not represented within this system (Konan et al., 2011; Polesello et al., 2019). The reliance on human scale dimensions also makes it difficult to apply directly to smaller porcine acetabula. For these reasons, the Outerbridge method was considered to have limited use in describing simulator generated damage.

The system is also fundamentally designed to quantify severity rather than classify the type of damage. This distinction is important because in vitro simulations often produce small, mechanism specific features that do not fit into an ordinal severity scale but can still indicate meaningful differences between loading conditions.

The Beck method was developed specifically for FAI and describes characteristic patterns such as malacia, debonding, cleavage and full thickness defects (Beck et al., 2005). This makes it conceptually appropriate for the types of damage expected in cam morphology. However, reliability studies show that differentiating between malacia and debonding is difficult, with poor agreement between observers (Nepple et al., 2012). This is likely because early cam related lesions often show mixed features. A further limitation is that the Beck system does not distinguish between different levels of severity and therefore does not represent the progression of the disease (Konan et al., 2011; Amenabar et al., 2015). While

valuable for identifying FAI related patterns, it does not fully capture the range of surface and subsurface changes seen in vitro.

Although the Beck categories are linked to FAI, they merge structurally different patterns such as labral tearing, delamination and surface fibrillation into the same grade. Combining these mechanisms limits their usefulness in simulator studies where identifying the type of tissue failure, rather than ranking its severity, is essential for interpretation.

The Konan system was also developed for the hip and places more emphasis on the progression of FAI related cartilage injury, distinguishing between softening, cleavage, delamination and exposed bone (Konan et al., 2011). This better reflects the sequential mechanical failure mechanisms described earlier in this chapter. The system also incorporates Ilizaliturri et al. (2008) zonal method to describe lesion location, which improves consistency and maps well onto the anterosuperior distribution typical of cam impingement (Ilizaliturri et al., 2008; Polesello et al., 2019). Despite this, some descriptors need adapting for smaller acetabula and certain categories remain difficult to apply in vitro.

Damage location is most commonly recorded using either the clock face method or the zonal method. The clock face method divides the acetabulum into twelve positions, with six o'clock at the transverse acetabular ligament and twelve o'clock directly opposite this (Beck et al., 2005). This system offers flexibility but is susceptible to perception errors in vivo because patient positioning alters the apparent location of the acetabular rim. Although these issues are less prominent in a disarticulated in vitro model, sample inclination and the irregular geometry of porcine acetabula can still influence accuracy.

The zonal method divides the acetabulum into six anatomically defined zones (Ilizaliturri et al., 2008). Because it relies on fixed landmarks rather than orientation, it is more reliable for the present study and was therefore used as the primary location descriptor.

Taken together, these limitations highlight that current clinical grading systems are not designed to classify the specific forms of damage produced in controlled in vitro settings. They focus predominantly on severity, whereas simulator studies require a mechanism based approach that can distinguish between subtle and structurally distinct patterns of failure.

None of the three systems examined was able to capture the full range of damage observed in the simulator. The Outerbridge system lacked descriptors relevant to FAI related patterns, the Beck system had difficulty distinguishing early lesion types and did not reflect progression, and the Konan system, although more representative, required modification for porcine anatomy. Important features such as chondrolabral separation, internal cleavage planes, the development of early bubbling and the distribution of blushing were not fully described by any single method.

In addition, the reliance on surface visualisation during testing meant that descriptors needed to be recognisable from photographs rather than from arthroscopic tactile assessment. This further limited the applicability of existing systems, which often depend on probing, depth assessment or clinical judgement.

For these reasons, a new in vitro classification approach was developed specifically for this project. It draws on elements from clinical systems but is adapted to the structural mechanisms outlined in Section 1.5.2 and the macroscopic appearances described in Section 1.5.3. Damage was assessed visually, photographed and recorded using structured written descriptors to ensure consistent reporting between samples.

1.6 Management of cam-type femoroacetabular impingement

Management of cam-type FAI typically follows a stepped approach, beginning with non-operative strategies before progressing to surgery. The overall aim is to reduce symptoms, improve function and, where possible, prevent further structural deterioration of the joint.

1.6.1 Non-operative management

Conservative treatment is recommended as the first line of management, particularly in individuals with early symptoms and no radiographic evidence of advanced degeneration. Several studies have shown that structured physiotherapy programmes can improve pain and function by strengthening periarticular muscles, improving lumbopelvic control and

modifying movement patterns that provoke impingement (Pasculli et al., 2023). Activity modification and non-steroidal anti-inflammatory medication are commonly used alongside physiotherapy, while image guided intra-articular corticosteroid injections can provide short term relief in selected cases (Pasculli et al., 2023).

Randomised controlled trials have compared conservative care with arthroscopic surgery. Griffin et al. (2018) and Palmer et al. (2019) both reported improvements in patients receiving physiotherapy-based management, although arthroscopy produced larger and more sustained improvements for most outcomes. These findings illustrate that non-operative strategies can be effective, but may be insufficient for individuals whose symptoms persist despite a structured period of conservative management. In clinical practice, surgery is considered when symptoms remain troublesome after several months of non-operative care, imaging confirms cam morphology, and the joint shows minimal degenerative change (Tönnis grade 0–1) (Hassan et al., 2022).

1.6.2 Surgical interventions

Surgical intervention is indicated for patients with persistent groin pain, positive impingement signs and imaging evidence of cam morphology after an adequate trial of conservative management. The overarching aim is to restore head–neck concavity, increase clearance during flexion and internal rotation, and reduce mechanical conflict at the acetabular rim. Intraoperative dynamic assessment of impingement is often used to confirm the site and extent of resection required (Philippon et al., 2007; Bedi et al., 2011).

The deformity associated with cam impingement is treated by performing an osteoplasty to recontour the femoral head–neck junction. Arthroscopy is now the most commonly used approach, allowing direct visualisation of the joint with minimal disruption to surrounding tissues. Using a round burr, the surgeon removes the excessive convexity until a more normal head–neck offset is restored. Typical resections are approximately 5–7mm in depth and 8–12mm in width, although the exact dimensions depend on the size and location of the cam (Philippon et al., 2007).

Open surgical dislocation was historically considered the gold standard because it offered complete visual access to the femoral head and acetabulum. Although less commonly used

today, it remains an important option for complex or revision cases where arthroscopic access is limited (Byrd, 2014; Hassan et al., 2022). Some procedures employ a combined arthroscopic–open approach, particularly when there are concomitant acetabular abnormalities that also require correction.

Despite widespread use, several limitations remain. Resection depth and width rely heavily on the surgeon's experience and their ability to judge the precise point at which normal concavity is restored. Over-resection can weaken the femoral neck, and resections greater than 30 percent of the diameter are considered biomechanically unsafe (Philippon et al., 2007). Conversely, under-resection can leave residual deformity, which is a recognised cause of ongoing symptoms and failure to return to high-level activity (Bedi et al., 2011).

Postoperative biomechanics do not always return to normal. Brisson et al. (2013) found that although gait improved after cam resection, hip kinematics in patients with FAI did not fully match those of healthy controls. A similar pattern was reported by Rylander et al. (2013), who observed normalisation of simple walking tasks but persistent differences during more demanding activities. These findings suggest that while surgery can alleviate symptoms, it may not completely restore the mechanical environment of the joint, either because of residual morphological abnormalities or because long-standing movement adaptations persist.

1.6.3 Why surgical practice has remained relatively stable?

Although surgical techniques have become more refined, the fundamental approach to cam correction has not changed dramatically in the last decade. This is largely because the underlying problem, the abnormal shape of the femoral head–neck junction and its mechanical interaction with the acetabular rim remains the same (Hassan et al., 2022). The core aim of restoring concavity has not altered . Current limitations are therefore less about surgical access and more about the incomplete understanding of the mechanical thresholds and movements that lead to damage. This lack of detailed biomechanical evidence helps explain why surgical outcomes vary and why some patients continue to experience symptoms despite technically successful procedures.

1.7 Selection and suitability of animal models for in vitro hip impingement studies

Human hip tissue is difficult to obtain, expensive, variable and not suitable for early stage experimental development where large sample numbers and pilot testing are required. For this reason, in vitro hip studies often rely on animal tissue. Animal joints therefore provide a practical alternative, but their suitability depends on how closely they reproduce the geometric, structural and mechanical conditions that govern human hip. When the goal is to reproduce the mechanics that drive chondrolabral damage rather than to match morphology alone, several characteristics become important. These include femoral head size and sphericity, cartilage thickness, cartilage stiffness and permeability, the capacity of the joint to deform under combined shear and compression, the structure of the labrum, and the maturity of the skeleton. Beyond these anatomical and mechanical factors, practical considerations such as availability, ethical sourcing, and consistency between joints also influence model selection.

The geometry of the femoral head is especially important because it governs congruency, load transfer and the orientation of shear (that is, the direction of sliding forces across the cartilage surface) as the head engages the acetabular rim. Quantitative comparisons by Taylor et al. (2012) show that porcine femoral heads provide the closest geometric match to human tissue. Human femoral heads measured 48.4 ± 3.6mm in diameter, while porcine heads measured 46.9 ± 2.6mm, a very small difference. In contrast, ovine heads were substantially smaller at 36.1 ± 2.1mm, and bovine heads were much larger at 54.2 ± 4.1mm. Taylor et al. (2012) also reported that porcine femoral heads demonstrated the smallest directional variation between anterior posterior and superior inferior dimensions among the animal species tested, making their overall shape the closest to human roundness. This is an important consideration when investigating cam type impingement studies. A head that is too small increases focal stresses and shifts contact to more inferior regions of the acetabulum, whereas a head that is too large increases contact area and reduces the sharp, localised shear that characterises human cam impingement. The close similarity between porcine and human diameters and directional shape therefore supports their use for reproducing realistic engagement mechanics in vitro.

Cartilage thickness and material properties are also important considerations when selecting an animal model. Human femoral head cartilage averages 1.82 ± 0.18mm in thickness (Taylor et al., 2012). Bovine (1.32 ± 0.13mm) and porcine (1.22 ± 0.05mm) cartilage fall within a broadly comparable range, although both are thinner than human tissue, while ovine cartilage (0.52 ± 0.10mm) is considerably thinner and therefore less able to distribute load physiologically. Beyond thickness, the mechanical behaviour of cartilage is central to reproducing the shear displacement that characterises rim loading. Human cartilage has a relatively high equilibrium modulus and low permeability, allowing it to maintain fluid pressurisation and limit compressive strain. Porcine cartilage, in contrast, is more compliant and highly permeable, with deformation reaching 28.82 ± 3% of its thickness under physiological loading (Taylor et al., 2012). Although this behaviour differs from that of mature human cartilage, it produces a consistent deformation pattern that still facilitates shear at the chondrolabral region. Ovine cartilage is substantially stiffer, with an aggregate modulus of 3.94 ± 2.52 MPa (Fermor et al., 2015), and its limited permeability shifts loading deeper into the tissue, reducing the development of shear planes associated with delamination. Bovine cartilage, while not as stiff as ovine, is thicker than porcine and distributes load over a broader contact area, which reduces the localised shear that drives separation at the rim. These differences have clear implications for modelling cam-type injury: species with cartilage that is too stiff (ovine) are likely to underestimate delamination, whereas species with cartilage that is too thick (bovine) may underestimate chondrolabral separation due to reduced focal stress.

Permeability, glycosaminoglycan content and tissue maturity also influence how the joint behaves under repeated loading. Porcine cartilage from an abattoir is immature and contains high GAG concentrations, which contributes to its higher permeability and greater deformation (Fermor et al., 2015). Although this differs from mature human cartilage, it allows fluid flow and strain patterns that are still compatible with reproducing shear-driven damage. Ovine tissue, sourced from skeletally mature animals, is less permeable and stiffer, producing loading conditions that favour deep compression over surface shear, which is not representative of early cam-type injury. Bovine tissue, although mature and readily available, exhibits large joint dimensions and a labrum that is thicker and less human-like, further altering the mechanics of rim engagement. The labrum itself differs substantially between species: porcine joints have a thin, underdeveloped fibrocartilage rim, bovine joints have a very thick labrum that changes how the head contacts the acetabular edge, while ovine labral

tissue is better developed but paired with a joint that is geometrically mismatched to the human hip.

While less commonly used due to ethical and practical barriers, other species further illustrate the variability across models. Athanasiou et al. (1995) showed that baboon hip cartilage most closely matched human tissue in stiffness, permeability and thickness, while canine hips also display anatomical similarity to human joints. Although these species are biomechanically attractive options, they are unsuitable for abattoir sourcing and therefore impractical for in vitro development work. Their inclusion in comparative studies remains useful, however, because they establish the biomechanical range within which human cartilage sits and emphasise where quadruped livestock models deviate from human hip behaviour.

When these factors are considered together, porcine joints offer the best balance for a load-based impingement simulation. They provide the closest match to human femoral head geometry, have cartilage that, although more compliant, still deforms in a predictable and interpretable way, and are readily available in large quantities from consistent age groups. Ovine joints, being smaller and stiffer, shift loading deeper and reduce shear at the rim, which limits their ability to replicate the characteristic delamination seen in cam-type impingement. Bovine joints, while robust and easy to obtain, are geometrically too large, have thicker cartilage and an oversized labrum, all of which distribute load away from the anterosuperior region and dampen the stress concentrations central to cam-related injury. Porcine tissue therefore remains the most appropriate compromise for this study, offering a practical, anatomically relevant and mechanically functional model for reproducing the shear-dominated conditions that drive chondrolabral and cartilage damage in human cam FAI.

1.8 Previous in vitro studies of mechanical damage in the hip joint

1.8.1 Experimental methods

Several methods have been used to simulate joint mechanics when testing natural cadaveric or animal tissue. These approaches can be broadly grouped into four categories: manual clinical examination techniques, robotic arm–based systems, mechanical testing with applied load and whole joint simulators originally designed for artificial implant testing.

The simplest approach involves manually manipulating the joint through specific motions, similar to a clinical examination. In these tests, the cadaveric or animal joint is moved through defined positions by hand while joint angles are measured using tools such as goniometers or motion capture markers (Goldsmith et al., 2015). Although these methods are straightforward and reflect typical clinical assessments, they suffer from poor repeatability and limited control over applied motions and loads.

A more controlled approach uses robotic arms to replicate joint motions. In these systems, the specimen is mounted in a custom jig to fix its orientation, and the robotic arm applies motion to one end of the joint (Birmingham et al., 2012; Goldsmith et al., 2015; Ng, G. et al., 2019; Uvodich et al., 2024). Goldsmith et al. (2015) compared robotic testing to manual clinical examinations and demonstrated that robotic systems provide greater accuracy and repeatability. However, their robotic setup had an important limitation, the device could not apply physiologically relevant loads, restricting the ability to simulate high-load activities. Similar limitations appear across other robotic arm studies. Ng, G. et al. (2019) and Birmingham (2012) applied only rotational torques, typically up to around 18Nm, without incorporating any substantial compressive loading.

Another approach is the use of mechanical testing rigs by applying axial load using a materials testing machine or actuator arm. In these studies the joint is typically potted or fixed in a specific orientation, and compressive forces are applied directly through the joint. Hapa et al. (2025) used this approach, applying axial loads ranging from 100 to 750N at varying cycle

counts. While this method allows for controlled and physiologically relevant loading, the downside is that the joint is usually held in a fixed position, meaning that load can be applied or motion can be applied, but not both simultaneously. This prevents replication of dynamic multi axis activities and restricts the ability to study load–motion interactions.

Whole joint simulators represent the only commonly used method that can apply both high compressive loads and controlled multi axis motion at the same time (Pallan, 2016; Groves et al., 2017; Jimenez-Cruz et al., 2022). These systems, although originally designed for artificial implant testing, allow combined movement cycles to be applied together with substantial axial forces. Previous in vitro simulation studies using whole joint simulators have achieved loads of around 2000N when testing animal tissue (Pallan, 2016). This demonstrates that whole joint simulators remain the closest available method for reproducing physiological loading conditions.

In summary, each simulation method presents clear strengths and limitations. Manual techniques lack precision and repeatability, and robotic arm systems, although highly controlled, are generally unable to apply realistic joint loading. Mechanical loading rigs allow meaningful forces but cannot reproduce combined load and motion. Whole joint simulators are less common and are typically used for implant testing, yet they offer the closest match to the combined movement and loading conditions observed in vivo. Given these considerations, whole joint simulation provides the most suitable approach for studies that require both controlled motion and physiologically relevant forces.

1.8.2 In vitro simulation (Whole joint)

Whole joint simulation has been adapted in different ways depending on the specific research questions being addressed. Groves (2015) and Groves et al. (2017) used controlled axial loading with single axis flexion extension motion to investigate lubrication behaviour in both hemiarthroplasty and complete natural hip joints. Their work provided systematic assessments of frictional change over time and highlighted how lubrication mechanisms transition under load. Pallan (2016) extended this approach by transferring the protocol to a multi axis simulator, which allowed combined motion to be applied alongside axial loading and supported the development of a repeatable labral damage model. More recently, Jimenez-Cruz et al. (2022) used the same simulator to explore the effect of increasing load

magnitude, aiming to recreate overload conditions representative of higher body mass or elevated joint forces. Taken together, these studies show that simulator based in vitro testing is used to answer focused mechanical questions, ranging from lubrication behaviour to alignment sensitivity and the initiation of early structural damage.

The initial simulator studies offer useful insight into how controlled in vitro setups can be used to examine the fundamental mechanical responses of the natural hip. Groves (2015) and Groves et al. (2017) used a friction simulator to examine both hemiarthroplasty and full natural joint models under flexion extension motion with axial loads ranging from 25N during swing to 800N during stance over 7,200 cycles. This design enabled a clear assessment of lubrication behaviour and demonstrated a shift from fluid supported contact to a more solid phase as fluid exudation progressed. The strength of this approach lies in the high level of control and the ability to isolate a single movement pathway. However, the restriction to a single axis of motion limits the extent to which the test environment reflects the combined kinematics present in vivo.

Pallan (2016) adapted the earlier friction simulator work for use in a multi axis whole joint simulator capable of applying the full ISO 14242 gait cycle, which includes flexion extension, abduction adduction, internal external rotation and an axial load profile. Although this cycle is commonly used for artificial hip implant testing, in this context it provided a controlled and repeatable way to expose natural tissue to combined motion and loading. Pallan applied peak loads of 750N, 1,500N and 3,000N. No visible damage was observed at 750N after 10,800 cycles, but clear labral and cartilage changes were reported at 1,500N, particularly when the acetabular inclination angle was increased to 60 degrees. At 3,000N the joint failed through subchondral collapse, demonstrating the rapid escalation in structural response once tissue tolerance is exceeded. Jimenez-Cruz et al. (2022) also used the ISO 14242 cycle, applying peak loads of 900N for the normal condition and up to 1,340N for overload conditions over 14,400 cycles. They consistently observed anterosuperior acetabular damage whenever the applied loads exceeded the normal condition, reinforcing that even relatively modest changes in force can shift the joint response from tolerance to failure.

Taken together, these studies show the value of simplified but controlled motion sets combined with realistic axial loading. While the protocols do not reproduce full in vivo gait exactly, they replicate the key movements involved using a standardised set of movements,

providing a close approximation that allows important mechanical variables to be systematically tested. The relatively short test lengths used by focus on the initiation of damage rather than long term degeneration, which is appropriate when the aim is to identify mechanical thresholds or mechanisms of early failure. A clear theme across the literature is the sensitivity of these set ups to alignment. In particular, findings on the effect of a 60° acetabular inclination angle illustrate how small differences in fixture position can alter both the severity and location of damage (Pallan, 2016). This highlights the importance of consistent positioning rather than representing a limitation of the simulator itself.

Overall, the literature demonstrates that whole joint simulators provide the strongest available means of combining controlled multi axis motion with substantial axial loads. They offer a level of control that allows specific mechanical questions to be addressed without the need to replicate full in vivo kinematics. This positions them as an appropriate and well supported choice when the primary aim is to study mechanisms of early damage, and this rationale aligns with the approach taken in the present work.

1.8.3 Replicating cam geometries

Experimental studies have used different methods to recreate cam type morphology, but each one has practical limitations. One of the earliest approaches was by Siebenrock et al. (2013), who used an animal model. They performed a fifteen degree intertrochanteric varus osteotomy in sheep to exaggerate the natural asphericity of the femoral head. After surgery, the sheep continued with their normal gait. This meant that the modified femoral head engaged with the acetabular rim during natural quadrupedal movement, producing damage patterns that appeared similar to cam type impingement. However, the loading experienced by the joint was entirely based on sheep biomechanics. Sheep gait, pelvic orientation and motion patterns differ greatly from humans, so the location and progression of damage do not reflect human impingement mechanics.

A later study by Hapa (2025) used the same surgical approach to replicate the cam like shape but did not test the tissue in living animals. Instead, the joints were removed and mounted in a mechanical jig where axial loads were applied. This approach removed the influence of sheep gait but still did not recreate the essential loading pathway that defines cam impingement. The testing was limited to axial compression and did not include combined

flexion, rotation or shear. As a result, although both the Siebenrock and Hapa studies successfully produced a cam like prominence, neither study recreated the three dimensional loading that occurs in the human hip during impingement.

Other studies have used artificial additions to recreate a cam. Examples include the use of PMMA inserts in Uvodich et al. (2024) or the five millimetre dome used by Birmingham et al. (2012). These designs offer more control over the size and position of the prominence, but they rarely match the anatomical shape of a real cam lesion. They are also made from materials that behave differently from native cartilage, which changes how the joint interacts during movement.

Overall, these methods show that it is possible to reproduce the appearance of a cam deformity but more difficult to recreate the three dimensional shape and the correct mechanical environment. This naturally shifts the focus away from trying to copy the exact geometry and towards recreating the conditions that actually generate damage. These include joint congruency, compressive loading, rotation and shear, and the combined movement pathway that leads to impingement.

Since experimental methods cannot fully reproduce the anatomical shape of a cam deformity or the complex motion of the human hip, the type of biological tissue used in testing becomes an important consideration. When the geometry is simplified, the natural characteristics of the tissue, such as cartilage thickness, femoral head shape, deformation behaviour and overall joint congruency, play a major role in how closely the mechanical conditions of impingement can be recreated. These factors therefore need to be considered when selecting an appropriate animal model for in vitro testing.

1.9 Hip Impingement and Activity

1.9.1 Mechanical Loading of the Hip Joint

Direct in vivo measurements of hip joint forces using telemeterised prostheses provide highly accurate data, yet are limited in scope. Bergmann et al. (2001) recorded contact forces during routine daily activities in four patients with instrumented implants, reporting peak forces of

approximately 2–3× body weight (BW) during walking and stair ascent, with torsional moments up to 83% higher during stair climbing compared to walking. Extreme events, such as stumbling, can generate forces exceeding eight times BW (Bergmann et al., 2010). While these datasets are essential benchmarks for implant testing and validation of computational models, their small sample size and restriction to low- to moderate-impact activities in older patients limit generalisability, particularly for young athletic populations who are at risk of cam FAI.

Indirect approaches combine optical motion capture with ground reaction forces and musculoskeletal modelling to estimate hip joint forces across broader populations and activities. While these methods allow investigation of healthy subjects and high-flexion tasks, they are prone to error from soft tissue artefact and marker placement. For instance, Lopez et al. (2024) reported hip joint centre errors of several centimetres and rotational errors exceeding 20° during squats and step-ups. Musculoskeletal models can partially overcome these limitations, providing peak hip joint reaction forces ranging from 0.5–6.4×BW across walking, squatting, lunging, and golf swings (Layton et al., 2021; Layton et al., 2022a). However, such datasets do not capture altered kinematics or compensatory strategies observed in pathology, nor do they fully replicate high-impact or sport-specific conditions that commonly provoke cam FAI. Moreover, most models assume simplified rigid segments and idealised muscle activation patterns, which may underestimate joint forces at extreme hip flexion, highlighting a key methodological limitation.

Collectively, these findings illustrate the trade-offs between accuracy and generalisability in hip force estimation. Direct measurements offer precision but limited applicability, while musculoskeletal models broaden scope but introduce uncertainty. For research into cam-type FAI, this underscores the importance of combining approaches and critically considering population and activity context.

1.9.2 Activities that Increase Prevalence of FAI

Epidemiological evidence indicates that sports involving extreme hip motion are associated with increased cam FAI prevalence. Doran et al. (2022) found higher prevalence in athletes relative to non-athletes, highlighting the role of activity-specific loading. Nawabi et al. (2014) further categorised sports into biomechanical groups, identifying “impingement” activities

requiring high hip flexion, adduction, and internal rotation as carrying the greatest risk. Ice hockey exemplifies this category, with the highest prevalence, while “cutting” sports such as football and “contact” sports like rugby also pose substantial risk due to rapid directional changes and impact loading.

While these associations are strong, it is still unclear whether repetitive activity actually causes cam morphology to develop, or whether people with certain hip shapes are more likely to take part in these high-risk sports in the first place. The category classification by Nawabi et al. (2014) is helpful, but it reduces complex, multi-planar movements into broad groups and does not fully capture how athletes move in real situations. It also does not take into account the compensatory strategies athletes may use to reduce the chance of impingement. These points highlight gaps in the current literature and suggest that future research needs to use longitudinal study designs and more detailed biomechanical measurements to better understand how activity and morphology are linked over time.

1.9.3 Effect of Hip Impingement on Hip Motion

FAI is often associated with reduced hip range of motion (ROM), influenced by both structural morphology and pain. Symptomatic individuals typically exhibit lower ROM compared to healthy controls, while asymptomatic cam morphology carriers may also show subtle reductions, indicating a structural contribution independent of symptoms (Diamond et al., 2015). Diamond et al. (2016) found reduced sagittal plane ROM during gait in symptomatic FAI, though overall gait biomechanics showed minimal differences. This likely reflects the fact that routine walking rarely challenges end-range hip motion, highlighting the need to evaluate activities approaching impingement-level flexion.

Squatting has emerged as a functional task to investigate FAI biomechanics due to the high flexion demand of the hip (Ayeni et al., 2014). Multiple studies demonstrate that FAI patients struggle to achieve maximal hip and pelvic ROM (Lamontagne et al., 2009; Diamond et al., 2017). Specifically, reduced sagittal pelvic motion and posterior tilt increase the likelihood of femoroacetabular contact (Lamontagne et al., 2009; Bagwell et al., 2016). Under constrained conditions, FAI patients adopt greater pelvic tilt, increased hip adduction, and slower squat descent to avoid painful end-range positions (Diamond et al., 2017). Interestingly, both Lamontagne et al. (2009) and Diamond et al. (2017) report minimal differences in hip angles

themselves, suggesting that compensatory pelvic strategies, rather than hip motion per se, drive functional limitation. Variability in reported squat depth between studies may reflect differences in ankle mobility, participant characteristics, or instructions, illustrating the challenge of standardising functional assessments.

Critically, these findings underscore the importance of evaluating both hip and pelvic contributions in FAI. Many studies rely on skin-mounted markers, which are susceptible to soft tissue artefact, potentially underestimating true motion. Additionally, subtle differences in compensatory strategies may not manifest in low-flexion activities, emphasising the need to examine tasks that mimic high-risk movements. Collectively, these insights highlight gaps in current understanding of FAI biomechanics and the importance of combining methodological approaches to capture both structural and functional contributors to impingement.

1.10 Computational models of Cam-Type Femoroacetabular Impingement

1.10.1 Geometric Representation of the Hip

Hip geometries for computational models can be obtained through either parameterised or subject-specific approaches. Parameterised models are mathematically derived from joint measurements and provide simplified shapes that are efficient to create and analyse. They are often used to investigate population-level trends, idealised deformities, or the influence of individual parameters on mechanics (Ng et al., 2016). Their main limitation is that they lack anatomical detail and cannot represent tissue complexity. For example, cartilage is highly structured, biphasic, and anisotropic, with tribological properties that influence load sharing between the solid matrix and synovial fluid (Chegini et al., 2009). These features are absent from simplified models.

Subject-specific models are reconstructed from CT or MRI scans and provide more realistic representations of individual anatomy (Ng et al., 2012). Anderson et al. (2010) showed that simplifying geometry can substantially alter predicted stresses and contact areas,

emphasising the importance of accurate anatomy. Despite being more realistic, subject-specific models are slower to produce, dependent on scan quality, and often require manual corrections for convergence. Segmentation can introduce further uncertainties, though smoothing applied during model creation does not appear to reduce geometric accuracy overall (Ng et al., 2012).

1.10.2 Types of Computational Models

Computational approaches to femoroacetabular impingement (FAI) vary in complexity and anatomical complexity. Finite Element Analysis (FEA) predicts cartilage stress, tissue deformation, and contact pressures within the hip joint. Parameterised FEA models, such as those by Chegini et al. (2009), have explored how variations in alpha angle or centre-edge angle affect stresses during walking or sitting. Subject-specific FEA, using MRI or CT-derived geometries, captures more realistic distributions of stress and reproduces clinically observed damage patterns (Ng et al., 2012; Jorge et al., 2014; Liu et al., 2017). While powerful, FEA is computationally intensive and prone to convergence issues, particularly at extreme motions.

Rigid surface models treat bony surfaces as non-deformable, allowing assessment of joint kinematics and impingement zones. Tools such as Clinical Graphics or HipMotion simulate joint rotation and detect collisions based on CT or MRI reconstructions (Kubiak-Langer et al., 2007; Tannast et al., 2007a; Audenaert et al., 2012). These approaches identify impingement locations and quantify motion limits, but they exclude soft tissues and are sensitive to joint centre alignment.

Simplified rigid models, such as the one applied in this thesis, use idealised or smoothed geometries to simulate motion efficiently. They do not resolve cartilage or labral mechanics, but they allow rapid simulation of activity-specific contact events without subject-specific imaging requirements. Jones et al. (2023) demonstrated the potential of this approach by running over 100 activity-based simulations in minutes, capturing the influence of cam morphology, hip alignment, and movement type. Such models are particularly valuable when the focus is on comparing large numbers of motions rather than predicting precise tissue stresses.

1.10.3 Motion and Loading in Computational Models

Hip motion is commonly modelled using standard range-of-motion tests, predefined clinical manoeuvres such as flexion–adduction–internal rotation (FADIR), or activity-based simulations of daily tasks like squatting, stair climbing, or walking (Chegini et al., 2009; Audenaert et al., 2012; Ng et al., 2012; Jones et al., 2023). Range-of-motion studies define kinematic limits and impingement zones, whereas activity-based approaches better capture how contact evolves during realistic movements.

Joint loading is usually incorporated from experimental datasets. The work of Bergmann et al. (2001) remains foundational, having measured in vivo hip forces using instrumented arthroplasty implants. This data later expanded (Bergmann et al., 2010), provide peak and time-resolved loading profiles widely used to scale or drive computational models. While accessible and well curated, these datasets represent older arthroplasty cohorts and may not fully capture the demands of younger, active cam populations or high-flexion tasks (Ng et al., 2016).

1.10.4 Contact Pressure and the Role of FEA

Contact pressure is a key outcome in cam-type impingement research because it reflects how altered hip shape concentrates loads on cartilage and labral tissue, leading to early degeneration. FEA is the most common method for predicting these pressures. By dividing the joint into elements, FEA allows prediction of stresses, strains, and deformations under applied loads. This makes it possible to examine how variations in morphology and movement redistribute pressures, providing a link between in vivo forces and tissue-level consequences (Chegini et al., 2009; Ng et al., 2012; Jorge et al., 2014; Liu et al., 2017).

1.10.5 Benefits and Drawbacks of FEA Compared with Simplified Models

FEA provides detailed insight into tissue-level mechanics and can reproduce clinically observed damage patterns (Ng et al., 2012; Jorge et al., 2014; Liu et al., 2017). It allows variation in geometry and material properties to be studied systematically (Hellwig et al.,

2016; Cooper et al., 2018). However, its limitations include computational demand, dependence on high-quality imaging, and simplifying assumptions about cartilage and soft tissue behaviour (Chegini et al., 2009; Liu et al., 2017).

Rigid and simplified models, by contrast, prioritise computational efficiency. They are well suited to mapping impingement zones, estimating range of motion, and performing large-scale or parametric analyses (Kubiak-Langer et al., 2007; Anderson et al., 2010; Audenaert et al., 2012; Cooper et al., 2017). Jones et al. (2023) further showed that simplified models can simulate activity-specific mechanics across large datasets in a fraction of the time required for FEA, making them practical for screening movements or morphologies.

1.10.6 Applications of FEA to Impingement Damage and Motion Limits

FEA has been applied extensively to investigate how cam deformities alter hip loading and restrict motion. Chegini et al. (2009) demonstrated that increased alpha angles and reduced acetabular coverage elevate cartilage stress. Ng et al. (2012) reported that during squatting, cam hips exhibited dramatically elevated cartilage/bone stresses up to ~15 MPa in the anterosuperior acetabulum. Jorge et al. (2014) similarly observed high contact pressures during extreme flexion and internal rotation, with peaks reaching around 11–12 MPa in acetabular cartilage and approximately 14 MPa in the labrum, notably at the chondrolabral transition. Liu et al. (2017) confirmed the link between deformity severity, flexion angle, and stress magnitude. Hellwig et al. (2016) also showed that cam hips display altered fluid load support and increased radial stresses, consistent with clinical patterns of delamination and labral tearing.

Other studies have used FEA to evaluate surgical interventions. Alonso-Rasgado et al. (2012) demonstrated how osteochondroplasty redistributes load away from the femoral head–neck junction, while Arbabi et al. (2010) developed a faster penetration-depth approach that strongly correlated with FEA stress predictions. Beyond stress analysis, FEA has also revealed how impingement reduces achievable motion, with Jorge et al. (2014) noting instability at extreme flexion–rotation postures. Rigid body models complement these findings by confirming that bony contact is the primary constraint on motion (Tannast et al., 2007a; Audenaert et al., 2012).

1.10.7 Gaps in Current Models and Contribution of This Work

Despite progress, important gaps remain. Many models rely on generic range-of-motion tests or a limited set of clinical manoeuvres, rather than the activities patients report as symptomatic. FEA provides tissue-level insight but often uses simplified or averaged loading, reducing activity relevance (Chegini et al., 2009; Liu et al., 2017). As discussed in a review by Ng et al. (2016), subject-specific loading coupled to the joint model is preferable, yet many studies still rely on the Bergmann datasets, which do not capture the variability of younger cam populations or high-flexion tasks (Bergmann et al., 2001; Bergmann et al., 2010).

A further limitation concerns the integration of motion and load data. Models often apply joint forces in isolation from kinematic patterns, making it difficult to assess how specific activities drive impingement mechanics. The Layton datasets provide a step forward in this respect (Layton et al., 2022b). The data covered a spectrum of daily activities and reported detailed hip joint reaction forces and loads for over 13 tasks. These datasets extend beyond traditional instrumented implant recordings, capturing the motion and loading characteristics from the general population and were free from any conditions affecting their movement.

This study addresses the first of these gaps by applying an activity-based, simplified rigid model in 3D (Jones et al., 2023). The model enables rapid simulation of real-life tasks, mapping when and where contact occurs. By focusing on sliding distance, dominant direction of impingement, and peak impingement load, the approach allows large-scale comparison of activities without the computational demands of FEA. Motion and force inputs were taken from the Layton dataset (Layton et al., 2022b) to preserve physiological relevance. These data were used to compare activities rather than to predict absolute tissue stresses, thereby avoiding over-interpretation while still capturing activity-specific mechanics. In this way, the work complements detailed FEA studies by identifying the most demanding scenarios, providing a robust foundation for subsequent in vitro testing under realistic boundary conditions.

Chapter 2

2 Introduction

2.1 Rationale

Femoroacetabular impingement syndrome (FAI), and particularly cam-type impingement, is increasingly recognised as a significant contributor to early hip degeneration in young and active adults. A recent National Joint Registry report on non-arthroplasty hip procedures found that cam resection accounted for approximately 95.6% (7732/8573 number of pathways) of surgical interventions (NAHR, 2024), indicating both the scale of the problem and ongoing reliance on surgical management. Current evidence suggests that cam morphology develops during adolescence, likely in response to repetitive high loading from sporting activity (Agricola et al., 2013; Agricola et al., 2014; Morris et al., 2018). Cam-type impingement is widely considered the most destructive form of FAI, and has been strongly linked with the development of labral damage and early osteoarthritis (Ganz et al., 2008).

In cam-type impingement, the abnormal femoral head–neck morphology causes repetitive abutment between the femoral head and acetabular rim during motion. Arthroscopic and cadaveric observations show that damage typically progresses in an “outside–in” pattern (Beck et al., 2005; Jannelli et al., 2019). During this the acetabular cartilage is compressed centrally and the labrum is displaced outwards . This leads to delamination at the cartilage–labral junction and separation of the cartilage from the subchondral bone. Unlike the labrum, acetabular cartilage is not innervated. Therefore, symptoms often present only after substantial structural degeneration has already occurred, limiting early intervention potential.

Although the clinical presentation and surgical management of cam-type FAI are well established, the mechanical factors that drive the onset and progression of cartilage damage are not clearly understood. In particular, there is limited understanding of how the magnitude, duration, and direction of contact during daily movements influence vulnerability at the chondrolabral junction. Improving this mechanical understanding is important for several reasons. These reflect the wider, longer term aims of the research:

- It may support earlier diagnosis, before irreversible cartilage damage occurs.
- It may refine surgical decision-making, particularly regarding who is most likely to benefit from cam resection.
- It may inform rehabilitation and activity modification strategies to reduce tissue loading post-intervention.

This thesis developed a parametric method to investigate the mechanical factors related to damage in cam-type hip impingement, combining computational and experimental techniques and improving our methods for experimentally testing the damage mechanism.

To do this, three key parameters were considered throughout the thesis:

- Sliding distance: defined computationally as the arc-length of the contact point trajectory along the acetabular rim during impingement. Experimentally, it was measured as the rotational excursion of the femoral head relative to the acetabulum under controlled motion profiles. Shorter sliding distances were hypothesised to increase damage susceptibility by limiting fluid reabsorption and leaving cartilage in a low-pressure, shear-vulnerable state.
- Load: defined as the joint contact force acting across the hip during a movement, informed by musculoskeletal modelling and scaled for in vitro simulation. Higher loads increase contact pressure and local stress at the cartilage surface, leading to greater deformation and a higher likelihood of mechanical damage. Repeated exposure to elevated loads can amplify these stresses over time, increasing the risk of surface wear and structural disruption in the tissue.
- Direction of sliding: considered relative to collagen fibre orientation at the cartilage–labral junction; movements parallel to fibre orientation are expected to increase shear susceptibility.

This thesis first established an in vitro simulation method for applying controlled variations in mechanical loading and motion, and for characterising the resulting damage in natural hip tissue. Computational modelling was then used to determine physiologically relevant ranges of sliding distance, load, and motion direction during daily activities. These computationally derived parameters were then considered in the experimental setup, allowing the influence of specific mechanical conditions on chondrolabral damage to be examined in a controlled manner.

2.2 Aim and Objectives

The aim was to develop and apply a complementary experimental and computational methods to investigate how clinically relevant mechanical parameters influence damage at the chondrolabral junction in cam-type femoroacetabular impingement.

Objectives:

- To develop an in vitro natural hip simulation method capable of applying controlled and repeatable variations in mechanical loading and motion conditions, and to establish a reliable damage assessment protocol suitable for quantifying surface changes at the cartilage–labral junction. *(This corresponds to Chapter 3: method development and refinement.)*
- To determine the ranges of sliding distance, load, and motion direction that occur during activities of daily living in cam-type hips using a computational hip impingement model, and to identify conditions most likely to place the cartilage–labral interface at risk of damage. *(This corresponds to Chapter 4: computational parameter derivation.)*
- To apply selected parameter ranges to natural hip tissue using the in vitro simulation methods and assess how variations in mechanical conditions influence the development and distribution of cartilage damage. *(This corresponds to Chapter 5: parameterised experimental testing.)*
- To evaluate the combined computational and experimental findings and consider the implications for understanding clinical progression of chondrolabral damage,

surgical planning, and rehabilitation strategies. *(This corresponds to Chapter 6: Discussion.)*

Chapter 3

3 Development of experimental natural hip simulation using a parameterised approach.

3.1 Introduction

Pain in the hip joint is often associated with abnormal joint morphology, such as cam femoroacetabular impingement syndrome (FAI). This type of morphology causes soft tissue damage to the hip joint, resulting in associated pain. Understanding the mechanism of damage in the hip joint is important and may assist in improving treatments and rehabilitation of patients in the long term. Clinical studies consistently identify the anterosuperior chondrolabral junction as the earliest site of degeneration in cam-type FAI, driven by shear forces acting simultaneously with elevated compressive load (Ganz et al., 2003; Beck et al., 2005). While these mechanisms are well described in vivo and in computational models, few natural tissue studies have isolated the specific mechanical factors responsible for initiating early damage. This chapter addresses that gap by evaluating how load, sliding distance and direction influence damage in controlled in vitro conditions.

This chapter aimed to develop an in vitro simulation that parametrically assessed the causes of damage at the chrondrolabral junction. The objectives of this chapter were:

- To advance natural hip simulator testing methods and quantification of damage at the chrondrolabral junction.

- To assess parameters (such as load, direction and sliding distance) and their effect on damage.

This chapter discusses the development of experimental methodologies. It includes information on sample preparation and in vitro methods, the equipment required for the simulations, and the setup of the components. This research builds on previous work at the Institute of Medical and Biological Engineering, detailing adaptations and improvements to existing methods. Specifically, this includes enhancements to the acetabular alignment process and a new methodology for characterising damage to natural hip samples following in vitro simulation.

The developed methodologies were then used to investigate the effect that different in vitro simulation input parameters (e.g., load, sliding distance, and direction) had on damage at the cartilage-labrum junction. A comparison of the effects of changing these parameters was used to identify conditions that replicate the damage observed clinically.

3.2 Preparation for in vitro simulator testing

An overview of the stages of preparation for in vitro simulation is described in Figure 10. Preparation required included the acquisition and dissection of porcine tissue, as well as aligning and fixing the sample so that the femur and acetabulum were in neutral alignment and the centre of rotation coincided with that of the simulator. Methods were adapted in this study to improve the accuracy and repeatability of component alignment by holding the sample in place during fixation.

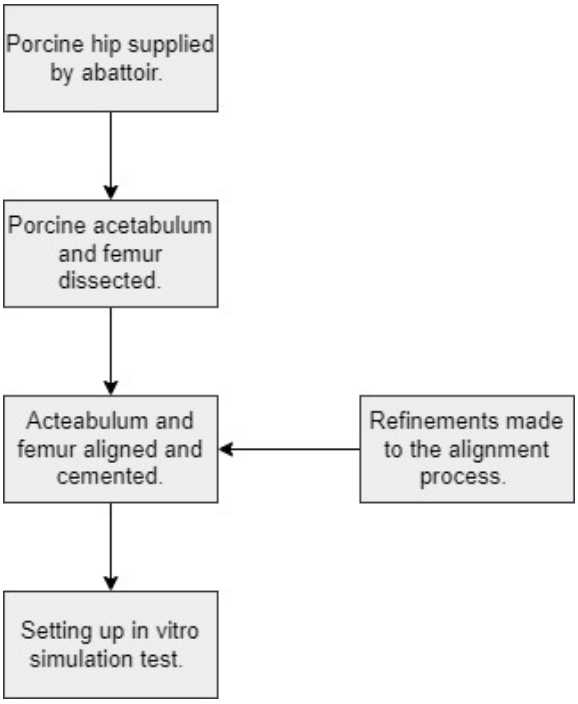

Figure 10: Overview of preparing a porcine tissue sample for in vitro simulation testing.

3.2.1 Porcine hip dissection

Porcine hip tissue from animals approximately six months old at slaughter was used in this study. These samples from the food chain provided consistent tissue age, availability, and cost-effectiveness, making them favourable for early-stage in vitro testing. Such tissue is a practical option for mimicking human hip anatomy in terms of geometry (described by (Taylor et al., 2012; Groves, 2015)). However, six-month-old pigs were not skeletally mature and can exhibit features such as open growth plates and underdeveloped labral structures. As outlined in the literature review (see Literature Review 1.7), porcine femoral head cartilage thickness is comparable to that of humans, although its mechanical stiffness is lower due to incomplete maturation (Athanasiou et al., 1995; Taylor et al., 2012). These characteristics support the use of scaled physiological loads in this study and reinforce that the focus is on comparing the relative influence of mechanical parameters rather than reproducing absolute human stresses.

This study used right porcine hind legs sourced from a local abattoir (J Penny, Rawdon, Leeds) within 24 hours of slaughter. Dissected samples were frozen at -18 °C immediately after preparation and underwent only one freeze–thaw cycle before testing. Samples were defrosted overnight and used the next day to preserve tissue integrity. The duration of

storage was approximately 6 months; however, the primary focus was on maintaining a consistent freeze–thaw cycle of one. Limiting samples to a single freeze–thaw cycle reduced variability and potential degradation of mechanical properties that can be associated with repeated freeze-thaw cycles (Blaker et al., 2024). Collecting multiple samples at one time and storing them in this manner allowed for enhanced test planning and ensured that samples could be selected based on comparable size.

Porcine acetabular and femoral heads were dissected from the hind limbs. Equipment used during dissections is listed in section 8.1 Appendix. Before the dissection of the porcine leg, the area was prepared with protective plastic sheeting and cutting boards to protect the environment, and appropriate personal protective equipment was worn. The dissection was approached from the posterior of the hind leg sample to reduce the likelihood of causing damage to the joint (Figure 11a). The first step in the dissection process was to remove all the excess soft tissue from around the femur and pelvic bone using a scalpel. Anatomical landmarks were used to aid the dissection process. For example, features on the pelvic bone were used to help identify the position of the joint capsule.

Following the soft tissue removal, the femur and pelvic bones were visible, and muscles and ligaments surrounding the joint capsule were then removed (Figure 11b). The capsule contained synovial fluid that maintained joint lubrication during the dissection process, and contact with the scalpel was avoided to reduce the risk of damage to the cartilage surfaces and labrum. The joint was disarticulated, and once exposed, the ligamentum teres was dissected close to the femoral head (taking care not to damage the head) (Figure 11c). When exposed to the air, articulating surfaces were regularly sprayed with phosphate buffered solution (PBS). Remaining ligaments, tendons and muscles were removed from the femoral and acetabular samples.

Acetabular and femoral head samples were further sectioned to ensure they could be appropriately fixed in the simulator. The distal femur was resected to a length of 50mm (approximately) from the centre of rotation of the femoral head (COR) (Figure 11d). Additionally, the greater trochanter was resected to prevent impingement (Figure 11e). The greater trochanter in porcine hips is more pronounced than in humans and can cause impingement in the articulating joint.

The periacetabular bone was resected, leaving approximately 5mm of thickness remaining, which was sufficient to provide fixation in bone cement and allow space to manipulate the sample orientation as it was set up.

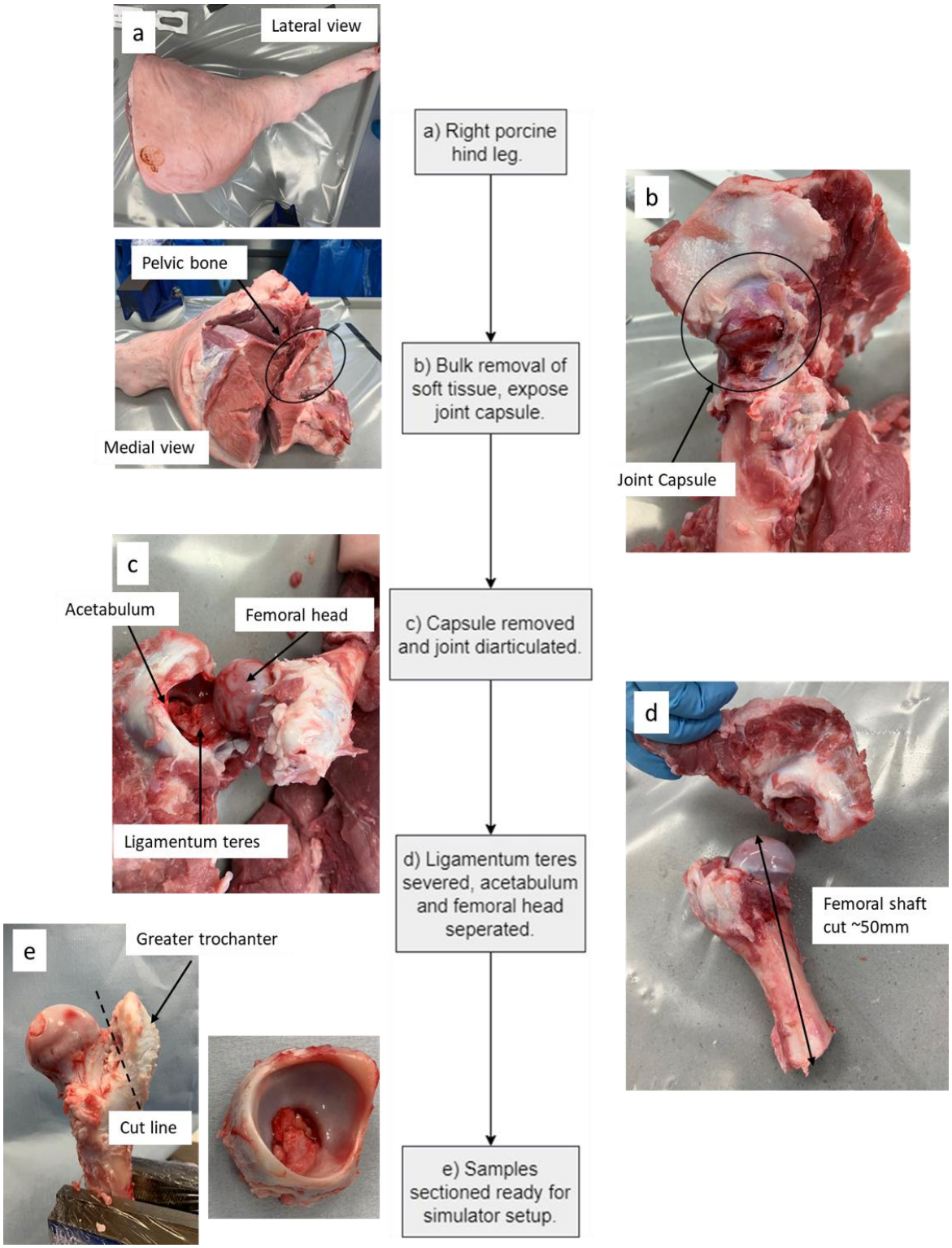

Figure 11: Right porcine hind leg. a) (Top) Lateral view of porcine hip and (Bottom) medial view of porcine hip with pelvic bone. b) Location of the hip joint capsule. c) Joint disarticulation and ligamentum teres severed. d) The femur's distal end was cut to the required length for potting. e) (Left) Dashed line represents cut line for removing the greater trochanter to prevent impingement. (Right) Acetabulum before potting.

The primary structures of interest in this study were the labrum, the acetabulum's lunate surface and the femoral head's articulating surface. These structures were identified on the dissected samples and visually assessed to confirm they were intact (see Figure 12). Any acetabula and femoral heads displaying visible damage, such as damage to the articular cartilage or labrum, tears, scratches and non-uniform shape, were discarded and excluded from testing. Damage can occur accidentally during harvesting or processing at the abattoir, for example, hematomas forming in the acetabular fossa during the hanging process. This protocol ensured that any visually observable damage could be accurately attributed to the testing process.

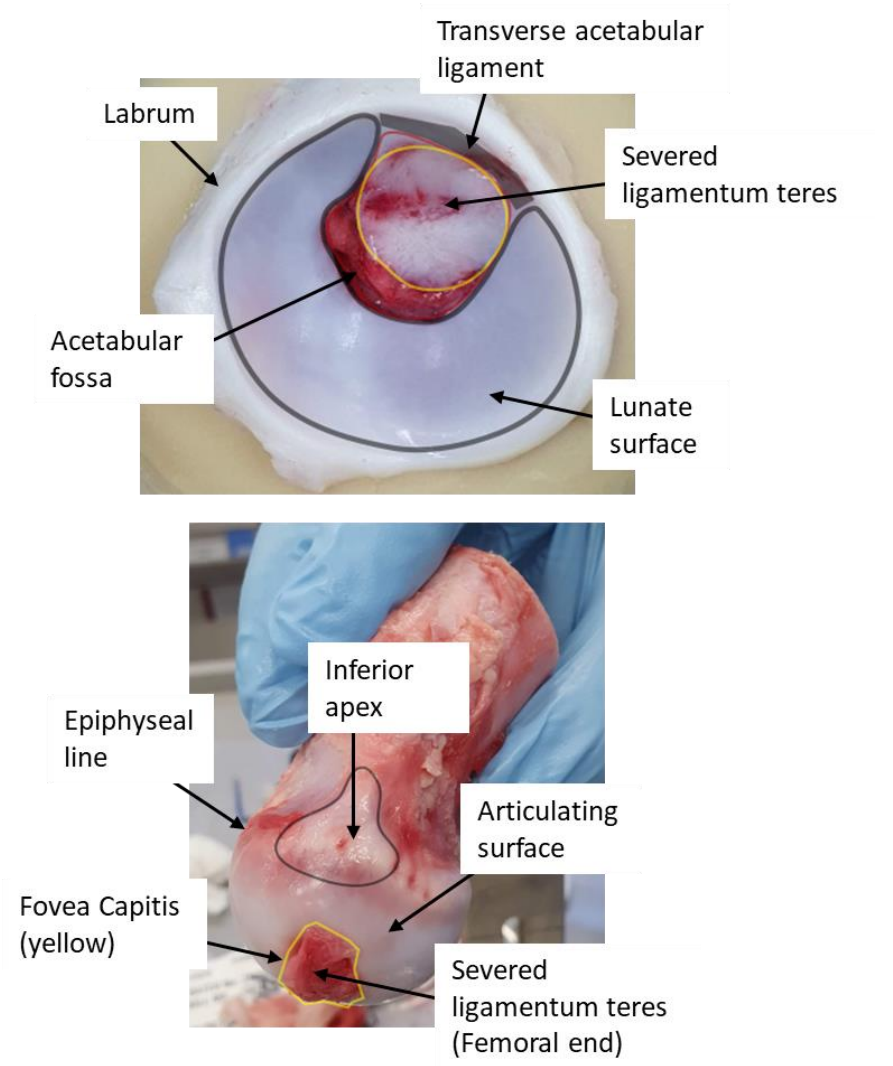

Figure 12: Annotations of the right harvested porcine acetabulum and femur show the main structures of interest.

3.2.2 Geometric measurements

Geometric measurements, which were taken for each sample, were adapted from methods developed in previous work involving natural tissue. These measurements were used to assist in positioning samples during the alignment process. To minimise inaccuracies between users when taking measurements, a measurement protocol was followed.

The diameter of the femoral head was measured using a circular guide; the diameters on the guide ranged from 32.5mm to 46mm (increasing in 0.5mm increments (Figure 13)). The proximal end of the femoral head was placed into the template, and the diameter was recorded at the point where the epiphyseal line was parallel to the guide and the head fit

into the template hole. This method captures the larger diameter as porcine femoral heads are slightly oval.

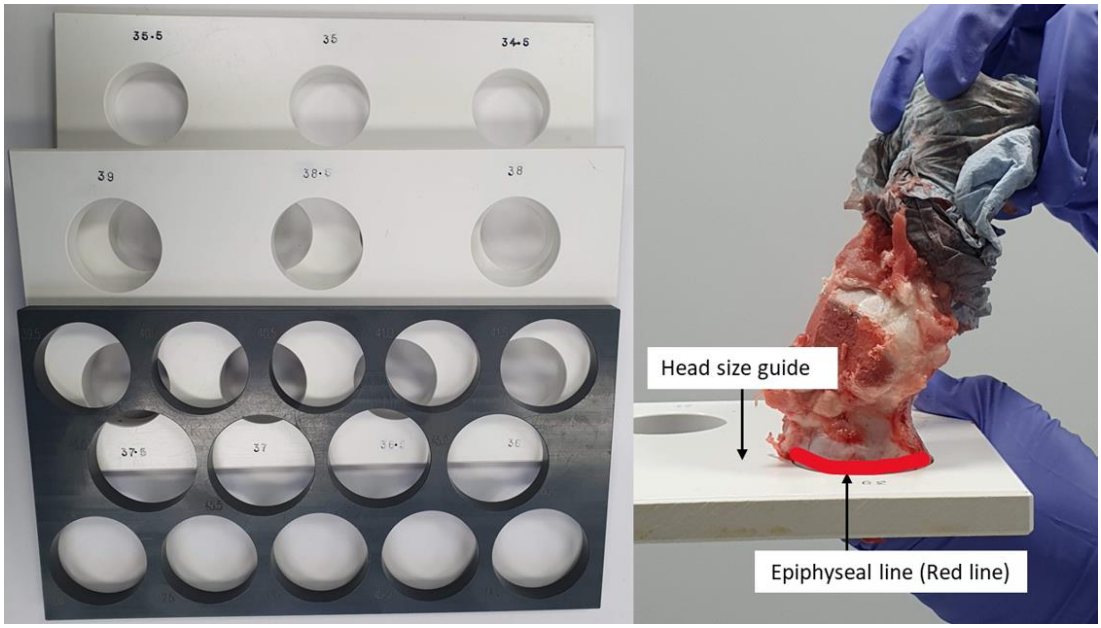

Figure 13: (Left) Circular templates used to measure femoral head size. (Right) Femoral head size was measured using the circular guide; the proximal end of the femur was placed into one of the holes, and once the epiphyseal line was parallel to the guide, this was considered the correct head size.

Geometric measurements, which were taken for each sample, were adapted from methods developed in previous work involving natural tissue (Lizhang, 2010; Groves, 2015). These measurements were used to aid in positioning samples during the alignment process. To minimise variation between users, surgical-style circular templates, similar to those used clinically, were employed as a guide for measuring femoral head diameter. This approach is an efficient and repeatable method for capturing the maximum diameter, taking into account the slight ovality of porcine heads. The diameter of the femoral head was measured using a circular guide; the diameters on the guide ranged from 32.5 mm to 46 mm, in 0.5 mm increments (Figure 13). The proximal end of the femoral head was placed into the template, and the diameter was recorded at the point where the epiphyseal line was parallel to the guide and the head fit into the template hole.

The level of accuracy in this measurement was important as femoral head size was directly used to determine the setup height of the acetabulum during alignment in the simulator. Even a small error in the femoral head measurement would alter the defined centre of

rotation relative to the simulator, which could lead to misalignment and potential changes in joint contact mechanics. While repeat measurements of the same sample were not carried out, the use of the surgical-style guide minimised operator error by providing discrete measurement options, reducing subjectivity compared to manual calliper placement.

For completeness, acetabular diameters were also measured using callipers in two directions: perpendicular to the TAL (from the centre of the TAL to the labrum opposite) and parallel to the TAL at the widest part of the socket (Figure 14). These measurements were not required for simulator setup or determination of the centre of rotation, which was based on femoral head size. Instead, they were used to assist in characterising and sorting samples for testing. As variability between users can occur when identifying anatomical landmarks, all acetabular measurements were performed by a single operator to ensure consistency.

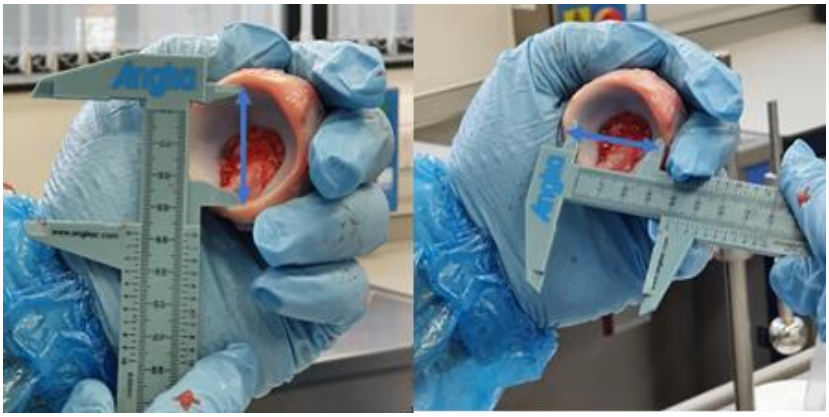

Figure 14: Measuring the diameter of the acetabulum, with the TAL positioned inferiorly. (Left) Perpendicular measurement of the acetabulum starting in the centre of the TAL. (Right) Parallel measurement of the acetabulum.

3.2.3 Setup and alignment of porcine samples for in vitro hip simulation

Following dissection, the head and acetabular components were set in fixtures so that the natural joint and hip simulator centres of rotation were coincident. The acetabulum was potted first, ensuring alignment of the socket centre with the hip simulator axis for the centre of rotation. Then the femoral bone was potted to align with the socket. This method was adapted from previous works (Lizhang, 2010; Groves, 2015; Pallan, 2016).

When aligning the acetabulum, it was important to manage various aspects of positioning, such as inclination, rotation, and height. In the alignment rig, these were measured as the angle of the socket rim in relation to the horizontal, the socket's rotation from a neutral position where the TAL was positioned, and the depth of the acetabulum in the vertical direction, respectively. This process is described in detail in the following sections.

The equipment used to align, cement and pot the sample is shown in Figure 15 and Figure 16, and listed in the Appendix 8.1.

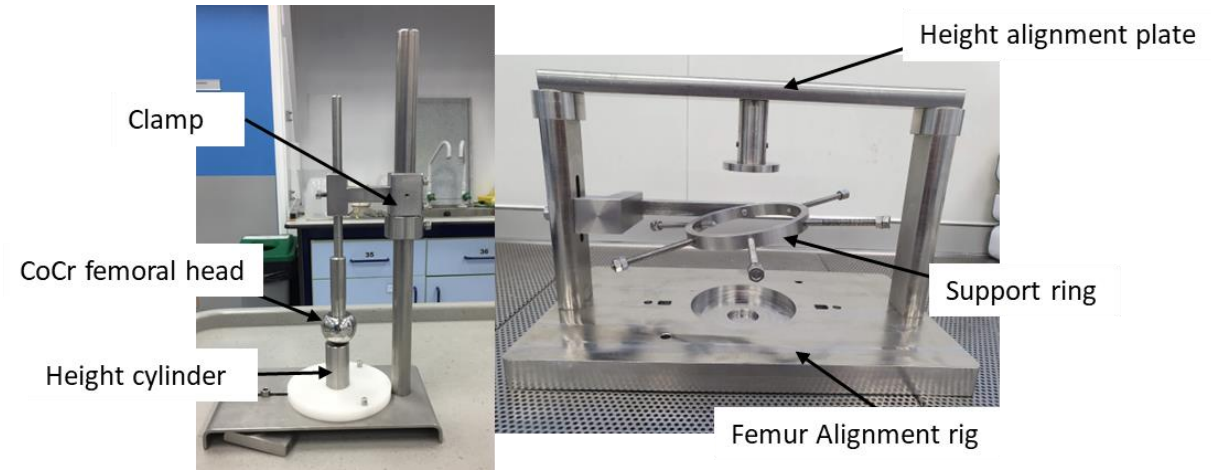

Figure 15: Cementing rig used for aligning the acetabulum (left) and femur (right) correctly.

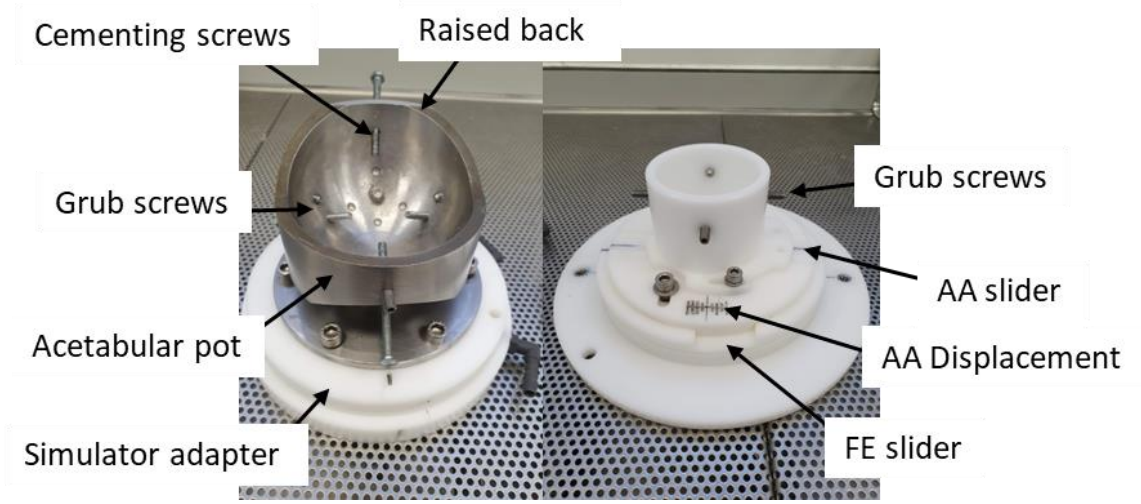

Figure 16: Potting fixtures used for in vitro simulations, (left) acetabular pot and (right) femur pot.

During the alignment process, the first step was to measure the natural femoral head size using a template (Figure 17a; see Section 3.2.2). The measured head size was used to determine the setup height of the acetabulum. An artificial CoCr head and cylinder of

corresponding size were selected. The cylinders and heads varied in size; the cylinder represents the height of the COR of the simulator plus half the diameter of the femoral head. The artificial head was placed on the rig and was lowered onto the cylinder. The clamp at the side was then tightened, and the acetabulum height was set (Figure 17b). The cylinder was then replaced with the acetabular pot. The sample was then positioned in the centre of the pot. The centre of the transverse acetabular ligament (TAL) was positioned towards the raised edge of the cup holder at approximately 30° version from the horizontal plane running through the centre (Jimenez-Cruz et al., 2022). The inclination angle was measured to the desired angle based on the testing parameters (Figure 17c). Using the acetabulum height rig, the artificial head was lowered into the acetabulum, and the height of the acetabulum was verified to ensure it matched the working simulator height (Figure 17d). The sample was then secured in place using the cementing screws.

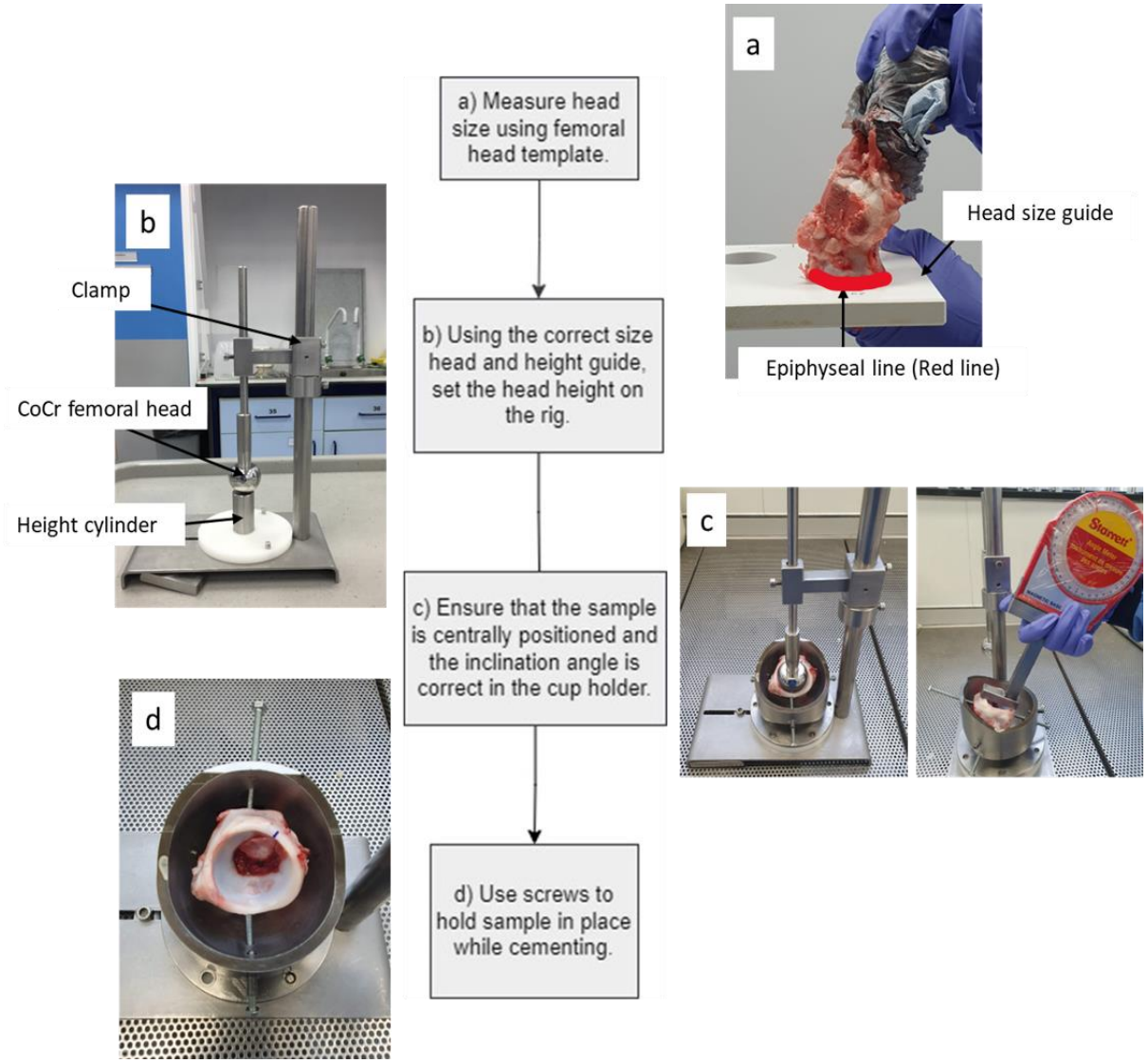

Figure 17: Overview of alignment & cementing process of the acetabulum. a) Femoral head size was measured using a template; the proximal end of the femur was placed into the template. When the guide reached the epiphyseal line, this was considered the correct head size. b) Height rig used to set the correct height of the acetabulum in the pot. c) Sample was positioned centrally, and the centre of the TAL was positioned 30° from the sagittal plane of the acetabular pot. Inclination angle was measured to desired angle. d) Using screws, the sample was held in place, and cement was poured in.

The next stage was the potting of the femoral head using the femoral cementing rig. The pot containing the setup acetabulum was placed onto the base of the femoral alignment rig (Figure 18a). The femoral sample was inverted and placed through the support ring (Figure 18b). The inferior apex of the femur was positioned so that it aligned with the centre of the TAL (Figure 18c). Cementing screws on the support ring were tightened to keep the sample in place. The height guide was then placed over the femoral alignment rig and was used to

determine the correct height of the head Figure 18d). The distal end of the femur was positioned in contact with the alignment plate.

The sample with the supporting ring attached was removed from the rig and inverted (Figure 18e). The acetabular pot was replaced with the femoral pot. The supporting rig was then reattached to the rig in its new position at the previously noted height. The height guide was then used to double-check that the femoral head was at the correct height (Figure 18f). The top of the femoral head was in contact with the alignment plate. Finally, cement was poured into the pot and allowed to cure.

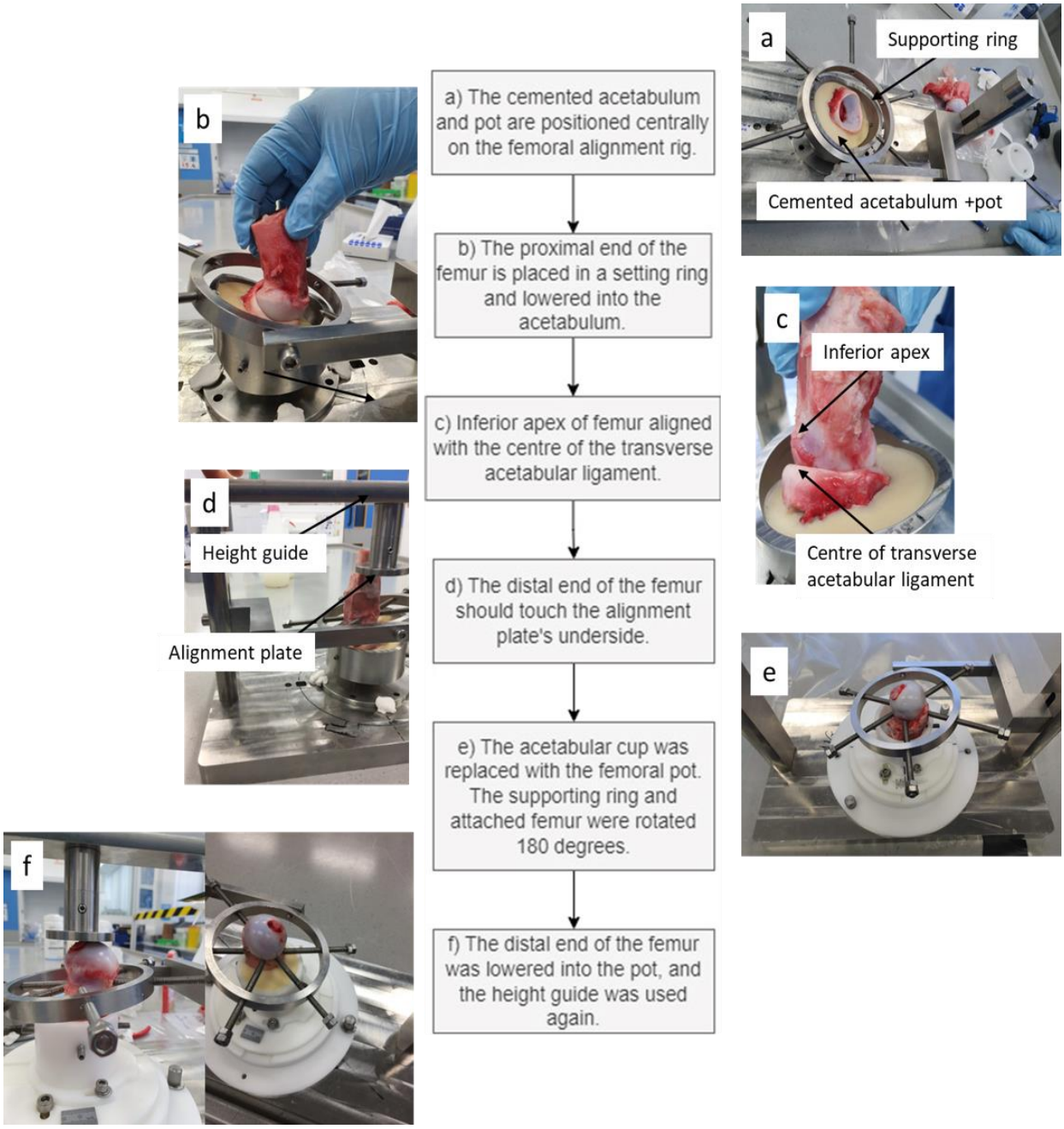

Figure 18: Overview of femur alignment and cementing process. a) The acetabular pot was mounted onto the femoral alignment rig. b) Proximal end of the femur was attached to the support ring. c) This was lowered into the acetabulum, and the inferior apex was aligned with the centre of TAL. d) Height guide placed across the top of the femoral potting rig; the distal end of the femur was in contact with the underside of the alignment plate. e) Femur removed from the supporting ring and inverted 180°. Supporting ring replaced. The acetabular pot was replaced with the femoral pot on the rig. f) (Left) The distal end of the femur was placed into the mounted femoral pot, and the height of the femur was checked using the height guide. (Right) The correctly aligned femur was then fixed into position with supporting screws, and cement was poured into the femoral pot and left to cure.

3.2.4 Refinement of acetabulum alignment method

During pilot testing, several limitations were identified in the acetabulum alignment protocol, which was initially adapted from Groves (2015) and Pallan (2016). These limitations affected sample stability, anatomical positioning and freedom of labral movement. Addressing these issues was essential to improving the accuracy and reproducibility of testing. A revised protocol was developed based on specific design requirements, including stable cementation, correct anatomical alignment, and prevention of labral impingement.

Previous in vitro studies have shown that small deviations in acetabular alignment can noticeably alter where the femoral head makes contact with the rim and, consequently, the pattern of damage generated. Pallan (2016) demonstrated that even minor errors during cementing or positioning resulted in contact occurring at different acetabular regions, while Groves (2015) observed that insufficient joint stability produced diffuse or inconsistent lesions. Together, these findings highlight the sensitivity of natural hip tissue to alignment and justify the refinements made here to improve test repeatability and physiological relevance.

In the original method, samples were manually held in place during cementing, which risked misalignment. To solve this, four holes were added to the acetabular pot to allow screws to fix the sample in place while the cement cured (Figure 19). This ensured that the centre of rotation of the acetabulum was coincident with that of the simulator, improving stability and reducing unwanted displacement.

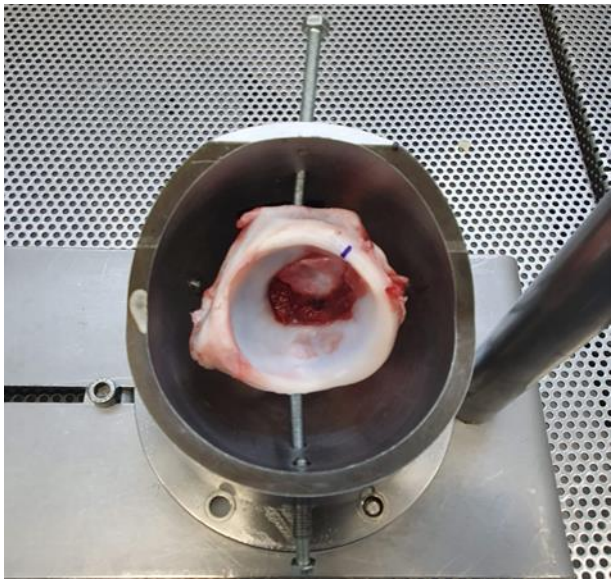

Figure 19: Revised acetabular pot design, four holes added equidistant around the outside of the pot. Screws were used to help maintain sample positioning and alignment during the cementation process.

The previous alignment positioned the transverse acetabular ligament (TAL) at 12 o'clock. However, this did not reflect the natural position of the TAL, which follows the slightly anteverted orientation of the acetabulum. The setup was refined by rotating the centre of the TAL 30° clockwise from the AB plane, aligning the sample more closely with the anatomical neutral position (Figure 20). This allowed for more natural joint mechanics and improved contact between the articulating surfaces.

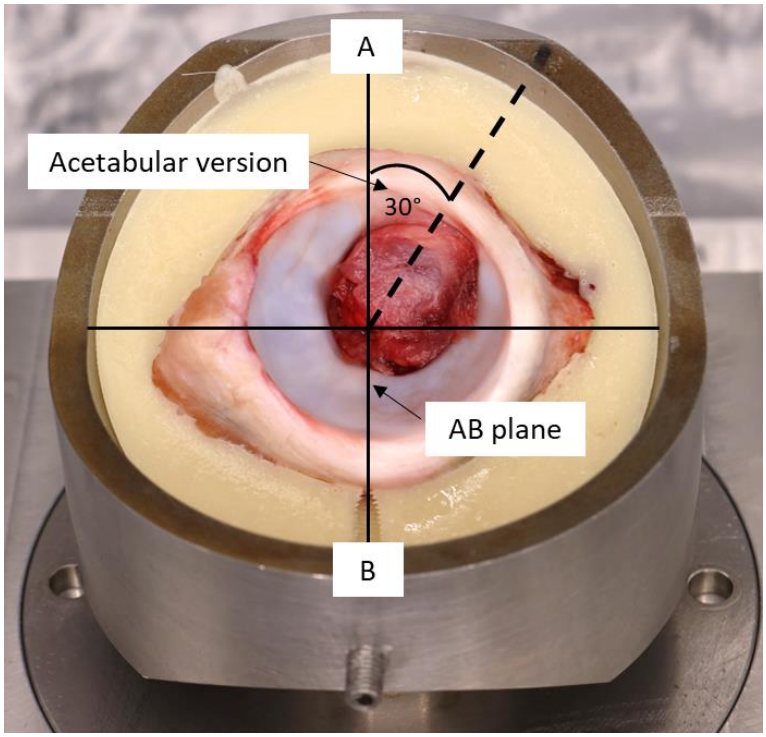

Figure 20: Porcine acetabulum positioned in the centre of the pot to ensure that the centre of rotation was coincident with the simulator. The centre of the TAL was rotated 30° clockwise from the AB plane; this was done to maintain the sample's neutral position.

In early tests, the cement mantle extended to the labrum, limiting potential labral movement and increasing the risk of unintended damage. The revised protocol reduced the cement height at point B to preserve the unconstrained labrum (Figure 21). This ensured that any observed damage was due to test conditions rather than setup artefacts.

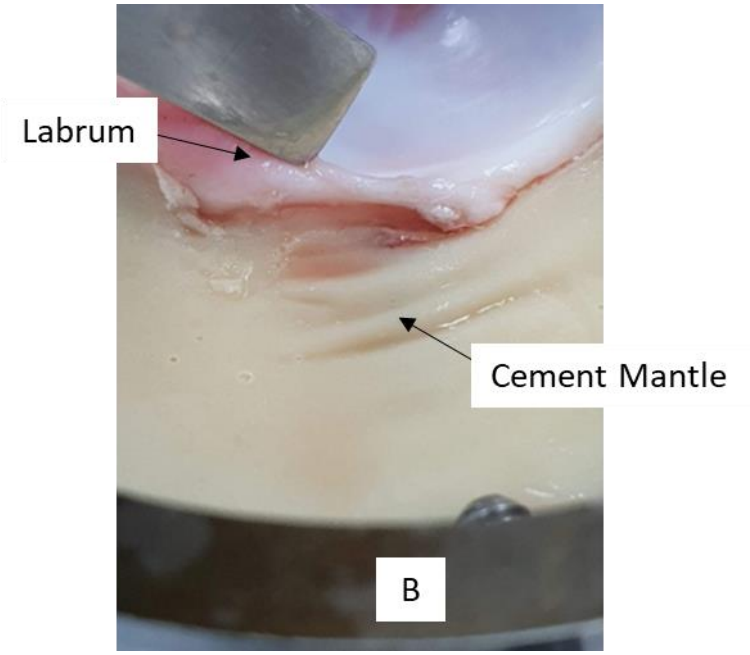

Figure 21: The cement mantle was the same height as the labral edge of the porcine acetabulum. The restricted movement of the labrum during testing could lead to unwanted damage caused by the labrum abutting the cement mantle. A successful simulation required an unconstrained labrum edge.

These refinements to the alignment process addressed specific limitations in the original protocol and were summarised in Table 3. The table outlines each adaptation made, the reasoning behind it, and the improvements it brought to the setup.

Table 3: Summary of the refinements made to the acetabular alignment process, including the justification for each adaptation and the added value to the accuracy and stability of the simulation.

Adaptation	Justification	Value added
Use of screws to hold the sample during cementation (Figure 17c & d).	Prevented movement during curing and ensured the acetabulum's centre of rotation aligned with that of the simulator.	Improved sample stability, prevented misalignment, and ensured accurate joint contact during testing.
Adjusted the acetabular orientation by rotating TAL 30° clockwise from the AB plane.	More accurately represented the neutral anatomical position and natural version of the acetabulum.	Enhanced anatomical accuracy of the setup improves the relevance of simulator results to in vivo conditions.
Reduced the height of the cement mantle.	Prevented the labrum from abutting against the	Enabled free-floating movement of the labrum and more physiologically

	cement, avoiding restriction or damage.	accurate joint mechanics during testing.

These improvements made the testing setup more stable, accurate, and anatomically accurate. The method could benefit other researchers conducting hip joint simulations, especially where labral behaviour or accurate articulation is critical. It provides a robust, repeatable approach that supports more complex test conditions and greater comparability with in vivo results.

3.2.5 In vitro hip simulator test setup

In vitro simulation testing was conducted using pre-existing fixtures from a study completed by Pallan (2016). Some modifications were made to these fixtures, for example, drilling holes to allow for alignment screws and altering the femoral adaptor to facilitate better setting of the centre of rotation. Equipment used in simulations is listed in Appendix 8.1, Figure 22 is an image of the simulator used and Figure 23 is a schematic of the simulator fixtures that have been used.

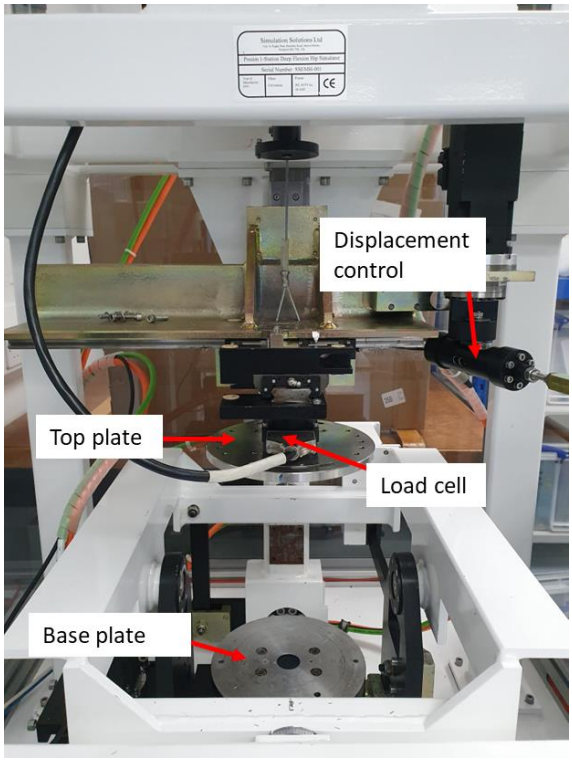

Figure 22: Single station hip simulator.

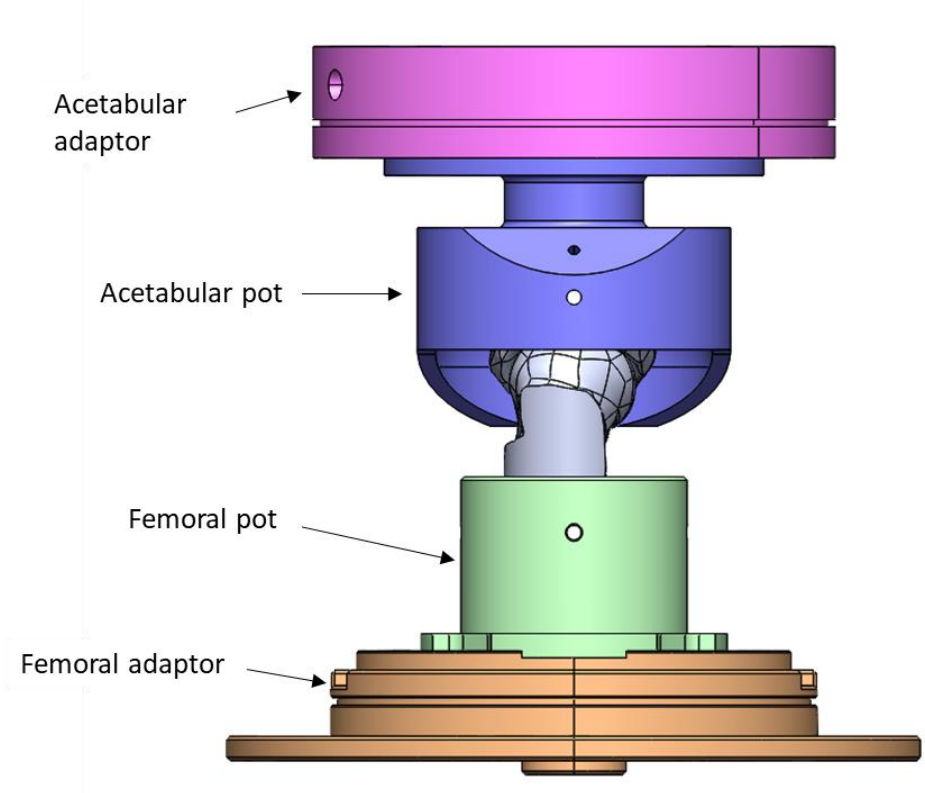

Figure 23: Schematic of simulator fixtures, (from top down) acetabular adapter (pink), acetabular pot (blue), femoral pot (green) and femoral adapter (orange).

3.2.5.1 Simulator capabilities

An electromechanical single-station hip simulator (SSHS) (Simulation Solutions Ltd., Stockport, UK) was used for the in vitro simulations. Electro-mechanical actuators applied programmable loads, motions and displacements, which were calibrated to tolerances of ±50N for load, ±0.03° for rotation, and ±0.2mm for displacement (Table 4). The simulator had three controlled degrees of freedom: flexion-extension, abduction-adduction, and internal-external rotation (Figure 24). As well as the ability to apply axial load and displacements in the medial-lateral and anterior-posterior directions. These displacements could be either left free or fixed, depending on the requirements of the test scenario. The ability to adapt the load and motion parameters in this way made the SSHS suitable for exploring the influence of specific conditions on joint behaviour.

These tolerances are narrow relative to the input ranges used in this study. For example, the peak axial load applied was 900N, making the load calibration tolerance approximately 5.5% of the peak value. Such a margin was not expected to significantly alter the contact mechanics or damage outcomes observed, especially when compared with the typical variation seen between studies with different joint geometries or input profiles. Similarly, the angular and displacement tolerances represented small fractions of the full motion range and were considered unlikely to introduce errors that would affect the interpretation of the results. Additionally, real-time feedback from the simulator was utilised to monitor the agreement between demand and actual waveforms during testing. The close alignment of these waveforms demonstrated that the applied motions were consistent with the programmed input, confirming the simulator's performance accuracy under the conditions of this study.

Table 4: Single station hip simulator programmable ranges, accuracy of each motion, location motion is applied through.

Load/Motion	Programmable Range	Accuracy	Location of motion
Load	4500N	± 50N	Cup
Flexion/Extension	± 60°	± 0.03°	Head
Internal/External Rotation	± 25°		Head
Abduction/Adduction	± 25°		Head

Medial-Lateral Displacement	± 5mm and ± 1kN	±0.2mm	Head
Anterior-Posterior Displacement	± 10mm		Head

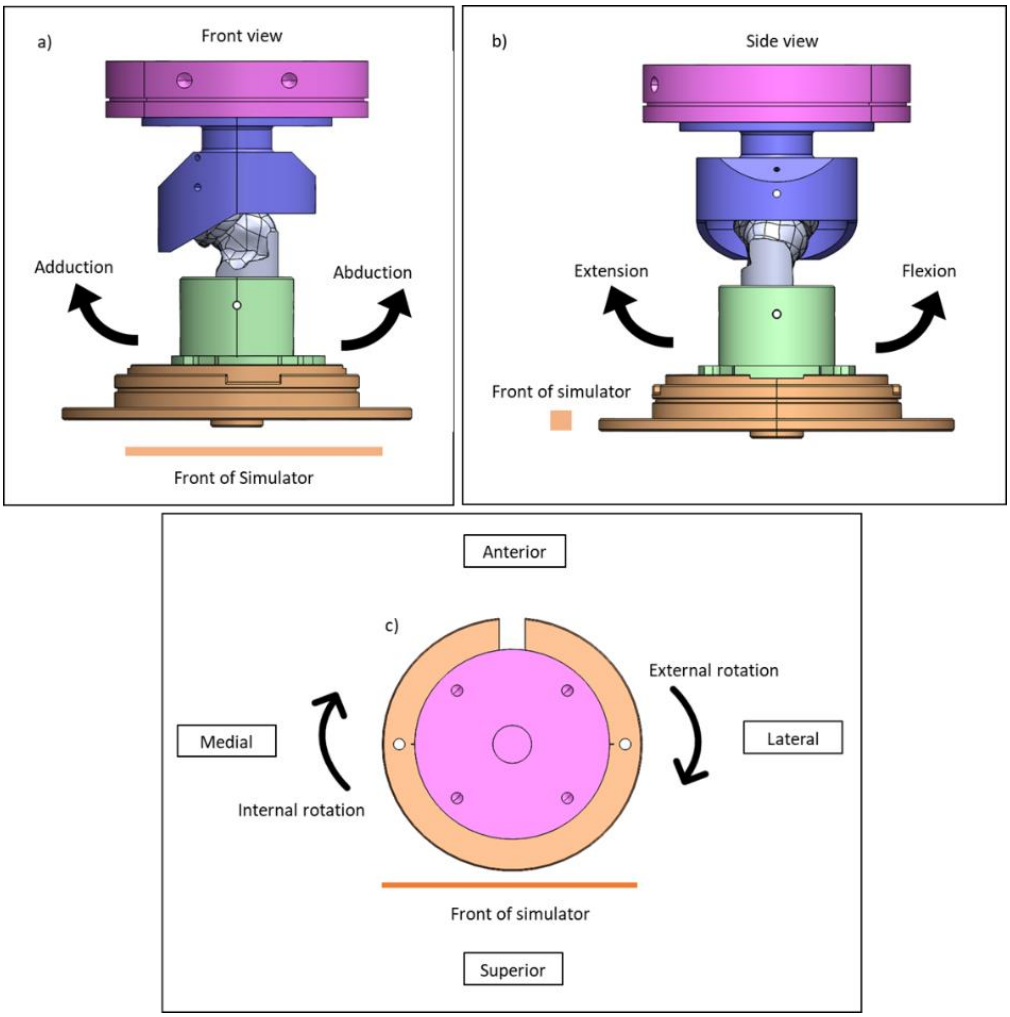

Figure 24: Virtual representations of the simulator component and direction of motions produced. a) Front view: adduction and abduction motions. b) Side view: flexion and extension motions. c) Top view: internal and external rotation.

3.2.5.2 Specimen mounting

Before mounting the femoral head and acetabular samples (as shown in Figure 25) into the simulator, a gaiter was placed around the femoral adaptor-pot fixture and secured using a step-less clamp. The purpose of the gaiter is to form a watertight seal around the samples, maintaining lubrication during testing. The femoral adaptor-pot fixture was attached to the base plate of the simulator, and the acetabular adaptor-pot to the top plate (Figure 25a). The

top plate with the acetabulum attached was then lowered onto the femoral head until the two were concentric (Figure 25b). A spring was placed above the top plate to hold the two fixtures in position. The gaiter was then secured around the acetabulum and held in place with a jubilee clip (Figure 25c).

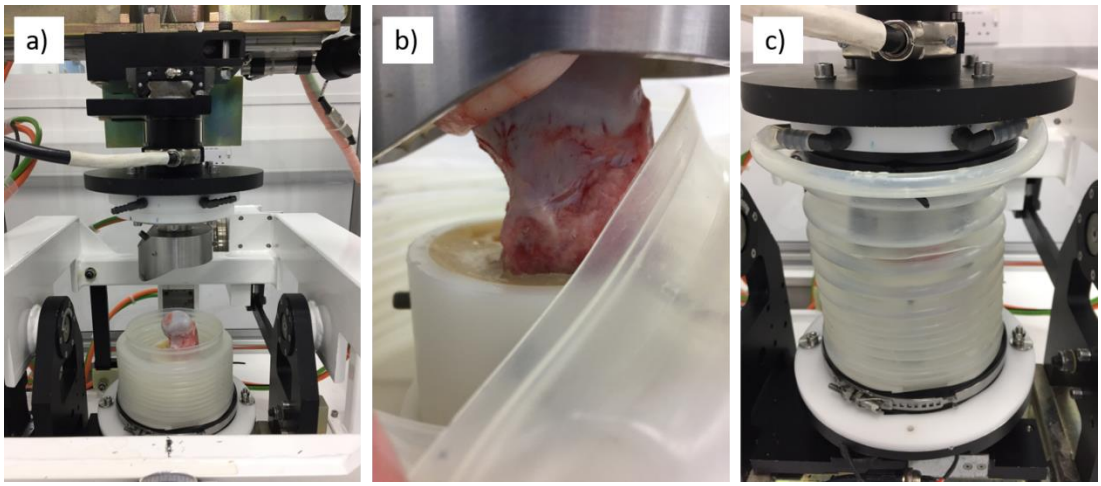

Figure 25: a) Components set up within the simulator. b) Acetabulum lowered onto the femoral head until concentric. c) Gaiter covers the simulator set-up and is filled with Ringer's solution to keep the sample lubricated during testing.

3.2.5.3 Lubrication

The silicone gaiter was filled with solution to ensure all articular surfaces were fully submerged during testing, with approximately 1000 ml of Ringer's solution used for each test. Synovial fluid plays a critical role in maintaining the normal function of synovial joints, acting as both a lubricant and a nutrient medium for the surrounding cartilage and soft tissues. It provides boundary and fluid-film lubrication through its protein and hyaluronan content, while also maintaining osmotic and ionic balance within the joint environment. When replicating in-vivo conditions in an in-vitro test setup, the choice of fluid medium is therefore important, as it influences tissue hydration, load transfer, and cellular viability. In the current study, Ringer's solution was used instead of protein-based lubricants such as bovine serum to provide a physiologically relevant ionic environment during short-term (4 hour) simulation. Ringer's maintains an osmotic pressure and electrolyte composition comparable to that of native synovial fluid, helping to prevent tissue swelling or desiccation that may occur in dry or non-isotonic conditions (Zimmerman et al., 2021). Previous studies have shown that for short test durations, Ringer's solutions preserve cartilage metabolism

and matrix integrity more effectively than saline, while avoiding the variability and protein deposition associated with serum-based media(Reagan et al., 1983; Gradinger et al., 1995; Gulihar et al., 2013; Sardana et al., 2019). Thus, the use of Ringer's solution offered a controlled and biochemically stable environment sufficient for maintaining tissue integrity throughout the four-hour test period, without introducing the confounding effects of protein adsorption that can influence surface interactions during longer-term or wear studies.

3.2.5.4 Calibration

Calibration of the SSHS was performed before in vitro simulations. The machine was calibrated in accordance with the University of Leeds standard operating procedure. Simulator loads, torques and displacements were calibrated using an external load cell and slip gauges. This was done to ensure the simulator was operating within the expected range. The external 5kN load cell (Omega DP25B-S-230) was left to warm up for 30 minutes before use, which helped reduce the likelihood of drift in the load cell signal. Using the ProSim simulator software, the automatic load calibration function was used to calibrate the axial and medial-lateral forces, flexion-extension, abduction-adduction, and internal-external torques. The external load cell was mounted to the simulator in different positions relative to each of the forces or torques being measured. Five different loads were applied to the external load cell, and the output reading was recorded in the software, which calculated the calibration constant.

Medial-lateral and anterior-posterior displacements were calibrated using the automatic displacement calibration function within the simulator software. Slip gauges were used to move displacement sensors a known distance. This information was then recorded in the software, and the demand position was calibrated against the known actual position.

3.3 Development of damage characterisation methods

A variety of methods have been used clinically to describe damage to the labrum and cartilage observed during hip arthroscopy (Beck et al., 2004; Ilizaliturri et al., 2008; Konan et al., 2011; Barros et al., 2019). However, there are no reported methods to characterise damage caused by in vitro experiments. This section outlines the advantages and

disadvantages of methods used clinically in terms of their applicability to an in vitro setting; the development of a method for characterising in vitro damage is then detailed.

The overall aim was to create a successful damage characterisation method for use following an in vitro simulation. The method needed to record damage, such as delamination and other cartilage changes and provide good intra and inter-user repeatability.

3.3.1 Development of Photogrammetry method

Photography was important for recording areas of damage or morphological changes to the labral and cartilage surfaces. Images were taken from a top view of the acetabulum and femoral head: before testing, at 2 hours and post-test (4 hours). Three different views were captured at each imaging interval: wide lens, macro lens, and a close-up. Magnified images were taken of any areas of interest, particularly the articulating surface of the acetabulum and the labrum. To ensure consistency of the photos and to limit the impact of external factors, all images were taken under the same lighting conditions, using a light box. A consistent distance between the sample and the camera (Canon EOS 750D) lens was maintained throughout, using a tripod. Camera settings for each image remained constant and are detailed in Table 5. Maintaining the same camera settings was crucial for a reliable visual comparison between time points. Any changes in exposure, aperture, or white balance could have affected the appearance of the tissue surfaces and potentially influenced the classification of damage severity.

Table 5: Camera settings used during photogrammetry of tissue samples.

Setting	Wide Lens	Macro Lens	1:1 Close-up shot
PhotoBox light source (Position of the dial)	1/8	1/8	N/A
ISO	200	400	1600
Aperture	8	8	16
Shutter speed	60	100	100

Following the initial pilot study, a small artefact was identified in some of the images of the acetabulum. This was due to the LED light strip on the top of the PhotoBox (Figure 26). An

attempt was made to mitigate this by using polarising film to reduce the effect of the reflection. However, this approach was unsuccessful, resulting only in a reduction in the overall brightness of the image.

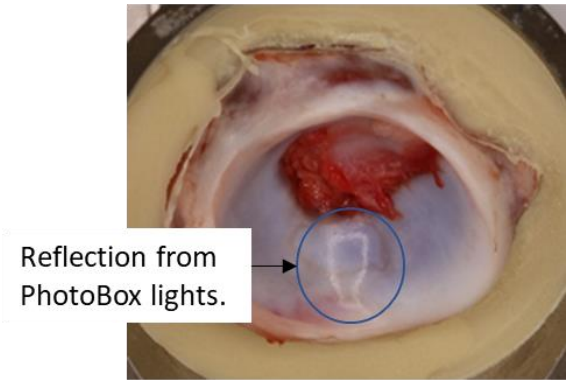

Figure 26: Reflection of the PhotoBox light strip seen in images of the acetabulum.

A study was conducted to compare images taken by two different users using the photography methodology. This demonstrated consistent images when the same settings are used (Figure 27).

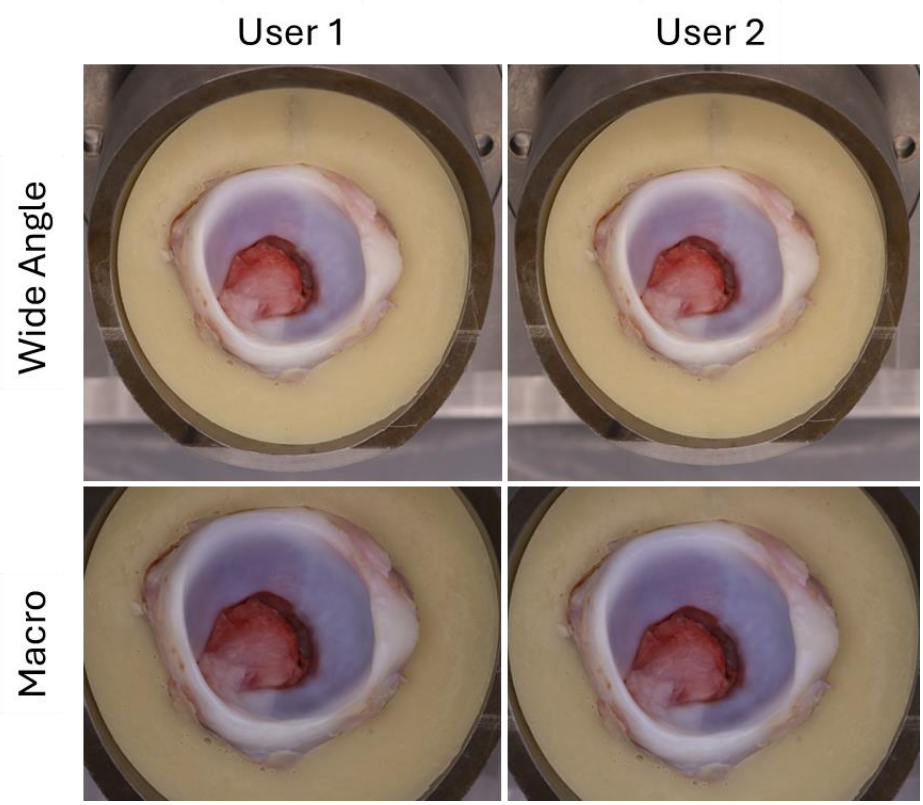

Figure 27: Comparison of porcine hip images captured by two different users using the same photography methodology. Top row: wide-angle images; bottom row: macro images. Consistent image quality and perspective were achieved across users when identical camera settings were applied.

3.3.2 Damage characterisation methodology

A consistent and replicable approach to classifying damage was important for in vitro testing studies, especially where damage was subtle and subject to interpretation. Unlike existing clinical classification systems that often focus on scoring damage severity, the method developed in this study aimed to classify the type of damage observed. This was particularly important for ensuring consistency between samples, enabling comparison across future studies using this protocol, and addressing the lack of an established system tailored to in vitro simulation damage, particularly in porcine acetabula. The classification system is based on clinical descriptors from existing literature, modified for visual, image-based assessment of simulated damage. The six descriptors identified were: Scratch/Indentation, Tear/Flap, Separation from Cartilage, Blushing, Fibrillation, and Delamination (or bubbling). These descriptors mirror clinical damage types documented in studies such as Beck et al. (2005) and Konan et al. (2011), but are specifically adapted for visual evaluation of porcine tissue

during testing. Each descriptor and its potential mechanism of formation are described below.

The method for characterising damage in this study was developed because no existing system was designed for classifying the specific types of damage created during in vitro simulations of the hip. The focus of existing methods, such as the Outerbridge classification or ICRS scoring system, is on ranking or grading the severity of damage seen in clinical settings, rather than describing the type of damage. The Beck classification, although designed for the hip, combines different types of damage, such as labral tears and cartilage fibrillation, into the same grade (Beck et al., 2005). This approach did not suit the aims of this study, which was to identify the specific type of damage generated during testing rather than its severity. Therefore, a simple, image-based system was created that could be applied consistently and allow future studies to replicate the same approach.

Findings were recorded in an information sheet (Appendix 8.2), with observed damage matched to descriptors and documented based on the appearance of each type of damage. Samples were characterised at three points during testing: pre-test, 2 hours, and post-test. Table 6 outlines descriptor names, definitions, and example images where relevant. Descriptors such as tear/flap, separation from cartilage, and fibrillation were included in the classification system even though they were not observed, as they are frequently mentioned in related clinical literature and may be seen in future tests.

Table 6: Descriptors used in classifciation of damage created during in vitro simulations.

Type of damage	**Description**	**Image**
Scratch/ indentation	Surface-level dents or abrasions typically found on the articulating surface of the acetabulum. May result from abrasive wear due to dislodged cement or bone debris. Reflective surfaces sometimes obscure these in images.	
Tear/Flap	Minor cuts or flaps on the labral tissue, typically caused by trauma or repeated motion. Suggestive of overuse failure.	N/A

Separation from cartilage	Detachment at the chondrolabral junction, where the labrum separates from the cartilage due to compressive and tensile forces.	N/A
Blushing	A visual change in cartilage colour, potentially indicating subsurface deformation or fluid loss.	Pre and post-test example of blushing. 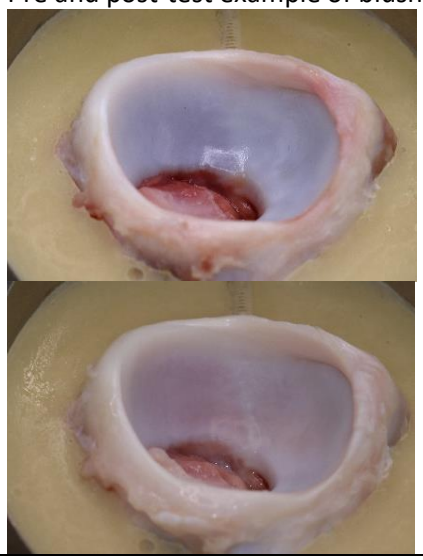
Fibrillation	Fraying of the superficial cartilage surface. Indicative of early degeneration or surface fatigue.	N/A

Delamination (or bubbling)	Bubbling initiated: Represents the very onset of surface fatigue or shear. Appears as the first small raised spots on the cartilage surface, but with minimal disruption to the surrounding tissue. Bubbling (established): Represents early to intermediate fatigue or shear at the cartilage surface. Appears as raised or vesicle-like formations, indicating local matrix separation, but with the surface layer still largely intact. Delamination: Refers to a more severe form of surface damage where a layer of cartilage has fully separated or lifted from the underlying tissue. It indicates advanced mechanical failure, often following or developing from bubbling if the stress continues. Delamination corresponds to a clear loss of material and structural integrity, rather than just a visual surface change.	

While the main goal of this system was to classify damage types rather than severity, specific descriptors can also serve as indicators of relative progression. For instance, blushing signifies an early visual change, whereas scratching indicates surface-level disruption, and delamination or bubbling points to more advanced fatigue or shear failure. Although not measured on a numerical scale, these descriptors offer a qualitative understanding of damage progression. This enables comparisons across testing conditions to be made based on the types of damage observed.

Overall, this classification method was designed to provide a clear and consistent way of describing damage type, rather than severity, which was better suited to the study's aims. The system is image-based and straightforward, making it reproducible for future work.

However, it relies on visual inspection, which can introduce subjectivity and is limited by the resolution of available imaging.

3.3.2.1 Location of damage

To describe the location of damage on the acetabular surface, the zonal method was adopted (Figure 28), as described by Ilizaliturri et al. (2008). This method divides the acetabulum into six zones, utilising fixed anatomical landmarks to ensure consistency and repeatability. Three lines were drawn: one at the anterior edge of the acetabular notch, one at the posterior edge, and a third at the superior margin of the notch. These divisions create six distinct zones across the articular surface. For consistency, the femoral head was also divided into six mirror-image zones, allowing for comparative analysis of damage location on both articular surfaces. The ligamentum teres was used as an additional anatomical landmark and corresponds to zone six.

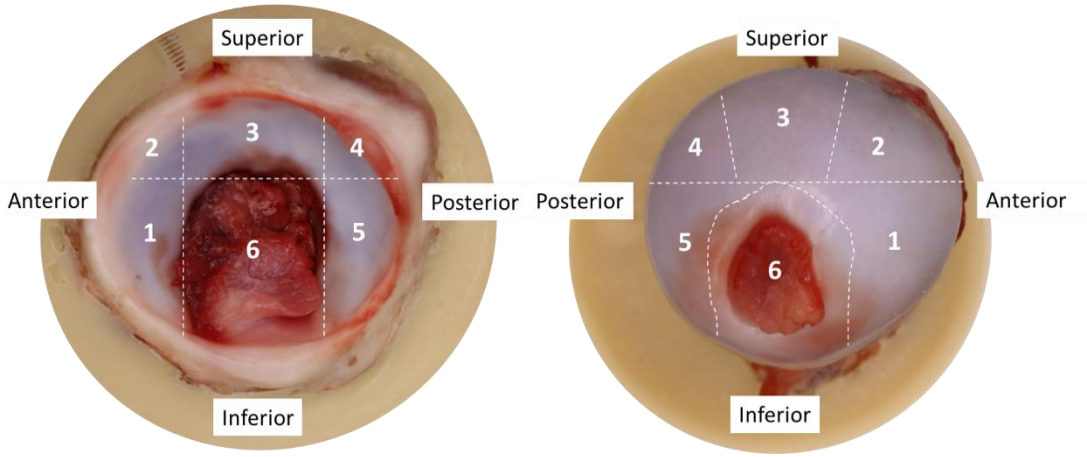

Figure 28: To assist in describing the location of damage, the hip was split into zones using the Ilizaliturri et al. (2008) zonal method. The acetabulum was divided into six zones using the acetabular notch as an anatomical landmark. This was then mirrored onto the femoral head.

This method was chosen over the alternative clock-face method due to its lower susceptibility to perception errors (Ilizaliturri et al., 2008; Konan et al., 2011). While the clock-face technique divides the acetabulum into twelve sections using a standardised orientation, it can be influenced by variations in sample orientation and geometry, especially in in vitro studies using porcine samples. In contrast, the zonal method's reliance on anatomical landmarks, rather than imposed angles, offers improved reliability in describing damage location.

Nonetheless, potential sources of error exist in this approach. These include variability in identifying the exact margins of the acetabular notch, which may differ across samples, and the irregular morphology of the porcine acetabulum, which could affect the consistency of zone definition. To minimise this, care was taken to align samples consistently and to apply the same visual criteria when identifying landmarks.

3.3.2.2 Reproducibility study

To assess the reproducibility of the damage characterisation method, a study was conducted to evaluate both inter and intra-observer reliability. A set of eight sample images, comprising both wide-angle and macro views, was selected to represent the full range of observed damage categories (i.e., no change, Scratching, Blushing, Delamination). For intra-observer testing, one observer characterised the damage at three different time points: immediately after testing (using the physical sample), from images after testing, and again two weeks later using the same images (each time blinded to previous observations). Inter-observer testing involved two additional observers with varying levels of experience, but possessing a working knowledge of hip joint anatomy, who each independently assessed the image set used for the intra-observer study.

As shown in Table 7, there was agreement in characterisation across all three observations for seven out of eight samples in the intra-observer study. The only exception was Sample 4, which was characterised as “scratching” when examined directly after testing but categorised as “no change” when assessed via images. This suggests that minor or subtle damage features, such as scratches, may be more challenging to detect solely through images. Overall, the intra-observer reliability was high, demonstrating that the method was consistent when used by the same individual.

Table 7: Intra-observer reproducibility in damage classification across three time points. Shows the classifications made by one observer using the physical sample immediately after testing, then from images, and repeated two weeks later. (No change (green), Scratching (blue), Blushing (yellow), Delamination (red)).

Sample Number	Immediately after testing	From Images	From images two weeks later
1	No change	No change	No Change
2	Delamination	Delamination	Delamination
3	No change	No change	No change
4	Scratching	No change	No change
5	Blushing	Blushing	Blushing
6	Scratching	Scratching	Scratching
7	Blushing	Blushing	Blushing
8	Delamination	Delamination	Delamination

Interobserver findings are summarised in Table 8. Full agreement was seen in three of the eight samples. In four cases, two out of three observers agreed, and in one case (Sample 3), there was no agreement among any of the observers. This suggests moderate inter-observer reproducibility.

A breakdown of pairwise observer agreement is shown in Table 9, which demonstrates that Observer 3 agreed more frequently with other observers. This is likely because Observer 3 developed the damage characterisation criteria and had the most experience applying it. This indicated that with proper training and familiarity, the reproducibility of the classification system can be improved.

Table 8: Inter-observer reproducibility in damage classification for eight samples by three observers at one time point.

Sample Number	Observer 1	Observer 2	Observer 3b
1	No change	No change	No change
2	Scratching	Delamination	Delamination
3	Delamination	Blushing	No change
4	No change	No change	No change
5	Blushing	Blushing	Blushing
6	Scratching	No change	Scratching
7	No change	Blushing	Blushing
8	Delamination	Scratching	Delamination

Table 9: Pairwise inter-observer agreement. Summarises the agreement between each pair of observers across the eight samples. Tick indicates agreement, cross indicates disagreement. Totals at the bottom indicate the overall frequency of agreement for each pair.

Sample	Observer 1 vs Observer 2	Observer 1 vs Observer 3	Observer 2 vs Observer 3
1	✅	✅	✅
2	❌	❌	✅
3	❌	❌	❌
4	✅	✅	✅
5	✅	✅	✅
6	❌	✅	❌
7	❌	❌	✅
8	❌	✅	❌
Agreement Count	3/8	5/8	5/8

A qualitative classification method was selected because subtle damage features, such as blushing or scratching, were often difficult to capture using automated image processing. In some cases, the edges of these features were diffuse, making quantitative pixel-based classification unreliable. The key aim of the damage analysis was to identify the type of damage rather than quantify its precise size or depth. Therefore, subjective assessment by a trained observer was considered more appropriate for this study. The intra-observer results indicate that the approach is suitable for single user classification, as was applied consistently throughout this project. The inter-observer study highlights that classification becomes more robust with familiarity and training. Future use of this method by other researchers would benefit from clear training guidelines and reference images.

Finally, although inter-observer variation was present, the high agreement between the most experienced user and others suggests that this method can be robust, provided clear criteria are followed. Refining the protocol with standardised definitions and possibly incorporating semi-quantitative image tools may further enhance reproducibility in future studies.

3.4 Development of natural (porcine) hip in vitro simulation methods.

The purpose of this study was to develop an in vitro simulation method, whereby individual parameters were tested in isolation to better understand their impact on damage in the hip joint. Load, sliding distance and direction at the cartilage labral junction were identified as parameters that were likely to affect the damage in the joint.

This section presents the findings of natural in vitro simulations that investigate three damage-causing parameters. Following a set of tests under Initial Control conditions, parameters were investigated in turn, and incremental adjustments were made depending on damage observed (Figure 29). The combination of parameters was either carried forward to the next stage of testing or disregarded as a parameter that did not result in any further damage. Throughout this testing, adjustments continued to be made to improve the simulation's accuracy and repeatability, and the results informed a final selection of parameters that induced damage. These were referred to as Refined Control conditions and were then used in subsequent in vitro simulations.

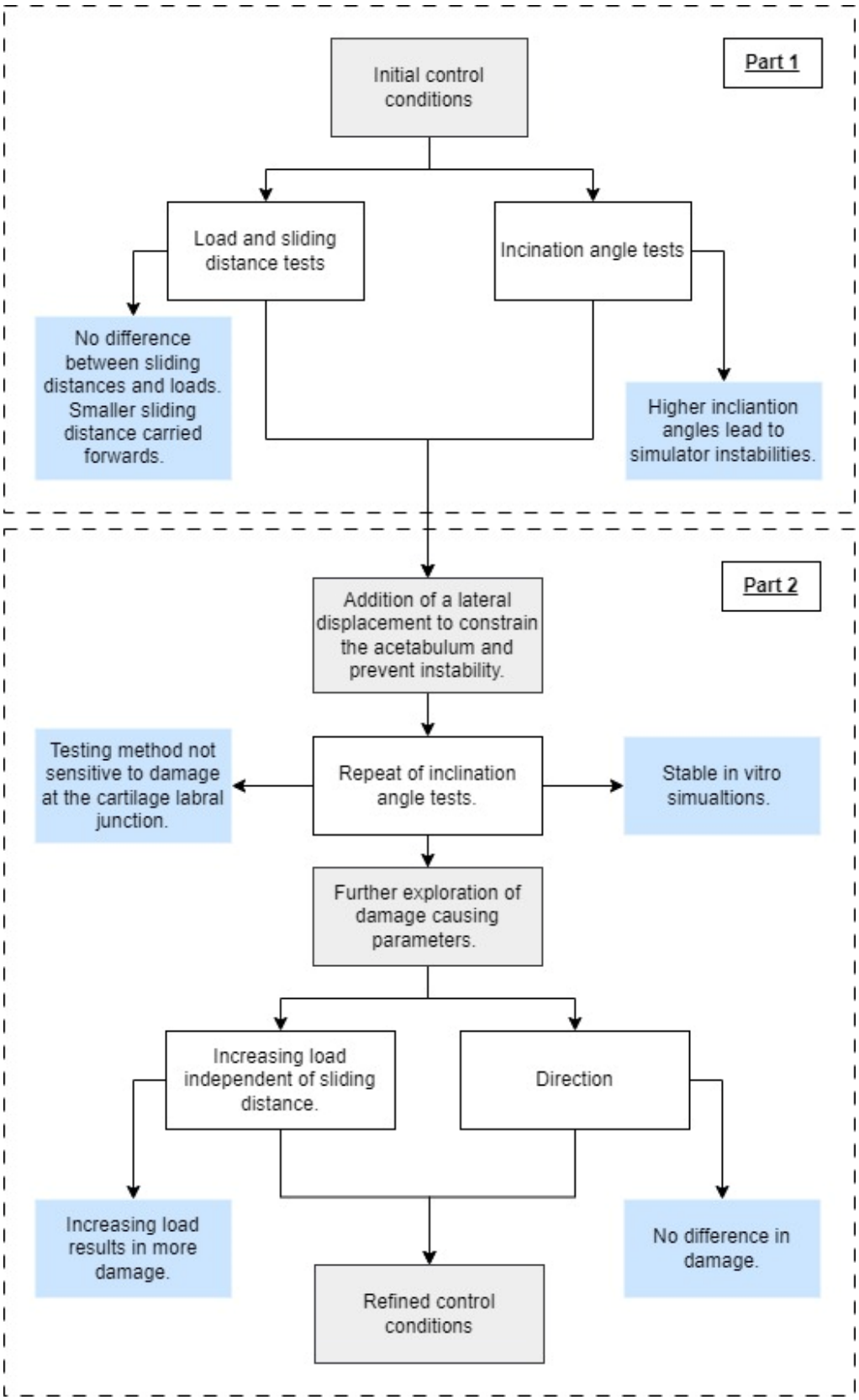

Figure 29: Flow chart showing development of testing methodologies for in vitro porcine testing, and assessment of damage causing parameters.

3.4.1 Testing Parameters

The following testing was used to define the Refined Control parameters that caused damage at the cartilage labrum junction. The studies varied parameters (sliding distance, direction, and load) that were expected to affect damage. The different parameters assessed are shown in Table 10:

Table 10: Matrix of testing parameters used in in vitro simulations; letters denote testing code.

	Sliding distance	**Inclination angle (°)**	**Load (N)**		
			900N	1130N	1500N
Parallel motion	+/-20°	35°	A	C	
	+/- 10°	35°	B	D	
		45°		E	
	+/-10° +1mm ML Dis	35°		F	H
		45°		G	
Perpendicular motion	+/-10° +1mm ML Dis	35°			I

The testing process was divided into two parts (Figure 29). Preliminary testing to develop methods and understanding in terms of effects of parameters (part 1) and optimisation of methods to develop a control set of parameters that result in damage (part 2). Test cases undertaken are detailed below, letters denote tests as described in Table 10.

Part 1:

- Observation of damage resulting from the Initial Control set of parameters based on previous studies (Jimenez-Cruz et al., 2022) (A).
- The effect of load on damage in the hip joint. (B vs D)
- Comparison of damage for two different sliding distances. (A vs B) (C vs D)
- Effect of moving the contact closer to the cartilage labral junction. (D vs E)

Part 2:

- Maintaining sample stability. The effect of the new method of stabilising samples on previously tested parameters.
    - Load (F vs H)
    - Inclination angle (F vs G)
- The effect of directional changes on damage in the hip joint. (H vs I)

3.4.2 Part 1: Preliminary testing

In Part 1, preliminary testing was conducted to assess the damage caused by the Initial Control parameters. Scaling protocols were applied to the Initial Control parameters derived from the literature, and tests were systematically completed. Parameters were adjusted based on the observed damage in the joint; the greater the severity of the damage, the more beneficial the parameter was deemed to be. This testing aimed to identify damage causing parameters.

3.4.2.1 Methods: Preliminary testing

Initial control parameters for testing were informed by previous natural in vitro studies using porcine tissue. In particular, Jimenez-Cruz et al. (2022) conducted walking simulations based on the ISO gait profile commonly used for artificial hip implant testing, which was scaled for porcine hips. This approach provided a physiologically relevant starting point for defining loads, angular motions, and inclination angles, ensuring that the simulator conditions reflected both established standards and the mechanical limits of the tissue.

Porcine hip scaling method to determine peak load

Porcine tissue served as a substitute for human hips in this study due to its similar geometry and greater availability for in vitro testing. However, structural differences mean that porcine tissue is more susceptible to overloading and premature damage if directly subjected to human-equivalent hip joint forces. For this reason, scaled loading conditions were applied to ensure that the porcine tissue could be tested under physiologically relevant conditions without compromising the integrity of the samples.

The purpose of scaling was to reproduce human physiological loading and simulate the tissue damage or degradation that occurs under typical or adverse conditions, while remaining within the mechanical limits of porcine cartilage. To achieve this, experimental data from quadrupedal animals was used to inform the load profile, recognising that pigs are quadrupeds and distribute their weight differently from humans. Previous studies often simplified this by assuming even weight distribution between four limbs, with two hooves in contact during gait, resulting in estimated constant loads of 400N and peaks of 800N for an 80kg pig (Lizhang, 2010; Groves, 2015; Pallan, 2016).

However, a study by Thorup et al. (2007) found that joint loading in pigs was not evenly distributed between the forefeet and the hindfeet, which could suggest that the highest load through a porcine leg could be considerably more. In a study by Bergmann et al. (1999), hip joint forces in sheep were measured using an instrumented joint prosthesis. Given the shared quadrupedal gait, these data were considered broadly comparable to porcine hips. Bergmann et al. (1999) reported regression equations relating hip joint force (% body weight, BW) to walking speed, providing both median (R^{med}) and absolute maximum (R^{abs}) values. For the present testing, the absolute maximum was selected to create the most severe loading scenario:

$$R^{abs}(\%BW) = 97 + (2.6 \times speed(km/h))$$

To use the Bergmann et al. (1999) data to inform this experimental simulation, an appropriate testing speed had to be calculated. The hip simulator adheres to ISO 14242, which prescribes a 1 Hz frequency to replicate cyclical human gait. Based on a human stride length of 1.38 m, this frequency corresponds to a walking speed of ~5 km/h. The following equation was used to calculate the speed in km/h:

$$Speed\ (\mathrm{km}) = \left(\frac{3600\ \mathrm{cycles}}{1\ \mathrm{h}}\right)\left(\frac{(1.38\ \mathrm{m})}{1\ \mathrm{cycle}}\right) = 4{,}968\left(\frac{\mathrm{m}}{\mathrm{h}}\right) = 4.968\left(\frac{\mathrm{km}}{\mathrm{h}}\right)$$

For this testing simulation, the speed was rounded to 5km/h. Using the calculated speed and average weight of a pig (80kg), a R^{abs} value of 898N was calculated (see calculations below). This was rounded to 900N and used as the peak load in testing.

$$97 + (2.6 \times 5) = 110\%BW$$

$$\frac{(110 \times 80)}{9.8} = 898N \sim 900N$$

An estimated average porcine weight was required to calculate an appropriate peak load and was initially obtained from the literature. As some samples had not yet been dissected, a value of 80kg was used (Lizhang, 2010; Groves, 2015; Pallan, 2016). After testing, the actual average weight of the specimens was found to be 84kg. This resulted in a calculated load of 942N, differing by 42N from the original estimate.

By scaling in this way, the testing protocol ensured that porcine tissue was loaded within realistic physiological limits while accurately modelling the extremes of human gait conditions. This provided a controlled yet translationally relevant loading method for assessing cartilage and labral tribology in the hip simulator.

Parameter selection

An increase in joint load and consequently contact pressure is known to contribute to greater cartilage damage. In this study, three loads were applied: 900N, 1130N, and 1500N. Based on a porcine scaling method, 900N was identified as the peak load for a scaled gait cycle and was therefore selected as the Initial Control load. This load served as a physiologically relevant baseline for testing. To systematically assess the effect of increased loading, subsequent tests were carried out at 1130 N and 1500 N, representing nominal 25% and 50% increases, respectively. These incremental increases were chosen to evaluate whether higher loads beyond the baseline physiological range would result in measurable or progressive cartilage damage. Each load was applied in succession, beginning with the lowest. Testing progressed to the next load only if substantial damage was not observed at the previous level.

In this study, sliding distance refers to the angular motions applied to the femoral head. Sliding distances of ±10° and ±20° were selected based on arc length calculations using the average porcine femoral head diameter of 35.6 mm, reported by Taylor et al. (2012). These calculations (Figure 30) showed that ±5° (~1.6mm) produced minimal uncovering of the femoral head, offering negligible sliding movement and were therefore excluded. ±10° (~3.1mm) and ±20° (~6.2mm) produced a more substantial arc length, promoting surface uncovering, which was considered beneficial for allowing cartilage recovery during testing. Additionally, fixture design limitations and potential for impingement were also considered when defining the upper limit of angular motion. The ±20° input also aligns with flexion–extension values reported in porcine gait studies, such as those by Jimenez-Cruz et al. (2022), supporting its physiological relevance.

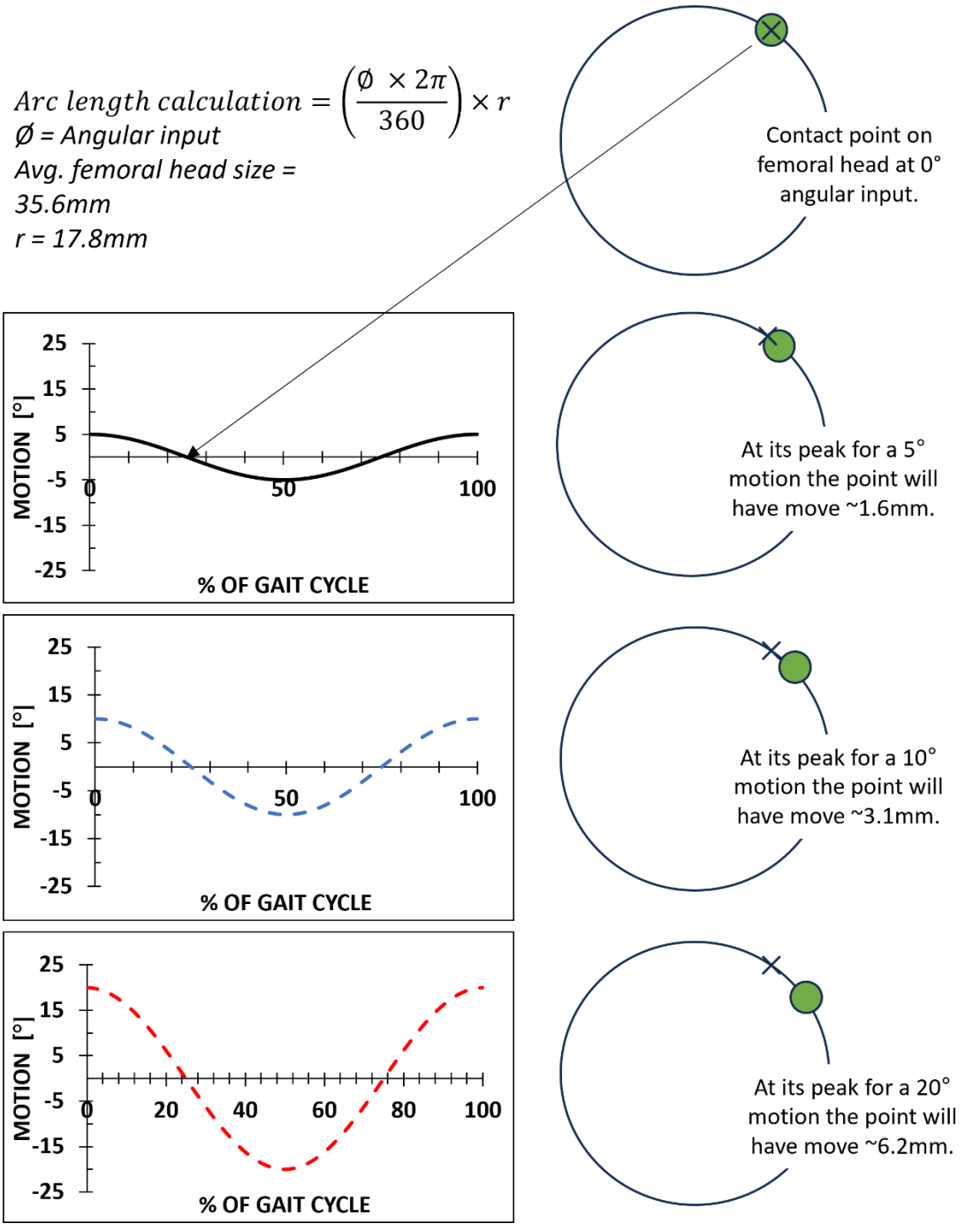

Figure 30: Illustration of angular input and resulting arc lengths for a porcine femoral head (average diameter 35.6 mm). Graphs show angular motion across the gait cycle for ±5°, ±10°, and ±20°. Diagrams on the right depict the estimated arc length travelled by the contact point at peak angular displacement: ~1.6 mm for 5°, ~3.1 mm for 10°, and ~6.2 mm for 20°.

The inclination angles used in this study (35°, 45°, and 55°) were selected to represent progressively more adverse loading conditions. An angle of 35° aligns with ISO 14242, the international standard for artificial hip implant wear testing, and is considered clinically relevant; using this standard ensures that simulator testing is performed under validated,

reproducible conditions, building on a tried-and-tested framework. Accounting for the 10° transposition between the body and the simulator, this corresponds to approximately 45° in vivo (Ali et al., 2016). Increasing the inclination angle moves the load point toward the acetabular rim, creating edge-loading conditions. While edge loading is typically associated with artificial implants, certain natural hip pathologies, such as cam-type femoroacetabular impingement (FAI), produce similar localised stress and shear forces (Pallan, 2016). The higher angles of 45° and 55° were therefore chosen to replicate these adverse mechanical environments, representing physiologically plausible extremes and allowing exploration of how increased rim loading could influence damage.

Testing was run for 4 hours at 1 Hz, totalling 14,400 cycles. Based on an average stride length of 1.38m (Ardestani et al., 2016), which is twice the length of a simulator cycle, this equates to approximately 10km of walking. Testing was paused once at the halfway point for inspection. The 4-hour duration was selected based on preliminary comparisons with 6-hour tests, which showed minimal difference in damage. Given practical constraints, such as lab access and the need to avoid overnight testing or repeated refrigeration, 4 hours was considered the most appropriate duration.

Simulator setup

The experimental setup was designed so that medial-lateral (ML) and anterior-posterior (AP) displacements were unconstrained, allowing the motion to follow the natural, non-uniform shape of the porcine femoral head and acetabulum (Figure 31). Motion was applied to the femoral head while the acetabulum remained fixed, with vertical load applied through the acetabulum. Movements parallel to the cartilage-labral junction were generated using flexion-extension, and perpendicular movements using abduction-adduction. Although a unidirectional motion was applied through the simulator, the unconstrained ML and AP axes allowed for some small translation in these directions as the components interacted. These small additional motions were not directly measured but were considered acceptable as they reflected the natural fit of the sample within the simulator.

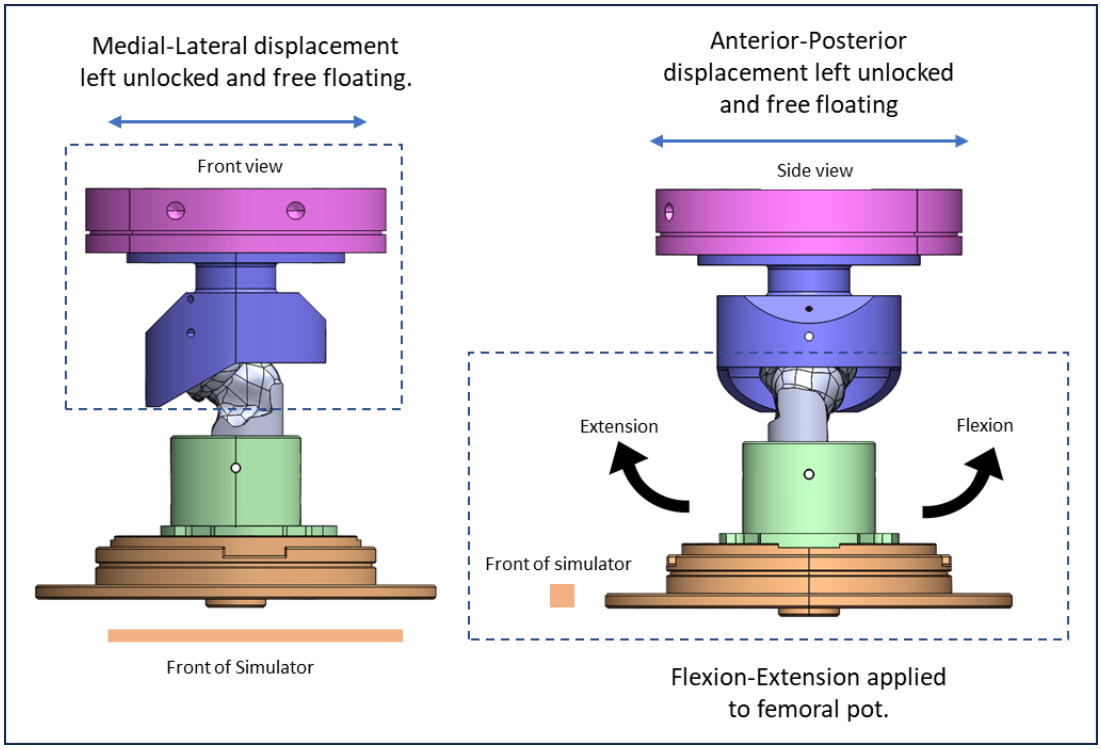

Figure 31: Front and side view diagrams of the initial experimental setup within the simulator. Both medial-lateral and anterior-posterior displacements were not restricted and left to move freely. Flexion-extension movements were applied to the femur; the acetabulum remained in a fixed position.

In vitro simulation results were recorded by photogrammetry as detailed in Section 3.3.1. In addition to categorising observed endpoint damage, images were taken to aid in comparison between testing parameters. Three repeats were completed for each set of parameters (see Appendix 8.3 for all photogrammetry). However, only pre and post-test images for a single sample are presented in this section. The sample chosen is the one that best illustrated the type of damage observed for that set of parameters.

Load and motion profile

The hip simulator input profile consisted of a load and a motion waveform (Figure 32). Peak load and applied motion for each test varied depending on the parameter set used. Nevertheless, all load waveforms followed a similar pattern of a simplified gait cycle, in as much as they started at 300N and then increased to a peak value at 30% of the cycle time, the load then reduced, and from 60% of the cycle time until the end of the cycle, a constant load of 300N was applied. All motions were applied as sinusoidal waveforms.

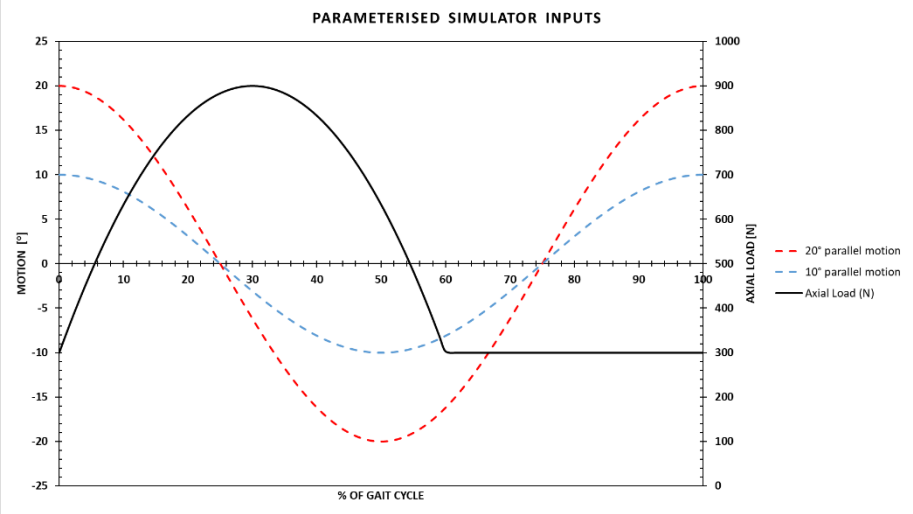

Figure 32: Parameterised simulator inputs. Axial force is applied for 60% of the gait cycle and increases gradually until it reaches its peak load at 30% of the gait cycle. It is then reduced, and the remaining cycle consists of a constant dwell period.

3.4.2.2 Results: Preliminary testing

This section presents the results obtained from preliminary in vitro simulation tests. All damage observations were recorded for each test using photogrammetry. The tests conducted in this investigation include Initial Control parameter tests, comparisons of sliding distances and loads, and assessments of the effect of moving the loading point closer to the cartilage labrum junction.

The first test conducted focused on the investigation of Initial Control parameters (A1-3) (Figure 33). Samples revealed no visible damage to the acetabulum. However, a noticeable change in colour of the articulating surface and labrum was observed across all samples. This colour alteration resulted from blood being displaced from the tissue during the simulation and mixing with the surrounding Ringer's solution, which turned red from its original transparent state.

Sliding distance: +/-20°	Axial load: 900N Inclination angle: 35°		
	A1 - No change	A2 - No change	A3 - No change
Pretest	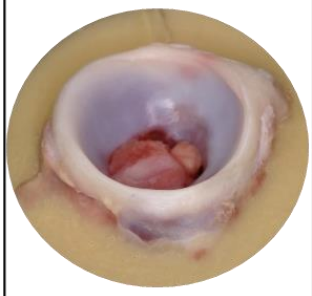		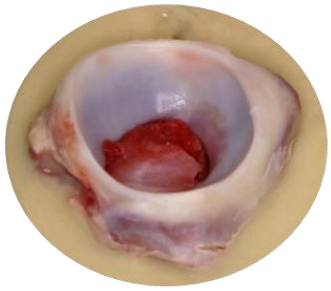
Post-test			

Figure 33: Photogrammetric results of in vitro simulations using Initial Control parameters (n=3).

Two sliding distances were investigated: ±20° and ±10° flexion–extension movements parallel to the cartilage–labral junction. These sliding distances were examined under two loads, 900 N and 1130 N. At 900 N and ±20°, no visible damage was observed (A-3). At ±10°, two samples showed scratching (B1, B2), while one showed blushing (B3) (Figure 34). At 1130 N and ±20°, two samples exhibited scratching (C2), one of which also displayed blushing (C1), while the third sample dislocated (C3) (Figure 35). At ±10°, two samples showed blushing (D2), one showed both scratching and blushing (D1), and one showed no change (D3).

Axial Load	Sliding Distance (°)			
	+/-20		+/-10	
900N	A	A1 – No change A2 - No change A3 – No change	B	B1 - Scratching B2 - Scratching B3 – Blushing
	 A2 Pre-test	 A2 Post-test	 B1 Pre-test	 B1 Post-test

Figure 34: Photogrammetric results from sliding distance comparison at 900N.

Axial Load	Sliding Distance (°)			
	+/-20		+/-10	
1130N	C	C1 - Scratching/Blushing C2 - Scratching C3 – Dislocated	D	D1 - Scratching/Blushing D2 – Blushing D3 – No change
	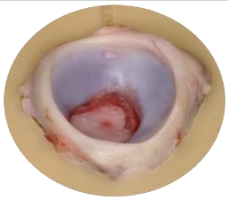 C3 Pre-test	 C3 Post-test	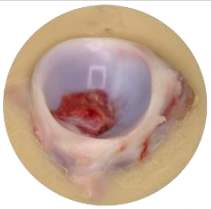 D2 Pre-test	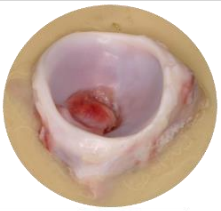 D2 Post-test

Figure 35: Photogrammetric results from sliding distance comparison at 1130N.

The next parameter set, composed of elements from the previous two sets, compared load at the shorter sliding distance, as earlier tests with this sliding distance and a higher load indicated increased damage (Figure 36). At 900 N, two of the three samples exhibited scratching (B1, B2), and one showed blushing (B3). At 1130N, two samples showed blushing (D2), one showed both scratching and blushing (D1), and one showed no change (D3).

Sliding Distance (°)	Axial Load	
	900N	1130N
+/-10	B: B1 - Scratching B2 - Scratching B3 – Blushing	D: D1 - Scratching/Blushing D2 – Blushing D3 – No change
	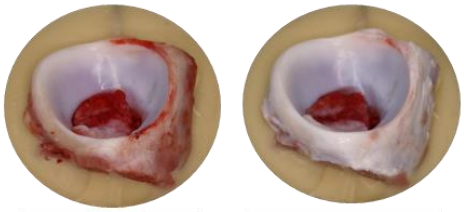 B1 Pre-test B1 Post-test	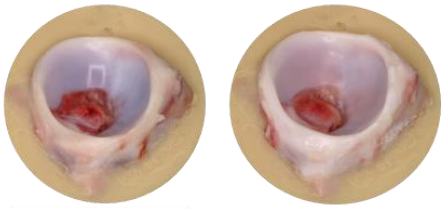 D2 Pre-test D2 Post-test

Figure 36: Photogrammetric results from two different loads (900N and 1130N) at a shorter sliding distance.

The final parameter set investigated the impact of increasing the inclination angle and moving the point of contact closer to the cartilage labral junction (Figure 37). At a 35° inclination, the simulation remained stable, and a full four-hour test was successfully completed. The damage observed at this inclination was characterised by blushing and scratching (D1-3). At the higher inclination, the sample became unstable, and dislocation occurred in all three repetitions.

Load 1130N	Inclination Angle (°)	
	35°	45°
Sliding distance +/- 10°	D: D1 - Scratching/Blushing D2 – Blushing D3 – No change	E: E1 - Dislocated E2 - Dislocated E3 – Dislocated
	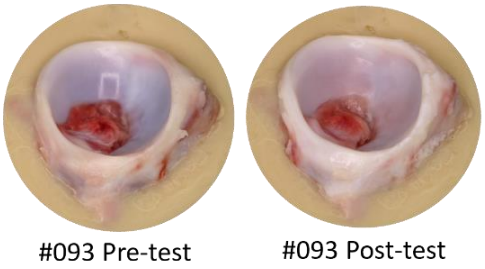 #093 Pre-test #093 Post-test	

Figure 37: Photogrammetric results from changing inclination angle at load of 1130N and sliding distance of ±10°.

3.4.2.3 Part 1: Findings and implications

Preliminary simulations conducted under the Initial Control conditions showed that the combination of load, sliding distance, and inclination angle influenced both the type and progression of damage at the cartilage–labrum junction. The shorter sliding distance of ±10° produced the most consistent changes, with several samples showing early indicators of damage such as scratching and blushing. In contrast, the ±20° distance rarely generated visible effects, suggesting that shorter arcs kept the contact point in the same region for more of the motion and placed greater mechanical demand on that area. Increasing the applied load from 900N to 1130N also increased the prevalence of damage, although signs of instability became more apparent at higher loads, with one sample dislocating at 1130N.

Inclination angle had a distinct influence on both stability and the nature of damage. At 35°, tests remained stable and generated superficial changes such as blushing and scratching. However, increasing inclination to 45° shifted contact towards the rim and consistently caused instability, with all samples dislocating before test completion. This indicated that inclination is a relevant parameter for recreating adverse mechanical conditions, but the simulator configuration used in Part 1 did not provide sufficient stability to support higher angles.

These findings revealed three key issues. First, certain parameter combinations (particularly shorter sliding distance and increased load) were more effective in producing early, clinically relevant damage. Second, although progressive patterns of damage were observed, variability between samples and the tendency for dislocation limited confidence in the repeatability of these results. Third, the consistent instability at higher inclinations highlighted the need for refinement of the setup to maintain control over joint articulation.

Overall, the Initial Control conditions demonstrated proof of concept that simulated impingement can reproduce damage within porcine tissue. However, they also emphasised the need to improve stability and repeatability before more detailed parametric testing could be undertaken. Refining the setup to balance physiological relevance with mechanical control was therefore essential before progressing to the Refined Control conditions in Part 2.

3.4.3 Part 2: Determining Refined Control parameters

Based on the preliminary results obtained under the Initial Control conditions in Part 1, refinements were introduced to improve the stability and repeatability of the in vitro simulations. The high rate of dislocation at greater inclinations and variability in damage outcomes indicated that the initial setup did not consistently reproduce clinically relevant patterns of cartilage damage. To address this, a lateral displacement was incorporated into the design to stabilise articulation and reduce dislocation. At the same time, the parameter sets that had previously produced damage (shorter sliding distance, higher loads, and altered inclination) were retained for reassessment. These adjustments formed the basis of the Refined control conditions in Part 2, which aimed to establish a robust testing configuration capable of reliably reproducing the damage processes associated with cam-type femoroacetabular impingement.

This section encompasses not only the refinement of control parameters but also systematic measurements of contact area and zonal mapping of damage locations. Contact area testing confirmed consistent femoral head–acetabulum engagement and assessed the influence of motion direction and sample geometry (see Section 3.4.3.1 and 1.4.3.3). Zonal damage analysis, using the Ilizaliturri et al. (2008) method, provided a systematic and clinically comparable framework for reporting the distribution of cartilage damage (see Section 1.3.2.1 and Section 1.4.3.4). Together, these approaches established a robust testing configuration capable of producing stable, repeatable, and physiologically relevant patterns of cartilage damage associated with cam-type femoroacetabular impingement.

3.4.3.1 Methods: Refined control parameters

Maintaining stability

A key limitation in Part 1 was maintaining sample stability during simulations. At higher inclination angles, there was a reduction in coverage of the femoral head by the acetabulum, which increased the risk of dislocation. In vivo, the surrounding joint capsule, muscle, and ligamentous structures help maintain joint stability. However, in the simulator, these were removed, which resulted in less control over joint positioning. To help counteract this and better maintain stability, a ~1 mm lateral displacement was applied to the acetabulum (Figure 38).

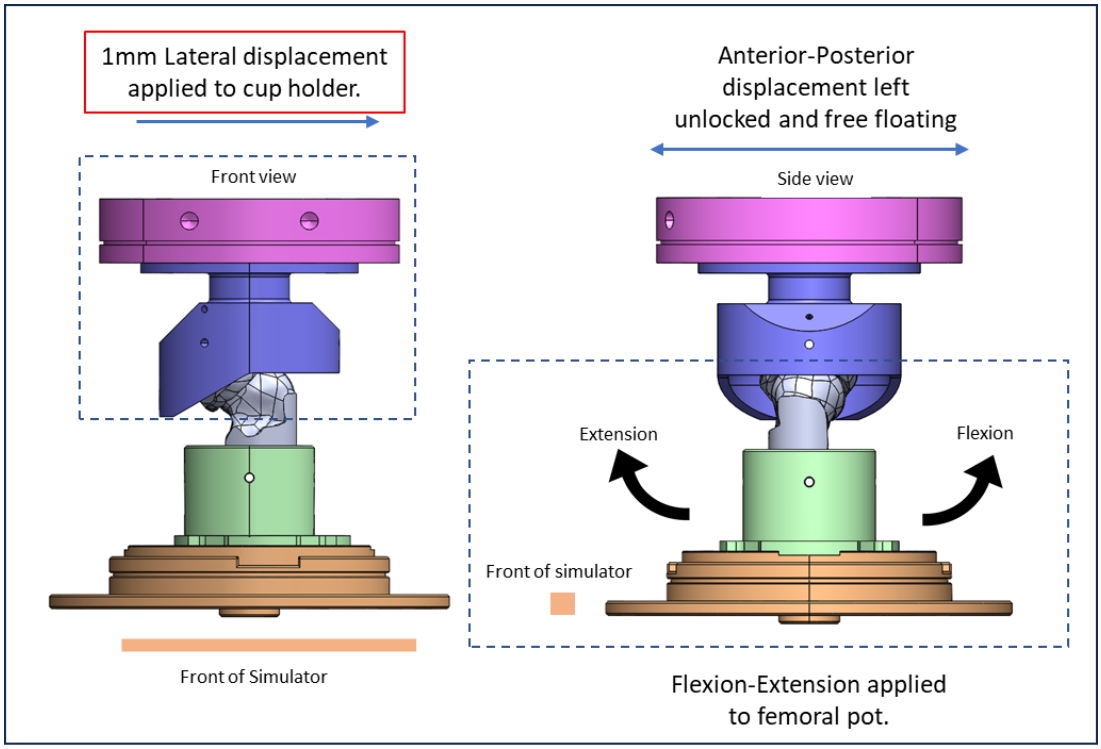

Figure 38: Model of simulator components, lateral displacement was applied to the acetabular pot, constraining the femoral head and preventing dislocation of the sample during testing.

In Part 1, both the ML and AP displacements were unconstrained, allowing the joint to move more freely and follow its natural articulation. While this setup aimed to preserve natural motion, it also led to increased instability and dislocation, particularly in the ML direction, due to variations in sample shape and its mounting method. Short trials were performed to find the most suitable lateral displacement. A displacement of 0.5mm was not sufficient to stabilise the joint, while 2mm caused the femoral head to crack within the cement mantle due to excessive lateral force. A 1mm displacement was found to be optimal; it stabilised the sample without disrupting the motion or causing additional damage. The lateral movement was designed to follow the same cyclic shape as the applied axial load (Figure 39). Rather than interfering with the sliding motion, the added displacement helped reduce unintended movement and wobble, thereby improving test consistency and ensuring that the sliding distance remained predominantly uniaxial and reflective of the input motions.

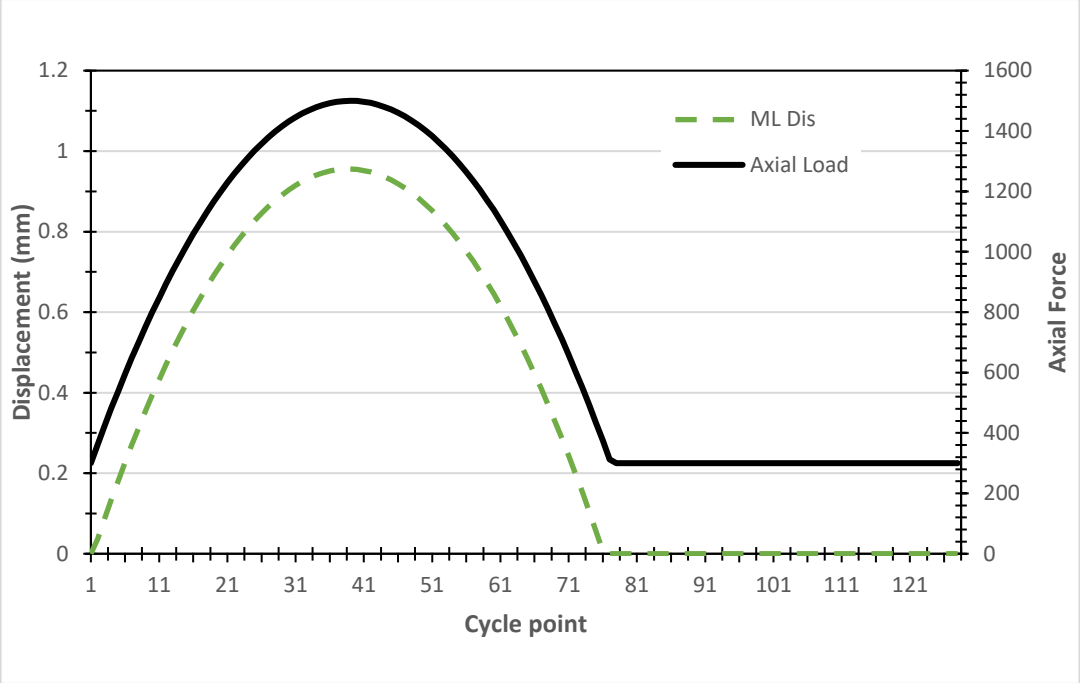

Figure 39: Typical simulator input, green dashed line represents the applied 1mm lateral displacement.

Direction of sliding

Direction in the simulation was described as movement parallel to and perpendicular to the cartilage labral junction. To achieve this, uniaxial motion inputs were adjusted, flexion-extension motions resulted in movements parallel to the junction and abduction-adduction motions were perpendicular to the junction (Figure 40). Directional sensitivity is expected because acetabular cartilage is anisotropic. Movements parallel to fibre orientation generate lower resistance to shear, whereas perpendicular movements generate higher shear stresses (Cashin et al., 2008). Including direction as a parameter, therefore, enabled evaluation of a structurally meaningful mechanical variable.

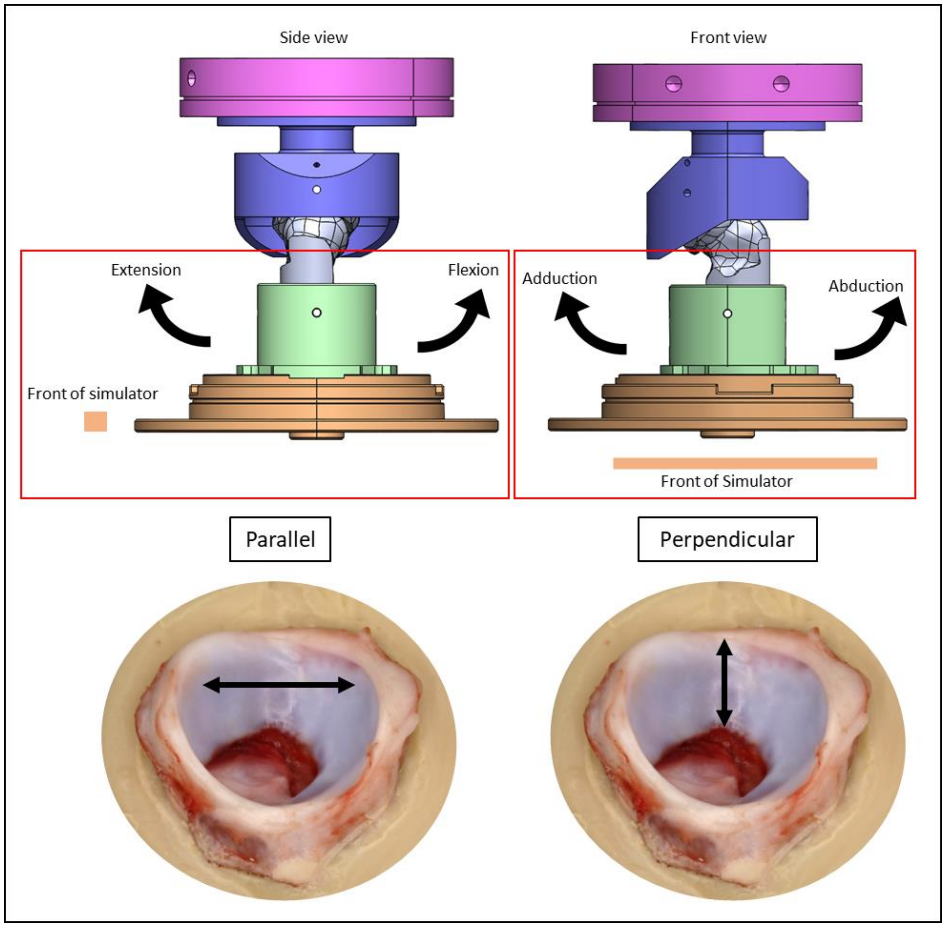

Figure 40: Model of simulator components. Movements parallel to the cartilage labral junction were completed using movements in the flexion-extension direction. Perpendicular movements were performed using abduction-adduction movements.

Contact area measurement

Contact area measurements were conducted to verify that the experimental setup generated consistent patterns of head–acetabulum engagement and to assess how motion parameters and sample geometry affected contact location. Establishing this repeatability was essential to ensure that subsequent parametric simulations could be interpreted in terms of genuine contact behaviour, rather than artefacts of the rig or testing procedure. This data also provided a baseline for interpreting the more complex damage and wear mechanisms.

Three acetabular samples with femoral head sizes of 37, 38.5, and 41.5mm were tested, with contact area measured three times for each sample to assess repeatability and the effect of head size. A second investigation was then carried out using one of these samples, in which the direction of motion was varied to assess directional effects. In this test, the standard

input load profile (see Section 3.4.2.1) was combined with a peak load of 1500N and a uniaxial motion to assess directionality. Movements applied parallel to the joint were performed in flexion–extension, whereas perpendicular movements were applied in abduction–adduction. Each condition was repeated three times to ensure repeatability. Including both repeat tests and variations in head size and direction ensured that any differences in contact area could be attributed to genuine effects of motion or geometry, rather than random variation in the measurements.

Contact area was measured by applying a thin layer of ink to the acetabular articulating surface (Figure 41a). The sample was positioned in the simulator with the corresponding femoral head, and 200 cycles of the input profile were applied under a peak load of 1500 N. Contact was defined as the area where ink was removed from the acetabular surface due to engagement with the femoral head (Figure 41b–c).

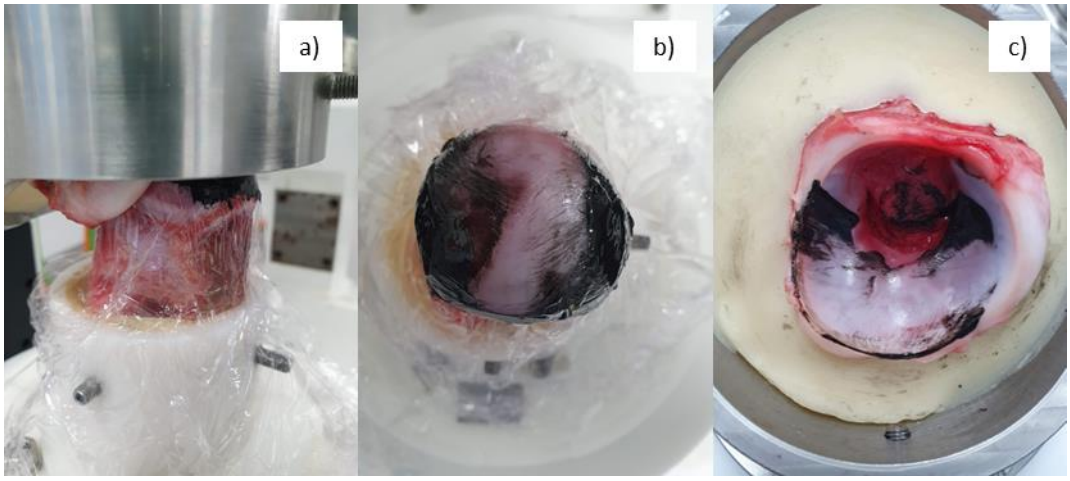

Figure 41: Contact area measurements: (a) Ink was smeared on the femoral head, the two parts were pushed together till concentric, and the simulator input profile was initiated. Ink was transferred from the head (b) to the acetabulum and was removed from areas where contact occurred (c).

3.4.3.2 Results: Refined control conditions

Inclination angle tests from Part 1 (Section 3.4.2.2) were repeated at 1130N with the addition of the 1mm lateral displacement (Figure 42). At a 35° inclination angle, all samples exhibited “bubbling”, which was interpreted as an advanced descriptor of damage progression compared to blushing. In some regions, “bubbling initiated” was observed, meaning small

bubbles were starting to appear but had not yet fully developed, in comparison to the bubbling, which indicated a clearly formed bubble. Blushing was still present, representing an earlier surface change. At the higher inclination angle of 45°, all samples remained stable, with two showing localised blushing (G2 & G3) and one presenting with a more extensive area of blushing (G1), but no bubbling.

Load 1130N	**Inclination Angle (°)**	
	35°	**45°**
Sliding distance +/- 10° + 1mm lateral displacement	F: F1 - Bubbling/Blushing F2 – Blushing/ Bubbling initiated F3 – Blushing/ Bubbling initiated	G: G1 - Blushing G2 - Blushing G3 - Blushing
	 F1 Pre-test  F1 Post-test	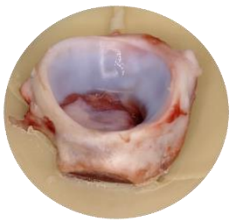 G2 Pre-test 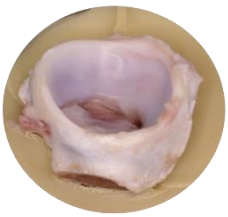 G2 Post-test

Figure 42: Photogrammetric results for inclination angle tests with a 1mm lateral head constraint to improve stability of the simulation. At 35°, both bubbling and blushing were observed, whereas at 45° only blushing occurred.

Findings from Part 1 (Section 3.4.2.2) suggested that a higher load of 1130N combined with a shorter sliding distance of ±10° was associated with the more progressive damage descriptors. This parameter set was repeated with the head constraint in place. Under these conditions, bubbling was observed on the articulating surface (F1-3) (Figure 43), representing a progression from the blushing and scratching recorded previously without the constraint (see Figure 36, parameter set D). When the load was further increased to 1500N, bubbling became more widespread across the surface, although no delamination was observed (H1 - 3).

Sliding distance (°)	Axial Load (N)			
	1130N		1500N	
+/- 10 + 1mm lateral displacement	F	F1 - Bubbling/Blushing F2 – Blushing/ Bubbling initiated F3 – Blushing/ Bubbling initiated	H	H1 - Blushing/ Bubbling H2 - Bubbling H3 Blushing/ Bubbling
	 F1 Pre-test	 F1 Post-test	 H2 Pre-test	 H2 Post-test

Figure 43: Photogrammetric results showing the effects of the new head constraint on increased loading in the acetabulum.

The final test compared damage in parallel and perpendicular directions at the higher load of 1500N and a sliding distance of ±10° (Figure 44). Parallel motion produced a broader spread of blushing across zones 2–4 of the acetabular surface (H1-3). In contrast, perpendicular motion generated a more concentrated area of blushing at the boundary between zones 2 and 3 (I1-3). Bubbling was only present in the parallel direction, indicating that the motion pathway influenced which descriptors were expressed.

Sliding distance (°)	Direction			
	Parallel		Perpendicular	
+/- 10 + 1mm lateral displacement	H	H1 - Blushing/ Bubbling H2 - Bubbling H3 Blushing/ Bubbling	I	I1 – Blushing I2 –Blushing I3 – Blushing
	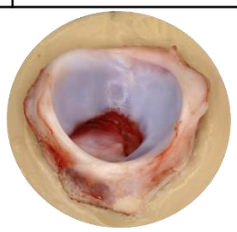 H2 Pre-test	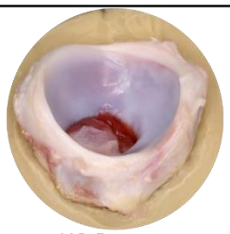 H2 Post-test	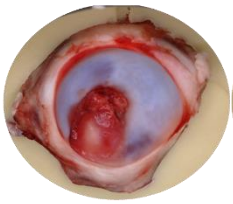 I2 Pre-test	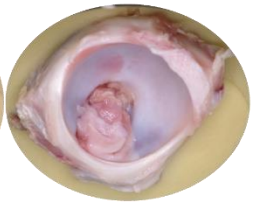 I2 Post-test

Figure 44: Photogrammetric results showing the impact of directional changes on damage in the hip joint.

3.4.3.3 Results: Contact area measurements

The contact area measurements confirmed that the simulator produced consistent and repeatable patterns of head–acetabulum engagement, validating the refined control conditions used in this chapter.

Repeatability was first assessed by performing three repeats for each of the three acetabular samples (#228, #174, and #122) under identical conditions (Figures 10–12). The results demonstrated consistent contact patterns across all repeats, indicating that the experimental method produces reliable measurements.

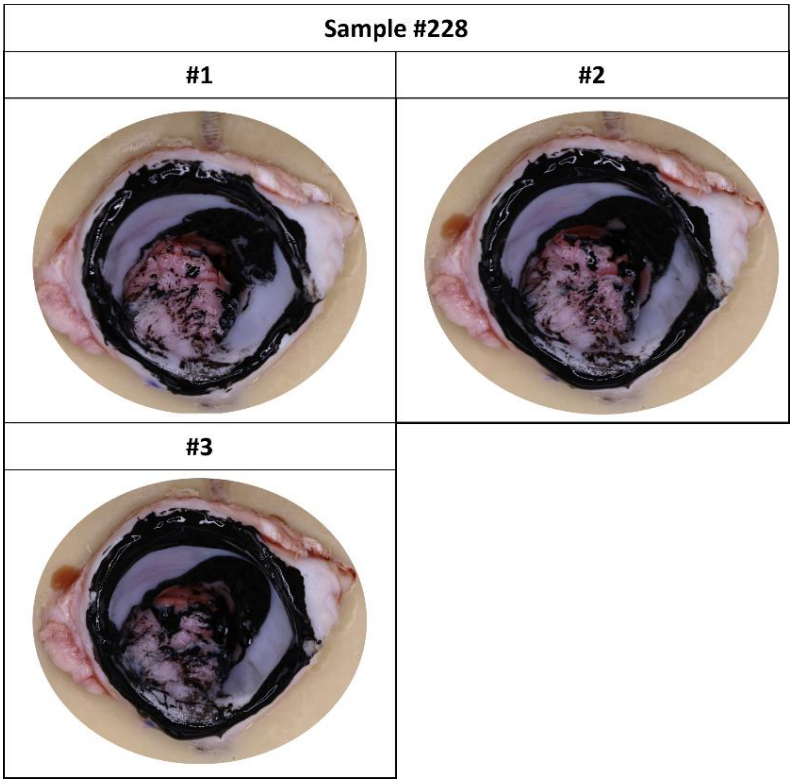

Figure 45: Photogrammetric results of contact space measurements for sample #228, repeated three times to determine repeatability of the contact area.

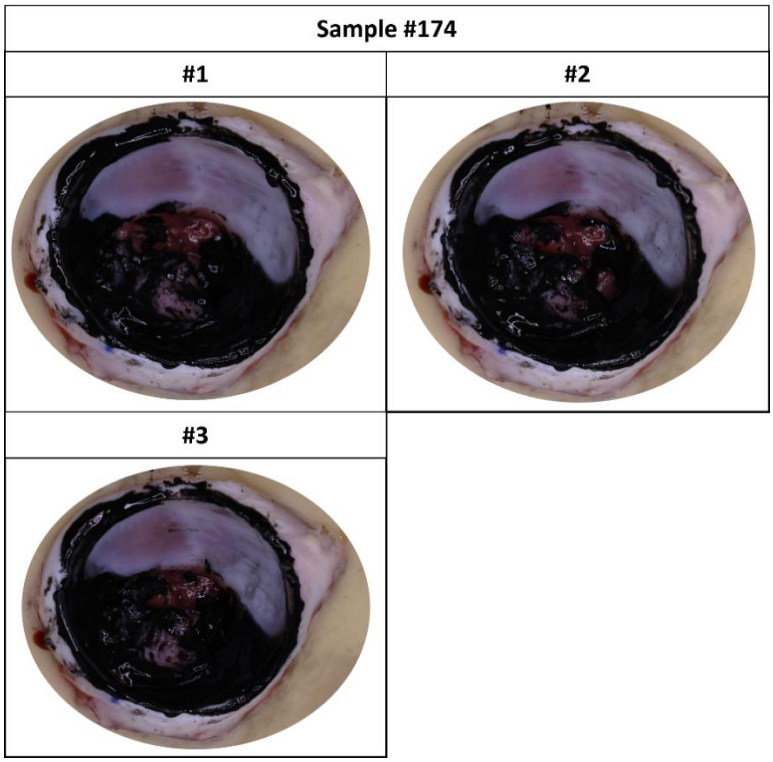

Figure 46: Photogrammetric results of contact space measurements for sample #174, repeated three times to determine repeatability of the contact area.

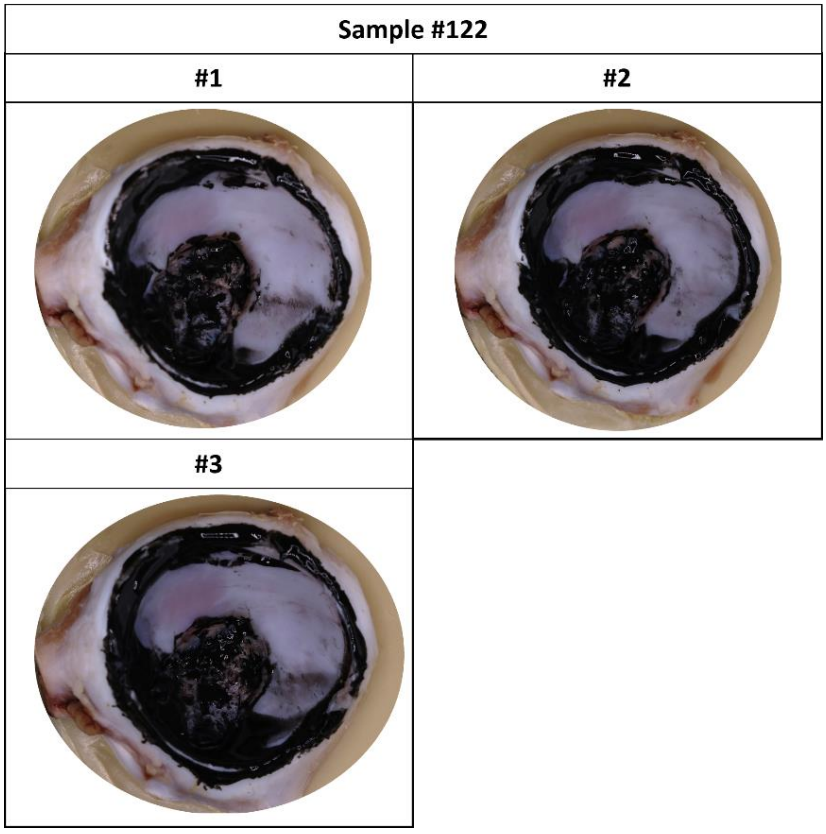

Figure 47: Photogrammetric results of contact space measurements for sample #122, repeated three times to determine repeatability of the contact area.

The effect of motion direction was then examined using a single sample (#174), with three repeats performed for both parallel (flexion–extension) and perpendicular (abduction–adduction) profiles (Figure 13). Contact areas were consistent across both directions, indicating that the orientation of the motion path did not substantially influence the location of engagement. This finding supports the decision to adopt a single-direction input in previous simulator studies.

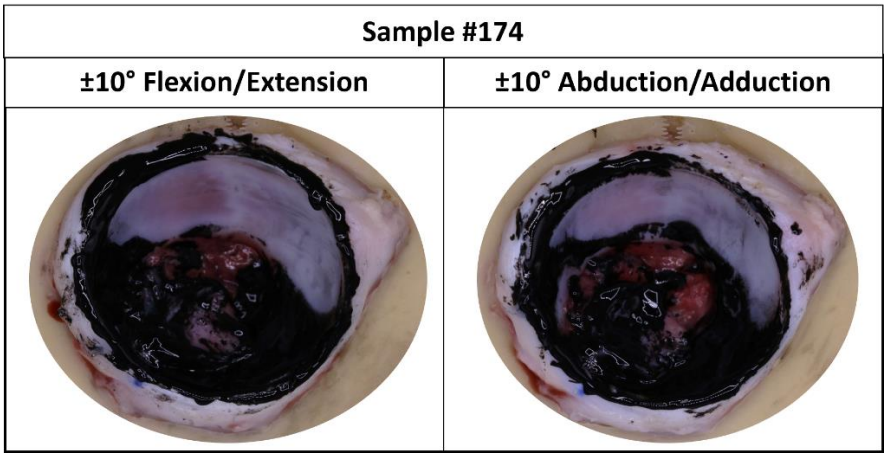

Figure 48: Photogrammetric results of contact area measurements for sample #174 under parallel and perpendicular motion profiles. One of three repeats for each case is illustrated.

3.4.3.4 Results: Incidences of zonal damage location & type

To systematically report the location of damage, the Ilizaliturri et al. (2008) zonal method was applied (Section 3.3.2.1). This approach allowed damage patterns to be summarised in a consistent and clinically comparable manner. For each tested sample, the presence and type of damage was recorded within each zone. Each occurrence of damage was recorded per zone, with individual incidence points assigned for each identified damage type. Where multiple damage types were present within a single zone, each type was counted separately, irrespective of the extent or progression of damage. These incidences were then summed across all samples. Incidents of zonal damage were compared for samples in parts 1 and 2 of the testing.

In Part 1 testing, damage was observed across multiple zones, with a relatively even distribution between Zones 2 (8 incidences), 3 (9 incidences), and 4 (6 incidences), and a single instance in Zone 1. No incidents were recorded in Zones 5 or 6 (Figure 49). When stratified by damage type, damage was limited to scratch/indentation and blushing, which co-occurred across Zones 2–4. Blushing accounted for the greater proportion of damage in these regions, while scratch/indentation was present at lower frequencies and was the only damage type observed in Zone 1.

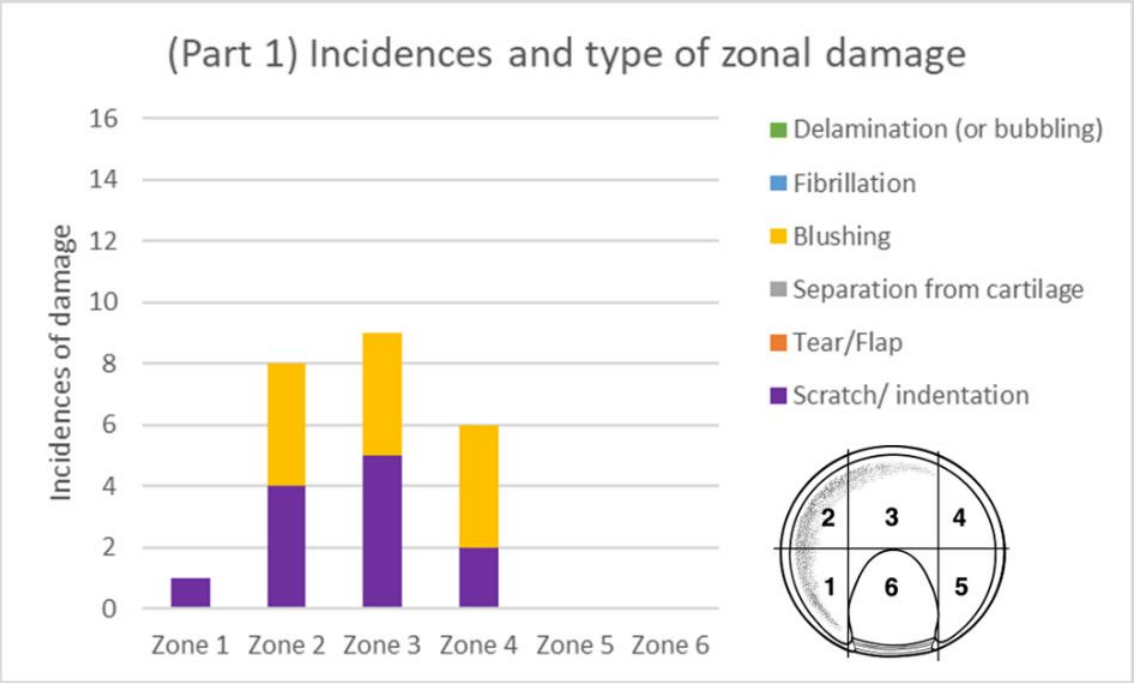

Figure 49: Distribution of acetabular damage in Part 1 testing, reported using the Ilizaliturri et al. (2008) zonal method. Each occurrence of damage was assigned one point per affected zone for each identified damage type. Where multiple damage types co-occurred within a zone, each was counted separately. Incidences per zone: Zone 1 = 1, Zone 2 = 8, Zone 3 = 9, Zone 4 = 6, Zones 5 and 6 = 0.

In Part 2 testing, damage was more localised, with the highest frequency observed in Zone 3 (14 incidences), followed by Zone 2 (9 incidences) and Zone 4 (7 incidences). No damage was recorded in Zones 1, 5, or 6 (Figure 50). When stratified by damage type, damage was composed of blushing and delamination (or bubbling) only. Blushing was observed across Zones 2, 3, and 4, whereas delamination (or bubbling) was restricted to Zones 3 and 4, with the greatest contribution in Zone 3. Zone 2 exhibited blushing alone, with no evidence of more advanced damage types.

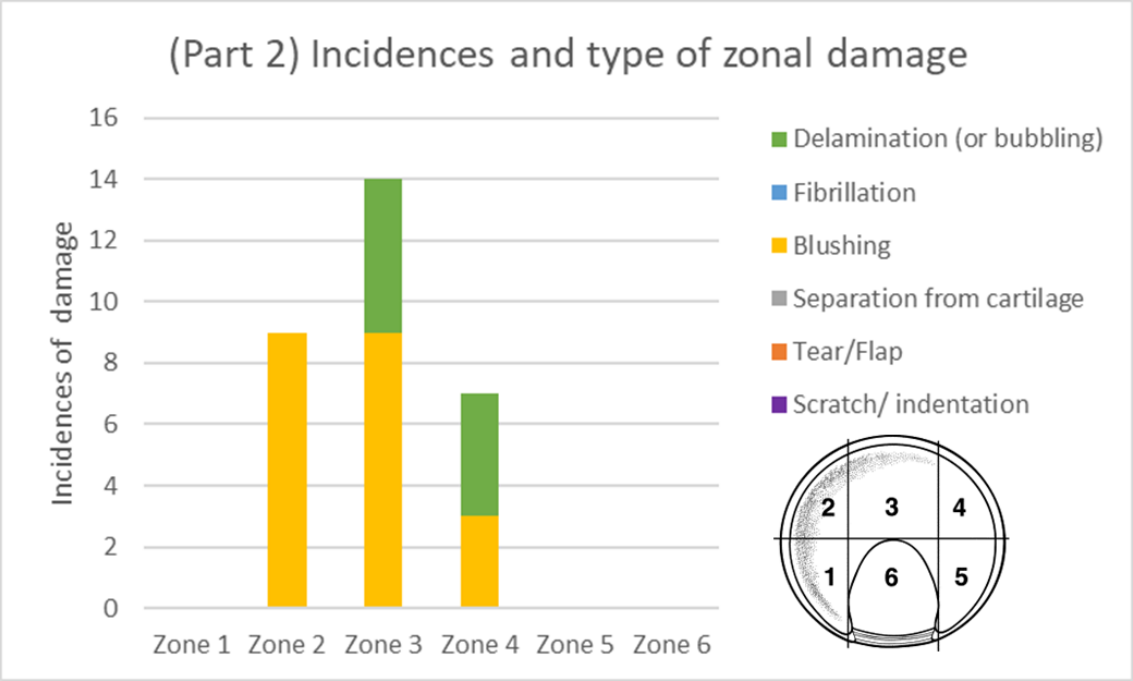

Figure 50: Distribution of acetabular damage in Part 2 testing, reported using the Ilizaliturri et al. (2008) zonal method. Each occurrence of damage was assigned one point per affected zone for each identified damage type. Where multiple damage types co-occurred within a zone, each was counted separately. Incidences per zone: Zone 1 = 0, Zone 2 = 9, Zone 3 = 14, Zone 4 = 7, Zones 5 and 6 = 0.

3.4.3.5 Part 2: Findings and implications

The overall findings, summarised in Table 11, indicate that the combination of joint stabilisation, shorter sliding distance, higher load and parallel motion produced the most progressive cartilage damage. Under these conditions, bubbling was consistently observed, representing a more advanced stage of surface disruption compared with blushing, which remained the earliest visible change. Inclination angle continued to influence the type and extent of damage, with higher angles limiting the appearance of advanced descriptors even after refinements were introduced. Motion direction also played a role. Parallel movements produced a broader spread of lesions, whereas perpendicular movements tended to generate more localised changes. Together, these results show that the Refined Control parameters, specifically parameter set H, provided a robust and reproducible configuration that produced progressive damage patterns in porcine tissue. This offers a reliable framework for subsequent sustained simulation studies.

Table 11: Summary of all parametrised testing and subsequent findings.

	Sliding distance	**Inclination angle (°)**	**Load (N)**		
			900N	1130N	1500N
Parallel motion	+/-20°	35°	A1 – No visible change A2 - No visible change A3 – No visible change	C1 – Scratching/Blushing C2 - Scratching C3 – Sample dislocated	
	+/- 10°	35°	B1 - Scratching B2 - Scratching B3 – Blushing	D1 - Scratching/Blushing D2 – Blushing D3 – No visible change	
		45°		E1 – Sample dislocated E2 – Sample dislocated E3 – Sample dislocated	
	+/-10° +1mm ML Dis	35°		F1 – Blushing/ Bubbling F2 -Blushing/ Bubbling initiated F3 – Blushing/ Bubbling initiated	H1 - Blushing/ Bubbling H2 - Bubbling H3 - Blushing/ Bubbling
		45°		G1 - Blushing G2 - Blushing G3 - Blushing	
Perpendicular motion	+/-10° +1mm ML Dis	35°			I1 - Blushing I2 - Blushing I3 - Blushing

The contact area measurements confirmed that the refined experimental method generated reliable and repeatable engagement patterns between the femoral head and acetabulum. Across three repeated tests, contact location remained consistent, indicating that the approach was robust to anatomical variation between specimens. Directional testing showed that the orientation of motion did not meaningfully alter contact area, supporting the use of a single direction input for later simulator studies. These findings validate the

refined control conditions and provide confidence that subsequent parametric outcomes reflect genuine effects of motion or joint geometry rather than experimental variability.

Zonal analysis further demonstrated the effect of stability measures on the distribution of acetabular damage. In Part 1, damage was spread relatively evenly across Zones 2 to 4, with an isolated incidence in Zone 1 that is not commonly reported in vivo. After stability improvements were introduced, damage became more concentrated in Zones 2 and 3, with Zone 3 showing the highest frequency. In addition to altering the spatial distribution of damage, the refinements also influenced the type of damage observed. Part 1 was characterised by lower-severity damage, primarily scratch/indentation and blushing, whereas Part 2 demonstrated the emergence of more advanced damage mechanisms, specifically bubbling (delamination). Notably, this progression in damage type was spatially linked, with advanced damage predominantly occurring in Zone 3. This combined shift in both location and type of damage indicates that the refined protocol not only improved joint stability but also enabled more physiologically relevant loading conditions, promoting both the initiation and progression of damage within clinically relevant anterosuperior region. Furthermore, the absence of damage in Zone 6, adjacent to the ligamentum teres, supports the interpretation that the observed lesions were impingement related rather than random or widespread. Using a zonal framework also enables direct comparison with clinical observations, strengthening the translational relevance of this study.

3.5 Discussion

The overall aim of this study was to develop an in vitro simulation method that could parametrically assess damage at the cartilage labral junction. This was achieved by refining sample preparation procedures, establishing a method for classifying visible damage, and systematically testing parameters identified from the literature to determine which were most likely to produce tissue changes. These steps resulted in a set of Refined Control conditions that consistently generated damage within the porcine hip joint.

Minimal damage was observed in the preliminary tests, which made distinguishing and categorising early changes challenging. Nonetheless, damage tended to increase with higher loads. After refinements were introduced, there was some sensitivity to sliding distance at

low loads, continued difficulty achieving stable tests at higher inclinations without additional support, and an apparent insensitivity to inclination and direction at high loads. A common finding across samples was a visible colour change, caused by blood being pressed from the joint surfaces, which has been reported previously in natural tissue simulations (Pallan, 2016).

Joint simulators are often used in simulating highly conforming artificial implants. These tests are well documented and informed by ISO testing standards. Natural tissue simulation, on the other hand, is not informed by standards and has been subject to less research. Successful simulations require the joint centres to be aligned with the centre of rotation of the hip simulator. For this to be successful, the sample needs to be disarticulated, realigned and then cemented into position. This alters the natural position of the joint but is required to inspect the articulating surfaces for pre-existing damage. The non-uniform geometry of natural tissue also increases the likelihood of dislocation. In this study, a lateral displacement was introduced to reduce the risk of dislocation, acting as a constraint to keep the femoral head in place. The addition of this constraint may have impacted the sample's ability to follow the natural curvature of the femoral head. However, it should be noted that the joint in vivo is usually surrounded by a joint capsule, tissue, muscles, and ligaments, all of which aid in ensuring the joint is constrained to a position, stabilising the joint.

The contact area study established the methodological reliability of the approach. Repeat tests showed consistent engagement patterns between the head and acetabulum, confirming that the contact markings were not artefacts of the rig or ink transfer process. Minor differences caused by head size were expected, but repeatability within samples demonstrated that the method was sufficiently stable for comparative parametric testing. Moreover, the comparison of parallel and perpendicular movements showed that motion direction had little influence on contact area. This was reassuring because the primary simulator studies used a single direction input. These findings confirm that the refined experimental design was robust, although anatomical variation remains a natural source of variability in studies using biological tissue.

Damage localisation provides the clearest indication that the refinements introduced in this study improved the physiological relevance of the simulations. While the preliminary configuration (Part 1) produced a wider and less consistent spread of lesions, the refined

method (Part 2), incorporating joint stabilisation and controlled displacement, directed damage to the anterior superior region, which is the site most commonly affected in cam type impingement. Importantly, this refinement not only altered where damage occurred, but also the type of damage that developed. Part 1 was limited to early-stage surface changes, whereas Part 2 produced more advanced damage mechanisms, including bubbling, which were localised to the same regions of peak contact. This suggests that the improved stability allowed sustained and repeatable loading in specific regions of the joint, facilitating the progression from initial surface response to more advanced structural disruption.

A qualitative visual classification method was chosen in this study to categorise the type of damage observed on porcine joint surfaces following in vitro simulation. The aim was not to quantify damage severity but to consistently identify the specific type of damage generated, such as scratching, blushing or delamination. This method was developed in response to a lack of classification systems tailored to in vitro hip simulations, particularly those involving porcine tissue. While more quantitative techniques, such as surface profilometry, digital image correlation, or pixel-based image processing, could have been used, they are often impractical for irregular, curved surfaces like the acetabulum and femoral head. Subtle forms of damage, such as blushing or early delamination (bubbling), can be diffuse or faint and may not be reliably detected using images alone. A reproducibility study was conducted to assess the consistency of this classification approach. It showed strong intra-observer agreement and moderate inter-observer agreement, suggesting that the method was robust when used by trained individuals. The benefit of this approach lies in its simplicity, reproducibility, and relevance to the study's aims; however, a key limitation is its reliance on observer interpretation. With further standardisation and the addition of reference image sets, this method could be adapted for broader use in future in vitro damage assessments.

One motivation for this study was the clinical observation that cam impingement often produces early damage at the cartilage labral junction. Although this method successfully reproduced progressive damage within the acetabulum, most changes appeared within the articulating cartilage rather than the junction itself. One likely explanation is that in porcine tissue the transition between cartilage and labrum is less defined than in mature human joints. Groves (2015) reported an indistinct transition zone in porcine hips, which is consistent with the juvenile tissue used in this study. Despite this limitation, porcine tissue

remained suitable for investigating mechanical pathways of damage because its joint shape is similar to the human hip and allows appropriate positioning and loading in the simulator.

It was anticipated that shorter sliding distances might increase damage due to reduced fluid entrainment and less time for fluid reabsorption between cycles. However, sliding distance showed little effect at the lower loads tested. The ±10° and ±20° distances produced similar outcomes at both 900N and 1130N, suggesting that the joint was relatively insensitive to this parameter unless load was sufficiently high. This finding highlights the dominant influence of load in initiating early surface changes.

Load emerged as the primary driver of damage. The Initial Control load of 900 N produced little visible change, consistent with previous findings at similar load levels (Pallan, 2016; Jimenez-Cruz et al., 2022). When load was increased, the appearance of blushing and, eventually, bubbling became more consistent. The Refined Control conditions included a load of 1500N, at which point bubbling was observed across multiple samples. Bubbling was considered a precursor to delamination because it represents early surface separation. Interestingly, bubbling was more clearly observed in this study than in other in vitro work. Jimenez-Cruz et al. (2022) reported blushing and labral tearing at a peak load of 1350N, while Pallan (2016) reported only blushing at 1500N, with delamination occurring only at very high inclination or at 3000N. One reason for the clearer bubbling in the present study may be the unidirectional motion path, which concentrated load in a more focused region of contact.

Damage severity also varied with motion direction. Perpendicular movements resulted in more concentrated blushing, whereas parallel movements produced blushing and bubbling across a wider area. This may relate to the orientation of collagen fibres at the cartilage labral junction. Cashin et al. (2008) reported that fibres in the anterior acetabulum are aligned parallel to the junction and attached to the labrum by a marginal intra articular projection. This alignment, combined with a less secure fibre attachment compared with the posterior region, may make the tissue more susceptible to failure when shear is applied along the direction of the fibres.

Finally, while bubbling was observed as a possible precursor to delamination, true delamination as reported in vivo (Beck et al., 2005; Jannelli et al., 2019) was not reproduced

under the simplified inputs tested here. This suggests that delamination may require more complex loading and motion patterns than those explored in this study.

Overall, this study established a method capable of reliably generating early cartilage damage under controlled and physiologically relevant loading conditions. The refinements introduced across the work improved joint stability, focused damage to regions consistent with cam type impingement and enabled meaningful comparison of mechanical parameters. Although the method did not reproduce full delamination, the appearance of progressive surface changes demonstrated that the model captures the early stages of impingement related tissue failure. These developments provide a practical and reproducible foundation for future simulation studies that seek to examine more complex loading paths, extended cycles or subject specific geometries.

Chapter 4

4 Sliding distance, dominant motion, and load during cam impingement.

4.1 Introduction

Cam femoroacetabular impingement (FAI) is defined by an abnormal overgrowth at the head-neck junction, preventing smooth rotation within the acetabulum (Philippon et al., 2007; Byrd, 2014). Cam FAI is known to cause damage in the joint, but the specific mechanisms of damage and the influence of individual mechanical factors remain poorly understood. The irregular geometry of the cam makes it difficult to reproduce consistently in a laboratory setting.

Computational modelling provides a way to overcome this challenge. It allows cam geometry to be represented directly and enables parameters linked to impingement to be studied under controlled conditions. This approach has become increasingly important in the field, as it can replicate complex motions that are otherwise difficult to reproduce in vitro and provides outputs that can be used to define experimental test conditions. In this way, modelling and in vitro testing complement each other: models identify the range and extremes of mechanical conditions, while experiments can then test the material responses and damage mechanism under those conditions.

This chapter aimed to quantify parameter ranges associated with cam impingement during activities of daily living and to identify which activities generate the most extreme conditions.

These findings were intended to provide the basis for future in vitro testing, ensuring that laboratory simulations capture physiologically relevant boundary conditions.

The objectives of this chapter were to:

- Use an established cam-type hip model to derive parameter ranges for sliding distance, load during impingement and dominant hip rotation across a set of activities of daily living.
- Identify activities that generate the highest or lowest values of these parameters as candidates for further investigation.
- Provide parameter ranges that can inform the design and boundary conditions of future in vitro tests, ensuring that experimental studies reproduce physiologically relevant conditions.

Using a cam hip shape model (Jones et al., 2023) and relative hip joint angle and force data for specific activities (Layton et al., 2022b), custom algorithms were developed to examine the three parameters of interest. Sliding distance was defined as the distance the cam travelled along the acetabular rim during impingement, which relates to the extent of cartilage contact and the time available for fluid reabsorption. Load during impingement was examined as a measure of potential increases in contact pressure within the joint, which may contribute to cartilage damage. Dominant hip rotation was considered in the context of fibre orientation at the cartilage labral junction, as certain directions of movement may compromise the mechanical stability of the joint.

The following sections outline the methods used, present the results, and discuss their implications for both the understanding of cam impingement and the design of future in vitro testing.

4.2 Overview

This section provides an overview of the approach used to quantify parameter ranges associated with cam-type impingement during activities of daily living and to determine which activities generated the most extreme conditions. To achieve this, existing datasets

and models were used as the starting point for this study. The motion and force data (Figure 51a–b) were taken from a previous gait laboratory study by Layton et al. (2022b) (Section 4.3.1), and a generic population based impingement model developed by Jones et al. (2023) (Section 4.3.2) was used to define the hip shape (Figure 51c). This model defined impingement based on a 3D set of points around the cam morphology and acetabular rim. From the set of available shapes, an anterior large cam was selected for further use in this study (Figure 51d). The current study made use of these existing resources and developed a new set of algorithms to derive the specific parameters needed.

One generic hip shape (Section 4.3.3) and a subset of motion and force data was selected based on their potential to result in impingement (Section 4.3.4). The goal was to capture the worst-case combinations across different activities. The impingement detection algorithm was applied to each motion case to identify those resulting in impingement (Figure 51e–f), which were then taken forward. The design and structure of this selection process, including the criteria for shape and data choice, were developed specifically for this work. More detail of the background data, existing model and selection processes is given in Section 4.3.

Building on this foundation, a set of new algorithms were developed to explore various impingement parameters. These included the identification of impingement ‘events’ and the calculation of sliding distances for each event (Figure 51g). In this study, an ‘event’ was defined as a continuous period during which a point on the cam surface passed beyond the edge of the acetabular rim. An ‘event’ began at the first time point when the point moved inside the rim and ended when it returned outside. This definition of ‘event’ is used in this context throughout the chapter. Events were filtered based on the longest sliding distances (Figure 51h) (Section 0), and these were used to define the average impingement window for each activity (Figure 51i). From the longest sliding distance, further outputs were calculated, including peak force (Figure 51j), joint angle amplitudes (Figure 51k), average sliding distance (Figure 51l), and impingement depth (Figure 51m). All algorithms in the blue boxes of Figure 51 were created specifically for this project and implemented in MATLAB.

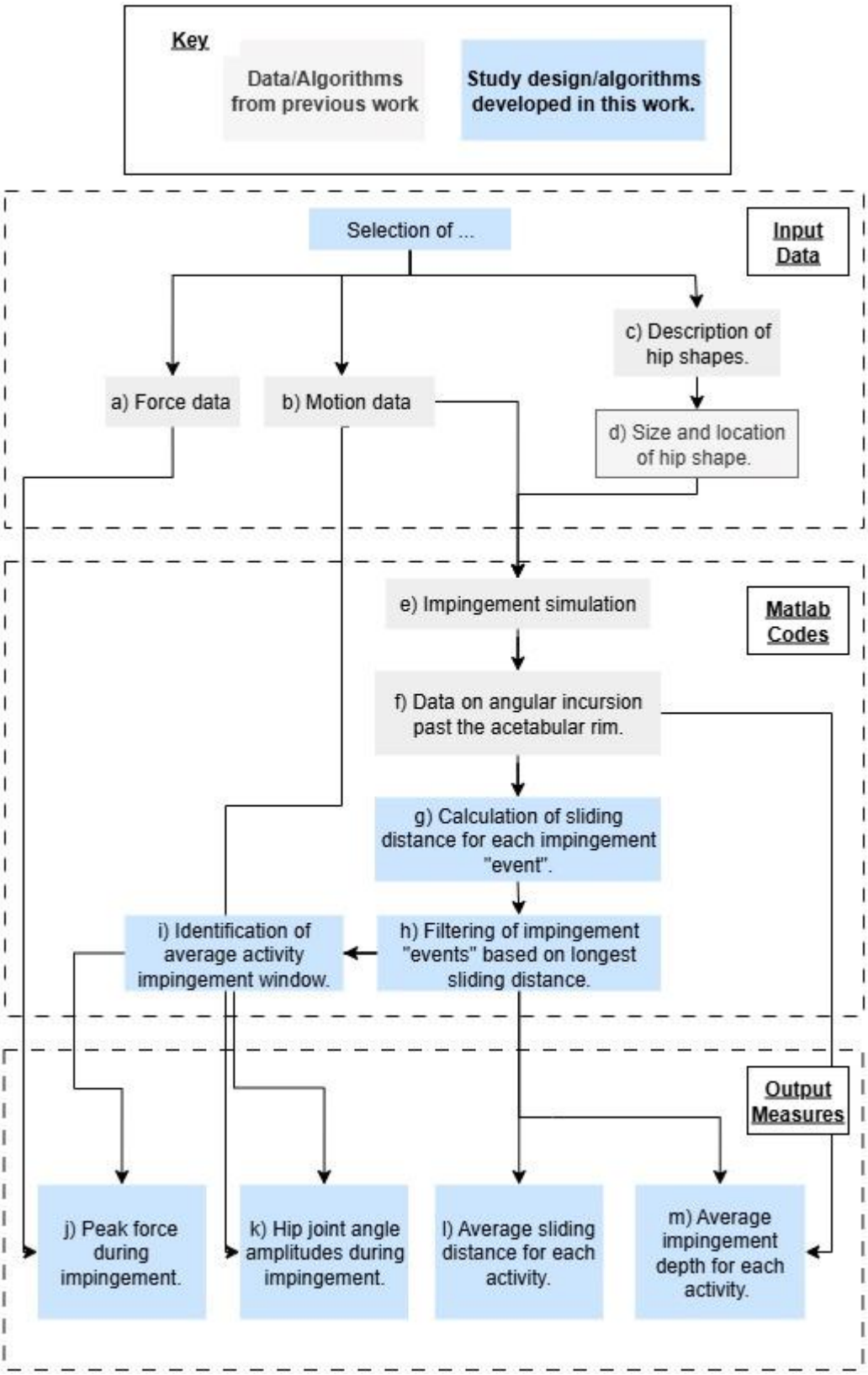

Figure 51: Flow chart showing the development of a computational model for the quantification of parameters associated with cam impingement.

4.3 Background methodology and case selection

This section provides details of the existing force and motion data (Section 4.3.1) and a brief summary of the existing computational impingement model (Section 4.3.2). The rationale for the selection of the hip shape used in the current work, from a set generated in a previous publication, is given in Section 4.3.3. Finally, the rationale for the selection of a subset of the hip joint motion and force cases for this work is given in Section 4.3.4.

All the computational work for this project was performed in MATLAB R2019 (The MathWorks, Inc., US). Using this software, a set of computational functions were created to assess motion and force data, generate graphs and calculate statistics.

4.3.1 Motion and force database

Motion and force inputs were sourced from Layton et al. (2022b). Data collection used a thirteen-camera Qualisys Oqus 3D motion capture system (Qualisys TM Medical AB, Gothenburg, Sweden) and two AMTI force platforms (Advanced Medical Technology Inc., Watertown, MA, USA). The dataset comprised 18 healthy subjects (10 male, 8 female) aged 20–70 years. All participants were free from conditions that affected their movement and were recruited from the general population.

Each participant performed thirteen activities, with five trials conducted for each activity. Due to marker occlusion, some trials were incomplete; a subset of data was analysed across participants and activities. Relative hip joint angles were calculated using Visual3D software (C-Motion Inc., Germantown, MD, USA) and joint reaction forces using AnyBody (version 6.0, AnyBody Technology, Aalborg, Denmark).

The selected dataset provides both hip angle and joint force data for a range of daily activities, many of which involve high flexion, adduction, and internal rotation, making them particularly relevant to cam-type femoroacetabular impingement. While derived from healthy participants, the data offer a consistent baseline for evaluating mechanical interactions between hip geometry and motion.

4.3.2 Hip joint shape and impingement model

Hip joint angles from the motion capture study were applied to a hip model that was created in MATLAB (Jones et al., 2023) and that work is summarised here. The computational impingement model represents the femoral head–neck junction and acetabular rim as rigid bodies with fixed centres of rotation. The purpose of the work was to assess impingement during a range of daily activities for two cam locations (anterior and superior) and four different joint alignment cases. Hip shapes and alignments in the study were not patient-specific, but rather defined based on a set of bony alignment measures taken from data available in the literature. Impingement was said to have occurred when a cam point moved past the acetabular rim points. The smallest angle between each cam point and the acetabular rim was calculated during each motion, so that the depth of impingement could be recorded.

The model is bone geometry-only, with no cartilage, labrum, or soft tissue effects included, and assumes fixed centres of rotation. As a result, it may overpredict the number or depth of incursions of the cam into the acetabulum, especially in scenarios where femoral head translation or resistance from surrounding structures would otherwise limit contact. The model also only considers the leading edge of the cam, not its full shape, which doesn't take into account how the broader protrusion influences impingement severity. Despite these limitations, this approach enables rapid screening of a large number of motions. Unlike finite element models, which can take over five days to run for 126 cases, this approach produces robust impingement results in under five minutes (Jones, A.C. et al., 2023). This makes it highly suitable for studies requiring multiple activity-based simulations. This model was deemed suitable given the scope and objectives of this study.

4.3.3 Hip geometry: Shape selection and definitions

4.3.3.1 Shape selection

The cam-type hip model developed by Jones et al. (2023) consisted of two cam locations (anterior and superior). From the set of cam morphologies developed in that study, an anterior cam with an alpha angle of 80° was selected. This choice was made to target the

most severe impingement scenarios, as the anterior cam produced impingement in all twelve daily activities assessed, whereas a superior cam caused impingement in only five (Figure 52) (Jones et al., 2021).

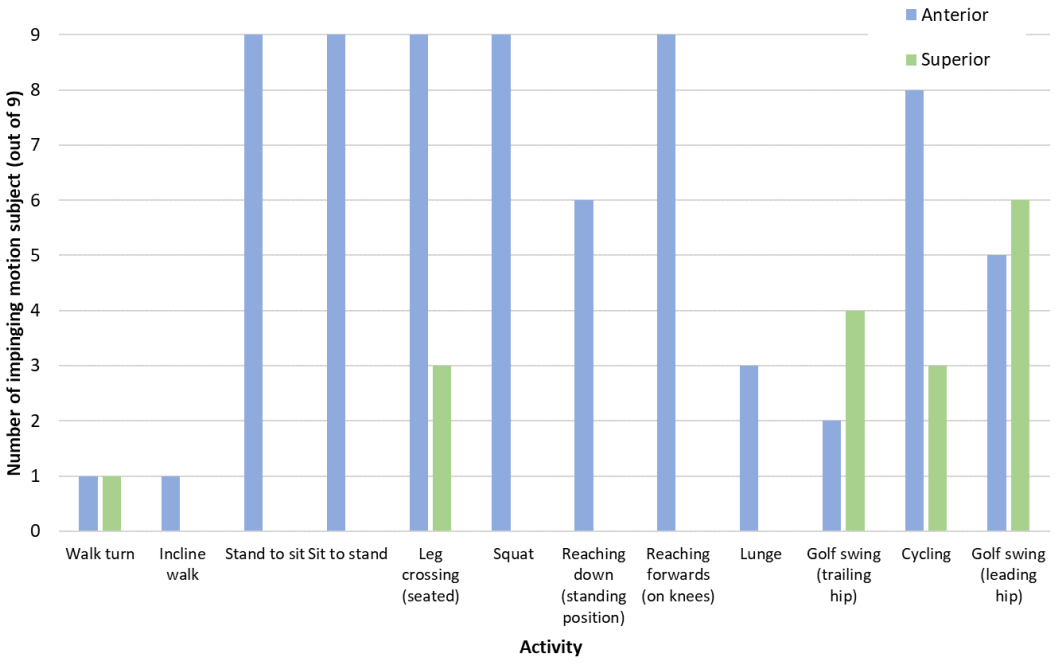

Figure 52: Findings from the Hip Impingement model by Jones et al. (2021). Two hip shape models were assessed: large superior (green) and small anterior (blue). Hip shapes were taken from literature, and each hip was aligned in a neutral position, defined by a set of bony alignment measures. Impingement incidences were higher in the anterior cam shape and were more likely to occur in non-walking type activities (replicated with permission).

4.3.3.2 Cam and actabular rim definition

The selected anterior cam was not created as part of the current work but was imported from the Jones et al. (2023) model. In MATLAB, the leading edge of the cam is represented by a discrete set of twenty-four points positioned along the femoral head–neck junction (Figure 53a – b). Each point was positioned in 3D space relative to the angle between a line along the femoral neck and a line from the femoral head centre to the cam edge (also known as the alpha angle). Population-level measurements were used to scale the femoral head and neck geometry (Nakahara et al., 2011) and the cam to achieve a target alpha angle of 80° (Sutter et al., 2012; Savage et al., 2021). The remaining cam circumference was proportionally scaled to match the maximum alpha angle along the entire circumference

(Sutter et al., 2012; Mascarenhas et al., 2018; Jones, A.C. et al., 2023). The points define the 3D geometry of the cam, which the code uses to detect impingement by comparing their positions relative to the acetabular rim.

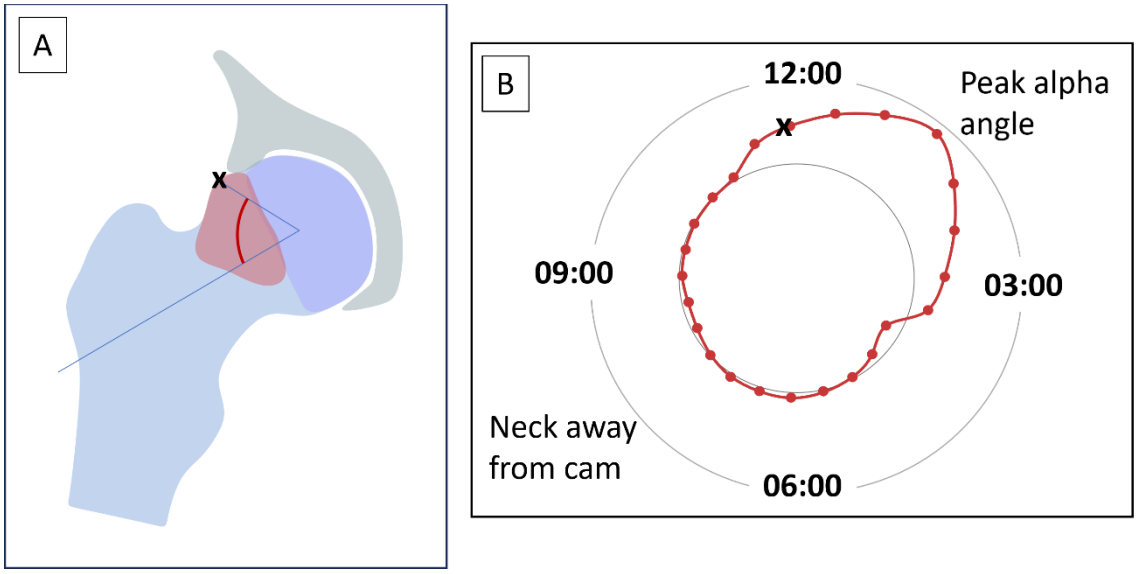

Figure 53: Illustration of the anterior cam edge points used in the computational model. a) The alpha angle for each cam edge point is defined as the angle between a line along the femoral neck and a line from the femoral head centre to the cam edge (red curve), equivalent to the clinical alpha angle. b) Clockface representation showing the 24 discrete cam-neck edge points used to define the cam geometry in the model. These points provide the basis for the 3D impingement detection in this study. (Adpated from (Jones et al., 2023).)

The acetabular rim was defined by twenty-one points distributed around the bony edge of the acetabulum, following the approach described by Jones et al. (2023) (Figure 54a-b). Outward-facing normal vectors of the acetabular plane were used to define the reference orientation for alignment with the femoral head-neck. Each point is referenced to a “clock face” orientation (12:00 superior, 3:00 anterior, 6:00 inferior, 9:00 posterior) and aligned with anatomical landmarks, including the anterosuperior prominence, psoas valley, notch, posterosuperior wall, and posteroinferior prominence. The rim points were positioned using published mean acetabular coverage angles from “normal” hips (Köhnlein et al., 2009; Steppacher et al., 2014; Kuroda et al., 2020).

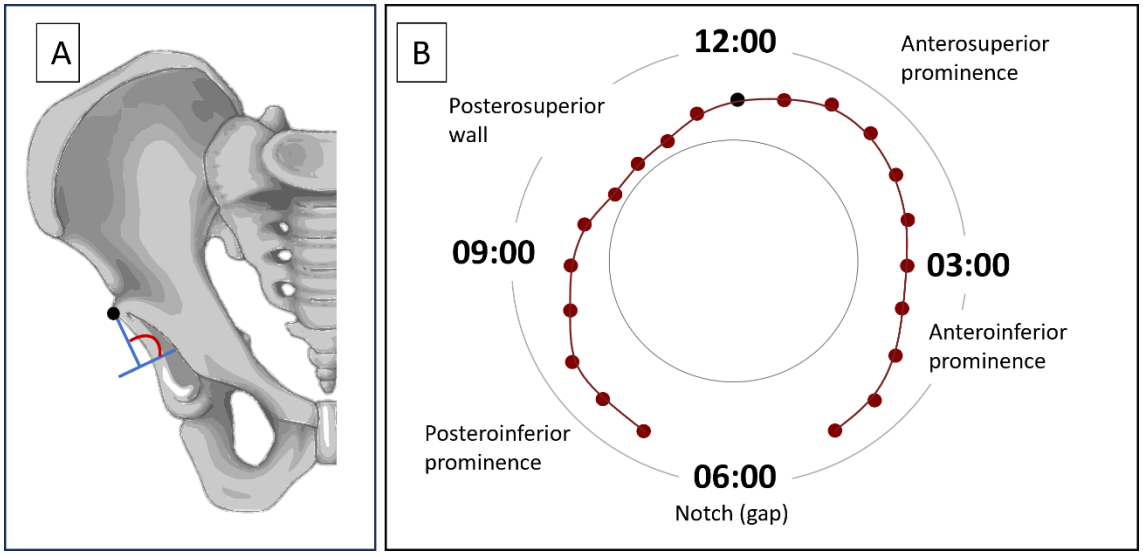

Figure 54: Representation of the acetabular rim points used in the computational model. (A) Example of the angle defining a rim point, measured between the outward-facing normal of the acetabular plane and a line from the socket centre to the rim point. (B) Clockface layout showing all 21 discrete rim points distributed around the acetabular edge, forming the geometric basis for 3D impingement detection. (Adapted from (Jones et al., 2023).)

This definition of the femoral cam and acetabular rim provided the geometric foundation for the impingement detection algorithms described in Sections 4.4, 4.5, 4.6. By explicitly defining the points in 3D space and their relative orientations, the model enabled identification of impingement events and calculation of parameters such as sliding distance, dominant direction, and peak load.

Figure 55 illustrates the MATLAB-based cam impingement model described above. This example shows a single time point during a squat activity for the anterior cam used in this study. The model visualises the femoral head and cam edge as a sphere because both femoral and acetabular points are referenced to a shared joint centre, with motion applied as rotations about this centre. The acetabular rim points (light blue) and cam edge points (black) are explicitly defined in 3D space, and red points indicate cam locations that have penetrated the acetabular rim, representing an impingement event. This visualisation demonstrates how the model tracks the relative positions of cam and rim points throughout motion cycles to detect impingement.

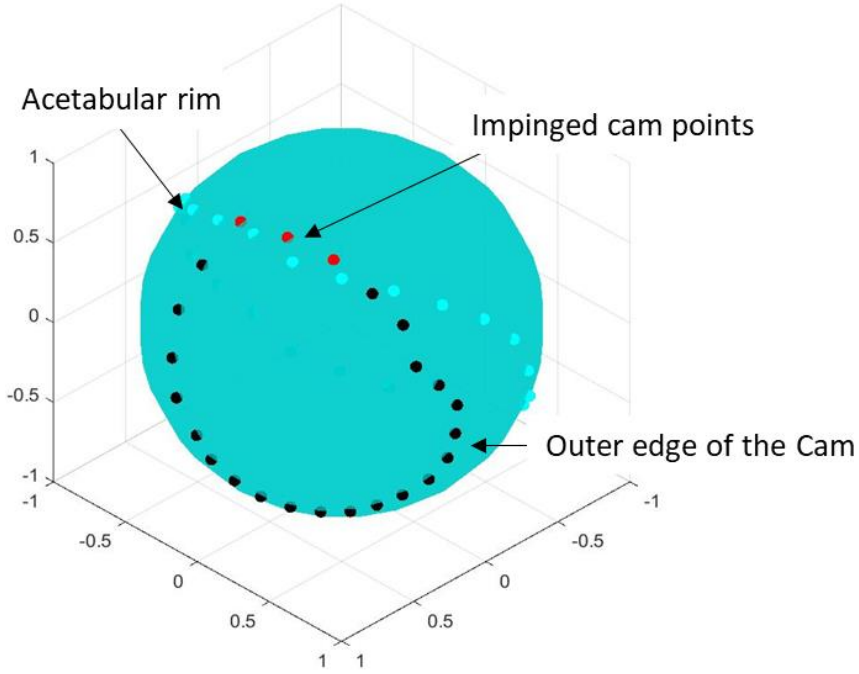

Figure 55: Example of the MATLAB cam impingement model during a squat activity. Black points represent the femoral cam edge, light blue points represent the acetabular rim, and red points indicate cam points that have penetrated the acetabular rim, signifying impingement. Both femoral and acetabular points are referenced to a common joint centre, giving the appearance of a spherical femoral head. This visualisation exemplifies how impingement is detected by comparing 3D positions of the cam and rim throughout motion.

4.3.4 Hip motion data selection

This section outlines the input motion and load data required for impingement analysis, explains why the dataset from Layton et al. (2022b) was appropriate for this purpose, and describes how the specific trials used in this study were selected.

To quantify impingement parameters, input data describing both hip joint angles and joint contact forces during a range of daily activities was required. The selected dataset needed to capture activities involving large hip motions, particularly high flexion, adduction, and internal rotation, since these movements are clinically associated with symptomatic impingement. It was also necessary that the dataset provided population-level data from healthy participants to represent normal pain-free motion patterns, offering a baseline against which early tissue damage could later be assessed.

The dataset reported by Layton et al. (2022b) met these criteria. It included kinematic and force data across a broad range of activities, many of which are flexion-dominant and therefore relevant to cam-type FAI. Healthy participants were used, which allowed motion and load inputs to be defined consistently, although this introduces the limitation that healthy kinematics may not fully reflect cam-affected hip behaviour. Importantly, this dataset provided both hip angle and joint force data across multiple activities in a single, consistent framework, making it uniquely suitable for this work.

From this dataset, ten activities were selected for analysis:

- Leg crossing (seated)
- Reaching forwards (on knees)
- Squat
- Sit to stand/stand to sit
- Cycling
- Reaching down (standing)
- Golf swing (leading hip)
- Lunge
- Golf swing (trailing hip)

Walking trials were excluded, as previous work showed they produced few incidences of impingement (Jones et al., 2021). Figure 56 summarises subject demographics and the number of trials per activity for both hip angle and joint force data. Joint contact force data were unavailable for leg crossing, cycling, and the leading hip golf swing.

	Participant Demographics																	
Participant	1	2	3	4	5	6	7	8	9	10	11	12	13	14	15	16	17	18
Age	24	44	70	69	32	28	51	26	52	37	26	66	69	20	25	31	65	60
Height (m)	1.79	1.72	1.75	1.53	1.68	1.63	1.81	1.78	1.74	1.73	1.71	1.75	1.66	1.68	1.69	1.73	1.81	1.75
Mass (Kg)	82.5	73.1	75.6	61.7	60.3	50.2	86.1	83.7	87.7	70.5	65.2	77.1	70.5	85.4	76.8	67.3	90.3	106.1
Sex	M	F	M	F	M	F	M	M	M	F	F	F	M	F	F	M	M	M
	Available hip angle data																	**Total no. of trials**
Stand to sit	5	5	0	4	5	4	3	0	0	5	0	0	0	4	0	0	0	0	35
Sit to stand	5	5	2	5	5	5	0	0	0	5	0	0	0	5	0	0	0	0	37
Leg crossing (seated)	1	5	0	4	5	5	5	0	5	5	5	0	5	2	5	5	5	0	62
Squat	1	5	4	0	5	5	0	0	5	5	5	5	0	2	5	0	0	0	47
Reaching down (standing position)	5	5	4	0	0	3	2	0	0	4	2	0	0	3	0	0	0	0	28
Reaching forwards (on knees)	5	5	0	3	5	5	5	5	4	5	5	3	5	5	0	0	0	0	60
Lunge	5	5	0	3	0	0	5	5	1	0	0	0	0	0	0	4	0	4	32
Golf swing (trailing hip)	0	0	5	0	0	0	0	0	1	0	0	0	0	0	3	5	0	0	14
Cycling	0	5	2	5	5	4	5	0	0	5	3	0	0	0	1	0	0	0	35
Golf swing (leading hip)	0	0	5	4	0	0	0	0	4	1	0	0	0	0	0	5	5	0	24
	Available hip force data																	**Total no. of trials**
Stand to sit	3	5	0	0	3	2	0	0	0	4	4	0	0	3	0	0	0	0	24
Sit to stand	4	5	0	0	5	2	0	0	0	5	5	0	0	3	0	0	0	0	29
Leg crossing (seated)	0	0	0	0	0	0	0	0	0	0	0	0	0	0	0	0	0	0	0
Squat	0	5	3	0	5	5	0	0	5	5	5	5	0	0	5	0	0	0	43
Reaching down (standing position)	5	5	4	0	5	4	0	0	5	5	4	1	4	0	1	0	2	0	45
Reaching forwards (on knees)	5	4	0	2	0	4	0	5	4	5	5	3	5	0	0	0	0	0	42
Lunge	0	5	0	5	5	5	0	0	5	5	4	4	5	0	3	4	4	1	55
Golf swing (trailing hip)	5	5	5	5	5	5	0	5	4	5	5	5	5	5	0	5	5	5	79
Cycling	0	0	0	0	0	0	0	0	0	0	0	0	0	0	0	0	0	0	0
Golf swing (leading hip)	0	0	0	0	0	0	0	0	0	0	0	0	0	0	0	0	0	0	0

Figure 56: Participant demographics for hip angle and force data used (Layton et al., 2022b). Table of available hip angle data that resulted in an impingement event and the total number of trials for each activity. Table of available hip force data.

In this study, all trials that resulted in an impingement event were included to capture the widest possible range of motions associated with impingement risk. All available impinging motion data were used to calculate sliding distances, and all available joint force data were used for the force analysis. As these datasets did not always overlap, the motion and force analyses were performed on different subsets.

The selected activities included loaded high-flexion movements, such as squatting and lunging, which are strongly associated with the biomechanics of cam FAI (Nawabi et al., 2014; Doran et al., 2022). Although the dataset did not account for the frequency or variety of motion types in daily life, the flexion-dominant tasks it contains are clinically relevant to impingement and provided a comprehensive motion and load dataset suitable for population-level analysis.

4.3.5 Data filtering method

For a single motion case (defined as a specific activity, subject, and trial), multiple impingement events could occur. In most cases, the cam passed in and out of the acetabulum

just once during the activity; however, some trials exhibited more than one event. For each motion case, the impingement event with the longest sliding distance was selected, and any additional events were discarded. This choice was justified biomechanically: a longer sliding path corresponded to the cam moving a greater distance across the acetabular rim, increasing the duration and area of potential contact. By extension, this represented the most extreme mechanical scenario for the joint and thus the greatest potential for tissue stress or damage, even though damage itself was not directly measured.

The number of successful trials per subject varied, so data were not interpreted at the subject level. Instead, activity averages were calculated to mitigate any uneven weighting that might have arisen from differences in trial success. All results were processed consistently. First, an average was calculated at the subject level for all successful trials. These were then averaged across subjects to generate activity-level outcomes.

Another consideration for avoiding subject-level interpretation was to reduce overinterpretation of potential mismatches between hip shape and motion. At the subject level, a particular combination of shape and movement could have been arbitrary and might not have corresponded to a real-world scenario. Investigating parameters at the activity level provided a more representative view of how the joint might behave under typical motions.

4.4 Quantifying sliding distance during cam-type hip impingement over a set of activities.

This subsection examines the sliding distance during impingement across various activities for a hip shape with a large anterior cam. Sliding distance reflects the relative motion between contact points on the femoral head and acetabular rim during an impingement event, capturing the extent of interaction beyond a single contact location. By quantifying this motion, it was possible to assess the complexity of the sliding path and identify activities where the longest sliding paths occur. Such information is important for hip simulations, as it highlighted the motions most likely to produce extensive cam travel within the acetabulum.

The study aimed to analyse sliding distance to:

- Quantify the mean and maximum sliding distances during impingement across activities.
- Identify which activities were associated with the longest sliding distances.
- Compare the different methods of calculating the sliding path to assess the complexity of the path.
- Express sliding distances in both angular and scaled linear units to allow anatomical interpretation and comparison with existing literature.

4.4.1 Method for quantifying sliding distance

A custom MATLAB algorithm was developed to calculate sliding distance during impingement events. The process is summarised in the flowchart in Figure 57. The algorithm used two inputs from the impingement model: the cam angle (Figure 57a) and cam position coordinates (Figure 57b), both were defined at multiple cycle points. The cam angle, defined as the smallest angle between each cam point and the acetabular rim, was used to identify impingement events, while the corresponding position coordinates defined the cam location at each cycle point. This data was generated by combining the single hip shape case and the large set of motion cases described in Section 4.3.

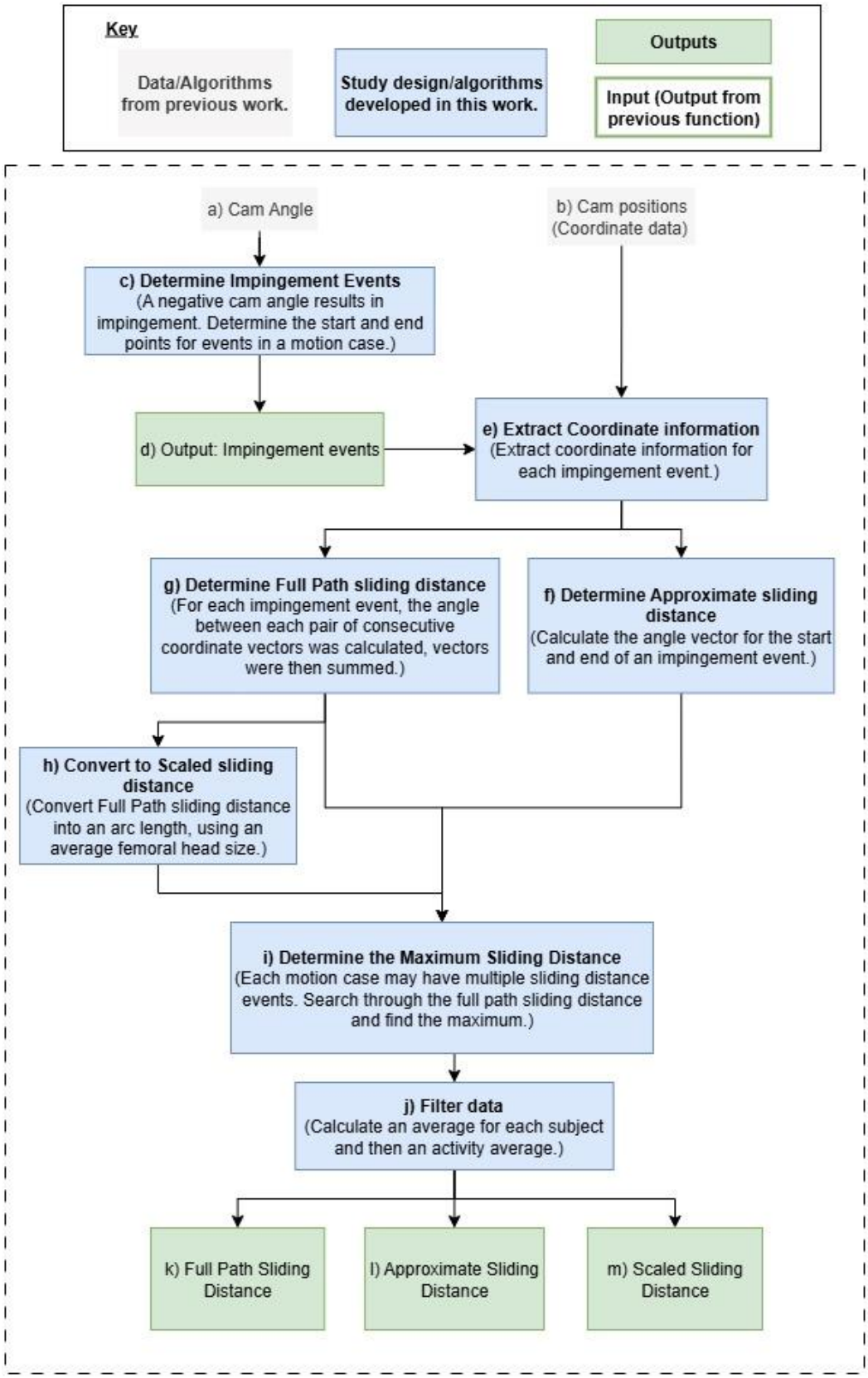

Figure 57: Flow chart outlining the algorithm developed to calculate sliding distance. Inputs from the impingement model (cam angles and cam positions) were used to identify impingement events and calculate sliding distances using three methods: full path, approximate, and scaled. Maximum values were extracted for each case and averaged at the subject and activity level.

The cam angle, provided for each cycle point, was used to identify impingement events (Figure 57c). Impingement occurred when the cam point passed beyond the acetabular rim, resulting in a negative angular value (Figure 58a). The function recorded the start and end cycle point of each event (Figure 57d). In parallel, the coordinate data for the cam point was extracted for the same events (Figure 57e).

For each impingement event, the sliding distance was calculated in three ways:

- Approximate: measured a single angle between the start and end position vectors of the event (Figure 57f, detailed in Figure 58b). This method provides a simple estimate of the overall displacement during impingement.
- Full Path: measured the cumulative angular travel of the cam edge point by summing the angles between consecutive position vectors within the event (Figure 57g, detailed in Figure 58c). This approach captures the length of the complete 3D trajectory of the cam point, including changes in direction along the articular surface.
- Scaled: converted the Full Path distance into an arc length using an average femoral head radius (Figure 57h).

The algorithm then identified the maximum sliding distance for each motion case (Figure 57i) and calculated averages at the subject and activity level (Figure 57j). The outputs of this process were maximum values for Full Path, Approximate, and Scaled sliding distance (Figure 57k–m).

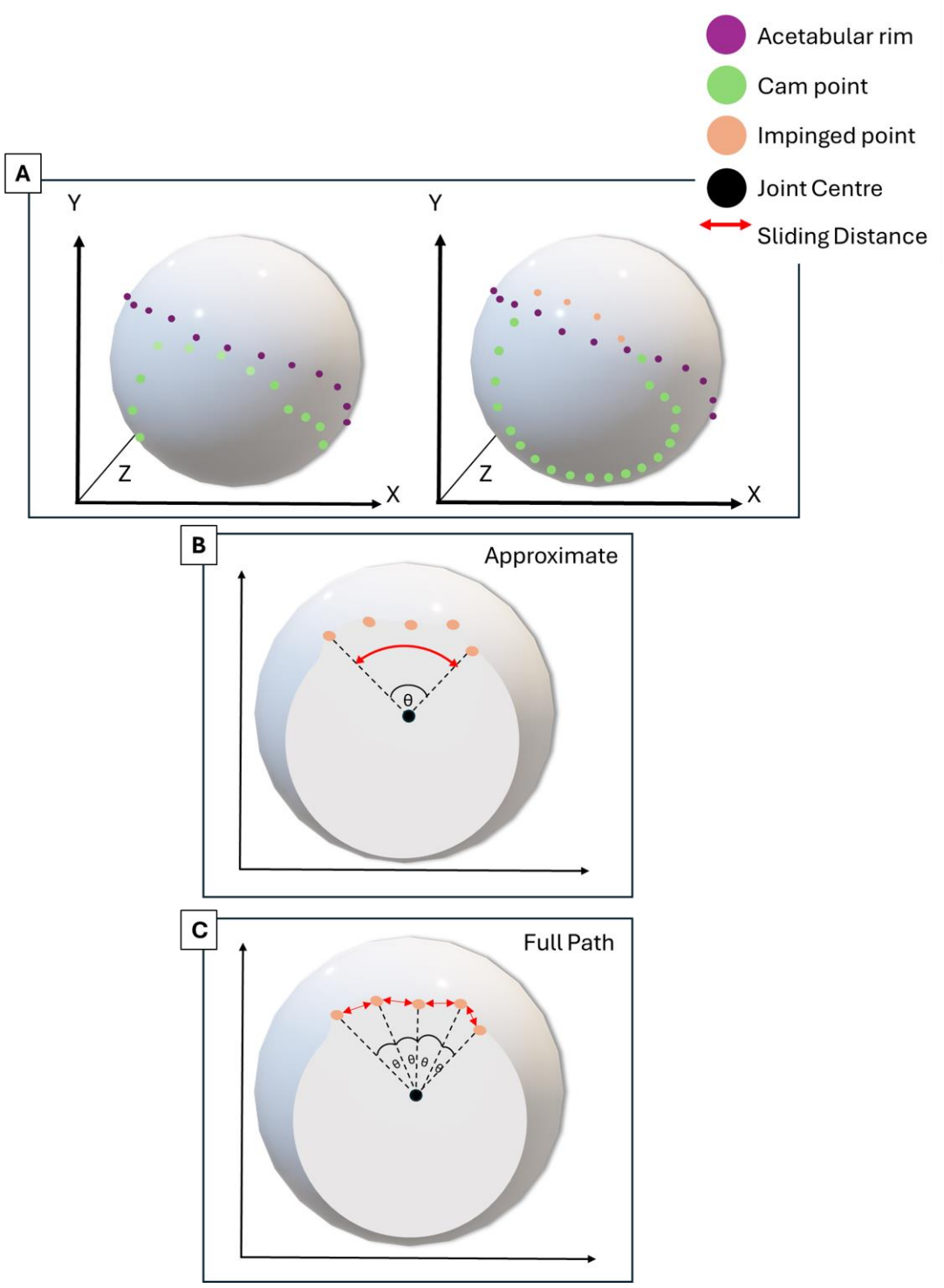

Figure 58: Illustration of the sliding distance calculation for the cam impingement model. (A) 3D representation of all cam points (green) and acetabular rim points (purple). Cam points that have penetrated the rim are shown in orange, representing impingement. (B-C) Visualisation of a single cam point at successive cycle points during motion. (B) Approximate sliding distance, measured as the angle between the start and end points of the impingement event. (C) Full Path sliding distance, calculated by summing the angles between consecutive cam points throughout the entire impingement event. The black circle indicates the joint centre used as a reference for angle measurements.

The Full Path sliding distance is expected to be equal to or greater than the Approximate distance. The Approximate method calculates the angular distance between the cam point at the start and end of the impingement event, forming a single arc across the spherical surface. In contrast, the Full Path method sums the angular distances between consecutive time points along the cam's trajectory. This is similar to comparing the straight-line distance between two points to the length of a winding path, where the winding path will always be equal to or longer.

Scaled sliding distance converted the Full Path angular distance into a linear arc length, expressed in millimetres, using an average femoral head radius. The underlying model represents the femoral head on a unit sphere, allowing angular positions and displacements to be compared independently of size, with all points defined in standardised spherical coordinates.

The average head diameter used in this study was based on a summary of four previously published datasets (Table 12). Differences in reported sizes likely reflect demographic variation, such as gender and ethnicity. A mean diameter of 48mm was selected to reflect a generalised adult population and provide a consistent reference for converting angular measures to millimetre values. As the cam shape used in this study represents a large morphology typical of symptomatic FAI patients, applying a representative average diameter was considered an appropriate approach to estimate Scaled sliding distances.

Table 12: Mean femoral head diameters for four different studies were found within the literature, and an average femoral head size was calculated.

Reference	Mean Femoral Head Diameter (mm)
Mascarenhas et al. (2018)	43
Nakahara et al. (2011)	44.8 +/-3.6
Young et al. (2013)	52 +/-5.3
Unnanuntana et al. (2010)	52.09 +/-4.43
Mean	48mm

Using this scaling, the sliding distance was calculated for all cam points that resulted in an impingement event. For analysis, only the longest sliding distance from each trial was included in the results. For the Full Path method, the mean and standard deviation were

calculated across all subjects for each activity, as well as the mean across all activities. The mean Approximate sliding distance was also calculated across subjects for each activity to enable comparison between the two methods.

4.4.1.1 Verification of sliding distance method

To verify the sliding distance methodology, a random motion case was selected and analysed using the custom code. The first stage of the process involved detecting whether impingement events occurred. In this sample case, the code detected two impingement events (cam points 11 and 12), with start and end points at frames 97–101 and 95–101, respectively. Inspection of the raw data confirmed that these cycle points corresponded to negative cam angles, thereby validating the detection.

The event detection function produced an event array (Figure 59), which listed all impingement events for a motion case. The event array was then cross-referenced with the raw cam angle data, confirming that the identified points matched regions of negative cam angles. This provided assurance that the event detection function was operating as intended.

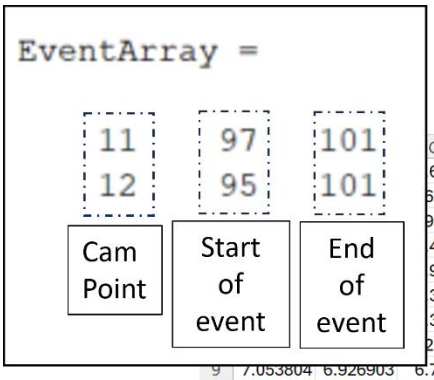

	CS	CT	CU	CV	CW
	62206	65.63526	65.39928	65.10254	64.865
	6.6314	46.64074	46.43899	46.18664	45.98541
	9.5274	39.47068	39.246	38.97757	38.75277
	44685	32.35561	32.11819	31.84206	31.60946
	96432	27.85034	27.67352	27.47324	27.28755
	39124	21.26829	21.11427	20.94359	20.77886
	38207	17.24794	17.11165	16.96545	16.81904
	2.3181	12.18201	12.06394	11.94059	11.81152
9	7.053804	6.926903	6.77326	6.656751	6.599076	6.54332	6.461523
10	2.325797	2.162016	1.983334	1.852167	1.788226	1.730207	1.65109
11	0.306879	0.132581	-0.0572	-0.18433	-0.22266	-0.24951	-0.30295
12	-0.00648	-0.19415	-0.3933	-0.5172	-0.53651	-0.53934	-0.57035
13	0.64778	0.458656	0.258318	0.144752	0.152144	0.180752	0.17717
14	2.544592	2.376217	2.186117	2.097232	2.155397	2.240397	2.280688
15	3.912623	3.749383	3.565383	3.491059	3.575759	3.691353	3.759545
16	6.70715	6.51625	6.324441	6.237626	6.293235	6.378991	6.432152
17	12.33243	12.14528	11.95816	11.88189	11.95617	12.06339	12.13626
18	19.40465	19.21538	19.02679	18.95606	19.04549	19.17068	19.25933
19	27.48793	27.29397	27.10102	27.03575	27.14441	27.29263	27.40098
20	36.53342	36.31284	36.09225	36.01004	36.11634	36.26454	36.36932
21	45.48254	45.22582	44.96895	44.86111	44.95496	45.09175	45.18141
22	60.16514	59.88357	59.602	59.49106	59.61142	59.78121	59.89609
23	76.16005	75.95174	75.73066	75.78386	76.22859	76.77067	77.20623
24	86.35319	86.65737	86.94613	86.97402	86.66308	86.27227	85.96012

Figure 59: Left) Output from the impingement event detection function. Column 1: cam point; Column 2: start of event; Column 3: end of event. Right) Cross-referencing with raw data confirmed that these values corresponded to negative cam angles, verifying that the detection function operated correctly.

Once impingement events were identified, the next step was to calculate the sliding distance. This was achieved using the coordinate data associated with the start and end points of each event. The code outputted three different measures: scaled sliding distance, approximate sliding distance, and full path sliding distance. An example of this output is shown in Figure 60.

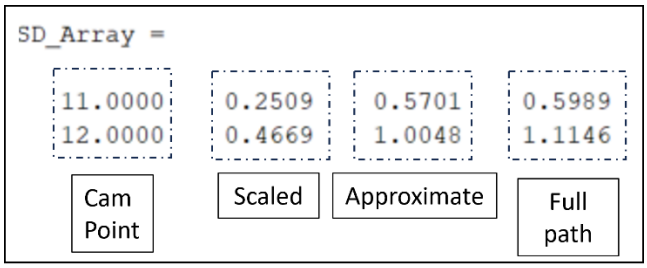

Figure 60: Sliding distance array output from the code for a single motion case, showing the scaled (mm), approximate (°), and full path (°) sliding distances associated with detected impingement events.

The next step was to determine the maximum full path sliding distance of the two events and pull this information into a new array. This ensured that only the longest sliding distance from each motion case was used in further analysis. In the example shown, cam point 12 produced the longer Full Path sliding distance (1.1146°) compared to cam point 11 (0.5989°). This value was then stored in a new array that contained the maximum sliding distance results for each motion case (Figure 61).

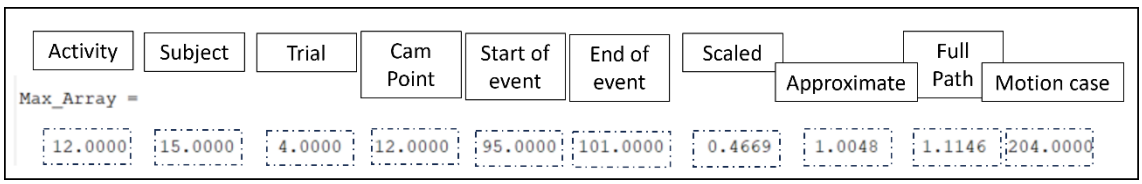

Figure 61: Output from the code showing the maximum results array. The first three columns (activity, subject, and trial) are included to track individual cases. Only the longest full path sliding distance (in this example, cam point 12) was identified and carried forward for further analysis.

To further verify that the code was correctly calculating sliding distances, the coordinate data for a single impingement event (cam point 11) was taken and recalculated manually in Excel. The same three sliding distance methods (scaled, full path, and approximate) were reproduced using the underlying equations. Figure 62a shows the formula for calculating the angle between two vectors, which underpins the sliding distance method. Figure 62b provides a screenshot of the computational code, while Figure 62c demonstrates the replication of this calculation in Excel.

a

Dot product

$$\theta = \cos^{-1}\left(\frac{v \cdot u}{\| v \| \| u \|}\right)$$

Magnitude

b

```
uMag = norm(u);
vMag = norm(v);
DotProd=dot(u,v);
angles =  acosd((dot(u,v))/(uMag.*vMag));
```

c

```
=DEGREES(ACOS(SUMPRODUCT(B2:D2,B3:D3)/(SQRT(SUMPRODUCT(B2:D2,B2:D2))*
SQRT(SUMPRODUCT(B3:D3,B3:D3)))))
```

	A	B	C	D	E	F	G	H	I	J	K	L
1		A(x)	B(y)	C(z)	Angles							
2	v1	-0.04954	-0.97607	-0.21175	)))							
3	v2	-0.05114	-0.97662	-0.20879	0.1453							
4	v3	-0.05072	-0.97716	-0.20634	0.1413							
5	v4	-0.05008	-0.97769	-0.20402	0.1166							
6	v5	-0.05032	-0.97808	-0.20204								
7												

Figure 62: Verification of the sliding distance calculation: (a) formula for calculating the angle between two vectors, (b) screenshot of the computational code, and (c) replication of the calculation in Excel.

The comparison between manual Excel calculations and outputs from the computational model is presented in Figure 63. The results aligned perfectly, confirming that the code was correctly implementing the sliding distance methodology.

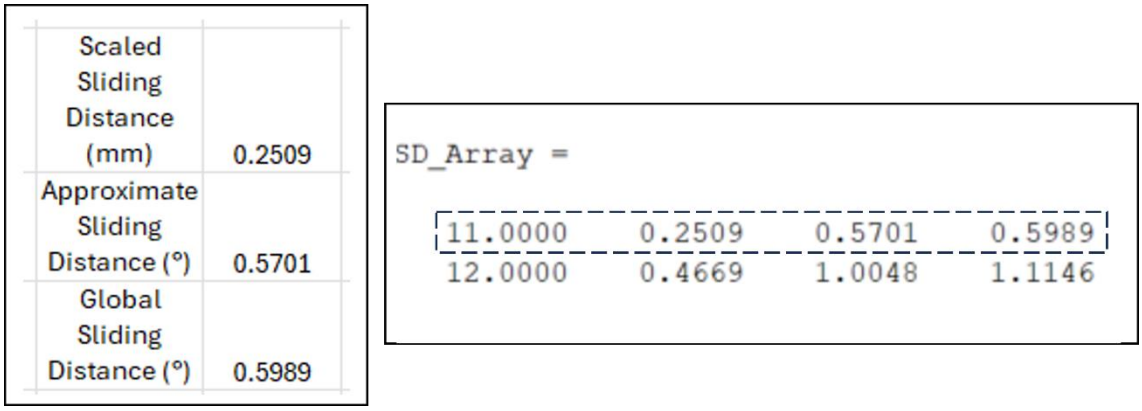

Figure 63: Verification of sliding distance values by comparison between manual Excel calculations (left) and computational code output (right). The two methods aligned, confirming the correct implementation of the methodology.

4.4.2 Results from sliding distance study

The mean Full Path sliding distance at the point of impingement across all activities was 34°. The longest recorded sliding distance for an activity was 81° (±34°) for the leg crossing activity, and the shortest was 4° (±2°) for the trailing hip golf swing, as shown in Table 2. Standard deviation was highest for the leg crossing activity and lowest for the golf swing. This variation likely reflects differences in how individual subjects executed the same activity, for example, by adopting greater or lesser hip rotation during squatting or leg crossing. While the primary focus is on activity-level averages, standard deviation highlights the potential range of sliding distances across subjects. The extent of variability differed between activities, with tasks involving larger angles of rotation, such as leg crossing or cycling, showing greater spread compared to more constrained tasks like the trailing golf swing (Figure 64).

Table 13: Mean and standard deviation of the Full Path sliding distance calculated across all subjects for each activity. Mean sliding distance across all activities was calculated.

Activity	Full Path Sliding Distance (°)	Standard Deviation (°)
Leg crossing (seated)	81	34
Reaching forwards (on knees)	55	18
Squat	40	17
Sit to stand	35	10
Cycling	33	24
Stand to sit	31	8
Reaching down (standing position)	26	21
Golf swing (leading hip)	21	19
Lunge	19	10
Golf swing (trailing hip)	4	2
Mean Overall Sliding Distance	**34**	

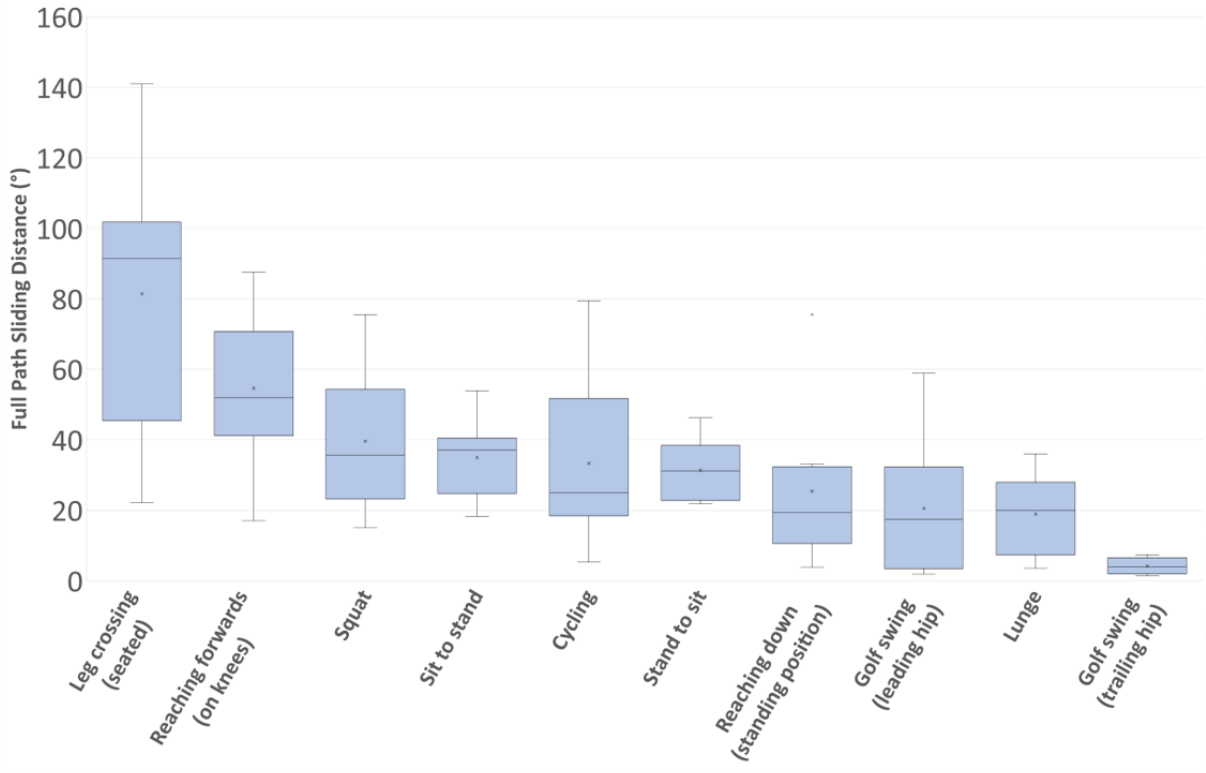

Figure 64: Subject Full Path sliding distances for each activity during impingement. The outer box is the interquartile range, the median is represented by the line going through the box, the cross is the mean, and the two whiskers on either side are the minimum and maximum values.

Approximate and Full Path sliding distances were compared (Figure 65) for all activities. The Approximate method resulted in smaller sliding distances than the Full Path method,

providing confidence in the calculations. The differences in recorded sliding distances offer a simple measure of the complexity of the cam's path during impingement. Activities where both methods resulted in similar sliding distances, such as the trailing golf swing, suggest that the cam stays close to the edge of the acetabular rim. Activities with larger differences, such as reaching forward while kneeling, indicate that the cam path extends further into the acetabulum during impingement.

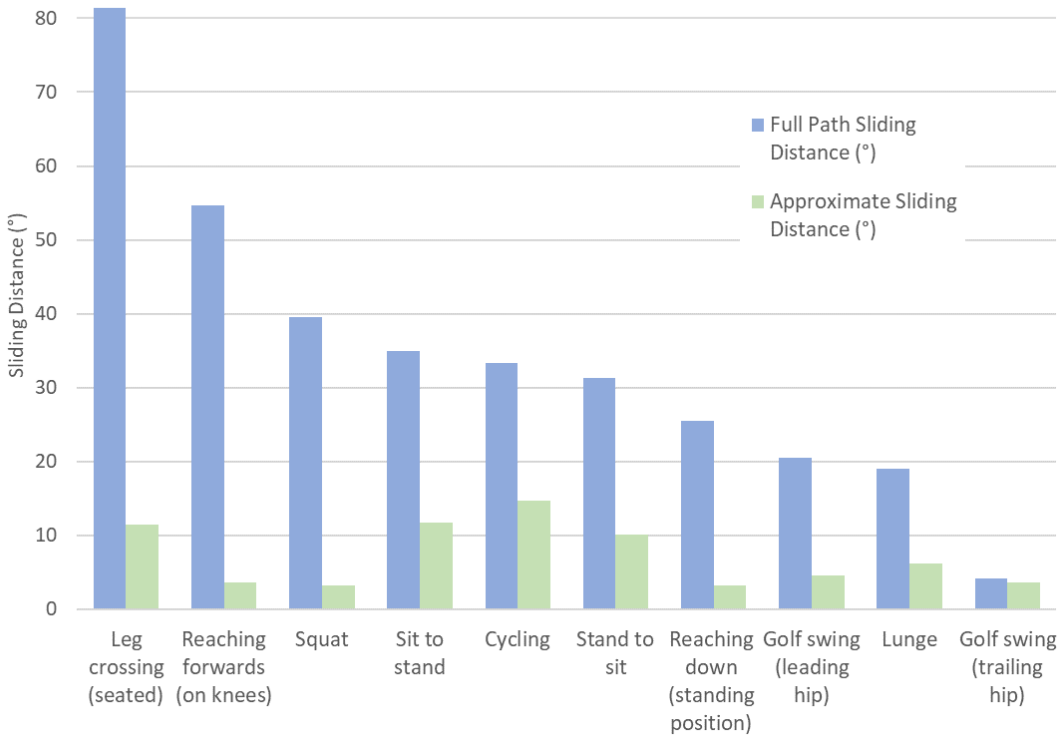

Figure 65: Comparison of methods used to calculate subject maximum sliding distance. Full Path sliding distance (blue) resulted in higher recorded sliding distances than the Approximate method (green).

Using an average femoral head size (48 mm) based on literature findings, the Scaled sliding distance was calculated for all activities (Table 14). A sliding distance of 34mm, more than half the diameter of the average human femoral head size, was recorded during the leg crossing activity.

Table 14: Mean Scaled sliding distance for all activities and standard deviation.

Activity	Scaled Sliding Distance (mm)	Standard Deviation (mm)
Leg crossing (seated)	34	14
Reaching forwards (on knees)	23	8
Squat	17	7
Sit to stand	15	4
Cycling	14	10
Stand to sit	13	3
Reaching down (standing position)	11	9
Golf swing (leading hip)	9	8
Lunge	8	4
Golf swing (trailing hip)	2	1

4.4.3 Discussion of sliding distance study

This study presents the first dataset of activity-specific sliding distances for cam morphology, providing quantitative insight into cam travel across a range of daily activities. The sliding distance algorithm quantified cam motion across ten activities for a large anterior cam shape. Mean Full Path sliding distances ranged from 4° (±2°) in the trailing hip golf swing to 81° (±34°) in leg crossing, corresponding to 2 mm to 34 mm when scaled to a 48 mm femoral head. The average Full Path distance across all activities was 34°. Leg crossing consistently produced the longest paths with the greatest variability between subjects, while the trailing hip golf swing produced the shortest and most consistent paths. These numerical ranges form the basis for defining rotational excursions in the subsequent in vitro simulations, with the upper values representing high demand conditions that may promote shear related damage, and the lower values serving as low demand comparators.

The methodology used to quantify sliding distance is an important consideration when interpreting these results. Full Path distance captured the entire cam travel across the acetabular rim during impingement, while the Approximate method provided a simplified estimate based on the angular difference between impingement onset and offset. Although both measures described similar trends between activities, the Full Path method consistently produced larger values because it accounted for changes in cam travel direction during the impingement window. This distinction is relevant because real hip movements rarely follow

perfectly planar paths; the rim contact point often shifts as pelvic orientation, femoral rotation and flexion interplay throughout a motion. The consistency between the two methods supports the robustness of the numerical outputs, but the greater detail provided by Full Path distance makes it more suitable for defining rotational inputs for in vitro simulation.

Direct comparisons with published values are limited because sliding distance is not commonly reported for natural hips. However, Bennett et al. (2002) described sliding distances of approximately twenty two millimetres in highly conforming hip replacements under comparable functional loads. When scaled to an average natural femoral head, this sits within the mid range of the sliding distances reported here, supporting the plausibility of the model outputs. The longer sliding distances recorded during leg crossing and squat reflect the deeper patterns of flexion and pelvic rotation associated with these movements, and align with known clinical and biomechanical observations that deep flexion tasks intensify cam engagement. Although natural hip studies rarely quantify contact path length, the broader movement patterns in the literature reinforce the trends observed here.

Understanding sliding distance in the context of femoroacetabular impingement provides additional insight into potential damage mechanisms. Longer sliding distances indicate that the cam travels further while engaged with the acetabular rim, which increases the potential for cumulative shear exposure and potentially contributing to early surface changes at the cartilage labral junction. This aligns with experimental and clinical evidence showing that repetitive shear loading can disrupt the superficial collagen network and initiate early degeneration. Activities producing long sliding distances, such as deep flexion movements, may therefore represent higher risk scenarios for initiating early damage. In contrast, activities with minimal sliding distance likely pose limited mechanical threat because the cam disengages quickly, reducing cumulative shear. If future in vitro studies aim to replicate movements beyond gait, the sliding distance data presented here suggest that tasks such as sit to stand or squat may be more appropriate for modelling early impingement related tissue damage.

There are, however, several limitations associated with this work. A single large anterior cam morphology was applied uniformly to all subjects, which removes the variability in cam size and orientation seen clinically and may influence the timing and location of impingement.

The femoral head was represented as a unit sphere to allow activity comparison, but this simplification removes subject specific curvature that may influence the exact travel path. The algorithm describes cam travel at the bony interface and does not account for cartilage deformation, labral engagement or joint translation, meaning that sliding distance alone cannot fully characterise the mechanical environment. Finally, although sliding distance highlights kinematic differences between activities, it must be interpreted alongside load and rotational direction to understand the combined mechanical exposure that contributes to impingement related tissue damage. Despite these limitations, the sliding distance ranges reported here provide a clear and physiologically grounded set of rotational parameters for use in the subsequent in vitro simulations.

4.5 Peak load during impingement

This subsection examines the peak resultant hip joint load during impingement across a set of activities. Joint loading is a critical factor for understanding the mechanical environment of the hip and the potential for damage when cam morphology is present. Identifying whether peak forces coincide with impingement is particularly important for hip simulations, as it defines the loading conditions that should be reproduced in experimental or computational models. Linking load magnitude with the timing and location of impingement provides a more complete picture of the stresses acting on the joint.

The study aimed to analyse peak load to:

- Quantify the average peak hip joint load across activities, expressed relative to body weight.
- Determine whether maximum loads occur during impingement or elsewhere in the cycle, and identify the cycle point relative to the onset and offset of impingement.
- Examine inter-subject variability by comparing the maximum and minimum peak loads for each activity.
- Explore how peak load interacts with impingement depth and timing across different motions.

By addressing these aims, this work provides a framework for applying realistic loading conditions in hip simulations, ensuring that both the level and timing of peak force are represented when modelling impingement.

4.5.1 Methods for determining peak load during impingement

In the source dataset (Layton et al., 2022b), hip joint contact force data was not available for all activities or motion trials. Specifically, the leg crossing, cycling, and leading hip golf swing activities did not have associated force data. Additionally, some trials for the remaining activities were incomplete, with either missing force or motion data.

To generate representative force profiles for each activity, mean values were first calculated for each subject using all successful trials. These subject means were then averaged at each cycle point to obtain an overall activity profile.

The impingement window for each activity was defined from the motion data by tracking the position of the femoral cam relative to the acetabular rim. The start of impingement was identified when the cam entered the rim boundary, and the end when it exited. This method ensured consistent detection of impingement events across trials and subjects. The window used for analysis corresponded to the trial with the greatest sliding distance for each subject (Section 4.4.1), providing a consistent reference for activity-level comparisons.

Peak load was then evaluated over two periods: the full activity cycle and the impingement window. Within this window, peak force was expressed as a multiple of body weight (xBW), using pre-normalised data from the original dataset to enable comparison between subjects of different sizes.

The MATLAB algorithms developed to process this data are summarised in Figure 66 (flowchart). The main input was raw X, Y, and Z joint contact force vectors from the dataset. These were used to calculate the resultant joint contact force throughout each activity (Figure 66b). From here, the subject and activity average forces were computed (Figure 66c–d), along with the peak resultant force for each motion (Figure 66e–f). A further comparison was made between the volunteer with the highest peak force and the one with the lowest (Figure 66k–m), to visualise inter-subject variability in loading profiles.

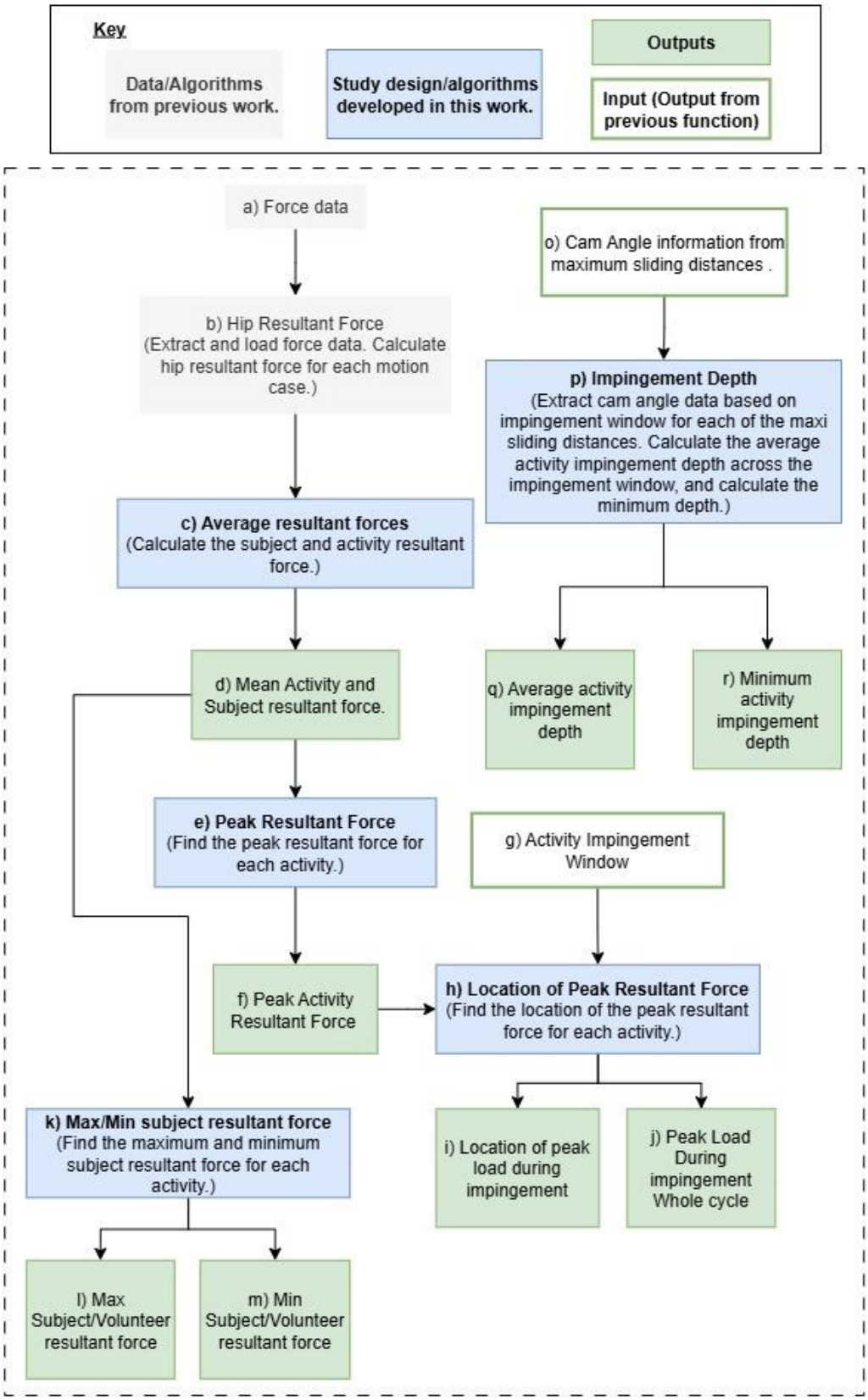

Figure 66: Flowchart showing how force and angular data from the impingement model were processed to generate outcome measures, including peak load, impingement depth, and their locations. Functions developed in this work are shown in blue, with their inputs and outputs in white and green.

The cycle point of the peak load during impingement was determined by extracting cam angle data corresponding to the impingement window (Figure 66g–h). This enabled the detection of the angular location of peak force within the impingement region (Figure 66i), alongside the peak force value over the full cycle (Figure 66j).

Impingement depth was estimated from the angular distance between the cam points and the rim during impingement. For each trial, angular depth data were extracted from the same cam angle information used to identify the maximum sliding distance (Section 4.4). All time points outside the impingement window were set to zero before averaging, ensuring that only the time period of interest contributed to the activity-level average depth (Figure 66o–r). In addition, the minimum activity impingement depth across the whole cycle was also recorded to characterise the range of penetration during peak contact.

4.5.1.1 Verification of peak loading method

To verify the load calculation method, the hip joint force data was imported into the computational model. For each trial, the resultant hip force was calculated by combining the three orthogonal force components (anterior–posterior, superior–inferior, and medial–lateral). The formula used within the computational model to calculate the resultant force is shown in Figure 17a, while the equivalent hand-written Excel formula is shown in Figure 17b.

a)

```
HipResForce(tr,cyc,sub,act) = sqrt(AP_F(cyc)*AP_F(cyc) + ML_F(cyc)*ML_F(cyc) + PD_F(cyc)*PD_F(cyc));
```

b)

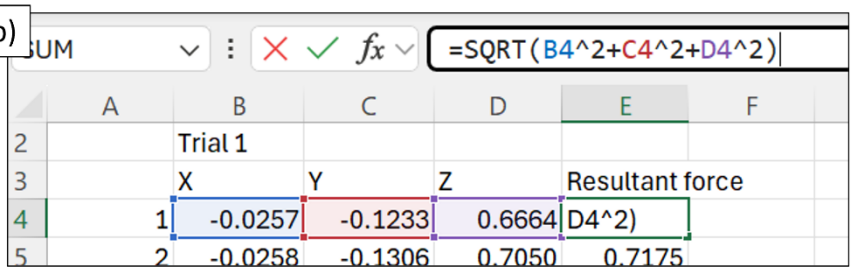

Figure 67: (a) Formula within the computational model used to calculate the resultant hip force from the three orthogonal force components. (b) Equivalent hand-written Excel formula used to verify the computational calculation.

To confirm the accuracy of the computational method, a representative random sample of force data from one of the activities was extracted, and the resultant forces were calculated

independently in both the computational model and Excel. Figure 18a presents the resultant force values obtained from the computational model, and Figure 18b shows the results from the Excel verification. Both calculations produced identical results, confirming that the model correctly calculates the resultant hip force.

a)

```
Columns 1 through 15

    0.6782    0.7175    0.6110    0.6817    0.6698    0.6276
```

b)

	Subject 1			
	Trial 1			
	X	Y	Z	Resultant force
1	-0.0257	-0.1233	0.6664	0.6782
2	-0.0258	-0.1306	0.7050	0.7175
3	-0.0205	-0.1131	0.6001	0.6110
4	-0.0219	-0.1280	0.6692	0.6817
5	-0.0191	-0.1252	0.6577	0.6698
6	-0.0154	-0.1146	0.6168	0.6276

Figure 68: (a) Resultant force values calculated by the computational model for a sample activity. (b) Verification of the same results using hand-written Excel calculations. Both methods show identical resultant force values, confirming the accuracy of the computational approach.

Once the resultant force was calculated for each trial, it was then averaged at the subject level and subsequently at the activity level. From these averaged force profiles, the peak resultant force was identified along with the corresponding cycle point in the activity at which this peak occurred.

4.5.2 Results from peak loading study

Before presenting the load results, it is important to acknowledge an inconsistency identified in the impingement window for the golf swing activity (Figure 69). The method used to calculate the window (averaging the start and end points of subject-level impingement events) did not perform reliably due to large inter subject variability. Impingement occurred at the start of the cycle for some subjects and at the end for others, and averaging these produced a window positioned in the middle of the cycle, which does not represent the true

timing of impingement. Because the impingement window for the golf swing cannot be defined accurately, all golf swing load results have been removed from this section.

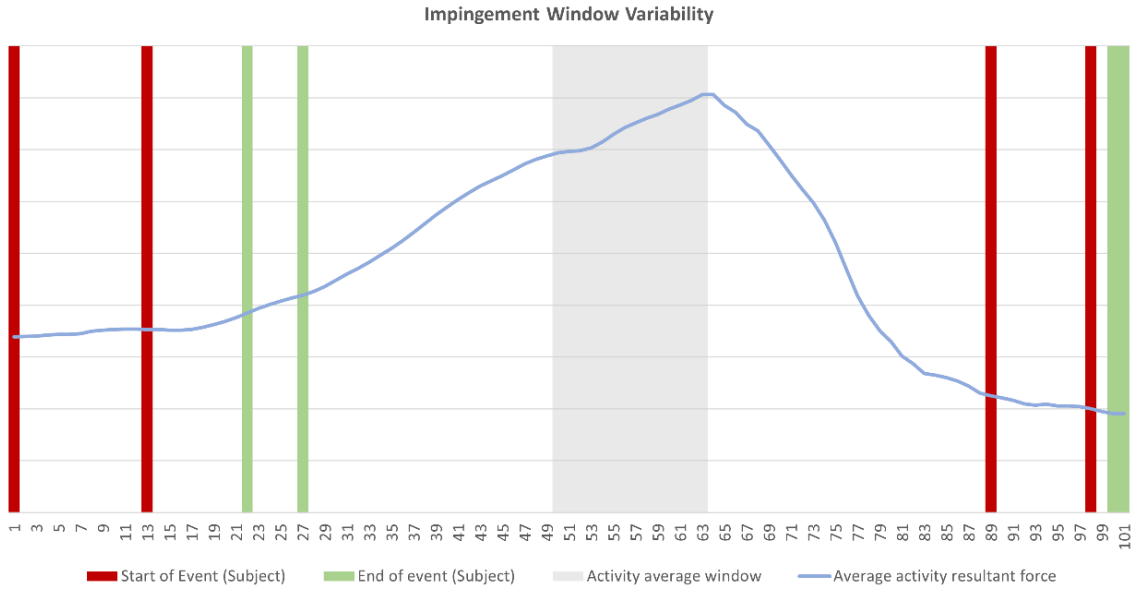

Figure 69: Variability of the start and end point of impingement events at the subject level for the Golf Swing activity. Average activity impingement window (light grey), average activity resultant force (blue), the start (red) and end (green).

Peak hip joint load was assessed across the whole activity cycle and within the impingement window (Table 15). Average peak loads varied across activities, with sit to stand showing the highest load at 6.4xBW and reaching forwards the lowest at 0.5xBW. The low load for reaching forwards likely reflects the kneeling posture, which distributes load across knees, shins, and feet, while the high load in sit to stand arises from the large moment arm generated during the transition from sitting to standing (Layton, 2020).

Table 15: Activity mean peak hip load (xBW) across the whole cycle and during impingement.

Activity	Average (Whole cycle) xBW	Average (During impingement) xBW
Sit to stand	6.4	6.4
Squat	4.3	4.3
Stand to sit	4.2	4.2
Reaching down (standing position)	3.5	3.5
Lunge	3.1	0.9
Reaching forwards (on knees)	0.5	0.5

For most activities, the peak load occurred within the impingement window, indicating that the maximum load coincides with impingement (Figure 70). The lunge was the clear exception. In the lunge, peak load was observed towards the end of the cycle (cycle point 101), showing that high load does not coincide with impingement for this activity.

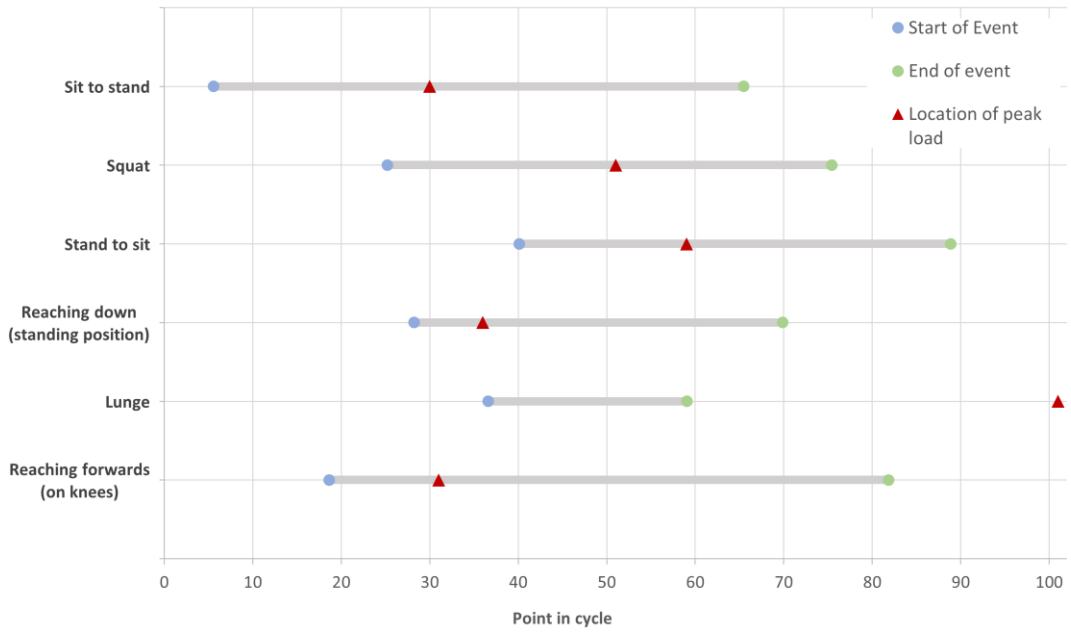

Figure 70: Location of impingement window for each activity. Start (blue circle) and end (green circle) of the impingement window, and the peak load (red triangle) throughout the entire cycle.

Inter-subject variability was examined using the maximum and minimum loads for each activity (Table 16). Sit to stand exhibited the largest variability, with a maximum of 11.5xBW

and a minimum of 3.3xBW, whereas reaching forwards showed low variability, with values close to the activity average. Reporting maximum and minimum values illustrates extremes in loading and highlights whether the average is representative, particularly for identifying outliers.

Table 16: Average peak load during impingement for each activity and the point in the cycle when the impingement occurred. The maximum and minimum subject peak load for each activity across the whole cycle.

Activity	Average (During impingement)		Max. Subject		Min. Subject	
	xBW	Cycle point	xBW	Cycle point	xBW	Cycle point
Sit to stand	6.4	30	11.5	30	3.3	31
Squat	4.3	51	6.8	57	2.1	50
Stand to sit	4.2	59	5.5	56	1.9	62
Reaching down (standing position)	3.5	36	6.2	69	2.2	27
Lunge	3.1	101	5.2	101	1.4	32
Reaching forwards (on knees)	0.5	31	0.7	42	0.4	41

The relationship between peak load, impingement depth, and timing was visualised by overlaying mean, maximum, and minimum resultant forces with impingement depth and windows (Figure 71). For sit to stand, peak load aligned closely with maximum impingement depth and the standing phase of the activity. In contrast, the lunge displayed decoupling between load and impingement, suggesting that high peak load does not necessarily coincide with deep impingement. Additionally, the kneel reach activity demonstrated substantial impingement depth with very low peak load, indicating that load magnitude is not solely determined by impingement severity.

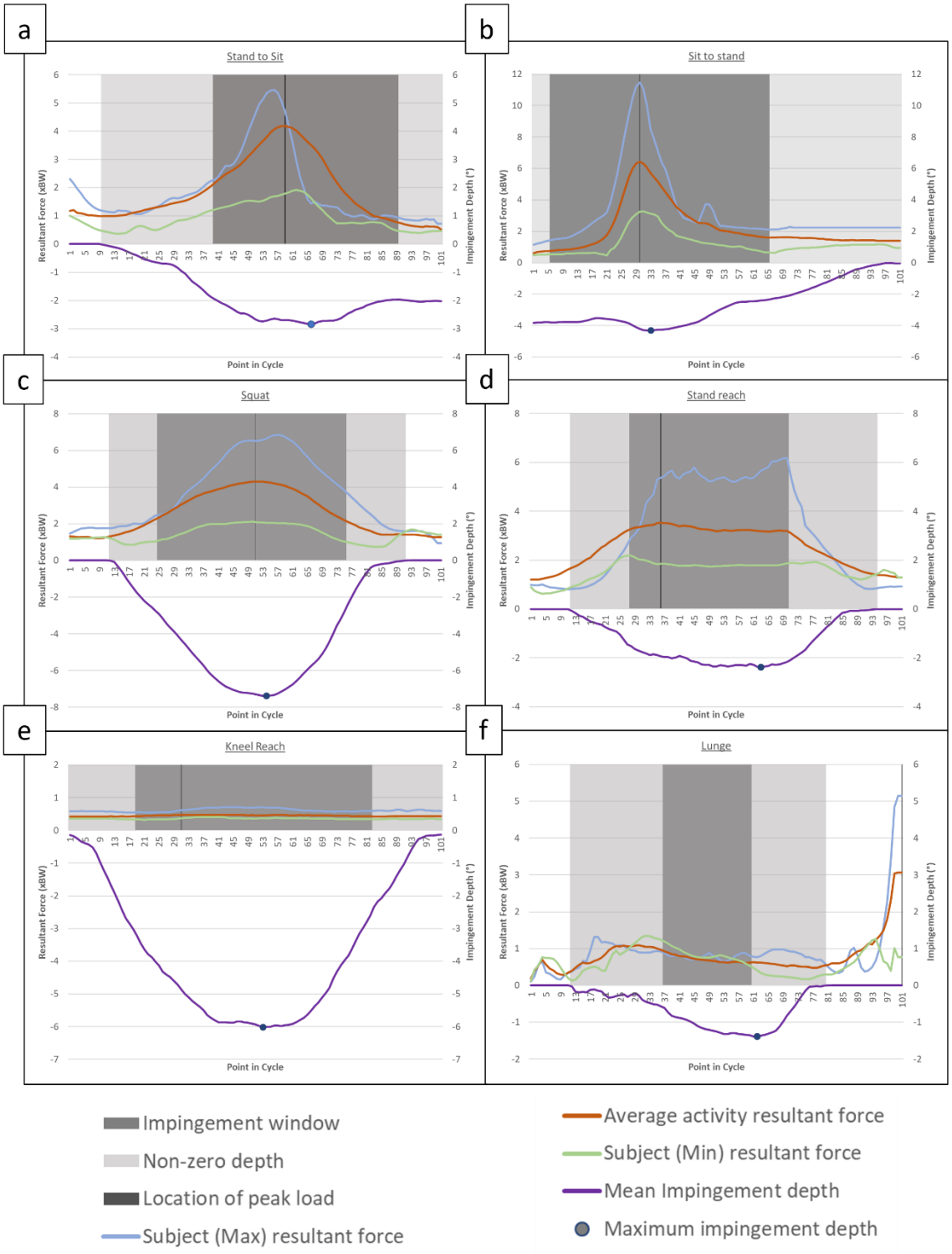

Figure 71: Average activity (red), maximum (blue) and minimum (green) subject resultant force for the whole activity cycle. Average activity impingement depth (purple), the minimum impingement depth (blue dot). Impingement window (dark grey) based on previous impingement event data, non-zero depth (dark grey) based on average activity impingement depth.

4.5.3 Discussion of Peak load during impingement

This study identified clear ranges of peak hip joint load during impingement that can be used to inform parametric in vitro testing. Peak loads varied considerably across activities and subjects, with sit to stand producing the highest average peak load at 6.4xBW and an individual maximum of 11.5xBW. Squat and kneel reach also generated substantial loads, averaging 4.3xBW and 3.5xBW respectively, whereas reaching forwards on the knees produced the lowest load at 0.5xBW. These results provide a set of realistic loading magnitudes that can be applied in experimental investigations, particularly for evaluating how different levels of mechanical stress contribute to cartilage or labral damage. Using these values as conditions ensures that in vitro testing reflects physiologically relevant loading scenarios.

The timing of peak load relative to the impingement event provides insight into how mechanical stress and contact severity interact. For most activities, the peak load occurred within the impingement window, indicating that the greatest mechanical stress aligned with the moment of bony contact. Sit to stand exemplifies this pattern, where maximum load, average impingement depth, and maximum impingement depth all occurred at closely aligned cycle points. This suggests a synergistic mechanical effect where deep penetration and high load combine to produce greater joint stress. In contrast, the lunge demonstrated a clear decoupling, with peak load occurring late in the movement while the impingement event occurred earlier. This reflects activity specific differences in movement strategy and shows that high load alone does not always coincide with impingement. These observations reinforce the need to consider both load magnitude and contact timing when assessing potential risk.

Comparison with existing literature indicates that the impingement loads predicted by the model fall within physiologically realistic ranges when evaluated against studies that use similar motion analysis driven musculoskeletal modelling approaches. Amiri and Bull (2022) used the FreeBody model to estimate hip joint contact forces across seven activities of daily living and showed that their predictions for walking, stair ascent and transitions closely matched values obtained from validated implant datasets, with peak forces typically ranging between 2 and 6xBW depending on task demand. Varady et al. (2015) applied an AnyBody based model to a range of everyday and occupational tasks and reported walking loads of

approximately 2-3xBW and peak forces of around 6xBW during high demand load transfer activities. The peak loads observed in the present study fall within the upper end of these ranges, which is expected given that impingement occurred during movements that place the hip near its functional limits. These parallels indicate that the loading patterns generated by the model are mechanically plausible and provide credible input ranges for the subsequent in vitro simulations.

Interpreting these findings in the context of femoroacetabular impingement provides insight into which activities may present greater risk of early tissue damage. High loads occurring simultaneously with rim engagement may contribute to elevated compressive and shear stresses at the cartilage labral junction, particularly during movements that challenge the hip toward deep flexion. Prior studies by Lamontagne et al. (2009) and (Diamond et al., 2019) have shown that squat and similar high flexion tasks increase mechanical demand, alter hip kinematics and require greater muscular effort in both FAI and healthy groups, indicating that these movements naturally elevate joint loading and may exacerbate impingement related stresses. Sit to stand showed a similar pattern in the present study, producing some of the highest loads and aligning them with the impingement window. In contrast, movements such as kneel reach entered deep flexion but did so under comparatively low load, suggesting that their mechanical risk may be limited despite the presence of impingement kinematics. These distinctions highlight the importance of considering both the magnitude and timing of load when assessing the severity of impingement related tasks, and they provide guidance for selecting activities that may be suitable for in vitro testing if future studies wish to extend beyond gait based loading protocols.

Several limitations are specific to the interpretation of the load predictions. The joint reaction forces were derived from a healthy cohort, meaning that the values represent the loading characteristics of normal gait cycles and transitions rather than the altered movement strategies often seen in individuals with cam morphology. The musculoskeletal modelling pipeline used to generate the hip forces assumes rigid body behaviour, simplified muscle recruitment and no explicit representation of soft tissue structures such as the labrum or cartilage, all of which influence real joint force transmission. In addition, muscle co contraction and subject specific pelvic tilt, which can substantially affect hip joint forces in deep flexion, are not fully captured in the model. These limitations mean that the predicted peak loads should be viewed as physiologically plausible loading conditions for

healthy movements entering the computational impingement window, rather than precise representations of patient specific impingement forces. Nevertheless, they provide a consistent and credible basis for defining compressive inputs for subsequent in vitro testing.

4.6 Determine the dominant hip rotation during impingement.

This subsection examines whether motion during impingement is dominated by a single anatomical rotation. The motion data contained hip joint angles in flexion–extension, abduction–adduction, and internal–external rotation. Although analysis in anatomical planes does not provide an exact description of movement relative to the acetabular rim, it can reveal whether a single rotation dominates once contact occurs. Identifying such dominance is important for understanding which motions may be key drivers of rim damage. In the context of simulator testing, this information is valuable because it allows test design to prioritise reproduction of the most mechanically relevant rotation rather than attempting to replicate the full three-dimensional motion path.

The study aimed to analyse dominant rotation in order to:

- Determine whether hip motion during impingement is dominated by a single anatomical rotation.
- Compare rotation dominance during the impingement event with dominance across the whole activity.
- Identify which rotations should be prioritised for further investigation in the context of in vitro testing.

By addressing these aims, this work highlights the role of rotation dominance in impingement mechanics and provides guidance for designing targeted simulation studies.

4.6.1 Methods for determining dominant hip rotation

The procedure for determining dominant hip rotation is shown in Figure 72. The algorithm takes two main inputs: the hip motion dataset (Figure 72a) (Layton et al., 2022b) and the impingement window based on the longest sliding distance results from the preceding impingement analysis (Figure 72c). Hip motion data is first read into the function (Figure 72b) and matched to the corresponding longest sliding distance records so that only the relevant data for each trial are extracted (Figure 72d).

For each anatomical rotation (flexion extension, abduction adduction, and internal external rotation) the maximum and minimum angles are identified within the impingement window (Figure 72e) and across the entire trial (Figure 72f). These values are then used to calculate motion amplitude for each rotation (Figure 72g), producing separate amplitude datasets for the impingement window (Figure 72h) and the whole event (Figure 72i).

Amplitudes are first averaged at the subject level (Figure 16j, l, m) and then across subjects to obtain activity level mean amplitudes for both the impingement window (Figure 16k, o) and the whole event (Figure 16k, p). The dominant rotation for each activity is identified by selecting the rotation with the largest average amplitude and comparing it with the sum of the other two. If the largest value exceeds this sum, it is classified as the dominant rotation (Figure 16n). The outputs from this step are the dominant rotation for the impingement window (Figure 16q) and for the whole event (Figure 16r).

Finally, the magnitude of dominance is calculated as the ratio of the largest amplitude to the sum of the other two amplitudes (Figure 16s). This produces the final output, the relative dominance of hip rotations for both the impingement window and the whole event (Figure 16t), which can be used to compare movement patterns between activities.

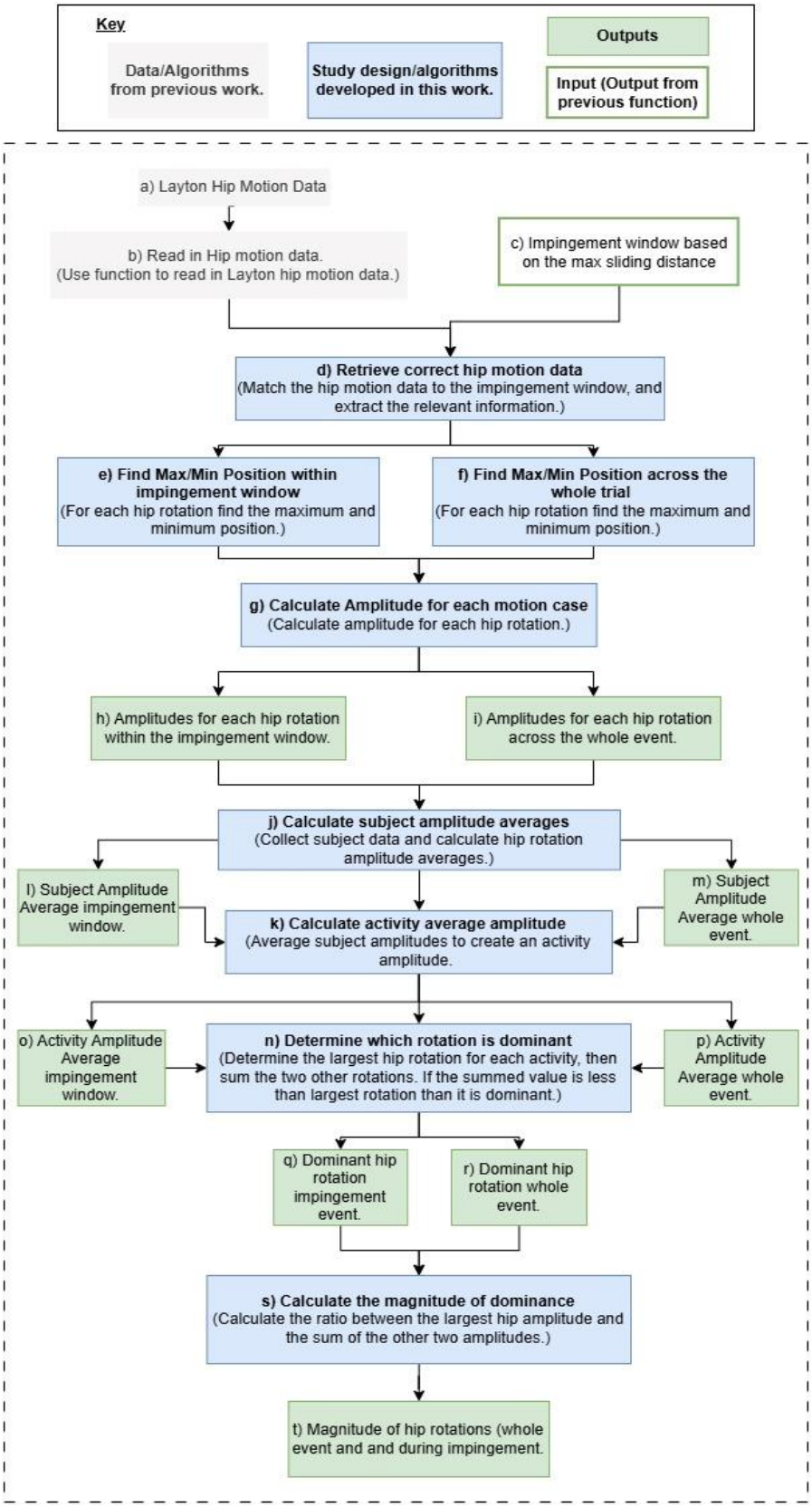

Figure 72: Flowchart showing algorithm for determining dominant hip rotation from motion data and impingement analysis outputs. Process identifies rotation amplitudes, selects the dominant rotation, and quantifies its relative dominance within the impingement window and across the whole event.

Figure 73 illustrates how rotation dominance was calculated for two example activity averages over the whole event. Dominance was assessed by first determining the amplitude of each hip rotation. The dominant rotation was identified if the largest amplitude (a) was greater than the combined amplitudes of the other two rotations (b + c), using the condition a > b + c. In the example shown, flexion extension was dominant for Activity 1, whereas no rotation was dominant for Activity 2.

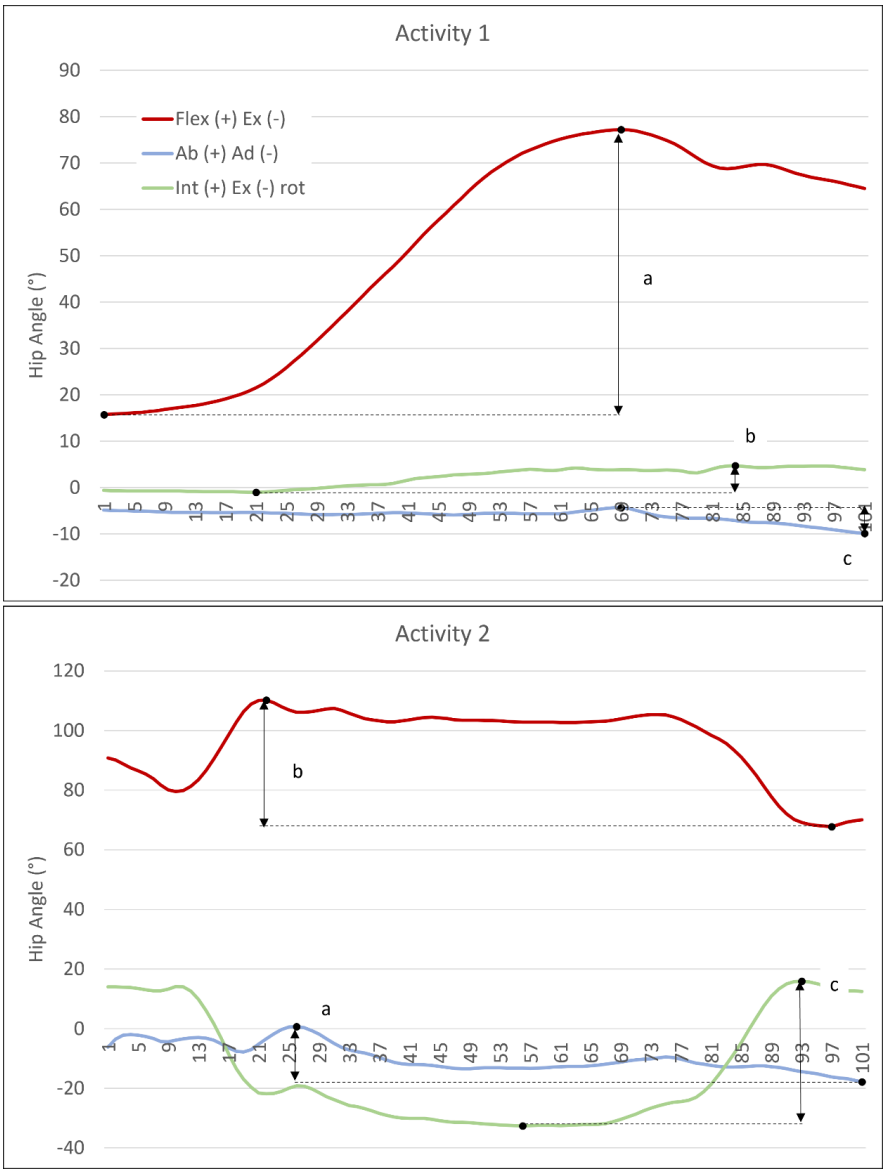

Figure 73: Raw hip angle data for a single trial from two activities. Amplitude for each hip rotation is calculated. Dominance was defined by the following equation $(a > b + c)$. *Magnitude of dominance was calculated as the ratio of the largest amplitude to the sum of the other two. Red represents the flexion-extension, blue abduction-adduction and green internal-external rotation.*

Dominance was also evaluated specifically during impingement. The impingement window was defined based on earlier analysis, using the cam point associated with the longest sliding distance in each trial. The start and end of this event were used to set the impingement window. Dominance was then recalculated only within this period. In Figure 74 this window is shown by the shaded region. For Activity 1 no dominant rotation was present within the impingement window, despite dominance being observed across the whole activity.

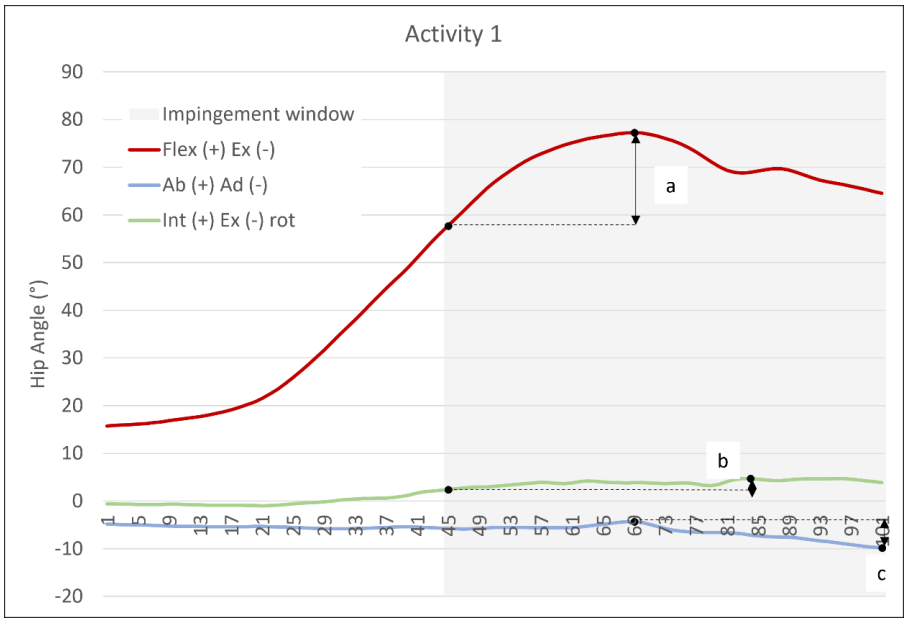

Figure 74: Raw hip angle data for an activity with impingement windows shaded in grey. Amplitude for each hip rotation is calculated. Dominance was defined by the following equation $(a > b + c)$***. Magnitude of dominance was calculated as the ratio of the largest amplitude to the sum of the other two. Red represents the flexion-extension, blue abduction-adduction and green internal-external rotation.***

In addition to identifying whether dominance occurred, the magnitude of dominance was calculated to indicate the strength of any dominant rotation. The dominance magnitude was defined as the amplitude of the largest rotation divided by the sum of the amplitudes of the other two rotations. A ratio greater than 1 indicated dominance, with larger ratios reflecting stronger dominance. For example, values close to 1 indicated marginal dominance, while values of 2 or above showed that one rotation contributed most of the motion during that activity.

This measure provides context for interpreting kinematic behaviour. Larger dominance magnitudes indicate that one anatomical rotation clearly governed the motion, which may

have a greater influence on the location and severity of damage. Conversely, lower magnitudes indicate a more balanced motion pattern, suggesting that the mechanism of damage may be distributed across multiple rotations rather than being driven primarily by a single plane of motion.

4.6.1.1 Verification of dominant hip rotation methods

To verify the method for determining the dominant hip rotation, a trial from the Hip motion data (Layton et al., 2022b) was selected as an example case. The data was first imported into the computational model. The data was organised into three columns corresponding to each hip rotation: flexion-extension, abduction-adduction, and internal-external rotation. The start and end points of the impingement event were also imported from the maximum sliding distance results (as described previously in Section 4.4.1, with verification provided in Section 4.4.1.1).

For each hip rotation, the minimum and maximum values were identified both across the entire activity and within the impingement window. These were used to calculate the amplitude of each rotation. The calculations were performed using both the computational model and hand-written Excel formulas for comparison.

- The maximum and minimum hip rotations during the impingement event were similarly calculated in the model (Figure 75a) and verified in Excel (Figure 75b).
- The maximum and minimum hip rotations across the full activity were obtained from the computational model (Figure 76a) and reproduced manually in Excel (Figure 76b) .

Results from both methods were in full agreement, confirming that the computational model accurately calculated the rotational amplitudes.

a)

During Impingement

Flex-Ext	Abb-Add	Int-Ext
MaxPosition = 77.2393	MaxPosition = -4.3164	MaxPosition = 4.7216
MinPosition = 56.1226	MinPosition = -9.8543	MinPosition = 2.2224

```
All_Amplitudes =

    5.0000    1.0000    1.0000   21.1167    5.5379    2.4991
```

b)

	Flex-Ext	Abb-Add	Int - Ext
max	77.2393	-4.3164	4.7216
min	56.1226	-9.8543	2.2224
amp	21.1167	5.5379	2.4991

Figure 75: (a) Maximum and minimum hip rotations and corresponding amplitudes during the impingement window calculated in the computational model. (b) Verification of the same results using hand-written Excel formulas. Both methods show consistent maximum, minimum, and amplitude values for each motion (flexion-extension, abduction-adduction, and internal-external rotation).

a)

	Flex-Ext	Abb-Add	Int-Ext
Whole Event	MaxPosition = 77.2393 MinPosition = 15.7221	MaxPosition = -4.3164 MinPosition = -9.8543	MaxPosition = 4.7216 MinPosition = -1.0019

```
wholeEvent_Amplitudes =

    5.0000    1.0000    1.0000   61.5172    5.5379    5.7234
```

b)

	Flex-Ext	Abb-Add	Int - Ext
max	77.2393	-4.3164	4.7216
min	15.7221	-9.8543	-1.0019
amplitude	61.5172	5.5379	5.7234

Figure 76: (a) Maximum and minimum hip rotations and corresponding amplitudes across the entire activity obtained from the computational model. (b) Verification of the same results using hand-written Excel formulas. Both methods show consistent maximum, minimum, and amplitude values for each motion (flexion-extension, abduction-adduction, and internal-external rotation).

Next, the amplitude of each hip rotation was used to identify the dominant rotation. The dominant rotation was defined as the motion with the largest amplitude (a), provided that this value was greater than the combined amplitudes of the other two rotations (b + c). The formula for this is shown in Figure 77a. The dominance calculation was implemented in both MATLAB and Excel for comparison. The MATLAB code is shown in Figure 77b, while the equivalent Excel formula is shown in Figure 77c.

a)

$$a > b + c$$

b)

```
% Calcualte the sum of all rotation directions.
SumOfTotalRotations = sum(DominantRotations,2);
% Find the amplitude of the rotations minus the maximum amplitude.
B=SumOfTotalRotations-MaxRotation;
% Store maximum amplidtude and the amplitude of the other two rotations
%combined next to each other.
C= [MaxRotation,B];

% Is the Dominant hip rotation larger than the other two rotations
% combined? Store answers in a new array "1" true and "0" false.
D=zeros(2,1);
for row=1:2
    if C(row,1)>C(row,2)
        D(row,1)=1;
    else
        D(row,1)=0;
    end
end
D;
```

c)

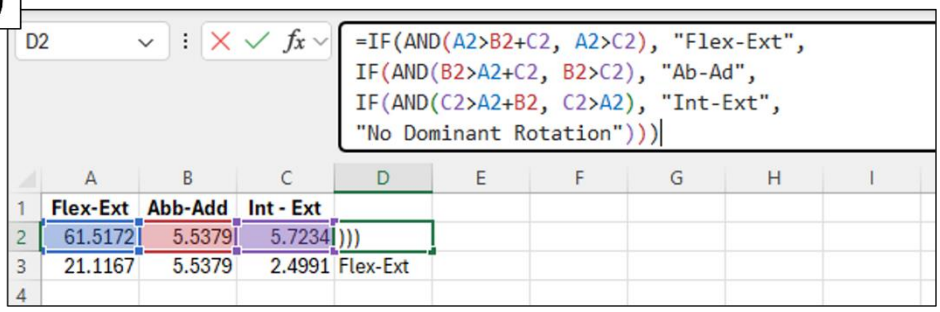

Figure 77: (a) Formula used to determine the dominant hip rotation based on amplitude comparison (a > b + c). (b) MATLAB code used to implement the dominance calculation in the computational model. (c) Equivalent hand-written Excel formula for verifying the MATLAB outputs.

The results obtained from both methods are summarised in Figure 78, demonstrating complete alignment between the two approaches. In the computational model, dominance was indicated by a logical output, where a value of 1 represented a true (dominant) result and 0 represented a false (non-dominant) result. These findings confirm that the computational model reliably identifies the dominant hip rotation and reproduces the same results as independently derived spreadsheet calculations.

a)

```
    5.0000   61.5172    5.5379    5.7234
    5.0000   21.1167    5.5379    2.4991
```

```
DominantRotations =

     1     0     0
     1     0     0
```

b)

Flex-Ext	Abb-Add	Int - Ext	
61.5172	5.5379	5.7234	Flex-Ext
21.1167	5.5379	2.4991	Flex-Ext

Figure 78: Comparison of results from the computational model and Excel verification for dominant hip rotation. Dominance is represented as a logical output, where 1 indicates a true (dominant) result and 0 indicates a false (non-dominant) result. Both methods produced identical outcomes, confirming the reliability of the computational approach.

4.6.2 Results from dominant hip rotation study

Seven out of ten activities showed dominance in the flexion–extension rotation, both during impingement and across the whole activity (Table 17). The remaining three activities, which were leg crossing and both golf swings, showed no clear dominance in any anatomical rotation in either case. Patterns of dominance were therefore consistent between the impingement window and the full activity cycle, with no activities switching from dominant to non-dominant or vice versa. Among the flexion–extension dominant activities, sit to stand demonstrated the greatest magnitude of dominance during impingement, with a ratio of 2.6:1. By contrast, the lowest ratio of flexion–extension dominance was observed in stand to sit, at 1:1.2. These results indicate that flexion–extension is the primary motion driving impingement across most activities, with sit to stand offering the clearest example of dominance in this direction.

Table 17: Average activity amplitude angle and dominant direction during impingement and throughout whole event. Colour coding in the last three columns shows wether the activity is dominant in accordance with the dominant direction formula. Green indicates a dominant direction and red not dominant.

Activity amplitude for impingement event (°)

Activity	Amplitude			Dominance			Magnitude (1 d.p)
	Flexion-Extension	Abduction-Adduction	Internal-External	F-E	A-A	I-E	
Stand to sit	23	5	7				1.2 : 1
Sit to stand	26	4	6				2.6 : 1
Leg crossing (seated)	27	11	39				1 : 1
Squat	24	5	7				2 : 1
Reaching down (standing position)	16	2	5				2.3 : 1
Reaching forwards (on knees)	28	5	9				2 : 1
Lunge	14	4	4				1.8 :1
Golf swing (trailing hip)	2	4	2				1 : 1
Cycling	25	6	13				1.3 : 1
Golf swing (leading hip)	8	12	11				0.6 : 1

Activity amplitude for whole trial (°)

Activity	Amplitude			Dominance			Magnitude (1 d.p)
	Flexion-Extension	Abduction-Adduction	Internal-External	F-E	A-A	I-E	
Stand to sit	69	9	14				3 : 1
Sit to stand	64	8	11				3.4 : 1
Leg crossing (seated)	35	12	47				1 : 1
Squat	77	11	13				3.2 : 1
Reaching down (standing position)	70	5	11				2.3 : 1
Reaching forwards (on knees)	64	6	15				3 : 1
Lunge	94	17	18				2.7 :1
Golf swing (trailing hip)	44	30	40				0.6 : 1
Cycling	44	11	20				1.4 : 1
Golf swing (leading hip)	30	36	57				0.9 : 1

4.6.3 Discussion of Dominant hip rotation

This study examined which anatomical rotation most strongly contributed to rim contact and whether that pattern was consistent between the impingement window and the whole activity. In seven of the ten activities, flexion extension was the dominant motion during impingement and across the full cycle, indicating that forward rotation of the femur relative to the acetabulum is the primary driver of cam contact in most tasks. Sit to stand showed

the highest dominance ratio (2.6:1), suggesting that flexion clearly governed the motion during impingement in this activity, whereas stand to sit showed only marginal dominance (1:1.2), reflecting a more balanced contribution of the three rotations. Leg crossing and both golf swings showed no dominant rotation, indicating that for some tasks impingement arises from more evenly distributed multi axis motion rather than from a single prevailing direction. These findings provide a basis for selecting flexion extension as the main rotational input for subsequent in vitro simulations, while recognising that some activities involve more complex motion paths.

This aligns with established descriptions of cam type FAI, where increasing flexion reduces anterior head neck clearance and initiates contact at the anterosuperior acetabulum (Tannast et al., 2007b). Although internal rotation was not identified as the dominant axis in this analysis, clinical and computational studies consistently report that flexion combined with internal rotation is a provocative movement pattern that increases local stresses at the cartilage labral junction (Beck et al., 2005; Chegini et al., 2009; Ng et al., 2012; Jorge et al., 2014). These comparisons suggest that the dominance patterns observed here reflect recognised impingement mechanics and support the use of a flexion based motion input for subsequent in vitro simulations. They also indicate that future rigs capable of incorporating controlled internal rotation may better capture the combined kinematic conditions associated with deep flexion tasks.

The dominance results also provide practical guidance for selecting activities for future experimental work. Activities with strong flexion dominance, such as sit to stand, could be more straightforward to reproduce in a uniaxial simulator, whereas activities without a clear dominant axis, such as leg crossing or the golf swings, may be less suitable for simplified in vitro reproduction. These tasks may instead warrant future simulator development that allows coupled rotations or complementary computational analyses to explore the combined kinematic pathways leading to impingement.

Several limitations are specific to the interpretation of rotation dominance. As dominance was defined using rotational amplitudes in anatomical planes, the measure reflects gross hip motion rather than the exact direction of cam travel relative to the acetabular rim. In addition, dominance describes which axis moves the most during impingement, but it does not indicate which direction produces the highest cartilage or labral stress. A rotation may

dominate the motion pattern without being the mechanically most damaging. Using a uniform idealised cam applied to healthy kinematic data may also alter the timing and relative contribution of each rotation compared with symptomatic cam populations, who frequently adapt their movement strategies. Finally, dominance is a kinematic measure and therefore should be interpreted alongside sliding distance and load when evaluating the mechanical severity of an activity. Despite these limitations, the findings provide a clear indication of which rotational axes are most influential and offer a strong rationale for selecting flexion based motion profiles in the subsequent in vitro simulations.

4.7 Discussion

The central aim of this chapter was to determine activity specific mechanical parameters that could be used to inform the design of subsequent in vitro simulations of cam type femoroacetabular impingement. By analysing sliding distance, peak load and dominant rotational direction across ten daily activities, this study derived quantitative ranges that reflect when and how impingement is most likely to occur during physiologically relevant movements. Collectively, these metrics provide a biomechanical basis for selecting representative loading and motion profiles for laboratory testing and offer new insight into the mechanical demands imposed on the hip during activities that challenge anterior clearance.

Across the three studies, several consistent themes emerged. Sliding distance varied substantially between activities, indicating that the extent of cam travel is strongly dependent on task requirements. Activities characterised by deep flexion, such as leg crossing and squat, produced the longest paths, while small excursion tasks generated shorter distances. Peak load also exhibited clear activity dependence, with sit to stand and squat producing the highest forces within the impingement window. These values fell within the upper range of loads reported in musculoskeletal modelling studies, supporting their physiological plausibility and their relevance for informing experimental loading inputs. Dominant rotational direction showed that flexion extension was the principal driver of rim contact in most tasks. These findings suggest that high mechanical demand during impingement is most likely when substantial cam travel coincides with elevated joint loading and when the hip approaches the combined motion patterns recognised clinically as provocative for cam morphology.

These metrics have direct implications for the development of the in vitro testing described in Chapter 3. The sliding distance ranges provide rotational excursions that can be reproduced experimentally, allowing the simulator to reflect activity relevant path lengths rather than relying solely on gait based values. The peak load results define a realistic spectrum of compressive forces for parametric testing, identifying loads that represent lower demand and those that are likely to amplify mechanical severity. The dominance results offer a principled rationale for adopting a flexion based uniaxial motion profile in the experimental setup, ensuring that the primary axis responsible for initiating impingement is represented even in a simplified simulation environment. These outputs enable the construction of controlled in vitro tests that are grounded in human movement data, improving the physiological relevance of the boundary conditions and strengthening the link between computational prediction and tissue level response.

The results also provide broader insight into activity specific mechanical demand in cam type FAI. Activities that combine long sliding distances with high forces and flexion dominated motion may present the greatest mechanical challenge at the cartilage labral junction. In contrast, tasks with short excursions or low loads are likely to be less mechanically severe even when rim contact occurs kinematically. While this study does not model tissue level stresses directly, the combined interpretation of the three metrics offers a qualitative indication of which movements may impose greater shear and compressive demand. Among the activities examined, sit to stand emerged as a particularly relevant candidate for further investigation. It consistently produced high peak loads, demonstrated clear flexion dominated motion, and aligned these loads with the impingement window, making it both mechanically demanding and feasible to reproduce in a uniaxial testing environment. Squat also demonstrated long excursions and flexion extension dominant patterns, suggesting potential relevance for future work using more advanced simulators capable of coupled rotations. These distinctions may help guide the design of targeted in vitro or computational studies aimed at identifying mechanical thresholds associated with early surface damage.

Several broader limitations should be considered when interpreting the metrics developed in this chapter. The analyses were based on healthy volunteer data and an idealised cam morphology. These choices allowed controlled comparison across activities, but they inevitably simplify the range of anatomical variation and movement adaptations seen in symptomatic populations. As a result, the onset and severity of impingement identified here

may differ from that experienced by individuals with clinically diagnosed cam morphology. Using a rigid-body model also meant that cartilage and labral deformation, capsular constraint and joint translation were not modelled. While this approach was necessary to ensure stable, reproducible simulations across ten activities, it does limit direct inference about tissue level mechanics.

Additional methodological considerations apply across the chapter. In some activities, incomplete data for certain subjects led to averaging at the activity level, reducing visibility of between-subject variation, particularly in tasks with sparse datasets. A single pelvic orientation was applied to all subjects, which does not capture variation in pelvic tilt or version that can influence impingement onset during deep-flexion tasks. The impingement detection algorithm operated with a discrete spatial and angular resolution (approximately 1 mm or 1 degree), which may influence the precise timing of contact.

Overall, the findings from this chapter establish a physiologically grounded set of boundary conditions for the experimental work that follows. By incorporating activity specific motions and loads, the subsequent in vitro simulations can more accurately reflect the mechanical environment associated with impingement and provide a clearer understanding of the parameters most likely to contribute to tissue level damage.

Chapter 5

5 Parameterised experimental natural hip testing: the effects of sliding distance and load

5.1 Introduction

Cam-type femoroacetabular impingement (FAI) produces characteristic patterns of joint damage, yet the translation from mechanical conditions to observable tissue-level changes remains difficult to establish. Computational modelling, as presented in the previous chapter, identified ranges of sliding distance, load, and direction associated with impingement during activities of daily living. However, while computational models are effective in defining mechanical boundary conditions, they cannot replicate the biological complexity of cartilage–labrum interactions. Experimental simulation was therefore required to determine whether the predicted conditions could generate clinically relevant patterns of damage in natural tissue.

The overall aim of this chapter was to experimentally assess whether parameters predicted computationally to cause hip joint damage could be reproduced and observed in vitro using natural tissue simulation. Building on the methodological framework developed in Chapter 3 and the parameter ranges established in Chapter 4, this study applied selected extremes of sliding distance and load to porcine hip joints within the physical constraints of the simulator. Direction of sliding was not re-examined, as prior experimental work had already shown that parallel motion was most representative of clinically relevant damage and aligned with computational predictions of flexion–extension as the dominant hip rotation.

The specific objectives of this chapter were to:

- Develop and apply an improved photogrammetry method for reliably documenting cartilage surface damage.
- Justify and apply computationally derived ranges of sliding distance and load within feasible simulator limits.
- Experimentally evaluate the influence of sliding distance and load on cartilage damage patterns.
- Identify the strengths and limitations of this parameterised experimental testing approach in replicating clinically relevant damage mechanisms.

This chapter represents the first application of computationally derived ranges to natural hip tissue, forming a critical link between earlier method development and the integrated experimental–computational protocol explored in the next chapter.

5.2 Development of a “photography fixture”

This section details the modifications made to the photogrammetry method, the setup of the parameterised in vitro tests, and the rationale behind the chosen experimental parameters. Due to simulator limitations, it was not possible to carry out testing across the full range of computationally derived parameters. The modifications applied to the experimental protocol and the resulting test matrix are explained, along with the reasoning behind the selected parameter combinations.

The aims of this section are:

- To describe the development of a repeatable photogrammetry setup to capture damage on the articulating surface of the acetabulum reliably.
- To justify the selection of sliding distance and load parameters for in vitro testing based on computationally derived ranges and previous experimental findings.
- To present the final parameterised test matrix and explain modifications made due to physical constraints of the simulator and tissue limitations.

Samples were all cemented at an inclined angle and then photographed from above. Initial testing showed that only a partial view of the acetabular surface was visible, which limited the analysis that could be completed using the photos (Figure 79a). To address this, the inferior portion of the cemented cup holder was raised so that the labral edge of the sample was parallel to the camera lens (Figure 79b). This adjustment provided a clearer and more consistent view of the articulating surface (Figure 79c).

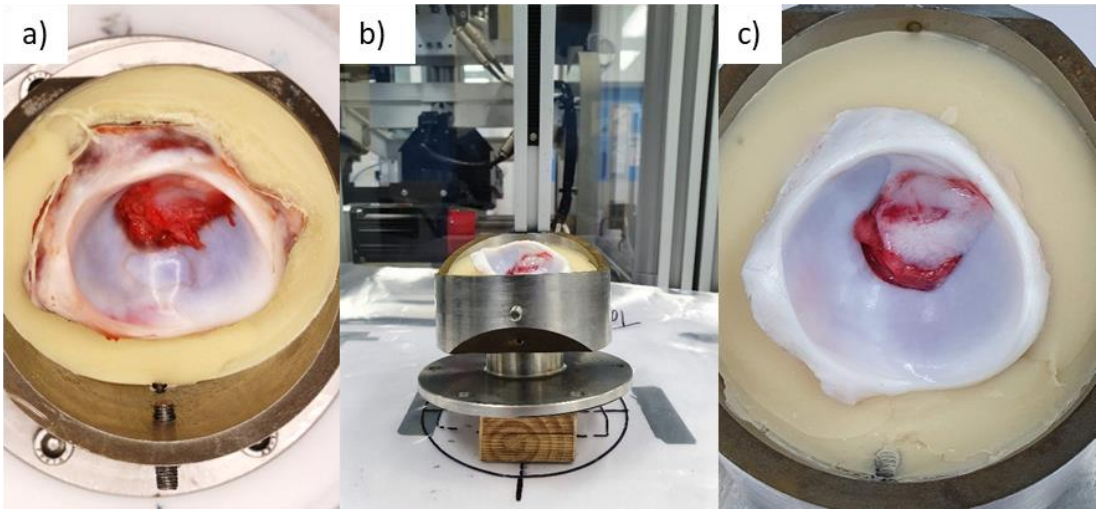

Figure 79: a) Samples were cemented at an inclined angle, and as such, parts of the articulating surfaces were obstructed in resultant images. b) The initial solution was to raise the inferior edge of the cup holder so that the labral edge was parallel with the camera lens. c) Inferior edge of the cup holder was lifted, and the overall view of the sample was more complete.

While this adjustment improved visibility, a dedicated fixture was required to provide repeatable control of sample orientation and camera positioning. Without such a fixture, image quality would remain dependent on improvised adjustments and operator judgement.

To achieve a reliable and repeatable solution, a dedicated photography fixture was developed. The fixture was designed to meet specific requirements that ensured consistent image quality while accommodating the constraints of the experimental setup. These requirements were translated into measurable design specifications and solutions (Table 18).

The main constraints included:

- Compatibility with the existing cup holder, which needed to be securely mounted without modification.

- Stability under the combined weight of the cemented sample and cup holder (approximately 1.7kg).
- Limited available space in the photography area, requiring a compact design.
- The need for cleaning between tests to avoid contamination.

The primary aim of improving image quality was addressed through specifications that focused on controlling sample angle, sample-to-camera distance, stability, and illumination.

Table 18: Design requirements, measurable specifications, and design solutions for a photography fixture.

Design Requirement	**Measurable design specification**	**Design solution**
Adjustable angle to correct for sample inclination	Range of 0–45° with secure locking at set positions	Angle adjustment mechanism with 5° and 10° guides for repeatable positioning
Secure attachment of the existing cup holder	The cup holder must remain stable with no visible movement or tilt	Existing mounting holes in the cup holder for precise positioning and secure fastening
Optimise image resolution and field of view	Vertical height of at least 20 cm; sample-to-light source distance ~70 cm	Fixture height set to bring the sample closer to the LED light source, improving illumination and focus
Stability under load	Base must remain stable with no tilt under a 1.7 kg load (weight of uncemented cup holder)	Increased base width and weight distribution to ensure stability
Ease of cleaning	Fixture to be made of corrosion-resistant, non-porous material	Manufactured from stainless steel for durability and rapid cleaning

Fixtures were designed using SolidWorks and manufactured in-house. A 3D render of the final design is shown in Figure 80, and the manufactured photography fixture is shown in Figure 81. Drawings of the fixture can be found in Appendix 8.4.

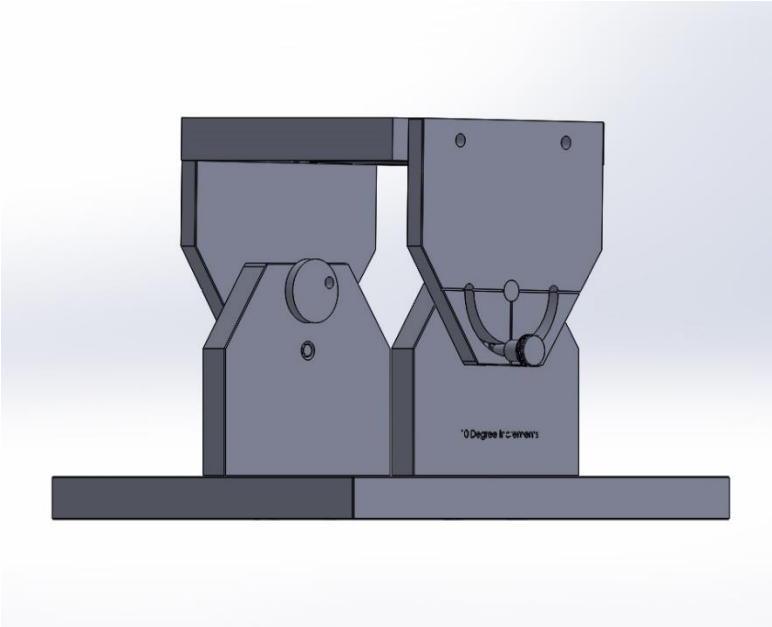

Figure 80: 3D render of photography fixture.

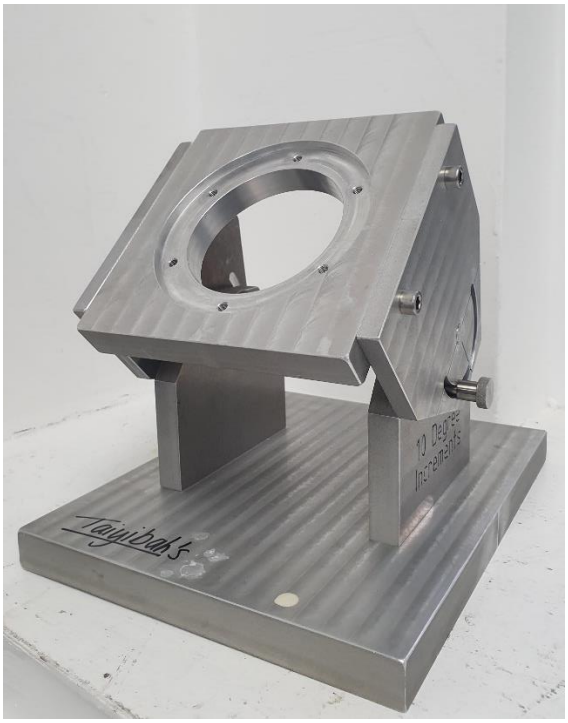

Figure 81: Photograph of the photography fixture.

The final fixture met all design specifications. The angle adjustment mechanism provided secure and repeatable positioning, enabling consistent photographic perspectives. The increased height ensured correct positioning relative to both the camera and the light source, improving resolution and illumination. The stainless steel construction allowed rapid cleaning without surface degradation from surface cleaners used to prevent cross-contamination with animal tissue, and the fixture remained stable under the full load of the sample and cup holder. These outcomes confirmed that the fixture successfully addressed the initial limitation of partial surface visibility and achieved the objective of producing consistent, high-quality images suitable for detailed surface analysis.

5.3 Rationale for simulator input settings and parameter justifications

This section details the rationale and methods used to define the simulator input parameters for in vitro testing. Each key parameter: motion direction, load, and sliding distance, was considered in turn, with decisions guided by computational predictions, previous experimental findings, and the mechanical limits of the simulator and porcine tissue.

Tests were designed using parameters considered to cause damage, informed by previous experiments (Chapter 3) and computational findings (Chapter 4) (Table 14). Each set of test parameters was intended to be compared to the Refined Control conditions defined at the end of Chapter 3. Due to simulator limitations, it was not possible to complete all the original tests proposed. Additional experimental cases were conducted to determine the simulator's limitations and establish a final set of parameters.

Table 19: Original proposed matrix of testing parameters as informed by experimental and computational findings. Each set of test parameters (white) would have been compared to the Refined Control conditions (green).

Sliding distance	Inclination angle (°)	Load (N)		
		1500N	2000N	2500N
+/-10° +1mm ML Dis	35°	(Refined Control conditions) H		
+/-2° +1mm ML Dis	35°			
+/-40° +1mm ML Dis	35°			

The experimental setup followed the same approach described in Chapter 3, including the cementation of porcine femoral heads, simulator configuration, and specimen preparation. Damage assessment employed the same methodology as described in Chapter 3 (Section 3.3.2). A dedicated photography fixture was introduced to improve consistency and image quality.

5.3.1 Direction of sliding

The direction of sliding was not further investigated in this chapter. Findings from the previous studies indicated that movements parallel to the cartilage labral junction were most likely to lead to damage, producing delamination compared with blushing for perpendicular movements. Computational work in Chapter 4 demonstrated that flexion-extension was the dominant rotation during impingement. In vivo movements parallel to the cartilage-labral junction are aligned with flexion extension, whereas perpendicular movements align with abduction adduction. Based on this information, flexion extension dominant motion was used throughout testing.

5.3.2 Load scaling and selection

5.3.2.1 Human to porcine scaling method

Simulator input loads were defined using outputs from the computational model. These were reported as a proportion of body weight; therefore, conversion was required before they could be used as simulator inputs.

To define physiologically relevant load inputs for porcine testing, human activity loads derived from computational findings were scaled according to the approach described in Chapter 3. Loads from the computational model were originally output as a proportion of body weight and could not be used directly as inputs for the simulator. Using the average weight of an FAI participant derived from the literature (75.7 kg; Table 20), these values were converted into absolute human loads (Table 21).

Table 20: List of heights and weights for FAI participant groups from literature.

Reference	Height (cm)	Weight (kg)
(Diamond et al., 2016)	175.6	75.5
(Savage et al., 2021)	180	75.4
(Malloy et al., 2019)	170	76.3
	Average	75.7

Table 21: Converted human and porcine loads for the average activity during impingement and maximum load for a subject for a set of activities.

Activity	Average activity load (N)		Max. subject load (N)	
	Human	Porcine	Human	Porcine
Sit to stand	4756	1427	8506	2552
Squat	3193	958	5077	1523
Stand to sit	3098	929	4056	1217
Reaching down (standing position)	2615	785	4583	1375
Lunge	2276	683	3822	1147
Reaching forwards (on knees)	351	105	526	158

To generate porcine-equivalent loads, a scaling factor of approximately 33.33% was applied to the human loads. This factor was derived from Chapter 3 (Section 3.4.2.1), where the peak load estimated for porcine walking (~900 N) was compared with a representative human peak load commonly used in ISO-standard hip implant testing (~3,000 N) (ISO 14242). Applying this ratio to the human activity loads provided a practical and physiologically reasonable approximation of porcine loads across different motions.

The input peak loads were derived from the ISO gait profile, commonly used for testing artificial hip implants, and scaled for porcine tissue. While the use of a single scaling factor does not account for activity-specific differences in motion speed or joint mechanics, it preserves the relative differences in load magnitudes between activities. The potential limitations of applying a gait-derived scaling factor to non-gait motions are acknowledged, but this method was considered the most appropriate given the available data and ensured that the simulator inputs remained within the mechanical limits of porcine tissue.

All human load data were normalised to a gait cycle. Therefore, information about the actual speed of activities was not available. The hip simulator operates in accordance with ISO 14242, which specifies a frequency of 1Hz to replicate cyclical human gait. Although this profile is designed primarily for implant testing rather than natural tissue, no equivalent standard exists for natural tissue-based studies, and it was therefore adopted here as a suitable alternative. All simulations were performed at this fixed frequency of 1Hz. This provided physiologically relevant loading conditions while ensuring consistent cyclic input across tests, allowing reliable comparisons between conditions and minimising the potential influence of time-dependent tissue degradation.

5.3.2.2 Load selection for testing

Findings from previous experimental tests have shown that increasing load resulted in a more progressive type of damage to the joint. Therefore, when selecting parameters for testing, only loads greater than the Refined Control (1500N) were chosen. None of the converted average activity porcine loads exceeded the Refined Control. Therefore, maximum subject loads were investigated. One activity demonstrated a higher load than the Refined Control, sit to stand (~2500N). This load was used in this study as it was representative of the maximum load possible across a selection of activities.

5.3.3 Sliding distance feasibility and planned ranges

Sliding distances were taken from outputted computational values. The maximum and minimum values were chosen because they represented the most extreme scenarios possible, and if damage were to occur, it would likely be at these two points. The maximum sliding distance was 81° for the leg crossing activity and the minimum sliding distance was 4° for the trailing golf swing. Due to simulator limitations, a sliding distance of 81° was not possible and would have resulted in impingement between the edge of the femoral head and the acetabular cup fixtures. This was observed when using the 'jog' function of the simulator to manually increment the rotation of the femoral head setup in controlled steps. Using this function, it was possible to define the maximum rotation angle before impingement occurred. The longest sliding distance possible was 70° (±35° in the simulator).

For testing, two sliding distances were therefore selected: 35° to represent the maximum achievable in the simulator, and 5° to represent the minimum achievable.

5.4 Initial Results from defined parameters

This section presents the initial in vitro results obtained from testing the parameter set defined in Section 5.3. A load of 2500N and sliding distances of ±35° and ±5°, oriented parallel to the cartilage–labral junction, were selected for initial testing based on the computational outputs. The aim of this stage was to assess the feasibility of these parameters within the constraints of the hip simulator and to refine the test conditions accordingly. Subsection 5.4.1 reports the outcomes of feasibility testing at high sliding distances and load, and the challenges presented. Subsection 5.4.2 describes the subsequent moment analysis used to identify a more practical sliding distance, while Subsection 5.4.3 summarises the final modified parameter set that was carried forward into the main testing.

5.4.1 Feasibility of testing within simulator constraints

Initial testing at a sliding distance of ±35° and a load of 2500 N resulted in sample failure (Figure 82). Cracking at the femoral shaft occurred at the cement mantle, leading to off-centre loading and subsequent dislocation of the femoral head. As shown in Figure 82c and

d, this caused a large indent and ridge to form along the femoral head cartilage surface where it came into contact with the cement mantle. On the acetabular side (Figure 82e), post-test inspection revealed cracking of the cement mantle at the inferior edge (Figure 82f), which destabilised the sample and exposed the cement mantle at the superior edge (Figure 82f). This exposure led to direct contact between the femoral head and the cement mantle, producing the observed damage to the articulating surface (Figure 82c & d). Cracking was initially attributed to the higher speed required to achieve the longer sliding distance at 1 Hz, which generated greater vibration and a tendency for anterior-posterior displacements.

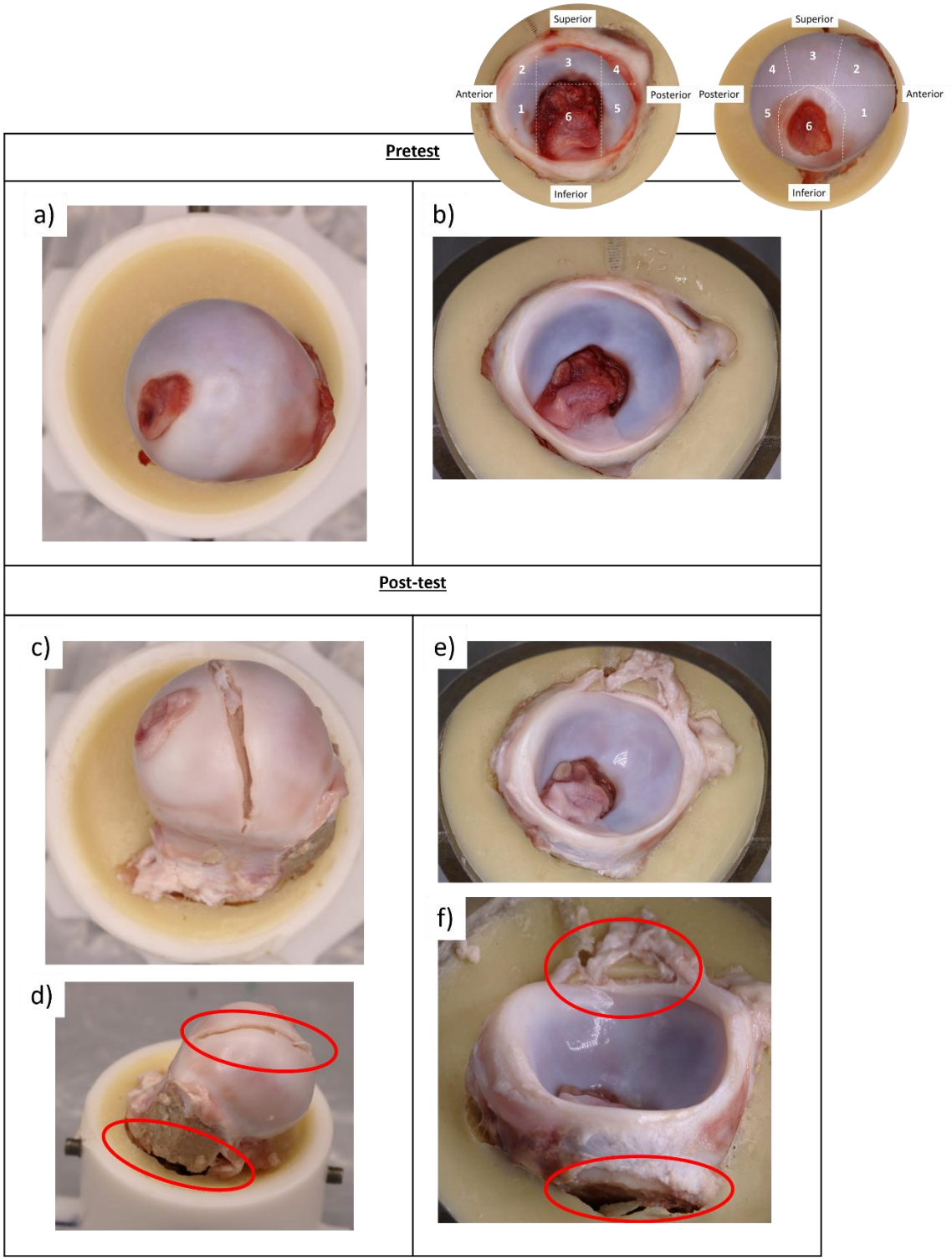

Figure 82: Pre- and post-test findings at ±35° sliding distance and 2500N load. Pre-test images show the intact femoral head (a) and acetabulum (b). Post-test, the femoral head displayed an indent and surface ridge from cement mantle contact (c,d). At the same time, the acetabulum showed cracking at the inferior edge and exposure of the cement mantle superiorly (e,f), leading to head–cement contact and sample dislocation.

The simulation frequency was reduced from 1 Hz to 0.5 Hz in an attempt to mitigate this effect. While vibration was reduced at the lower frequency, visible AP displacement persisted, and cracking of the femoral shaft still occurred. The extended simulation time (8 hours) at this frequency may also have contributed to tissue degradation, suggesting that vibration alone may not be the sole cause of the observed failure.

To further assess the effect of motion range, an additional test was carried out at a reduced sliding distance of ±20°. This value was chosen as it represented the longest sliding distance previously achieved without failure. Testing at ±20° provided a more stable set-up, defined here as reduced vibration and reduced observable AP displacement. A reduction in displacement was observed, but cracking at the femoral shaft was again apparent at the two-hour inspection point.

The reduced sliding distance test was also of methodological importance, as these data were subsequently used to calculate the moment in Section 5.4.2.

5.4.2 Moment analysis and selection of final sliding distance

Moments were calculated for failed and successful simulations, including the Refined Control conditions, to guide the selection of a feasible sliding distance (Figure 83). This analysis was required because the feasibility tests (Section 5.4.1) demonstrated that fracture of the femoral shaft and instability of the cement mantle limited the achievable motion range. Therefore, a more systematic approach was needed to define conditions that could be successfully simulated. In this context, the “longest sliding distance without risk of fracture” refers to the maximum distance achieved in previous tests that did not result in shaft cracking or destabilisation of the sample.

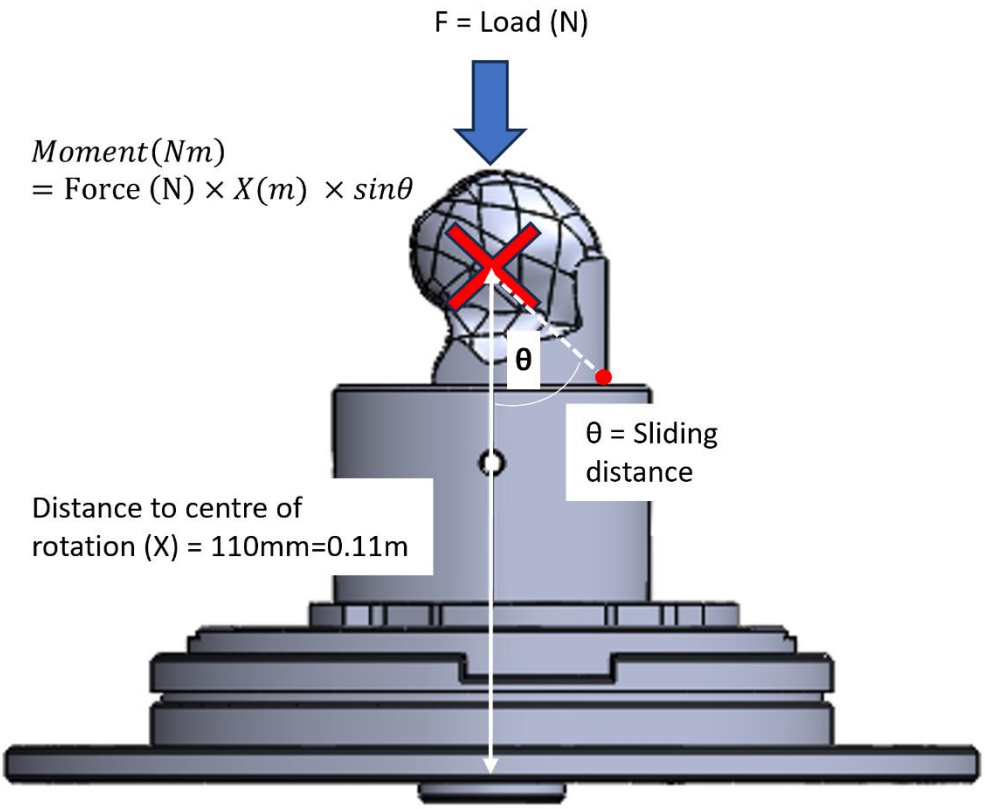

Figure 83: Diagram of femoral head setup in simulator, used to illustrate inputs for moment calculations.

Failed simulation at ±35° produced a moment of 158Nm at 2500N, while the Refined Control condition (±10°, 1500N) from earlier work produced 29Nm (Table 22). The longest previously successful sliding distance identified in earlier work was ±20°, which, at a reduced load of 1130N, produced 43Nm. However, when the same condition was attempted experimentally at 2500N in the present study, shaft cracking again occurred, and the calculated moment rose to 94Nm. This confirmed that the previously defined "longest successful" condition could not be reproduced under higher loading. A sliding distance of ±15° produced a moment of 71Nm, which was lower than the failed tests but higher than previously successful values, and was therefore selected as a practical compromise to define the modified testing setup. The choice of ±15°, rather than intermediate values such as ±17° (80Nm) or ±12° (57Nm), reflected a pragmatic, stepwise approach that minimised the number of pilot studies required.

Table 22: Findings of moment arm calculations, used to determine appropriate sliding distances for use in experimental testing. Green represents previous successful tests completed, Red represents tests that failed and Grey represents the sliding distance length to test.

(f) Force	1500	1130	2500	2500	2500	2500	2500	2500	2500
(x) Distance to centre of rotation	0.11	0.11	0.11	0.11	0.11	0.11	0.11	0.11	0.11
(θ) Sliding Distance	10	20	5	10	12	15	17	20	35
Moment (Nm)	29	43	24	48	57	71	80	94	158

To further explore whether moments could be reduced by lowering load instead of reducing motion range, additional values were calculated at 2000N (Table 23). At this load, moments ranged from 57Nm at ±15° to 126Nm at ±35°. Notably, ±25° at 2000N produced 93Nm, a value very close to the 94Nm observed for ±20° at 2500N. This indicated that although lowering the load allowed a wider motion range, the benefit in terms of reducing moments was minimal. At the lower end, ±15° and ±20° at 2000N produced 57Nm and 75Nm, respectively, suggesting that these conditions could have been viable alternatives to the selected 2500N ±15° condition.

Table 23: Calculated moments at a reduced load of 2000N across different motion ranges.

(f) Force	2000	2000	2000	2000	2000
(x) Distance to centre of rotation	0.11	0.11	0.11	0.11	0.11
(θ) Sliding Distance	15	20	25	30	35
Moment (Nm)	57	75	93	110	126

However, the study objective was to examine damage under near-maximum physiological loads. While there was a valid argument to adopt ±20° at 2000N, the overall direction of the work was to prioritise higher loading as this was more strongly associated with the onset and progression of cartilage damage (Chegini et al., 2009; Jorge et al., 2014; Ng et al., 2012; Alonso-Rasgado et al., 2012; Hellwig et al., 2016). Thus, the decision was made to retain 2500N and reduce the sliding distance, rather than reduce the load to increase the range of motion. This ensured that the subsequent in vitro findings reflected high-load damage mechanisms as closely as possible, while remaining within the mechanical constraints of the simulator.

5.4.3 Findings from Initial Parametric Tests

Initial feasibility testing demonstrated that a sliding distance of ±35° at 2500N resulted in sample failure, primarily due to femoral shaft cracking and disruption of the cement mantle. Moment analysis confirmed that longer sliding distances at this load generated excessively high moments, with failed simulations producing values of 158Nm (±35°) and 94Nm (±20°). By comparison, the longest previously stable condition (±20°) produced 43Nm. A sliding distance of ±15° was therefore selected as a compromise, balancing physiological relevance with mechanical stability. Selecting ±15° ensures that subsequent experiments capture cartilage and labral damage mechanisms that occur under near-maximum physiological loads, rather than being influenced by artefacts from sample failure. This compromise preserves high load relevance while avoiding excessive mechanical stress that could invalidate results or cause structural failure.

The final matrix of testing parameters (Table 24) was developed from this selection. In the next section, each set of test conditions was compared with the Refined Control condition, allowing for a systematic investigation of the effects of sliding distance, load, and inclination angle on cartilage and labral damage.

Table 24: Final matrix of testing parameters used in in vitro simulations; letters denote test code. Each set of test parameters (white) was compared to the Refined Control condition (green).

Sliding distance	Inclination angle (°)	Load (N)		
		1500N	2000N	2500N
+/-10° +1mm ML Dis	35°	(Refined Control conditions) H		J
+/-5° +1mm ML Dis	35°			K
+/-15° +1mm ML Dis	35°			L

5.5 Application of the Final Parametric Testing Matrix

Using the Modified parameter set defined in Section 5.4.3 and the Refined control parameters from Chapter 3, this section presents in vitro results exploring the effects of load and sliding distance on acetabular surface damage. The study systematically evaluates how these parameters influence damage severity and distribution under near-physiological conditions, which are achievable within the simulator.

5.5.1 Effect of load

The Refined Control conditions (H, 1500N) were compared with Condition J, which was identical apart from the increased load of 2500N derived from the computational outputs. At 1500N (H1–3), early signs of “bubbling initiated” were observed, where small bubbles were beginning to form. At 2500N (J1–3), bubbling became more clearly defined, representing a more advanced stage of damage progression compared to blushing (see Section 3.3.2). Increasing the load, therefore resulted in more pronounced surface damage, although the overall difference between 1500N and 2500N was limited. As a result, testing at 2000N was not undertaken, and sliding distance conditions were evaluated at 2500N (Figure 84).

Inclination Angle 35°	Axial Load (N)			
	1500		2500	
Sliding distance +/- 10° + 1mm lateral displacement	H	H1 - Blushing/ Bubbling initiated H2 - Bubbling H3 Blushing/ Bubbling initiated	J	J1- Blushing/bubbling J2 – Blushing/ bubbling J3- Blushing/ bubbling.
	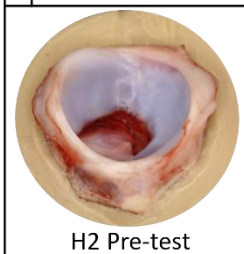 H2 Pre-test	 H2 Post-test	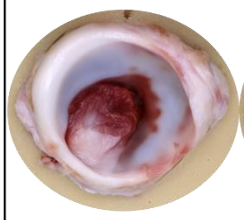 J3 Pre-test	 J3 Post-test

Figure 84: Photogrammetric results, increasing load comparison from 1500N to 2500N, change in observed blushing and bubbling.

5.5.2 Effect of sliding distance

Two sliding distances were compared: ±5° and ±15° (Figure 85). The shorter distance (±5°) produced apparent bubbling, representing a more advanced stage of damage progression (Figure 86a). In contrast, the longer distance (±15°) resulted in larger areas of blushing, with only bubbling initiation observed, indicating an earlier stage in the damage sequence (Figure 86b).

Inclination Angle 35°	Sliding distance (+ 1mm lateral displacement)			
	+/- 5°		+/- 15°	
Axial Load (N) 2500	K	K1 – Blushing/ Bubbling K2 – Blushing/ Bubbling K3 – Blushing/ Bubbling	L	L1 – Blushing. L2 – Blushing/Bubbling initiated L3 – Blushing/Bubbling initiated
	 K1 Pre-test	 K1 Post-test	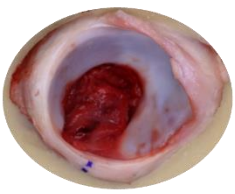 L2 Pre-test	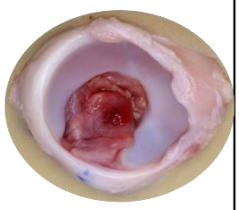 L2 Post-test

Figure 85: Photogrammetric results: Comparison of observed damage between extremes of sliding distance at 2500N. Shorter sliding distances showed more blistering, whereas longer sliding distances resulted in a larger spread of blushing.

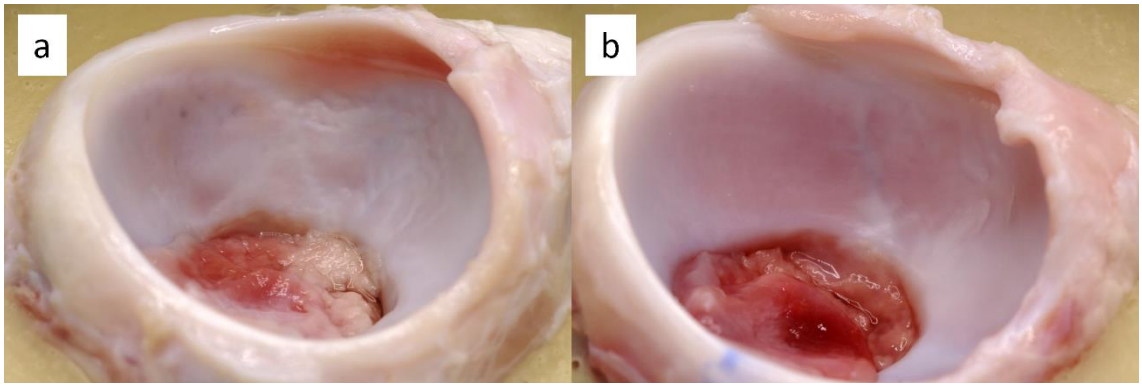

Figure 86: Close-up photogrammetric result of extreme sliding distance findings. a) (sample K1) Short sliding distance ±5°, with very prominent blistering. b) (sample L2) Long sliding distance ±15° greater area of blushing.

5.5.3 Incidences and type of zonal damage

Zonal analysis was conducted using the method described in Chapter 3 (Section 3.4.3.4). For each sample, the presence and type of damage were recorded within each zone, with incidence points assigned per damage type.

Damage was localised to Zones 2, 3 and 4, with no incidences observed in Zones 1, 5 or 6 (Figure 87). The highest frequency of damage was observed in Zone 3 (22 incidences), followed by Zone 2 (11 incidences) and Zone 4 (6 incidences). When considered by damage type, blushing was present across all affected zones (Zones 2–4). In contrast, delamination (or bubbling) was observed only in Zones 3 and 4, with the greatest contribution in Zone 3. Zone 2 showed blushing only, with no evidence of more advanced damage types.

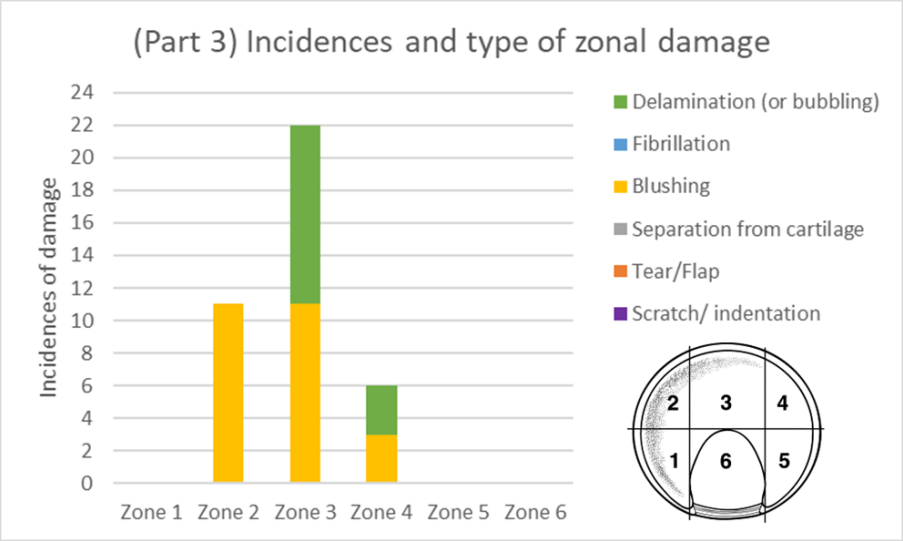

Figure 87: Distribution of acetabular damage in Part 1 testing, reported using the Ilizaliturri et al. (2008) zonal method. Each occurrence of damage was assigned one point per affected zone for each identified damage type. Where multiple damage types co-occurred within a zone, each was counted separately. Incidences per zone: Zone 1 = 0, Zone 2 = 11, Zone 3 = 22, Zone 4 = 6, Zones 5 and 6 = 0.

5.5.4 Findings and implications

The modified photogrammetry method was successfully implemented for the parameterised tests and provided clear, repeatable images of the acetabular surface. This enabled damage descriptors such as blushing and bubbling to be compared systematically between load and sliding distance conditions. The method retained sufficient sensitivity to detect subtle surface changes while remaining practical for use after extended simulation.

The findings from the parameterised tests showed that increasing load within the refined setup led to more advanced surface changes, but did not alter the fundamental type of damage observed. At 1500N, the Refined Control condition produced consistent blushing with occasional bubbling. When load was increased to 2500N, bubbling became more prominent and involved a larger area of the articular surface, although tearing or large-scale delamination was not observed. This suggests that, within the range tested, porcine acetabular cartilage can tolerate higher compressive loads without transitioning to gross structural failure, but that elevated load increases the likelihood and extent of early surface disruption.

Varying sliding distance produced clearer differences in the distribution and character of damage than load alone. Short sliding distance (±5°) resulted in more focal, intense changes, with blushing and bubbling concentrated over a relatively small region. In contrast, the longer sliding distance (±15°) generated a broader spread of blushing but fewer bubbling lesions, indicating a more diffuse but less advanced pattern of damage. These observations are consistent with the notion that shorter excursions maintain rim contact over a smaller area, potentially increasing local shear demand, whereas longer excursions distribute loading over a wider contact region and may reduce peak local stresses.

Zonal analysis further demonstrated that these changes in damage severity were also spatially organised. Damage was consistently localised to the anterosuperior region of the acetabulum (Zones 2–3), with additional involvement of Zone 4. The highest frequency of damage was observed in Zone 3. When considered alongside damage type, a clear pattern of co-localisation was observed. Blushing was present across Zones 2–4, whereas bubbling (delamination) was restricted to Zones 3 and 4, with the greatest concentration in Zone 3. This indicates that while early-stage surface changes occur across a broader contact region, progression to more advanced damage remains spatially confined to Zones 3 and 4.

The achievable sliding distances were restricted by the mechanical limits of the simulator and the strength of the mounting configuration. Larger angular excursions risked excessive moment generation at the fixture interfaces, which could lead to shaft cracking or disruption of the cement mantle. These constraints meant that only a subset of the computationally derived sliding distances could be reproduced in practice, reinforcing the importance of aligning theoretical parameter ranges with realistic simulator capabilities. An additional consideration was the inherent coupling between sliding distance and cycle characteristics: altering excursion without adjusting total cycle time inevitably changes angular velocity, and therefore sliding speed, even when the focus is nominally on distance alone. The tests in this chapter were designed to minimise these effects, but they highlight that speed and distance cannot be completely isolated in a cyclic simulator environment.

Overall, these findings demonstrate that both load and sliding distance influence the severity and distribution of surface damage, but that single-parameter extremes alone do not replicate the more complex combinations of factors present in vivo. Instead, the results help define a practical envelope of mechanical conditions within which natural tissue testing can

be conducted safely, while still generating meaningful and progressive changes in cartilage surface appearance.

5.6 Discussion

This chapter demonstrated that parameters derived from computational modelling can be applied experimentally to natural hip tissue to assess their influence on cartilage damage. The results showed trends in how load and sliding distance affected the severity and distribution of surface damage, and also highlighted the practical constraints involved when translating theoretical parameter ranges to an in vitro setting.

A central finding was that increasing load from 1500N to 2500N amplified the progression of observable surface changes but did not introduce fundamentally new damage types. At both load levels, blushing and bubbling remained the dominant descriptors, yet bubbling became more frequent and extensive at 2500N. This suggests that higher compressive forces increase the likelihood of fluid exudation and local matrix disturbance in the superficial zone, consistent with the behaviour of cartilage under elevated stress. However, the absence of tearing or large-scale delamination indicates that the tested load range remained below the threshold required to produce gross structural separation in this porcine model. In this way, the load comparison helps to identify a safe but mechanically challenging range for future studies that wish to probe the onset of more advanced damage.

The effects of sliding distance were more distinct. Short sliding distance produced damage that was more localised and, in some samples, more advanced, with concentrated areas of blushing and bubbling. Longer sliding distances, by contrast, generated a wider spread of blushing but little evidence of bubbling. This pattern suggests that when the cam travels through a small angular excursion, contact is maintained over a smaller region of the acetabular rim, increasing local mechanical demand during extended cycling. When the excursion is larger, the contact is spread over a larger area, which may reduce peak local shear and limit the progression from blushing to bubbling. These findings support the interpretation that sliding distance is a critical factor in determining how shear is distributed across the surface during repeated impingement.

The results emphasise that load and sliding distance interact to shape the damage response. High load alone did not create new damage types, and long sliding distance alone did not necessarily prevent surface change. Instead, the combination of higher load with shorter sliding distance appeared to be the most effective at generating progressive surface disruption within the constraints of the simulator. This interaction echoes the broader theme from the earlier chapters, where no single parameter fully explained the risk of damage and where combinations of motion, load and contact path were more informative.

The practical limitations of the simulator played an important role in constraining the parameter space. Achievable sliding distances were limited by fixture strength and the allowable moment at the shaft–cement interface, which meant that some of the longer excursions suggested by the computational model could not be implemented without risking failure of the setup itself. Similarly, the cyclic nature of the test meant that changes in sliding distance inevitably altered sliding speed unless cycle time was adjusted. Although the study aimed to focus on distance, it is important to recognise that small changes in speed accompany changes in excursion, and these may contribute to the observed trends.

There are also biological and anatomical considerations. The porcine acetabulum provides a convenient, accessible model with broadly human-like geometry, but the juvenile nature of the specimens and differences in chondrolabral structure mean that the response to repeated loading may not replicate that of mature human tissue. The tests did not include capsular restraint or active muscular stabilisation, and motion was constrained to a single axis, so the complex multi-planar movements seen in clinical impingement could not be fully represented. These factors may help explain why the damage remained confined to the cartilage surface and did not progress to more complex failure patterns at the chondrolabral junction.

Furthermore, the trends observed in this study offer helpful insights, but the strength of the evidence is limited. Only three specimens were tested per condition, and damage was assessed visually with photogrammetry rather than with histological or pressure-based techniques. These limitations reduce the extent to which findings can be generalised. Nonetheless, the consistent patterns across samples replicates suggest that the reported effects are meaningful within the tested framework.

Despite these limitations, the chapter demonstrates that computationally derived parameter ranges can be translated into feasible in vitro simulations and used to systematically examine the effect of load and sliding distance on early cartilage damage. The results define a set of mechanically challenging but realistic test conditions and highlight the importance of short sliding distance combined with higher load in driving surface-level changes under extended impingement. This provides a useful platform for future work, which may build on these findings to investigate different tissue types, more complex motion patterns or longer-term degeneration, and to further refine our understanding of how specific mechanical factors contribute to early joint damage in cam-type femoroacetabular impingement.

Chapter 6

6 Discussion

6.1 Introduction

The aim of this thesis was to develop and apply complementary experimental and computational methods to investigate how relevant mechanical parameters influence damage at the chondrolabral junction in cam type femoroacetabular impingement. The intention was to move beyond broad assumptions about joint loading and instead examine specific features of movement and force that may contribute to early tissue failure. Understanding these relationships are important because clinical symptoms of cam type impingement often emerge only once degenerative changes are well established, and earlier insight into the mechanical drivers of damage may support prevention, treatment planning, and patient management.

This work introduces novelty in both approach and focus. While previous natural tissue studies have often relied on limited motions or manual positioning, this study applied a controlled, multi-axis simulation to systematically vary load, motion, and direction. A computational cam impingement model was used to identify physiologically relevant parameter ranges during impingement, which were then applied experimentally, linking relevant hip load and motion parameters to the damage responses observed in natural tissue. Furthermore, sliding distance, a parameter previously used in artificial joint testing (Bennett et al., 2002), was adapted for natural hips, providing a new way to quantify contact between the cam and acetabular cartilage. By integrating computational modelling of cam type impingement with experimental testing on natural tissue, this work offers a novel framework for investigating femoroacetabular impingement.

The work achieved the planned objectives through the development and application of combined experimental and computational methods. A repeatable in vitro approach was established, enabling controlled variation of direction, loading and motion, together with a reliable method for documenting surface changes at the cartilage labral junction. Computational modelling of cam type impingement was then used to determine activity specific ranges of sliding distance, load, and motion direction, identifying conditions most likely to place the joint at risk of damage.

Selected parameters were successfully applied to natural tissue, demonstrating that variations in load and sliding distance produce measurable differences in the severity and distribution of damage. Finally, by considering these findings together, the work highlights that damage progression is influenced by the combined effect of mechanical parameters, and that replicating clinically relevant patterns of failure is likely to require testing approaches that integrate multiple parameters rather than varying them in isolation.

6.2 Discussion of findings

This work set out to investigate how specific mechanical conditions influence early damage at the cartilage labral junction in cam type femoroacetabular impingement. The findings demonstrate that damage in this region arises not from a single loading characteristic, but from the interaction between load, sliding distance, and direction. Taken together, the results from the experimental and computational components of this thesis show that patterns of early degeneration similar to that observed clinically emerge when high sliding distance occurs under elevated load during motion paths associated with hip flexion and internal rotation.

A key outcome of this work was the development of a repeatable in vitro method for testing natural hip tissue under controlled mechanical conditions. Previous studies using natural tissue have generally involved static positioning or single direction robotic motion, which limits the ability to vary conditions systematically (Uvodich et al., 2024; Hapa et al., 2025). The simulator based method developed here enabled consistent positioning of the femoral head neck region against the acetabular rim while allowing load and motion to be varied in a controlled manner. The accompanying damage assessment protocol provided a reliable

means of documenting surface level changes at the cartilage labral junction, capturing features such as blushing, scratching, and early delamination.

This method was designed to replicate patterns of damage observed in vivo, rather than to produce a clinically validated assessment. It allows examination of how changes in individual mechanical parameters influence the development of damage, providing a basis for in vitro testing that reflects in vivo–type tissue failure. This method makes it possible to examine how changes in individual mechanical parameters influence the development and distribution of damage, providing a basis for more physiologically meaningful in vitro testing.

The computational work identified physiologically relevant ranges of sliding distance, load and motion direction during daily activities, addressing the objective of defining meaningful parameter inputs for in vitro testing. The analysis showed that these parameters varied substantially between activities, reinforcing that impingement is a dynamic process rather than a static event, which aligns with clinical descriptions of cam type impingement occurring during motion.

Activities associated with symptom provocation in the literature, such as the squat, which has been shown to increase hip flexion demand, alter kinematics and elevate muscular effort in individuals with femoroacetabular impingement, also produced high mechanical values in the model (Lamontagne et al., 2009; Diamond et al., 2019). For example, in the present work the squat produced the second highest peak load and one of the longest sliding distances, aligning with its recognised role as a provocative movement. Similarly, sit to stand, which is commonly used clinically to reproduce anterior hip discomfort, demonstrated high loads that coincided with the impingement window. Although the model did not simulate damage directly, these patterns support the relevance of the identified parameter ranges. Importantly, these outputs allowed the in vitro testing to be grounded in realistic, activity specific biomechanics rather than arbitrary loading choices, emphasising the value of linking experimental boundary conditions to real human motion in future in vitro studies.

When the computationally derived parameter ranges were applied experimentally, patterns emerged. Increasing load alone did not consistently increase damage, nor did increasing sliding distance in isolation. Instead, the greatest damage occurred when high sliding distance was combined with high load. By design, the experimental setup targeted the

anterior superior cartilage-labral junction, and this approach successfully produced damage in that region, which is consistent with clinical observations describing early stage degeneration in cam-type hips. This suggests that the mechanism of damage is governed by shear forces acting at the interface while the tissue is simultaneously compressed, and that these characteristic separations of cartilage from the underlying bone and labrum occur specifically under conditions of high sliding distance combined with high load. The finding that the severity and location of damage varied between specimens also highlights the role of anatomical variation, such as acetabular rim shape and labral attachment thickness, in predisposing certain hips to injury. While porcine tissue provided a consistent model for these experiments, variation in human hips would be expected to be greater, potentially influencing the severity of damage.

In addition to the location and severity of damage, the type of damage observed provides further insight into the underlying mechanisms of tissue response. The predominant features identified in this study were blushing and early delamination (bubbling), both of which are consistent with early-stage cartilage damage. Blushing is likely associated with fluid exudation and disruption of the superficial matrix under compressive loading, reflecting the reliance of cartilage on fluid pressurisation for load support (Bhosale and Richardson, 2008; Little et al., 2011; Eschweiler et al., 2021). As this fluid support is reduced, the tissue becomes more susceptible to deformation and shear. The transition from blushing to bubbling observed under higher load and reduced sliding distance suggests progression from an initial surface response to localised matrix separation. This aligns with established damage pathways, where shear disrupts the superficial collagen network and repeated loading promotes separation between cartilage layers. Bubbling in this context is consistent with the early stages of delamination, where the more compliant superficial layers begin to separate from the stiffer underlying tissue. This progression is characteristic of cam-type impingement, where combined compressive and shear forces act at the anterosuperior acetabulum during joint motion (Beck et al., 2005; Keogh and Batt, 2008; Bsat et al., 2016). The localisation of these damage types to Zones 2 and 3 in this study supports this mechanism, suggesting that the applied loading conditions reproduced the early stages of clinically relevant chondrolabral damage.

Building on this, the results demonstrate that no single mechanical parameter is sufficient to reproduce these damage patterns in isolation. Instead, the combination of elevated load

with sustained sliding appears to be critical in driving both the location and progression of tissue damage. This has implications for how future in vitro studies should be designed. Experimental simulator testing may need to move away from protocols that vary load or motion independently, and instead adopt parameter combinations that reflect the coordinated conditions under which damage develops in vivo. This also offers insight into clinical practice. Cam resection may not fully normalise mechanics if high load and motion patterns persist post-intervention. Rehabilitation strategies that modify loading behaviour may therefore be important for preventing progression of damage, particularly in individuals with predisposing anatomical forms.

Overall, the combined experimental and computational approach used in this work offers a structured means of linking real movement patterns to tissue level damage responses. The findings reinforce the idea that early degeneration in cam type femoroacetabular impingement is driven by complex mechanical interactions, and that understanding these interactions is essential for improving diagnosis, treatment planning, and long term joint preservation.

6.3 Limitations

The limitations of this work should be considered when interpreting the findings. The simulations were carried out using porcine hip tissue, which differs from mature human tissue in several important respects. Porcine cartilage is thinner, and the transition between the acetabular cartilage and labrum is less distinct than in the human joint, which may influence both the appearance and progression of surface damage. The animals used were juvenile, meaning the cartilage and associated soft tissues had not reached full musculoskeletal maturity, which may affect fibre organisation and the ability of the tissue to resist mechanical loading. Because the tissue was non living, normal fluid pressurisation, collagen fibre recovery and biological adaptation were not present, so the samples could not respond to repeated loading as living tissue would.

Despite these differences, porcine hips provided intact joint structures, consistent geometry for mounting and alignment, and a practical and ethically accessible way to test mechanical conditions that cannot be reproduced in vivo. These advantages allowed controlled

investigation of load, sliding distance and motion direction, and the patterns of surface change observed are consistent with early chondrolabral damage described clinically in cam type impingement.

Several limitations should be considered when interpreting the computational findings. The movement data used to drive the model was obtained from a healthy cohort rather than individuals with symptomatic cam type impingement. Although this means the data does not capture the altered movement strategies often seen in people with symptoms, it also avoids compensatory behaviours that may reduce impingement and therefore provides a conservative estimate of the kinematic conditions under which impingement can occur. Only a single anterior cam morphology was applied, selected deliberately to reduce complexity and to reflect a common pattern of cam shape described in the literature. This approach does not represent the full range of cam orientations seen clinically, particularly more superiorly located cam lesions that may influence impingement in activities involving combined flexion abduction rotation. Nevertheless, using one well defined morphology allowed consistent comparison across activities.

The model also represented impingement as bony interference without contributions from ligaments, muscles or capsule. These soft tissue forces would be expected to increase joint reaction forces in deep flexion and therefore the peak loads reported here may underestimate the true forces that occur in vivo. Similarly, cartilage and labral deformation were not included because the aim was to isolate sliding distance, load and rotational direction as comparative mechanical parameters rather than to predict tissue stress directly. Despite these simplifications, the model provided a physiologically grounded means of identifying which activities push the hip toward positions and load levels associated with impingement, and therefore offered a meaningful basis for selecting experimental input conditions.

The study design required combining information from multiple model systems: human activity data informed the computational model; the computational model defined parameter ranges; and these parameters were applied to porcine joints under simplified loading. Each step introduced assumptions, and the translation between human movement, computational abstraction, and experimental tissue response is not direct. This means that the findings describe the mechanical relationships between load, sliding distance, and

damage susceptibility rather than a complete reproduction of clinical progression. However, the consistency of the observed damage location with known early clinical lesion patterns supports the relevance of the mechanical trends identified.

Although this work focused on cam-type femoroacetabular impingement, the experimental setup did not replicate the anatomical cam morphology itself. Instead, the approach reproduced the mechanical consequences of cam impingement. Specifically, the increased compressive shear and constrained sliding at the chondrolabral junction. This differs from studies that physically recreated cam morphology using grafted bone, shaped resection models, or 3D printed cam inserts (Siebenrock et al., 2013; Uvodich et al., 2024; Hapa et al., 2025). The decision not to impose a fixed cam shape was intentional, as the aim was to isolate the influence of mechanical parameters rather than evaluate the effect of cam geometry. However, it means that the findings describe how load and sliding distance influence damage susceptibility under impingement-like conditions, rather than linking damage to specific cam size or shape. Despite this, the alignment between the observed damage patterns and early clinical lesion locations supports the relevance of the mechanical behaviours replicated here.

Finally, assessment of tissue damage focused on surface level photography, which captured visible changes such as blushing, and early delamination. This method does not provide information about subsurface matrix disruption, failure of the collagen network, or changes in mechanical properties. As such, the extent of internal damage cannot be inferred from the surface appearance alone. However, the aim of the study was to identify the onset of damage rather than its full-depth progression, and surface disruption is recognised as an early marker of mechanical compromise at the cartilage labral junction. Within that scope, the imaging approach was appropriate.

6.4 Future work

The findings of this thesis highlight several areas where further research would be valuable. First, there is a need to examine the mechanical response of natural hip tissue under conditions that more closely replicate the combined multi parameter loading that occurs during daily activities. While this work isolated individual mechanical parameters to

understand their effects, clinical and cadaveric studies suggest that damage progression in cam type impingement is driven by the interaction of load, sliding, and motion direction, together with the stabilising contributions of the surrounding musculature and joint capsule (Beck et al., 2005; Ganz et al., 2008; Jannelli et al., 2019). These dynamic stabilising tissues guide joint rotation and constrain translation, meaning that mechanical loading in vivo is rarely driven by a single parameter in isolation. Future in vitro studies may therefore benefit from simulation methods that combine multiple parameters within a single testing protocol, supported by computational models capable of predicting their combined influence.

Second, the experimental work was limited to surface level damage assessment. The development of complementary methods to assess deeper structural change would enable a clearer understanding of how mechanical loading and movement translate into early degeneration. Imaging approaches such as contrast enhanced CT or MRI, or post test histological analysis, could be integrated alongside the photogrammetry method to determine whether changes observed on the surface correspond to alterations in underlying tissue structure. This would also support the development of mechanobiological models that link observed surface disruption with changes in cartilage matrix composition, collagen integrity, or permeability, allowing progression from mechanical damage to biological response to be more clearly understood.

Third, future computational work would benefit from incorporating subject specific cam morphology and subject specific movement data. The present work focused on reproducing the mechanical consequences of impingement, rather than the anatomical variability in cam shape. Previous studies have already demonstrated that variation in cam size, position, and shape influences impingement, but the interaction between these geometric variations and real damage patterns remains unclear (Jones et al., 2023). A useful extension of this work would be to combine specimen specific hip morphology with kinematic data collected from individuals with cam type impingement, rather than drawing activity patterns from a healthy population. This would allow the parameter ranges applied experimentally to more closely reflect the actual movements and loading patterns that occur in symptomatic hips.

Finally, there is scope to translate these findings toward clinical or rehabilitation contexts. The identification of parameter ranges most strongly associated with damage raises the possibility of patient-specific activity modification strategies to reduce mechanical stress at

the chondrolabral junction. Future work could explore whether targeted guidance on movement patterns, strength training, or load management following surgery could reduce recurrence or slow disease progression. Ultimately, this could inform surgical planning, postoperative rehabilitation, and patient-specific recommendations, bridging the gap between experimental modelling and clinical practice. Similarly, the computational and experimental approach developed here may be adapted to evaluate surgical resection strategies, by testing whether specific reductions in cam prominence reduce damaging mechanical conditions during daily movement.

6.5 Conclusion

This thesis set out to develop and apply a combined experimental and computational approach to investigate how mechanically relevant loading conditions influence damage at the cartilage–labral junction in cam type femoroacetabular impingement. By establishing a repeatable in vitro simulation method, determining physiologically relevant parameter ranges through computational modelling, and applying these parameters to natural hip tissue, this work provides new insight into the mechanical factors that contribute to early chondrolabral damage.

The development of the natural tissue testing method demonstrated that it is possible to apply controlled and repeatable variations in loading and motion to the acetabular rim while reliably documenting resulting surface changes. The computational modelling work identified typical ranges of sliding distance, load, and motion direction that occur during activities of daily living, providing a biomechanical basis for selecting experimentally relevant conditions derived from activity data, rather than arbitrarily defined. Applying these parameters in vitro showed that mechanical conditions strongly influence both the location and the severity of damage at the chondrolabral junction, and that damage patterns observed under specific parameter combinations were consistent with early lesion patterns described clinically.

Together, these findings support the view that the progression of tissue damage in cam type impingement is mechanically driven and sensitive to the magnitude and nature of loading during movement. While this work does not replicate the complete in vivo environment, it

demonstrates that experimentally induced loading conditions can reproduce in vivo–type damage patterns, strengthening the link between joint mechanics, impingement, and early degenerative change. This provides a basis for future studies that combine parameter interactions, incorporate subject specific morphology and movement, and explore how mechanical loading might be modified to slow or prevent tissue deterioration.

Overall, this thesis contributes a validated in vitro simulation method, a computational framework for identifying clinically relevant biomechanical parameters, and new evidence linking mechanical loading conditions to early cartilage and labral damage, providing a foundation for future research in modelling, surgical planning, and activity based rehabilitation in cam type femoroacetabular impingement.

Chapter 7

7 References

Agricola, R., Heijboer, M.P., Ginai, A.Z., Roels, P., Zadpoor, A.A., Verhaar, J.A.N., Weinans, H. and Waarsing, J.H. 2014. A Cam Deformity Is Gradually Acquired During Skeletal Maturation in Adolescent and Young Male Soccer Players:A Prospective Study With Minimum 2-Year Follow-up. **42**(4), pp.798-806.

Agricola, R., Waarsing, J.H., Arden, N.K., Carr, A.J., Bierma-Zeinstra, S.M.A., Thomas, G.E., Weinans, H. and Glyn-Jones, S. 2013. Cam impingement of the hip-a risk factor for hip osteoarthritis. *Nature reviews. Rheumatology.* **9**(10), pp.630-634.

Albers, C.E., Wambeek, N., Hanke, M.S., Schmaranzer, F., Prosser, G.H. and Yates, P.J. 2016. Imaging of femoroacetabular impingement-current concepts. *Journal of Hip Preservation Surgery.* **3**(4), pp.245-261.

Ali, M., Al-Hajjar, M., Partridge, S., Williams, S., Fisher, J. and Jennings, L.M. 2016. Influence of hip joint simulator design and mechanics on the wear and creep of metal-on-polyethylene bearings. *Proc Inst Mech Eng H.* **230**(5), pp.389-397.

Alonso-Rasgado, T., Jimenez-Cruz, D., Bailey, C.G., Mandal, P. and Board, T. 2012. Changes in the stress in the femoral head neck junction after osteochondroplasty for hip impingement: A finite element study. *Journal of orthopaedic research.* **30**(12), pp.1999-2006.

Amenabar, T., Piriz, J., Mella, C., Hetaimish, B.M. and O'Donnell, J. 2015. Reliability of 3 Different Arthroscopic Classifications for Chondral Damage of the Acetabulum. *Arthroscopy.* **31**(8), pp.1492-1496.

Amiri, P. and Bull, A.M.J. 2022. Prediction of in vivo hip contact forces during common activities of daily living using a segment-based musculoskeletal model. *Frontiers in Bioengineering and Biotechnology.* **Volume 10 - 2022**.

Anderson, A.E., Ellis, B.J., Maas, S.A. and Weiss, J.A. 2010. Effects of idealized joint geometry on finite element predictions of cartilage contact stresses in the hip. *Journal of Biomechanics.* **43**(7), pp.1351-1357.

Arbabi, E., Chegini, S., Boulic, R., Tannast, M., Ferguson, S.J. and Thalmann, D. 2010. Penetration depth method-novel real-time strategy for evaluating femoroacetabular impingement. *Journal of orthopaedic research.* **28**(7), pp.880-886.

Ardestani, M.M., Ferrigno, C., Moazen, M. and Wimmer, M.A. 2016. From Normal to Fast Walking: Impact of Cadence and Stride Length on Lower Extremity Joint Moments. *Gait & posture.* **46**, pp.118-125.

Athanasiou, K.A., Agarwal, A., Muffoletto, A., Dzida, F.J., Constantinides, G. and Clem, M. 1995. Biomechanical Properties of Hip Cartilage in Experimental Animal Models. *Clinical orthopaedics and related research.* **316**(316), pp.254-266.

Audenaert, E.A., Peeters, I., Vigneron, L., Baelde, N. and Pattyn, C. 2012. Hip Morphological Characteristics and Range of Internal Rotation in Femoroacetabular Impingement. *The American Journal of Sports Medicine.* **40**(6), pp.1329-1336.

Ayeni, O., Chu, R., Hetaimish, B., Nur, L., Simunovic, N., Farrokhyar, F., Bedi, A. and Bhandari, M.J.K.S., Sports Traumatology, Arthroscopy. 2014. A painful squat test provides limited diagnostic utility in CAM-type femoroacetabular impingement. **22**(4), pp.806-811.

Bagwell, J.J., Snibbe, J., Gerhardt, M. and Powers, C.M. 2016. Hip kinematics and kinetics in persons with and without cam femoroacetabular impingement during a deep squat task. *Clinical Biomechanics.* **31**, pp.87-92.

Barros, A.A.G., Vassalo, C.C., Costa, L.P., Gómez-Hoyos, J., Paganini, V.d.O. and Andrade, M.A.P.d. 2019. Reliability of the Arthroscopic Classifications of Hip Chondral Lesions. *Revista brasileira de ortopedia.* **54**(4), pp.440-446.

Beck, M., Kalhor, M., Leunig, M. and Ganz, R. 2005. Hip morphology influences the pattern of damage to the acetabular cartilage. *The Journal of Bone and Joint Surgery. British volume.* **87-B**(7), pp.1012-1018.

Beck, M., Leunig, M., Parvizi, J., Boutier, V., Wyss, D. and Ganz, R. 2004. Anterior femoroacetabular impingement: part II. Midterm results of surgical treatment. *Clin Orthop Relat Res.* (418), pp.67-73.

Bedi, A., Dolan, M., Hetsroni, I., Magennis, E., Lipman, J., Buly, R. and Kelly, B.T. 2011. Surgical Treatment of Femoroacetabular Impingement Improves Hip Kinematics: A Computer-Assisted Model. *The American Journal of Sports Medicine.* **39**(1_suppl), pp.43-49.

Bennett, D., Orr, J.F., Beverland, D.E. and Baker, R. 2002. The influence of shape and sliding distance of femoral head movement loci on the wear of acetabular cups in total hip arthroplasty. *Proceedings of the Institution of Mechanical Engineers. Part H, Journal of engineering in medicine.* **216**(6), pp.393-402.

Bergmann, G., Deuretzbacher, G., Heller, M., Graichen, F., Rohlmann, A., Strauss, J. and Duda, G.N. 2001. Hip contact forces and gait patterns from routine activities. *Journal of Biomechanics.* **34**(7), pp.859-871.

Bergmann, G., Graichen, F. and Rohlmann, A. 1999. Hip joint forces in sheep. *Journal of biomechanics.* **32**(8), pp.769-777.

Bergmann, G., Graichen, F., Rohlmann, A., Bender, A., Heinlein, B., Duda, G.N., Heller, M.O. and Morlock, M.M. 2010. Realistic loads for testing hip implants. *Bio-medical materials and engineering.* **20**(2), pp.65-75.

Bhosale, A.M. and Richardson, J.B. 2008. Articular cartilage: structure, injuries and review of management. *British Medical Bulletin.* **87**(1), pp.77-95.

Birmingham, P.M., Kelly, B.T., Jacobs, R., McGrady, L. and Wang, M. 2012. The Effect of Dynamic Femoroacetabular Impingement on Pubic Symphysis Motion: A Cadaveric Study. *The American journal of sports medicine.* **40**(5), pp.1113-1118.

Blaker, C.L., Ashton, D.M., Hartnell, N., Little, C.B. and Clarke, E.C. 2024. Tendon biomechanical properties are altered by storage duration but not freeze-thaw temperatures or cycles. *Journal of orthopaedic research.* **42**(6), pp.1180-1189.

Brisson, N., Lamontagne, M., Kennedy, M.J. and Beaulé, P.E. 2013. The effects of cam femoroacetabular impingement corrective surgery on lower-extremity gait biomechanics. *Gait & Posture.* **37**(2), pp.258-263.

Bsat, S., Frei, H. and Beaule, P. 2016. The acetabular labrum. **98-B**(6), pp.730-735.

Büchler, L. and Keel, M.J.B. 2019. *Fractures of the Hip.* 1 ed. Springer Cham.

Byrd, J.W.T. 2014. Femoroacetabular Impingement in Athletes:Current Concepts. **42**(3), pp.737-751.

Calais-Germain, B. 2007. *Anatomy of Movement.* Eastland Press.

Cashin, M., Uhthoff, H., O'Neill, M. and Beaulé, P.E. 2008. Embryology of the acetabular labral-chondral complex. *Journal of bone and joint surgery. British volume.* **90**(8), pp.1019-1024.

Chegini, S., Beck, M. and Ferguson, S.J. 2009. The effects of impingement and dysplasia on stress distributions in the hip joint during sitting and walking: A finite element analysis. *Journal of Orthopaedic Research.* **27**(2), pp.195-201.

Cooper, R., Mengoni, M., Groves, D., Williams, S., Bankes, M.J.K., Robinson, P. and Jones, A.C. 2017. Three-dimensional assessment of impingement risk in geometrically parameterised hips compared with clinical measures. *International Journal for Numerical Methods in Biomedical Engineering.* **33**(11), pp.n/a-n/a.

Cooper, R., Williams, S., Mengoni, M. and Jones, A. 2018. Patient-specific parameterised cam geometry in finite element models of femoroacetabular impingement of the hip. *Clinical Biomechanics.* **54**, pp.62-70.

Diamond, L.E., Bennell, L.K., Wrigley, V.T., Hinman, S.R., O'donnell, W.J. and Hodges, W.P. 2017. Squatting Biomechanics in Individuals with Symptomatic Femoroacetabular Impingement. *Medicine & Science in Sports & Exercise.* **49**(8), pp.1520-1529.

Diamond, L.E., Dobson, F.L., Bennell, K.L., Wrigley, T.V., Hodges, P.W. and Hinman, R.S. 2015. Physical impairments and activity limitations in people with femoroacetabular impingement: a systematic review. *British Journal of Sports Medicine.* **49**(4), p230.

Diamond, L.E., van den Hoorn, W., Bennell, K.L., Wrigley, T.V., Hinman, R.S., O'Donnell, J. and Hodges, P.W. 2019. Deep hip muscle activation during squatting in femoroacetabular impingement syndrome. *Clinical biomechanics (Bristol).* **69**, pp.141-147.

Diamond, L.E., Wrigley, T.V., Bennell, K.L., Hinman, R.S., O'donnell, J. and Hodges, P.W. 2016. Hip joint biomechanics during gait in people with and without symptomatic femoroacetabular impingement. *Gait & Posture.* **43**, pp.198-203.

Doran, C., Pettit, M., Singh, Y., Sunil Kumar, K.H. and Khanduja, V. 2022. Does the Type of Sport Influence Morphology of the Hip? A Systematic Review. *The American journal of sports medicine.* **50**(6), pp.1727-1741.

Eschweiler, J., Horn, N., Rath, B., Betsch, M., Baroncini, A., Tingart, M. and Migliorini, F. 2021. The biomechanics of cartilage-an overview. *Life (Basel, Switzerland).* **11**(4), p302.

Fermor, H.L., McLure, S.W., Taylor, S.D., Russell, S.L., Williams, S., Fisher, J. and Ingham, E. 2015. Biological, biochemical and biomechanical characterisation of articular cartilage from the porcine, bovine and ovine hip and knee. *Biomed Mater Eng.* **25**(4), pp.381-395.

Frank, J.M., Harris, J.D., Erickson, B.J., Slikker, W., Bush-Joseph, C.A., Salata, M.J. and Nho, S.J. 2015. Prevalence of Femoroacetabular Impingement Imaging Findings in Asymptomatic Volunteers: A Systematic Review. *Arthroscopy: The Journal of Arthroscopic & Related Surgery.* **31**(6), pp.1199-1204.

Ganz, R., Leunig, M., Leunig-Ganz, K. and Harris, W. 2008. The Etiology of Osteoarthritis of the Hip: An Integrated Mechanical Concept. *Clinical Orthopaedics and Related Research.* **466**(2), pp.264-272.

Ganz, R., Parvizi, J., Beck, M., Leunig, M., Nötzli, H. and Siebenrock, K.A. 2003. Femoroacetabular Impingement: A Cause for Osteoarthritis of the Hip. **417**, pp.112-120.

Goldsmith, M.T., Rasmussen, M.T., Turnbull, T.L., Trindade, C.A.C., LaPrade, R.F., Philippon, M.J. and Wijdicks, C.A. 2015. Validation of a six degree-of-freedom robotic system for hip in vitro biomechanical testing. *Journal of biomechanics.* **48**(15), pp.4093-4100.

Gradinger, R., Träger, J. and Klauser, R.J. 1995. Influence of various irrigation fluids on articular cartilage. *Arthroscopy.* **11**(3), pp.263-269.

Griffin, D.R., Dickenson, E.J., O'Donnell, J., Agricola, R., Awan, T., Beck, M., Clohisy, J.C., Dijkstra, H.P., Falvey, E., Gimpel, M., Hinman, R.S., Hölmich, P., Kassarjian, A., Martin, H.D., Martin, R., Mather, R.C., Philippon, M.J., Reiman, M.P., Takla, A., Thorborg, K., Walker, S., Weir, A. and Bennell, K.L. 2016. The Warwick Agreement on femoroacetabular impingement syndrome (FAI syndrome): an international consensus statement. *British journal of sports medicine.* **50**(19), pp.1169-1176.

Griffin, D.R., Dickenson, E.J., Wall, P.D.H., Achana, F., Donovan, J.L., Griffin, J., Hobson, R., Hutchinson, C.E., Jepson, M., Parsons, N.R., Petrou, S., Realpe, A., Smith, J. and Foster, N.E. 2018. Hip arthroscopy versus best conservative care for the treatment of femoroacetabular impingement syndrome (UK FASHIoN): a multicentre randomised controlled trial. *Lancet.* **391**(10136), pp.2225-2235.

Groves, D. 2015. *Geometric Variances in Hip Osteoarthritis and Tribology of the Natural Hip*. thesis, University of Leeds.

Groves, D., Fisher, J. and Williams, S. 2017. An in vitro simulation method for the tribological assessment of complete natural hip joints. *PLoS ONE.* **12**(9).

Gulihar, A., Bryson, D.J. and Taylor, G.J.S. 2013. Effect of Different Irrigation Fluids on Human Articular Cartilage: An In Vitro Study. *Arthroscopy.* **29**(2), pp.251-256.

Hapa, O., Aydemir, S., Sunay, F.B., Acan, A.E., Akkaya, P.N., Celtik, M., Husemoglu, R.B. and Salin, M. 2025. In Vitro Ovine Cam Impingement Model and Its Effect on Acetabular Cartilage. *Orthop J Sports Med.* **13**(3), p23259671251322757.

Hassan, M.M., Farooqi, A.S., Feroe, A.G., Lee, A., Cusano, A., Novais, E., Wuerz, T.H., Kim, Y.J. and Parisien, R.L. 2022. Open and arthroscopic management of femoroacetabular impingement: a review of current concepts. *J Hip Preserv Surg.* **9**(4), pp.265-275.

Hellwig, F.L., Tong, J. and Hussell, J.G. 2016. Hip joint degeneration due to cam impingement: a finite element analysis. *Computer methods in biomechanics and biomedical engineering.* **19**(1), pp.41-48.

Ilizaliturri, V.M., Jr., Byrd, J.W.T., Sampson, T.G., Guanche, C.A., Philippon, M.J., Kelly, B.T., Dienst, M., Mardones, R., Shonnard, P. and Larson, C.M. 2008. A Geographic Zone Method to Describe Intra-articular Pathology in Hip Arthroscopy: Cadaveric Study and Preliminary Report. *Arthroscopy.* **24**(5), pp.534-539.

Jannelli, E., Parafioriti, A., Acerbi, A., Ivone, A., Fioruzzi, A. and Fontana, A. 2019. Acetabular Delamination: Epidemiology, Histological Features, and Treatment. *Cartilage.* **10**(3), pp.314-320.

Jimenez-Cruz, D., Dubey, M., Board, T. and Williams, S. 2022. An in vitro methodology for experimental simulation on the natural hip joint. *PLOS ONE.* **17**(8), pe0272264.

Jones, A., Stewart, T., Maher, N. and Holton, C. 2021. Subject-specific assessment of cam-type femoroacetabular impingement across multiple activities. . In: *British Hip Society - Online*.

Jones, A., Stewart, T., Maher, N. and Holton, C. 2023. Can a Computational Model Predict the Effect of Lesion Location on Cam-type Hip Impingement? *Clinical Orthopaedics and Related Research®.* **481**(7), pp.1432-1443.

Jorge, J.P., Simões, F.M.F., Pires, E.B., Rego, P.A., Tavares, D.G., Lopes, D.S. and Gaspar, A. 2014. Finite element simulations of a hip joint with femoroacetabular impingement. *Computer methods in biomechanics and biomedical engineering.* **17**(11), pp.1275-1284.

Kappe, T., Kocak, T., Bieger, R., Reichel, H. and Fraitzl, C.R. 2011. Radiographic risk factors for labral lesions in femoroacetabular impingement. *Clinical orthopaedics and related research.* **469**(11), pp.3241-3247.

Katta, J., Jin, Z., Ingham, E. and Fisher, J. 2008. Biotribology of articular cartilage—A review of the recent advances. *Medical Engineering & Physics.* **30**(10), pp.1349-1363.

Kaya, M., Suzuki, T., Emori, M. and Yamashita, T. 2016. Hip morphology influences the pattern of articular cartilage damage. *Knee Surgery, Sports Traumatology, Arthroscopy.* **24**(6), pp.2016-2023.

Keogh, M.J. and Batt, M.E.J.S.M. 2008. A Review of Femoroacetabular Impingement in Athletes. **38**(10), pp.863-878.

Köhnlein, W., Ganz, R., Impellizzeri, F.M. and Leunig, M. 2009. Acetabular Morphology: Implications for Joint-preserving Surgery. *Clinical Orthopaedics and Related Research®.* **467**(3), pp.682-691.

Konan, S., Rayan, F., Meermans, G., Witt, J. and Haddad, F.S. 2011. Validation of the classification system for acetabular chondral lesions identified at arthroscopy in patients with femoroacetabular impingement. *The Journal of bone and joint surgery. British volume.* **93**(3), pp.332-336.

Kubiak-Langer, M., Tannast, M., Murphy, S.B., Siebenrock, K.A. and Langlotz, F. 2007. Range of Motion in Anterior Femoroacetabular Impingement. *Clinical orthopaedics and related research.* **458**(458), pp.117-124.

Kuroda, Y., Rai, A., Saito, M. and Khanduja, V. 2020. Anatomical variation of the Psoas Valley: a scoping review. *BMC Musculoskeletal Disorders.* **21**(1), p219.

Lamontagne, M., Kennedy, M.J. and Beaulé, P.E. 2009. The effect of cam FAI on hip and pelvic motion during maximum squat. *Clinical orthopaedics and related research.* **467**(3), pp.645-650.

Layton, R. 2020. *Understanding Movement and its Influence on Tribology of the Human Hip*. thesis, University of Leeds.

Layton, R., Messenger, N. and Stewart, T. 2021. Analysis of hip joint cross-shear under variable activities using a novel virtual joint model within Visual3D. *Proceedings of the*

Institution of Mechanical Engineers. Part H, Journal of engineering in medicine. **235**(10), pp.1197-1204.

Layton, R., Messenger, N. and Stewart, T. 2022a. Characteristics of hip joint reaction forces during a range of activities. *Medical Engineering & Physics.* **108**.

Layton, R., Messenger, N. and Stewart, T. 2022b. Data supporting characteristics of hip joint reaction forces during a range of activities. [Online]. [Accessed 2023]. Available from: https://doi.org/10.5518/1253

Leunig, M., Beaulé, P.E. and Ganz, R. 2009. The concept of femoroacetabular impingement: current status and future perspectives. *Clinical orthopaedics and related research.* **467**(3), pp.616-622.

Little, C.J., Bawolin, N.K. and Chen, X. 2011. Mechanical properties of natural cartilage and tissue-engineered constructs. *Tissue engineering. Part B, Reviews.* **17**(4), pp.213-227.

Liu, Q., Wang, W., Thoreson, A.R., Zhao, C., Zhu, W. and Dou, P. 2017. Finite element prediction of contact pressures in cam-type femoroacetabular impingement with varied alpha angles. *Computer methods in biomechanics and biomedical engineering.* **20**(3), pp.294-301.

Lizhang, J. 2010. *Tribology of hemiarthroplasty*. thesis, University of Leeds.

Lopez, S., Johnson, C., Frankston, N., Ruh, E., McClincy, M. and Anderst, W. 2024. Accuracy of conventional motion capture in measuring hip joint center location and hip rotations during gait, squat, and step-up activities. *Journal of Biomechanics.* **167**, p112079.

Lunn, D.E., Lampropoulos, A. and Stewart, T.D. 2016. Basic biomechanics of the hip. *Orthopaedics and Trauma.* **30**(3), pp.239-246.

Malloy, P., Neumann, D.A. and Kipp, K. 2019. Hip Biomechanics During a Single-Leg Squat: 5 Key Differences Between People With Femoroacetabular Impingement Syndrome and Those Without Hip Pain. *The journal of orthopaedic and sports physical therapy.* **49**(12), pp.908-916.

Mascarenhas, V.V., Rego, P., Dantas, P., Castro, M., Jans, L., Marques, R.M., Gouveia, N., Soldado, F., Ayeni, O.R. and Consciência, J.G. 2018. Hip shape is symmetric, non-dependent on limb dominance and gender-specific: implications for femoroacetabular impingement. A 3D CT analysis in asymptomatic subjects. *European radiology.* **28**(4), pp.1609-1624.

McCarthy, J., Noble, P., Aluisio, F.V., Schuck, M., Wright, J. and Lee, J.-a. 2003. Anatomy, Pathologic Features, and Treatment of Acetabular Labral Tears. *Clinical Orthopaedics and Related Research®.* **406**(1).

Morris, W.Z., Li, R.T., Liu, R.W., Salata, M.J. and Voos, J.E. 2018. Origin of Cam Morphology in Femoroacetabular Impingement. **46**(2), pp.478-486.

Mow, V.C., Kuei, S.C., Lai, W.M. and Armstrong, C.G. 1980. Biphasic Creep and Stress Relaxation of Articular Cartilage in Compression: Theory and Experiments. *Journal of biomechanical engineering.* **102**(1), pp.73-84.

NAHR. 2024. *Non-Arthroplasty Hip Registry - 8th Annual Report 2024.* 8th Annual Report ed. Non-Arthroplasty Hip Registry.

Nakahara, I., Takao, M., Sakai, T., Nishii, T., Yoshikawa, H. and Sugano, N. 2011. Gender differences in 3D morphology and bony impingement of human hips. *Journal of orthopaedic research.* **29**(3), pp.333-339.

Narvani, A.A., Tsiridis, E., Tai, C.C. and Thomas, P. 2003. Acetabular labrum and its tears. *British Journal of Sports Medicine.* **37**(3), p207.

Nawabi, D.H.M.D.F.R.S.C., Bedi, A.M.D., Tibor, L.M.M.D., Magennis, E.J.D. and Kelly, B.T.M.D. 2014. The Demographic Characteristics of High-Level and Recreational Athletes Undergoing Hip Arthroscopy for Femoroacetabular Impingement: A Sports-Specific Analysis. *Arthroscopy.* **30**(3), pp.398-405.

Nepple, J.J., Larson, C.M., Smith, M.V., Kim, Y.-J., Zaltz, I., Sierra, R.J. and Clohisy, J.C. 2012. The Reliability of Arthroscopic Classification of Acetabular Rim Labrochondral Disease. *The American journal of sports medicine.* **40**(10), pp.2224-2229.

Ng, Mario, L., Michel, R.L. and Paul, E.B. 2016. Hip Joint Stresses Due to Cam-Type Femoroacetabular Impingement: A Systematic Review of Finite Element Simulations. *PLoS ONE.* **11**(1), pe0147813.

Ng, Rouhi, G., Lamontagne, M. and Beaulé, P.E. 2012. Finite Element Analysis Examining the Effects of Cam FAI on Hip Joint Mechanical Loading Using Subject-Specific Geometries During Standing and Maximum Squat. *HSS Journal ®.* **8**(3), pp.206-212.

Ng, G., El Daou, H., Bankes, M.J.K., Rodriguez, Y.B.F. and Jeffers, J.R.T. 2019. Hip Joint Torsional Loading Before and After Cam Femoroacetabular Impingement Surgery. *Am J Sports Med.* **47**(2), pp.420-430.

Nordin, M., Frankel, V.H., Meere, P.A., Mullerpatan, R.P., Wilke, H.-J. and Leger, D. 2022. *Basic biomechanics of the musculoskeletal system.* Fifth edition / guest editors, Patrick A. Meere, MD, CM, Rajani Prashant Mullerpatan, MSc (PT), PhD, Hans-Joachim Wilke, PhD, MSc in Eng. ; editor & project manager, Dawn Leger, PhD. ed. Philadelphia, PA: Lippincott Williams & Wilkins.

Palastanga, N. 2002. *Anatomy and human movement : structure and function.* Fourth edition / Nigel Palastanga, Derek Field, Roger Soames. ed. Oxford: Butterworth-Heinemann.

Pallan, R. 2016. *Characterisation and In Vitro Simulation of the Natural Hip*. thesis, University of Leeds.

Palmer, A.J.R., Ayyar Gupta, V., Fernquest, S., Rombach, I., Dutton, S.J., Mansour, R., Wood, S., Khanduja, V., Pollard, T.C.B., McCaskie, A.W., Barker, K.L., Andrade, T., Carr, A.J., Beard, D.J. and Glyn-Jones, S. 2019. Arthroscopic hip surgery compared with physiotherapy and activity modification for the treatment of symptomatic femoroacetabular impingement: multicentre randomised controlled trial. *Bmj.* **364**, pl185.

Pascual-Garrido, C., Li, D.J., Grammatopoulos, G., Yanik, E.L., Clohisy, J.C. and Group, A. 2019. The Pattern of Acetabular Cartilage Wear Is Hip Morphology-dependent and Patient Demographic-dependent. *Clinical orthopaedics and related research.* **477**(5), pp.1021-1033.

Pasculli, R.M., Callahan, E.A., Wu, J., Edralin, N. and Berrigan, W.A. 2023. Non-operative Management and Outcomes of Femoroacetabular Impingement Syndrome. *Current Reviews in Musculoskeletal Medicine.* **16**(11), pp.501-513.

Petersen, W., Petersen, F. and Tillmann, B. 2003. Structure and vascularization of the acetabular labrum with regard to the pathogenesis and healing of labral lesions. *Archives of Orthopaedic and Trauma Surgery.* **123**(6), pp.283-288.

Philippon, M.J., Stubbs, A.J., Schenker, M.L., Maxwell, R.B., Ganz, R. and Leunig, M. 2007. Arthroscopic Management of Femoroacetabular Impingement:Osteoplasty Technique and Literature Review. **35**(9), pp.1571-1580.

Polesello, G.C., Viamont-Guerra, M.-R., Zego, F., Rabelo, N.D.D.A., Ricioli Junior, W. and Queiroz, M.C. 2019. Post-Treatment Classification for Acetabular Chondral Lesions in Hip Arthroscopy. *Revista brasileira de ortopedia.* **54**(6), pp.679-684.

Ranawat, A.S. and Kelly, B.T. 2005. Anatomy of the Hip: Open and Arthroscopic Structure and Function. *Operative Techniques in Orthopaedics.* **15**(3), pp.160-174.

Reagan, B.F., McInerny, V.K., Treadwell, B.V., Zarins, B. and Mankin, H.J. 1983. Irrigating solutions for arthroscopy. A metabolic study. *J Bone Joint Surg Am.* **65**(5), pp.629-631.

Rylander, J., Shu, B., Favre, J., Safran, M. and Andriacchi, T. 2013. Functional testing provides unique insights into the pathomechanics of femoroacetabular impingement and an objective basis for evaluating treatment outcome. **31**(9), pp.1461-1468.

Safran, M.R., Giordano, G., Lindsey, D.P., Gold, G.E., Rosenberg, J., Zaffagnini, S. and Giori, N.J. 2011. Strains across the Acetabular Labrum during Hip Motion:A Cadaveric Model. **39**(1_suppl), pp.92-102.

Safran, M.R. and Hariri, S. 2010. Hip Arthroscopy Assessment Tools and Outcomes. *Operative Techniques in Orthopaedics.* **20**(4), pp.264-277.

Sardana, V., Burzynski, J. and Scuderi, G.R. 2019. The influence of the irrigating solution on articular cartilage in arthroscopic surgery: A systematic review. *Journal of orthopaedics.* **16**(2), pp.158-165.

Savage, T.N., Saxby, D.J., Pizzolato, C., Diamond, L.E., Murphy, N.J., Hall, M., Spiers, L., Eyles, J., Killen, B.A., Suwarganda, E.K., Dickenson, E.J., Griffin, D., Fary, C., O'Donnell, J., Molnar, R., Randhawa, S., Reichenbach, S., Tran, P., Wrigley, T.V., Bennell, K.L., Hunter, D.J. and Lloyd, D.G. 2021. Trunk, pelvis and lower limb walking biomechanics are similarly altered in those with femoroacetabular impingement syndrome regardless of cam morphology size. *Gait & posture.* **83**, pp.26-34.

Schmidt, T.A., Gastelum, N.S., Nguyen, Q.T., Schumacher, B.L. and Sah, R.L. 2007. Boundary lubrication of articular cartilage: Role of synovial fluid constituents. *Arthritis & Rheumatism.* **56**(3), pp.882-891.

Seldes, R.M., Tan, V., Hunt, J., Katz, M., Winiarsky, R. and Fitzgerald, R.H. 2001. Anatomy, histologic features, and vascularity of the adult acetabular labrum. *Clinical Orthopaedics And Related Research.* (382), pp.232-240.

Siebenrock, K.A., Fiechter, R., Tannast, M., Mamisch, T.C. and von Rechenberg, B. 2013. Experimentally induced cam impingement in the sheep hip. *Journal of Orthopaedic Research.* **31**(4), pp.580-587.

Steppacher, S.D., Lerch, T.D., Gharanizadeh, K., Liechti, E.F., Werlen, S.F., Puls, M., Tannast, M. and Siebenrock, K.A. 2014. Size and shape of the lunate surface in different types of pincer impingement: theoretical implications for surgical therapy. *Osteoarthritis and Cartilage.* **22**(7), pp.951-958.

Sutter, R., Dietrich, T.J., Zingg, P.O. and Pfirrmann, C.W.A. 2012. How Useful Is the Alpha Angle for Discriminating between Symptomatic Patients with Cam-type Femoroacetabular Impingement and Asymptomatic Volunteers? *Radiology.* **264**(2), pp.514-521.

Tannast, M., Kubiak-Langer, M., Langlotz, F., Puls, M., Murphy, S.B. and Siebenrock, K.A. 2007a. Noninvasive three-dimensional assessment of femoroacetabular impingement. *Journal of orthopaedic research.* **25**(1), pp.122-131.

Tannast, M., Siebenrock, K.A. and Anderson, S.E. 2007b. Femoroacetabular impingement: radiographic diagnosis--what the radiologist should know. *AJR. American journal of roentgenology.* **188**(6), pp.1540-1552.

Taylor, S.D., Tsiridis, E., Ingham, E., Jin, Z., Fisher, J. and Williams, S. 2012. Comparison of human and animal femoral head chondral properties and geometries. **226**(1), pp.55-62.

Thorup, V.M., Togersen, F.A., Jorgensen, B. and Jensen, B.R. 2007. Biochemical gait analysis of pigs walking on solid concrete floor. *Animal : an international journal of animal bioscience.* **1**(5), pp.708-715.

Tronzo, R.G. 1984. *Surgery of the Hip Joint.* Springer New York.

Unnanuntana, A., Toogood, P., Hart, D., Cooperman, D. and Grant, R.E. 2010. Evaluation of proximal femoral geometry using digital photographs. *J Orthop Res.* **28**(11), pp.1399-1404.

Uvodich, M.E., Hooke, A.W., Braig, Z.V., Nieboer, M.J., Dugdale, E.M., Cross, W.W., Krych, A.J. and Hevesi, M. 2024. Simulated Cam Morphology of the Hip Changes Sacroiliac Motion During Hip Motion and Loading in a Cadaveric Model. *Arthroscopy, Sports Medicine, and Rehabilitation.* **6**(6).

van Klij, P., Reiman, M.P., Waarsing, J.H., Reijman, M., Bramer, W.M., Verhaar, J.A.N. and Agricola, R. 2020. Classifying Cam Morphology by the Alpha Angle: A Systematic Review on Threshold Values. *Orthopaedic Journal of Sports Medicine.* **8**(8), pp.2325967120938312-2325967120938312.

Varady, P.A., Glitsch, U. and Augat, P. 2015. Loads in the hip joint during physically demanding occupational tasks: A motion analysis study. *Journal of Biomechanics.* **48**(12), pp.3227-3233.

Yanke, A.B., Khair, M.M., Stanley, R., Walton, D., Lee, S., Bush-Joseph, C.A., Espinosa Orias, A.A., Inoue, N. and Nho, S.J. 2015. Sex Differences in Patients With CAM Deformities With Femoroacetabular Impingement: 3-Dimensional Computed Tomographic Quantification. *Arthroscopy: The Journal of Arthroscopic & Related Surgery.* **31**(12), pp.2301-2306.

Young, E.Y., Gebhart, J., Cooperman, D. and Ahn, N.U. 2013. Are the Left and Right Proximal Femurs Symmetric? *Clinical orthopaedics and related research.* **471**(5), pp.1593-1601.

Zimmerman, B.K., Nims, R.J., Chen, A., Hung, C.T. and Ateshian, G.A. 2021. Direct Osmotic Pressure Measurements in Articular Cartilage Demonstrate Nonideal and Concentration-Dependent Phenomena. *Journal of biomechanical engineering.* **143**(4).

Chapter 8

8 Appendices

8.1 Appendix A: Equipment list

Equipment	
Acetabular cup alignment rig	No.11 Blade
Allen keys	Paper towel
Assortment of femoral heads	Personal protective equipment
Assortment of height cylinders	Phosphate Buffered Saline (PBS)
Black tape	Plastic bag
Blade holder	Polymethyl methacrylate (PMMA)
Camera	Prepared tissue samples
Cementing cup	Scale
Chain mail glove	Single station hip simulator (SSHS)
Dissected and potted samples	Spatula
Femoral head potting rig	Tripod
Femoral sizing guide	Vaseline
Gaiter	
Hacksaw	
Inclinometer	
Lightbox	
Lubricant - ringer's solution	
No. 23 blade	

8.2 Appendix B: Damage characterisation information sheet

Sample Information Sheet

Sample ID:	
Dissection date:	

Dissection details			
Femoral head size (mm):			
(Horizontal) Acetabulum diameter (mm):		**(Vertical) Acetabulum diameter (mm):**	
Other observations @dissection:			

Test parameters			
Study No:		**Testing Date:**	
Inclination Angle (°):		**Number of cycles:**	
Motion (°):		**Load (N):**	
Observation(s)			
Pre-test observation(s):			

Observations @ 2 hours:		
Observations @ 4 hours:		
Damage characterisation *Use the correct Letter in the key to signify the type of damage that is visible in each zone.*		
Key:	A - Scratch/Indentation B - Tear/flap C - Separation from Cartilage	D - Blushing E - Fibrillation F - Delamination
Location of damage observed on the acetabulum:	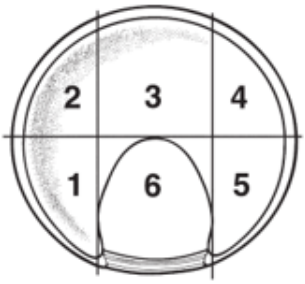 (Ilizaliturri et al., 2008)	
Location of damage observed on the femoral head:	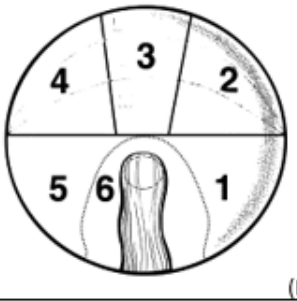 (Ilizaliturri et al., 2008)	

8.3 Appendix C: Parametric testing photogrammetry results

Sliding distance: +/-20°	Axial load: 900N		
	Inclination angle: 35°		
	A1 - No visible change	A2 - No visible change	A3 - No visible change
Pretest	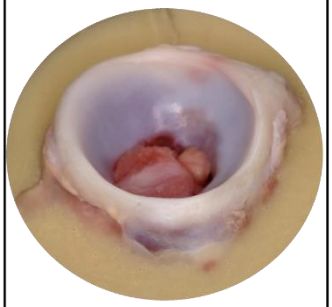		
Post-test	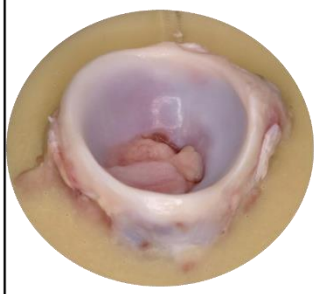		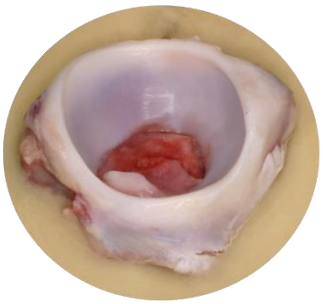

Sliding distance: +/-10°	Axial load: 900N Inclination angle: 35°		
	B1 - Scratching	B2 - Scratching	B3 – Blushing
Pretest	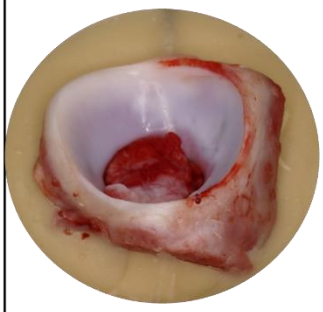	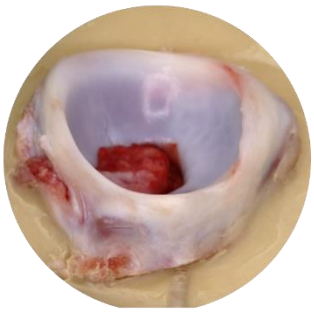	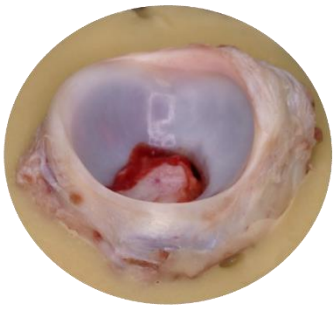
Post-test	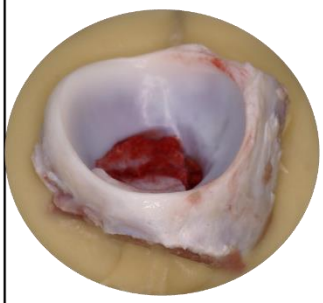	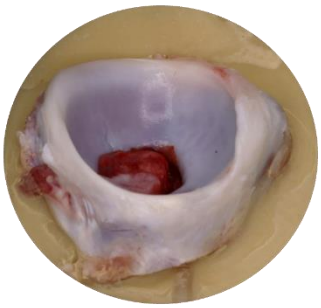	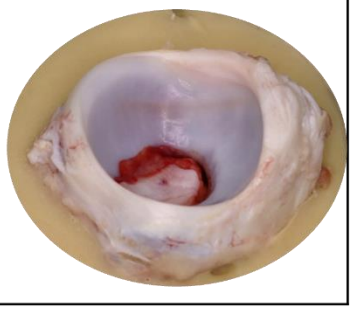

Sliding distance: +/-20°	Axial load: 1130N Inclination angle: 35°		
	C1 - Scratching/Blushing	C2 - Scratching	C3 – Sample dislocated
Pretest	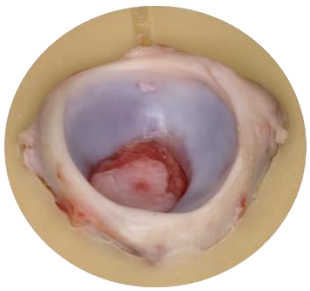	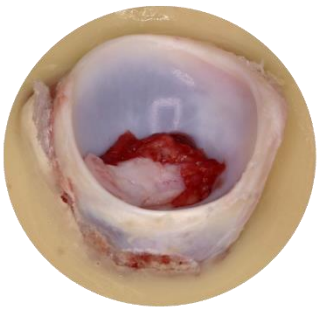	
Post-test		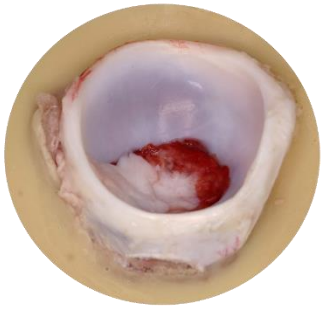	

Sliding distance: +/-10°	Axial load: 1130N		
	Inclination angle: 35°		
	D1 – Scratching/Blushing	D2 – Blushing	D3 – No visible change
Pretest	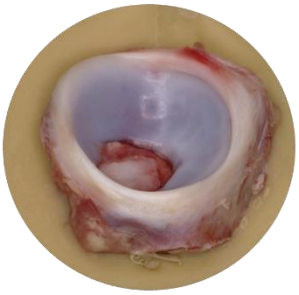	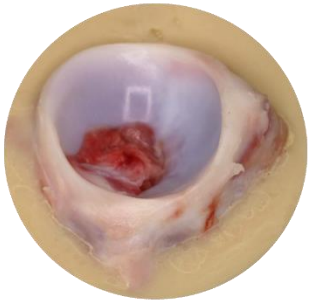	
Post-test		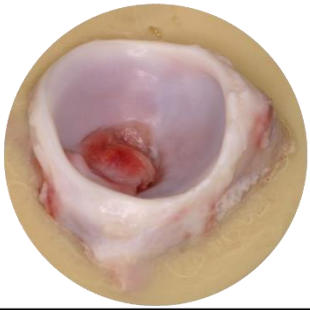	

Sliding distance: +/-10°	Axial load: 1130N		
	Inclination angle: 45°		
	E1 – Dislocated	E2 – Dislocated	E3 - Dislocated
Pretest			
Post-test			

Sliding distance: +/-10° + 1mm Lateral	Axial load: 1130N Inclination angle: 35°		
	F1 – Bubbling/ Blushing	F2 –Blushing/Bubbling initiated	F3 –Blushing/ Bubbling initiated
Pretest			
Post-test			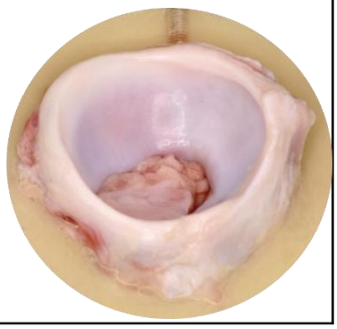

Sliding distance: +/-10°	Axial load: 1130N Inclination angle: 45°		
	G1 – Blushing	G2 – Blushing	G3 – Blushing
Pretest	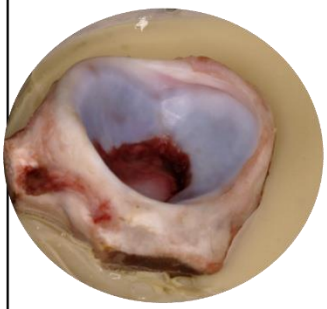	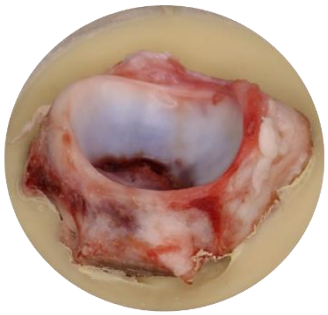	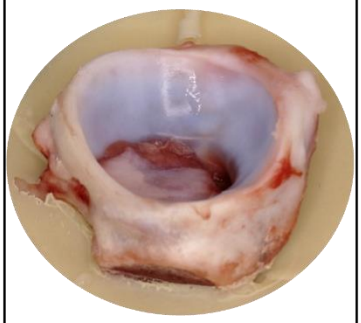
Post-test		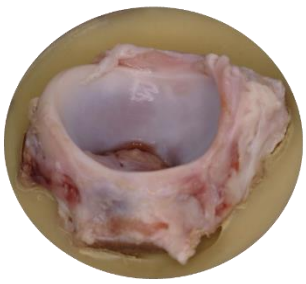	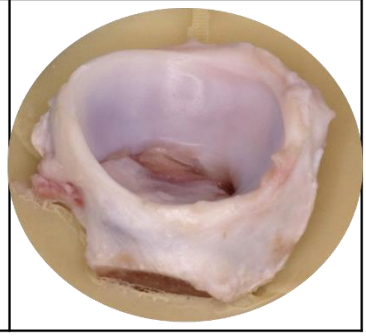

Sliding distance: +/-10° + 1mm Lateral	Axial load: 1500N Inclination angle: 35°		
	H1 – Blushing/ Bubbling	H2 – Bubbling	H3 – Blushing/ Bubbling
Pretest		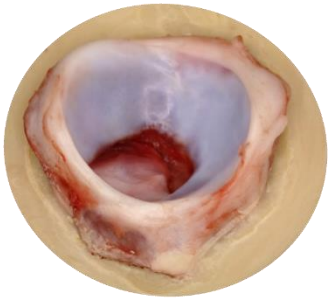	
Post-test		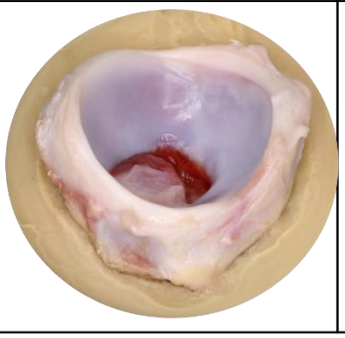	

Sliding distance: +/-10° + 1mm Lateral	Axial load: 1500N Inclination angle: 35° Direction: Perpendicular		
	I1 - Blushing	I2 –Blushing	I3 - Blushing
Pretest	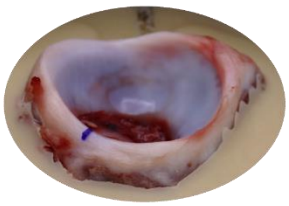	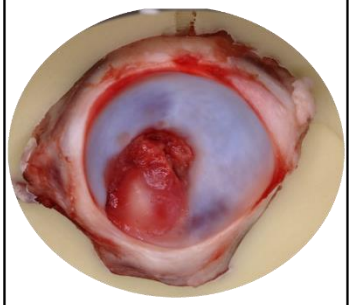	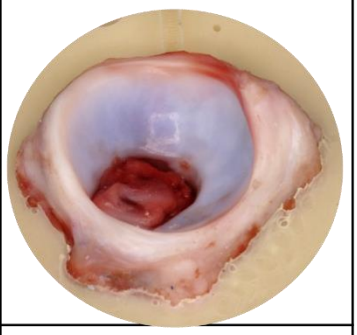
Post-test	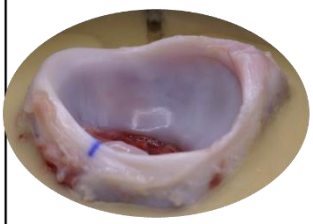	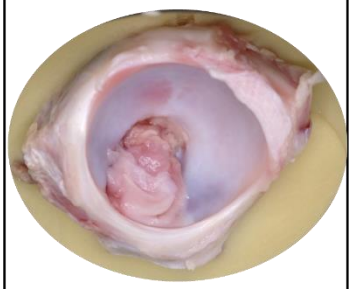	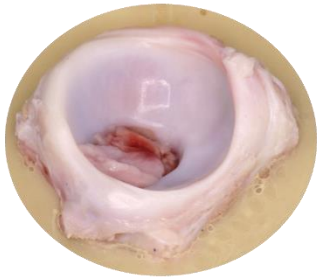

Sliding distance: +/-10° + 1mm Lateral	Axial load: 2500N		
	Inclination angle: 35°		
	J1 – Blushing/Bubbling	J2 – Blushing/bubbling	J3 – Blushing/bubbling
Pretest		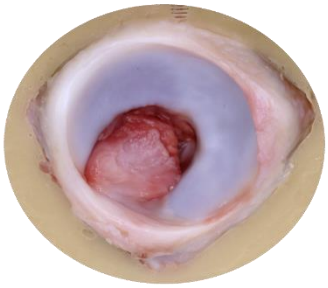	
Post-test	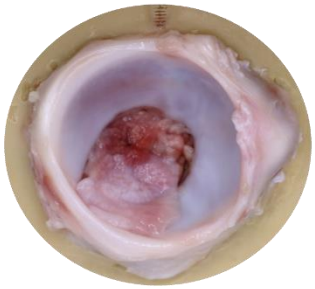		

Sliding distance: +/-5° + 1mm Lateral	Axial load: 2500N		
	Inclination angle: 35°		
	K1 – Blushing/Bubbling	K2 – Blushing/Bubbling	K3 – Blushing/Bubbling
Pretest	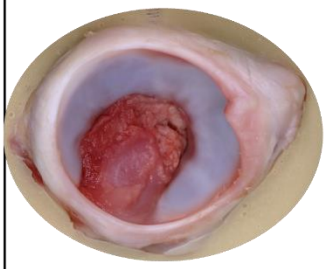		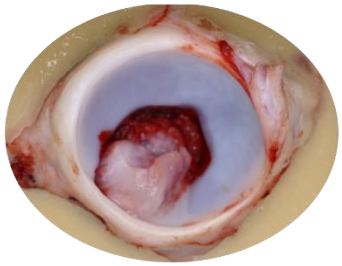
Post-test			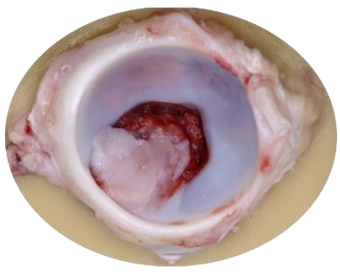

Sliding distance: +/-15° + 1mm Lateral	**Axial load: 2500N**		
	Inclination angle: 35°		
	L1 –Blushing	L2 –Blushing/Bubbling initiated	L3 – Blushing/Bubbling initiated
Pretest	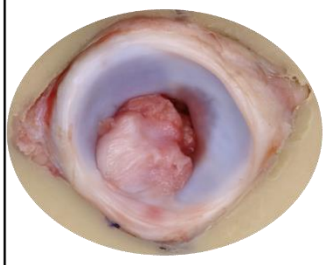	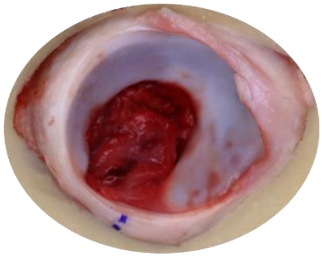	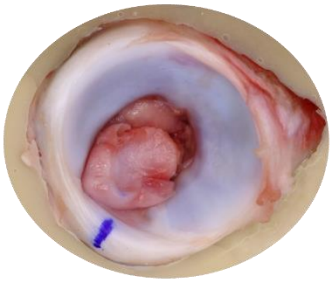
Post-test		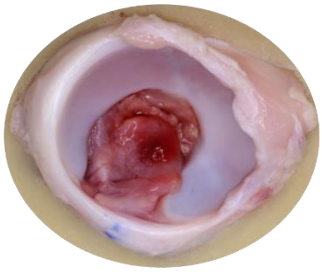	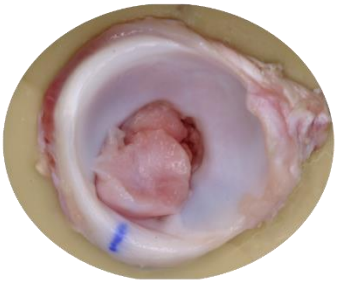

8.4 Appendix D: Photography fixture drawings

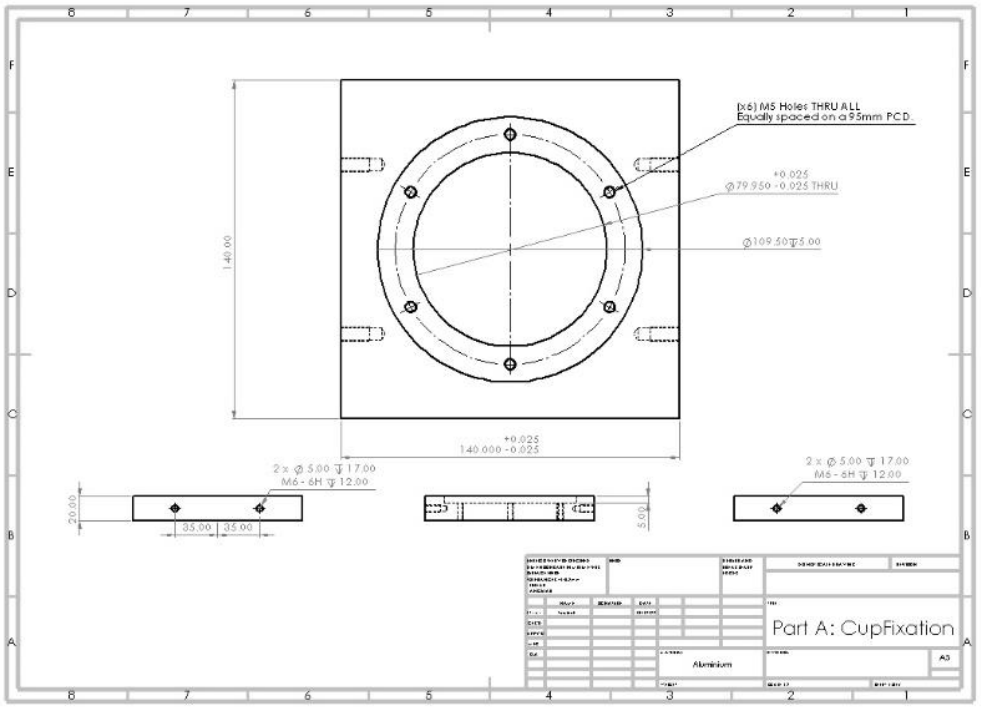

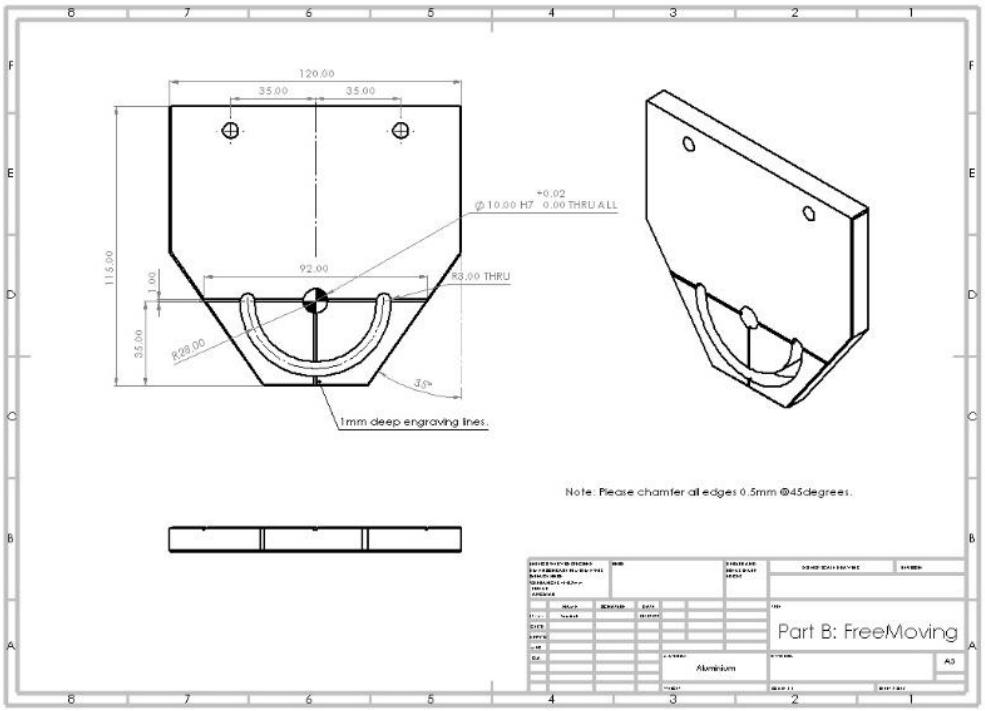

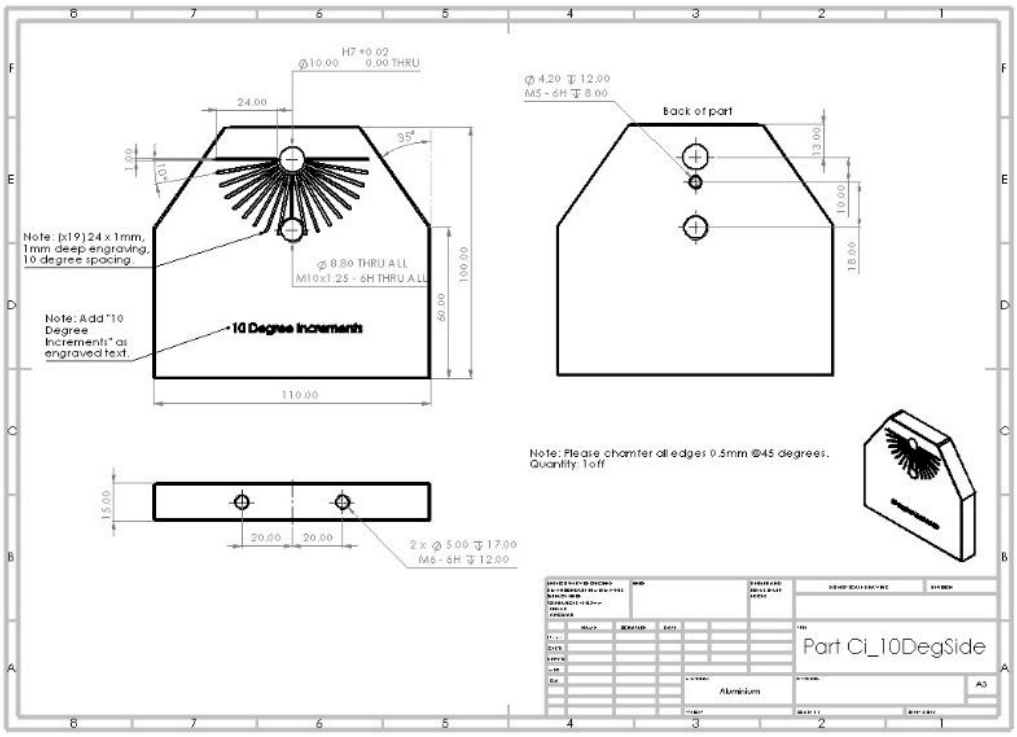
H7 +0.02
Ø10.00 0.00 THRU
24.00
35°
1.00
10.00
Note: (x19) 24 x 1mm, 1mm deep engraving, 10 degree spacing.
Ø 8.80 THRU ALL
M10x1.25 - 6H THRU ALL
100.00
60.00
Note: Add "10 Degree Increments" as engraved text.
10 Degree Increments
110.00
Ø 4.20 ↧ 12.00
M5 - 6H ↧ 8.00
Back of part
13.00
10.00
18.00
Note: Please chamfer all edges 0.5mm @45 degrees.
Quantity: 1 off
15.00
20.00
20.00
2 x Ø 5.00 ↧ 17.00
M6 - 6H ↧ 12.00
Part Ci_10DegSide
Aluminium
A3

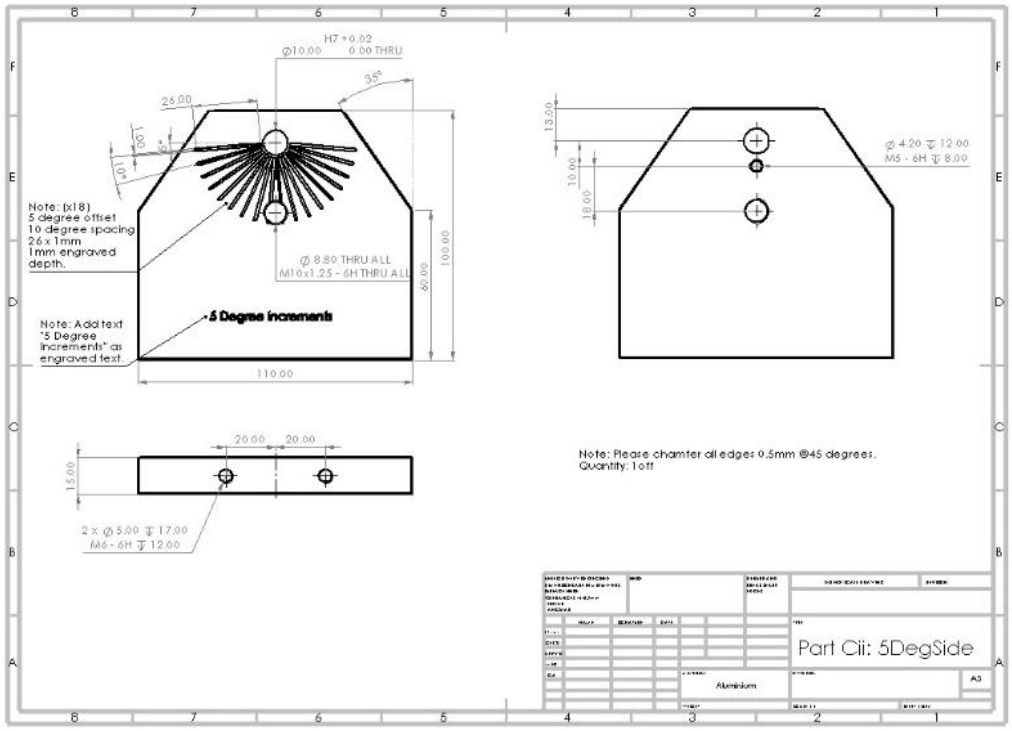
H7 +0.02
Ø10.00 0.00 THRU
35°
26.00
1.00
10.00
Note: (x18) 5 degree offset 10 degree spacing 26 x 1mm 1mm engraved depth.
Ø 8.80 THRU ALL
M10x1.25 - 6H THRU ALL
100.00
60.00
Note: Add text "5 Degree Increments" as engraved text.
5 Degree Increments
110.00
13.00
10.00
18.00
Ø 4.20 ↧ 12.00
M5 - 6H ↧ 8.00
20.00
20.00
15.00
2 x Ø 5.00 ↧ 17.00
M6 - 6H ↧ 12.00
Note: Please chamfer all edges 0.5mm @45 degrees.
Quantity: 1 off
Part Cii: 5DegSide
Aluminium
A3

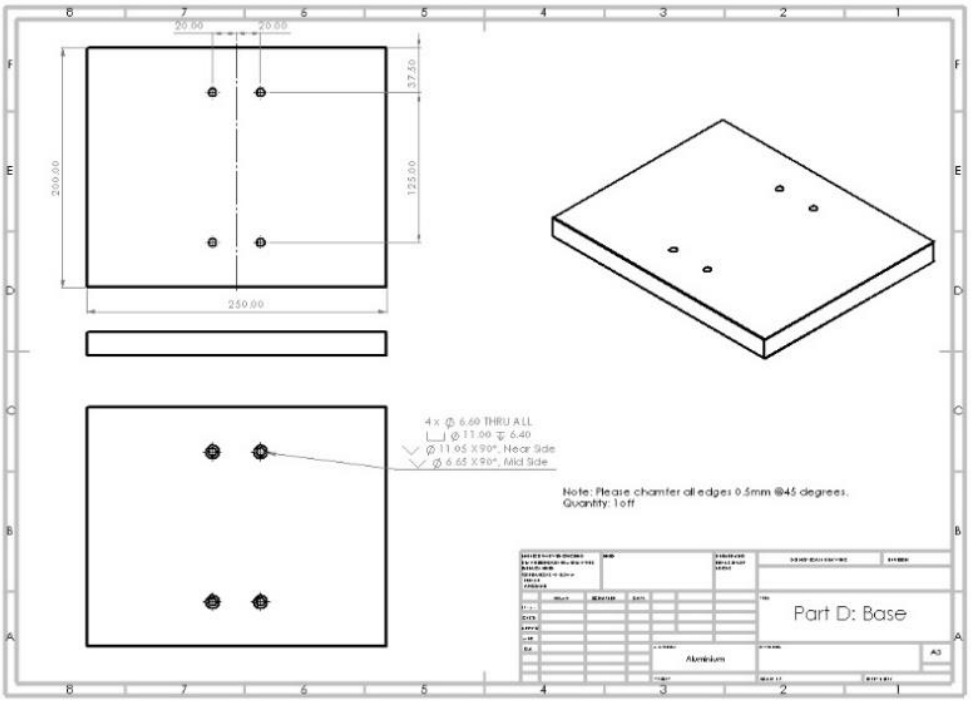
20.00
20.00
37.50
125.00
250.00
250.00
4 x Ø 6.60 THRU ALL
⌴ Ø 11.00 ↧ 6.40
Ø 11.05 X90°, Near Side
Ø 6.65 X90°, Mid Side
Note: Please chamfer all edges 0.5mm @45 degrees.
Quantity: 1 off
Part D: Base
Aluminium
A3

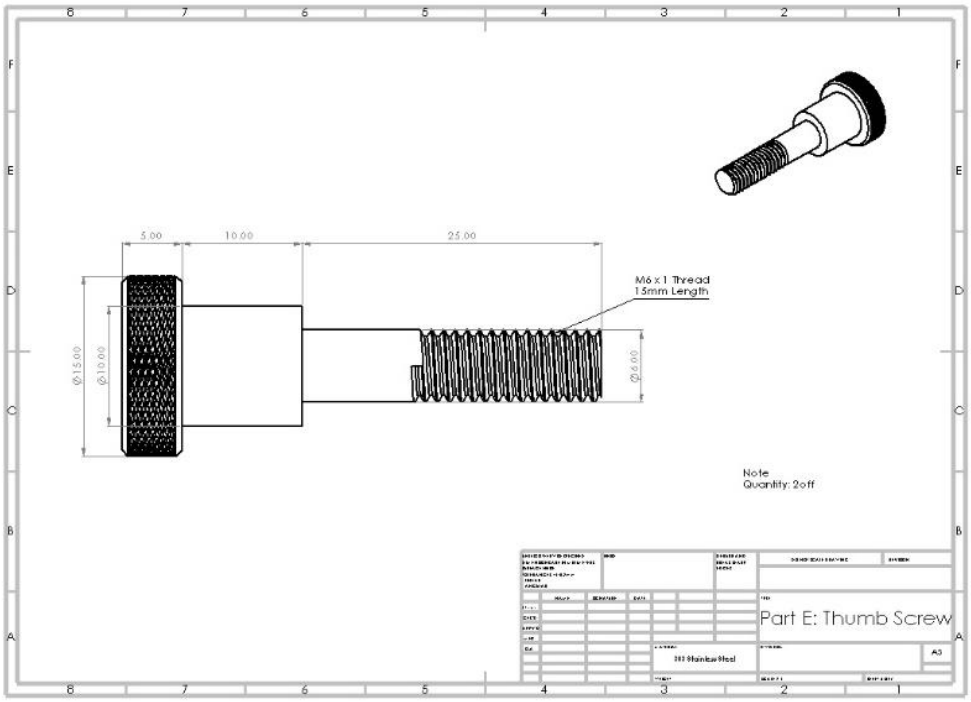
5.00
10.00
25.00
M6 x 1 Thread
15mm Length
Ø15.00
Ø10.00
Ø6.00
Note
Quantity: 2 off
Part E: Thumb Screw
A3

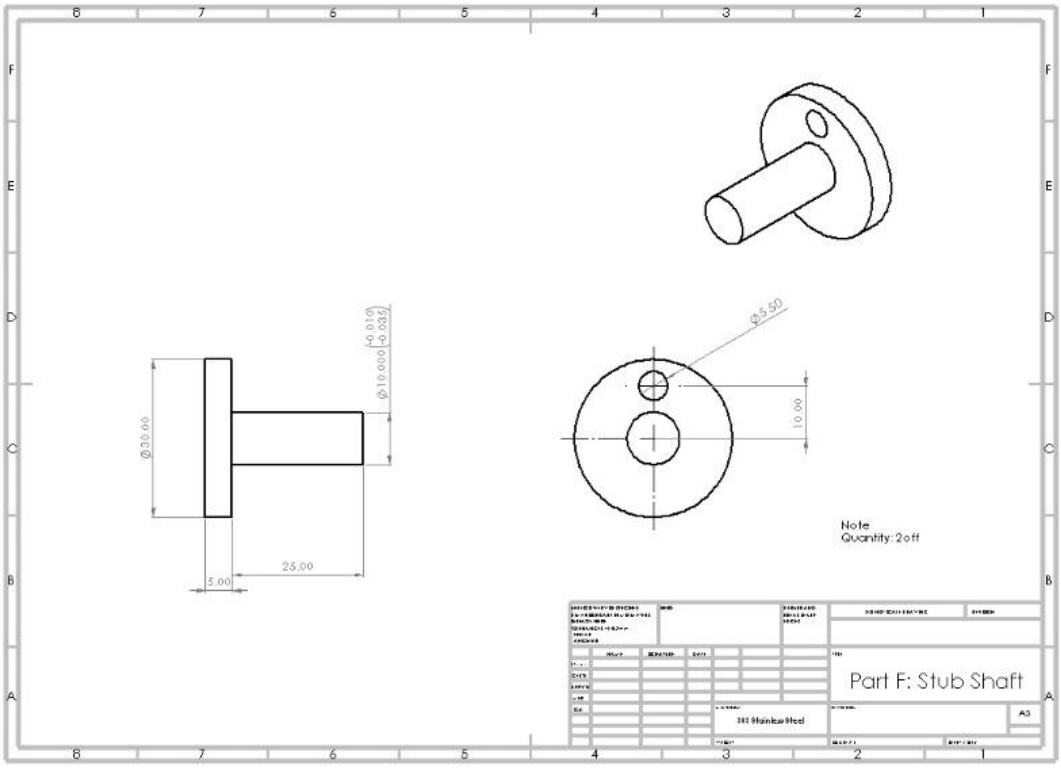
Ø30.00
Ø10.000 +0.019 -0.035
25.00
5.00
Ø5.50
10.00
Note
Quantity: 2 off
Part F: Stub Shaft
A3

8.6 Appendix E: Image permissions

Image permission for reference (Albers et al., 2016), reproduced with the permission of Oxford University Press.

- Licensee: Taiyibah Afzal
- Order Date: Nov 30, 2025
- License Number: 6158830769449
- Publication: Journal of Hip Preservation Surgery
- Title: Imaging of femoroacetabular impingement-current concepts
- Type of Use: Thesis/Dissertation

Image permission for reference Morris et al. (2018), reproduced with the permission of Oxford University Press

- Licensee: Taiyibah Afzal
- Order Date: Nov 30, 2025
- License Number: 6158900312848
- Publication: American Journal of Sports Medicine
- Title: Origin of Cam Morphology in Femoroacetabular Impingement
- Type of Use: Dissertation/Thesis